LOW-RANK MODEL EXPLOITATION OF ELECTROMAGNETIC INDUCTION SENSORS

A Dissertation
Presented to
The Academic Faculty

By

Charles Ethan Hayes

In Partial Fulfillment
of the Requirements for the Degree
Doctor of Philosophy in the
School of Electrical and Computer Engineering

Georgia Institute of Technology

August 2020

Copyright © Charles Ethan Hayes 2020

LOW-RANK MODEL EXPLOITATION OF ELECTROMAGNETIC INDUCTION SENSORS

Approved by:

Dr. James H. McClellan
Advisor
School of Electrical & Computer Engineering
Georgia Institute of Technology

Dr. Waymond R. Scott, Jr.
Co-Advisor
School of Electrical & Computer Engineering
Georgia Institute of Technology

Dr. Mark Davenport
School of Electrical & Computer Engineering
Georgia Institute of Technology

Dr. Alenka Zajic
School of Electrical & Computer Engineering
Georgia Institute of Technology

Dr. Aaron Lanterman
School of Electrical & Computer Engineering
Georgia Institute of Technology

Dr. Joseph Wilson
School of Computer & Information Science & Engineering
University of Florida

Date Approved: May 6, 2020

Each of you should use whatever gift you have received to serve others, as faithful stewards of God's grace in its various forms. If anyone speaks, they should do so as one who speaks the very words of God. If anyone serves, they should do so with the strength God provides, so that in all things God may be praised through Jesus Christ. To him be the glory and the power for ever and ever. Amen.

1 Peter 4:10-11

To all of my family for the loving and encouraging support over the past years.

Thank you so much! I love you all.

ACKNOWLEDGEMENTS

Thank you to all of my professors, family, friends, labmates, and coworkers. I have received so much support and encouragement from all of you. As iron sharpens iron, so have all of you sharpened me. I have learned so much over these past few years through conversations, collaborations, and experiences with all of you. I have learned so many lessons technically, professionally, and personally from all of you, and I cannot thank you enough.

I want to thank my professors, Prof. McClellan and Prof. Scott. I have enjoyed all of these past years being able to work with you. I can honestly say that I would not be at this point completing my PhD if I did not have you as my professors. I have appreciated all of the advice, lessons, conversations, and fellowship that we have shared over the past years. Both of you truly have been great professors to me and I cannot thank you enough!

I want to thank all of my family for their love and support through this process. My wife Ellen, Mom and Marc, Dad and Deanna, Ashley and Tim, Rachel and Kevan, my aunts and uncles, and DaddyCat. I know this has been a long journey coming and I cannot thank you enough for all of the encouragement and support over the years. I am so glad that we get to celebrate this achievement together!

Finally I want to thank God for providing me the ability and opportunity to enjoy this great life. I am humbled by all of the blessings He has provided me and the abilities He has supplied me. I never would have imagined the life He prepared for me so far and all of the doors He has opened to this point. I can never be grateful enough for the love and compassion He has shown me over the years and the comfort and guidance He has provided. I look forward to trusting Him in the years to come and pray that He continues to use me to share His love and compassion to those around me. All of the glory, and honor, and praise be His forever. Amen.

TABLE OF CONTENTS

LIST OF TABLES

LIST OF FIGURES

SUMMARY

Electromagnetic induction (EMI) sensors operate by generating a primary electromagnetic field and measuring the secondary electromagnetic field created from nearby conductive materials. One application of EMI sensors is to detect buried landmines for humanitarian demining missions, as well as military purposes. This research concentrates on improving the signal processing of EMI sensor data for detection, localization, characterization, and classification of targets buried under the surface of the earth.

This thesis draws from well-established techniques in mathematics and other fields to improve EMI processing capabilities. The primary contribution of this work is a new multi-measurement model formulation called the low-rank model for describing EMI data. A physical model for the EMI measurement matrix is written as a product of matrices and then connected to the singular value decomposition of the actual measurement matrix to obtain a new low-rank processing framework. This processing framework introduces new techniques for interference cancellation, detection, classification, localization, orientation, as well as new target features. It is shown that the low-rank framework can recover previously used target features for classification as well. Simulations, lab-collected data, and field-collected data for EMI sensors are used to validate the low-rank model and implement the various signal processing applications. Connections and comparisons to previous EMI processing strategies are provided.

CHAPTER 1
INTRODUCTION

This thesis investigates methods for improving the signal processing of electromagnetic induction (EMI) sensors for detection, localization, characterization, and classification of targets buried under the surface of the earth. EMI sensors operate by generating a primary time-varying electromagnetic field and measuring the secondary electromagnetic field created from the surrounding materials. The secondary field is mostly produced by conductive materials that support eddy currents generated by the primary field. The eddy currents are formed based on the size, shape, and composition of the conductive material, and, thus, the secondary field has a unique signature based on these factors. By measuring the secondary field, EMI sensors obtain information about nearby materials and the data can be processed to extract useful information.

EMI sensors can be used to detect objects hidden behind or beneath obstructions. This capability allows EMI sensors to detect objects buried beneath the surface of the earth. One application is the humanitarian demining of landmines. This is a global problem that affects a multitude of areas and peoples. It is estimated that landmines kill or injure a person every 20 minutes (or more than 20,000 people a year) and children are the most common victims [1]. There are a variety of techniques to aid in the demining process; however, it remains a challenging problem. EMI sensors and ground-penetrating radars (GPR) are the primary methods for detecting landmines for humanitarian demining. Both systems are often plagued by high false alarm rates due to confounding targets. EMI systems must become more sensitive to detect plastic landmines that only contain a small amount of conductive material [1]. Improving the capabilities of future EMI sensors through advanced signal processing will improve detection and reduce false alarm rates. This will provide more effective demining operations that are safer and cheaper in the future.

This thesis focuses on creating a holistic approach to the signal processing of EMI data. A new processing framework is created that exploits the same EMI model through data acquisition, data preprocessing, and all stages of data characterization and exploitation. This is accomplished by returning to the basic signal model and combining concepts from multiple previous EMI processing designs into a new representation for multiple measurements called the 'low-rank model'. The low-rank model provides insights into how one can jointly process EMI measurements for improved performance. A new framework has been designed to exploit the insights from the low-rank model. The framework exploits the low-rank model to provide a number of advancements to EMI signal processing. The framework provides insights into new target features that can be extracted, improved interference reduction through a re-designed preprocessing method, and clearly delineated a strategy for performing processing tasks independently.

The thesis has been organized into two main parts and further reference materials. Part I provides the reader with an in-depth tutorial of the EMI model and the low-rank model from a signal processing perspective. It begins with an introduction into the electromagnetic model of the measurements from an EMI sensor. This is followed by a review of previous signal processing approaches used to exploit EMI sensors for landmine and unexploded ordnance detection. The new low-rank EMI model is then developed and compared with previous processing models. Finally, a new signal processing framework is introduced that is designed to exploit the insights obtained from the low-rank model. Part II provides the reader with insights into some of the many signal processing applications enabled by the new low-rank model framework. Applications of the framework in Part II contain a method for preprocessing the data to remove interference, target detection, rank estimation, recovering target specific features known as the Discrete Spectrum of Relaxations, classification of EMI targets, performing target localization, and recovering the target's orientation. These applications build from various areas of signal processing literature and provide relevant background information as needed. Processing results are applied to sim-

ulated targets, lab-collected data, and EMI data collected under real-world scenarios as is appropriate throughout the thesis. This thesis also concentrates on a set of ten reference targets that are designed to showcase the low-rank model and framework across a representative set of targets. These reference targets are used to demonstrate the framework throughout the thesis. Finally, this thesis provides a variety of extra reference materials in the Appendix. There are three main groupings within the appendix: further EMI model details, maximum likelihood estimation of matrices, and reference tables for important definitions within this thesis. The important definitions appendix is of primary interest as it supplies the reader condensed tables for equations (C.1), mathematical variables (C.2), mathematical operations (C.3), and various acronyms (C.4) used throughout this thesis.

Part I

Development of the Low-Rank EMI Framework

CHAPTER 2
ELECTROMAGNETIC MODEL

This dissertation focuses on understanding and improving the signal processing for EMI systems. In order to exploit the measurements made by an EMI system, it is useful to define a mathematical model of the system measurements. This chapter is designed to give the reader a working knowledge of the electromagnetic model without being a detailed source for electromagnetic equations. The intent is to focus on the structure of the data that enables signal processing to exploit the data optimally.

2.1 Measurement Model

If the magnetic field created by the EMI system is assumed to be uniform across the entire target, then a target can be modeled as a sum of magnetic dipoles at the target's location [2]. This work is focused on small metallic objects for which it only takes a few centimeters between the sensor and target for the uniformity assumption to be true. Under this model, the target can be viewed as a point target at a single location. The strength and direction of the transmitter's magnetic field at the target's location can be described by a three-dimensional vector $\mathbf{h}_T(\ell_{TX} - \ell_M) \in \Re^{3\times 1}$, which is dependent on the location of the transmitter, ℓ_{TX}, and the location of the target, ℓ_M. This magnetic field is called the primary magnetic field and will induce eddy currents in the target that are quantified by the target's *magnetic polarizability*. The *magnetic polarizability* is a symmetric 3×3 matrix $\mathcal{M}$ that fully describes a magnetic point target and all of its magnetic dipoles. The induced dipole moment of the target is calculated as $\mathcal{M}\mathbf{h}_T(\ell_{TX} - \ell_M)$, which becomes the source of a secondary magnetic field. The secondary magnetic field will generate a signal in the receive coil which is measured and recorded by the sensor. Using a reciprocity argument [3], the measured signal can be determined from the induced dipole moment of the target and the receiver's mag-

netic scene. The receiver's magnetic scene is computed as if it is a transmitter and can be described as $\mathbf{h}_R(\ell_{RX} - \ell_M) \in \Re^{3\times 1}$ which depends only on the target location and the EMI receiver's location, ℓ_{RX}.[1] This arrives at a matrix-vector model for a single measurement,

$$\begin{aligned} S(\Delta p) &= \mathbf{h}_R(\ell_{RX} - \ell_M)^T \boldsymbol{\mathcal{m}} \mathbf{h}_T(\ell_{TX} - \ell_M) \\ &= \begin{bmatrix} h_{RX} \\ h_{RY} \\ h_{RZ} \end{bmatrix}^T \begin{bmatrix} m_{XX} & m_{XY} & m_{XZ} \\ m_{YX} & m_{YY} & m_{YZ} \\ m_{ZX} & m_{ZY} & m_{ZZ} \end{bmatrix} \begin{bmatrix} h_{TX} \\ h_{TY} \\ h_{TZ} \end{bmatrix}, \end{aligned} \tag{2.1}$$

where $\Delta p(\ell_{RX}, \ell_{TX}, \ell_M)$ denotes the vector distances $(\ell_{RX} - \ell_M)$ and $(\ell_{TX} - \ell_M)$ between the sensor and the target.

2.2 Types of Sensors

There are two main classes of EMI sensors: time-domain and frequency-domain sensors. These devices differ based on how they generate the primary electromagnetic field. A time-domain EMI sensor uses a high-powered step excitation. The sensor then measures the time derivative of the secondary field from the eddy currents by sampling the change in the electromagnetic field over time as the target releases the energy induced in the eddy currents. A frequency-domain EMI sensor creates a periodic time-varying primary electromagnetic field. This primary field is designed to activate the eddy currents of the target at a chosen set of activation frequencies. The sensor then measures the complex-valued secondary field from the eddy currents in the frequency domain at the activation frequencies and ratios them with a reference signal. These differences in operation cause differing constraints on the EMI sensor hardware design, but the underlying physical model being exploited is nearly the same. Both systems are measuring the *magnetic polarizability* of the target, $\boldsymbol{\mathcal{m}}$. The model for $\boldsymbol{\mathcal{m}}$ changes depending on whether it is being measured

[1] Multiple constants necessary when using reciprocity have been lumped into $\mathbf{h}_R$ to simplify notation.

with a time-domain system, $\boldsymbol{\mathcal{M}}(t)$, or with a frequency-domain system, $\boldsymbol{\mathcal{M}}(\omega)$ [4]. Even though there are operational differences, it is possible to create an agnostic signal processing framework based on a generalized *magnetic polarizability* $\boldsymbol{\mathcal{M}}(\phi)$, where ϕ is a generic measurement parameter, t or ω. This allows for a unified treatment and a broader comparison of signal processing methods. The main difference to note is that $\boldsymbol{\mathcal{M}}(t) \in \Re^{3\times 3}$ as opposed to $\boldsymbol{\mathcal{M}}(\omega) \in \mathfrak{C}^{3\times 3}$. Both of these matrices are symmetric (i.e., $\boldsymbol{\mathcal{M}}^T = \boldsymbol{\mathcal{M}}$) which implies that $\boldsymbol{\mathcal{M}}(\omega) \in \mathfrak{C}^{3\times 3}$ is, in general, not Hermitian.

2.3 Sum of Dipoles Model

The sum of dipoles (SoD) model [2] can be used to model the *magnetic polarizability* even further. The model describes a single point target as being made up of multiple magnetic dipoles. A magnetic dipole is the simplest magnetic target that can be used. An example of a physical dipole is a loop of wire that supports eddy currents that travel around the loop. The sum of dipoles model states that more complex point targets can be modeled by combining multiple magnetic dipoles with different magnitudes and orientations at a single location. Mathematically, this can be written in the frequency-domain and time-domain respectively as

$$\boldsymbol{\mathcal{M}}(\omega) = \alpha_0 \boldsymbol{\mathcal{M}}_0 - \sum_{k=1}^{K} \alpha_k \frac{j\omega/\zeta_k}{1 + j\omega/\zeta_k} \boldsymbol{\mathcal{M}}_k \tag{2.2a}$$

$$\boldsymbol{\mathcal{M}}(t) = \alpha_0 \boldsymbol{\mathcal{M}}_0 \delta(t) - \sum_{k=1}^{K} \alpha_k [\delta(t) - \zeta_k e^{-t\zeta_k} u(t)] \boldsymbol{\mathcal{M}}_k \tag{2.2b}$$

where $\boldsymbol{\mathcal{M}}_k \in \Re^{3\times 3}$ is the target's directional tensor[2] for the k$^{\text{th}}$ dipole, $\alpha_k \in \Re_+$ is the positive magnitude for the strength of the k$^{\text{th}}$ dipole, and $\boldsymbol{\mathcal{M}}_k$ is real, symmetric, and positive semidefinite due to the dipole's electromagnetic properties[3]. The summation terms in (2.2)

[2] In this work, tensor refers to the classic tensor definition from mathematics and physics. These are rank-two tensors (or matrices) that are formed from the outer product of vectors.

[3] Here it is assumed that the magnetic susceptibility of the target is positive, linear, and frequency independent. This is generally true for practical applications.

are due to the eddy current on the dipoles. The 0^{th} elements of (2.2) are not due to eddy currents but are due to the magnetic susceptibility of the target. Most time-domain systems start sampling after $t = 0$ to miss the effects of the delta functions so (2.2b) can be rewritten as

$$\boldsymbol{m}(t) = -\sum_{k=1}^{K} \alpha_k [-\zeta_k e^{-t\zeta_k} u(t)] \boldsymbol{m}_k \tag{2.3}$$

where the 0^{th} term does not contribute to the polarizability. Equation (2.2) can be rewritten as a generalized *magnetic polarizability*

$$\boxed{\boldsymbol{m}(\phi) = -\sum_{k=0}^{K} \alpha_k f_k(\phi) \boldsymbol{m}_k} \tag{2.4}$$

where for the frequency-domain system

$$\boxed{\begin{aligned} f_0(\omega) &= -1 && \text{(2.5a)} \\ f_k(\omega) &= \frac{j\omega/\zeta_k}{1 + j\omega/\zeta_k} && \text{(2.5b)} \end{aligned}}$$

and for the time-domain system

$$\boxed{\begin{aligned} f_0(t) &= 0 && \text{(2.6a)} \\ f_k(t) &= -\frac{1}{\tau_k} e^{\frac{-t}{\tau_k}} u(t) && \text{(2.6b)} \end{aligned}}$$

where the Fourier transform $f_k(\omega) = \mathfrak{F}\{\delta(t) + f_k(t)\}$ connects the two sensors, the sign of α_0 is moved into the f_0 term to make $\forall \alpha_k \in \Re_+$, and the time-domain sensor is often defined in terms of the decay rate $\tau_k = \zeta_k^{-1}$ instead of the relaxation frequency.

The factorization of the $\boldsymbol{m}(\phi)$ matrix in (2.4) also helps explain why $\boldsymbol{m}$ is symmetric and not Hermitian symmetric. The matrix component $\boldsymbol{m}_k$ is always real-valued and all of the other terms are scalars. This means that each dipole tensor will be symmetric regardless

of the type of EMI system taking the measurements.[4]

For frequency-domain sensors, it has been shown that an alternate representation to (2.5) is the *allpass* form:

$$\boxed{f_k(\omega) = \frac{1 - j\omega/\zeta_k}{1 + j\omega/\zeta_k}} \tag{2.7}$$

where this representation is obtained by redefining the coefficient terms α_k [5]. For processing data from the frequency-domain sensors, (2.7) is preferred in this effort because it causes the magnitude of the $f_k(\omega)$ values to be equal to one for any choice of ζ_k and ω. It should be noted that not all efforts should use (2.7) because it is achieved by mixing the magnetic response f_0 with the eddy current responses of f_k which can be counterproductive. However, in this work the preprocessing that is introduced minimizes this modeling impact.

2.4 Ortho-Point Target Assumption

The above model (2.4) can represent any EMI point target. However, most man-made targets are sufficiently symmetrical so that all the $\boldsymbol{m}_k$'s in (2.4) can be simplified when the coordinate system is oriented properly.[5] When the target is measured in its inherent coordinate system, all of the dipole moments are directed in the direction of one or more of the coordinate system's primary axis. This means that each dipole's directional tensor can be represented by a diagonal matrix $\vec{\boldsymbol{\Lambda}}_k \in \Re^{3\times3}$. This special type of target will be called an ortho-point target. The ortho-point target is a very common occurrence when searching for man-made items, and it allows for further processing and model exploitation. For this reason, it is worth also investigating EMI responses from ortho-point targets specifically.

The diagonal nature of $\vec{\boldsymbol{\Lambda}}_k$ is only true for the target's coordinate system, and the notation $\vec{\square}$ will be used for any variable that is defined in this coordinate system. The EMI sensor will not always measure the target in the target's coordinate system. Given an arbi-

[4] See Appendix A.1

[5] See chapter 7 in [2] for a discussion of target symmetry.

trary x-y-z coordinate system, there exists a unitary rotation matrix $\vec{\mathbf{E}} \in \Re^{3\times3}$ that can map it into the target's coordinate system. Using this, the dipole moment of an arbitrary x-y-z coordinate system can be written as

$$\mathcal{m}_k = \vec{\mathbf{E}}\vec{\mathbf{\Lambda}}_k\vec{\mathbf{E}}^T. \tag{2.8}$$

The definition in (2.8) can be inserted in (2.4) to obtain

$$\boxed{\mathcal{m}(\phi) = -\sum_{k=0}^{K} \alpha_k f_k(\phi)\vec{\mathbf{E}}\vec{\mathbf{\Lambda}}_k\vec{\mathbf{E}}^T,} \tag{2.9}$$

which is the sum of dipoles model for an ortho-point target.

This target coordinate system assumption can also be extended to the full *magnetic polarizability* to create

$$\mathcal{m}(\phi) = -\sum_{k=0}^{K} \alpha_k f_k(\phi)\vec{\mathbf{E}}\vec{\mathbf{\Lambda}}_k\vec{\mathbf{E}}^T = \vec{\mathbf{E}}(-\sum_{k=0}^{K} \alpha_k f_k(\phi)\vec{\mathbf{\Lambda}}_k)\vec{\mathbf{E}}^T = \vec{\mathbf{E}}\vec{\mathbf{\Lambda}}(\phi)\vec{\mathbf{E}}^T \tag{2.10}$$

where $\vec{\mathbf{\Lambda}}(\phi)$ is a 3×3 diagonal matrix that describes the target's response to the sensor and is dependent on the type of primary electromagnetic field. This shows that the target's response for ortho-point targets is completely described by

$$\vec{\mathbf{\Lambda}}(\phi) = -\sum_{k=0}^{K} \alpha_k f_k(\phi)\vec{\mathbf{\Lambda}}_k. \tag{2.11}$$

The matrix $\vec{\mathbf{\Lambda}}(t) \in \Re^{3\times3}$ will be real-valued for time-domain sensors and $\vec{\mathbf{\Lambda}}(\omega) \in \mathfrak{C}^{3\times3}$ for frequency-domain sensors.

This also means that for ortho-point targets the single measurement model can be de-

scribed as

$$\begin{aligned} S(\Delta p) =& \mathbf{h}_R(\ell_{RX} - \ell_M)^T \boldsymbol{\mathcal{M}} \mathbf{h}_T(\ell_{TX} - \ell_M) \\ =& \vec{\mathbf{h}}_R(\ell_{RX} - \ell_M)^T \vec{\mathbf{E}}^T \boldsymbol{\mathcal{M}} \vec{\mathbf{E}} \vec{\mathbf{h}}_T(\ell_{TX} - \ell_M) \\ =& \vec{\mathbf{h}}_R(\ell_{RX} - \ell_M)^T \vec{\boldsymbol{\Lambda}} \vec{\mathbf{h}}_T(\ell_{TX} - \ell_M) \end{aligned} \tag{2.12}$$

where the $\vec{\mathbf{h}} \in \Re^{3\times 1}$ vectors are aligned to the target's coordinate system and are defined as $\vec{\mathbf{h}} = \vec{\mathbf{E}}^T \mathbf{h}$.

When given an arbitrary *magnetic polarizability* from an ortho-point target, it is possible to obtain the target's coordinate system and the diagonal response representation from (2.10) by factoring the matrix into

$$\boxed{\boldsymbol{\mathcal{M}} = \vec{\mathbf{E}} \vec{\boldsymbol{\Lambda}} \vec{\mathbf{E}}^T.} \tag{2.13}$$

For real-valued matrices from time-domain sensors, this is an eigendecomposition of $\boldsymbol{\mathcal{M}}$. For complex-valued matrices from frequency-domain sensors, this decomposition can be obtained through a specialized Autonne-Takagi factorization as shown in Appendix A.3. Note that because of the special nature of $\boldsymbol{\mathcal{M}}$ under the ortho-point assumption, the $\vec{\mathbf{E}}$ term does not change based on the ϕ measurement.

2.5 Example EMI Targets

Throughout this effort, it is useful to have a few reference targets that illustrate the application of the signal processing for EMI sensors. The reference targets are shown in Fig. 2.1. These images demonstrate a method of visually describing EMI targets. Based on the model in (2.4), these plots show the $\alpha_k \boldsymbol{\mathcal{M}}_k$ terms. Because $\boldsymbol{\mathcal{M}}_k$ is symmetric, only the unique values need to be plotted.

For ortho-point targets, the dipoles have been rotated to the target coordinate system so that $\vec{\boldsymbol{\Lambda}}_k$ is plotted. This will cause the XY, XZ, and YZ components to always be zero

because $\vec{\mathbf{\Lambda}}_k$ is diagonal. The XX, YY, and ZZ components contain the three values that correspond to the target's x-y-z coordinate system.

These values correspond to a specific relaxation frequency but are independent of the type of measurements (ϕ) and position information (Δp). A target can be uniquely visualized by plotting these values across the measurable range of an EMI sensor. The plots in Fig. 2.1 show the targets' $\boldsymbol{m}_k$ components along the Y-axis and the relaxation frequencies across the X-axis. To make the plots more readable, the log of the relaxation frequencies in Hz, $f_\zeta = \zeta/2\pi$, are plotted in decades[6].

These reference targets are simplified target models. The main simplification is that each component value is $\alpha_k \boldsymbol{m}_k \in \{0, 1\}$ except for the final two targets. Removing the relative amplitudes removes an extra dimension of actual targets and is intended to allow the reader to more easily track the impacts of the signal processing on EMI targets. This simplification has no impact on the signal processing, but it does make some of the reference targets less realistic. The last two targets have amplitude variations in $\alpha_k \boldsymbol{m}_k$ to illustrate how the amplitudes are represented throughout the model.

Reference targets one and two represent the most basic targets that an EMI sensor can measure. Target one (which will be referred to as RT-01) represents a single wire coil. It can be represented mathematically as

$$\boldsymbol{m} = -f_{3.7}(\phi) \begin{bmatrix} 1 & 0 & 0 \\ 0 & 0 & 0 \\ 0 & 0 & 0 \end{bmatrix} \tag{2.14}$$

where the subscript of f represents the relaxation frequency in decades. Target two (which will be referred to as RT-02) is a target that is made of three wire coils, each coil pointing along one of the orthogonal coordinate axes. The mathematical representation of the target

[6]Here and in the remainder of this work, the frequencies are often presented as decades where $f_{decades} = log_{10}(f_\zeta/f_o) = log_{10}(f_\zeta)$ where $f_0 = 1Hz$ and the f_0 is suppressed in the notation.

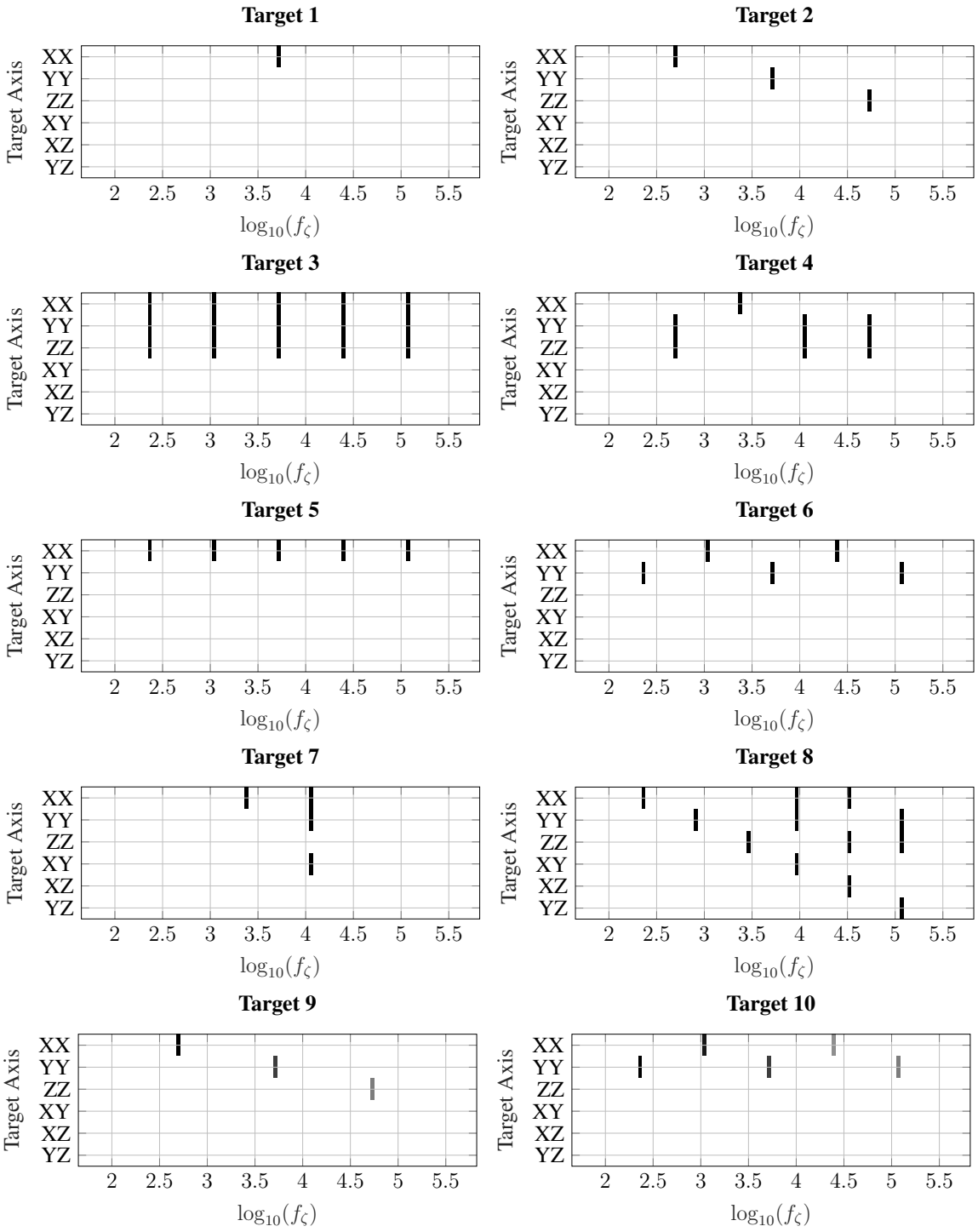

Figure 2.1: Reference targets' relaxation frequency representations.

is

$$m = -f_{2.7}(\phi)\begin{bmatrix}1&0&0\\0&0&0\\0&0&0\end{bmatrix} - f_{3.7}(\phi)\begin{bmatrix}0&0&0\\0&1&0\\0&0&0\end{bmatrix} - f_{4.7}(\phi)\begin{bmatrix}0&0&0\\0&0&0\\0&0&1\end{bmatrix}. \tag{2.15}$$

These targets could be physically created even with the shown magnitudes if desired. The physical representation of these targets are shown in Fig. 2.2.

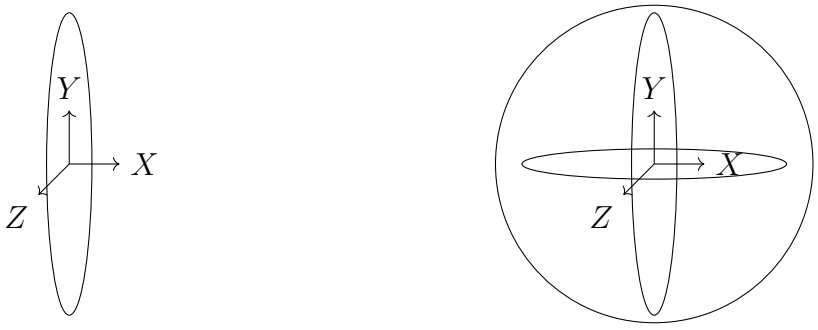

(a) RT-01 (b) RT-02

Figure 2.2: Physical shapes of coil reference targets. (a) is a single wire coil. (b) is a target with three orthogonal wire coils.

Reference targets three and four represent a special class of EMI targets known as degenerate targets. Degenerate targets have at least one axis of rotational symmetry. When a target has symmetry, it means that multiple eigenvalues of $\boldsymbol{m}(\phi)$ are exactly the same and the rotation matrices $\vec{\mathbf{E}}$ are not unique. See Appendix A.2 for further details on degenerate targets. Target three (which will be referred to as RT-03) is an example of a target that has symmetry in all three dimensions. A realistic target such as a sphere would have three-dimensional symmetry like target 3.[7] The mathematical representation of the target is

$$\boldsymbol{m} = -\sum_{k=\mathcal{A}_3} f_k(\phi) \begin{bmatrix} 1 & 0 & 0 \\ 0 & 1 & 0 \\ 0 & 0 & 1 \end{bmatrix} \tag{2.16}$$

where the set of frequencies is $\mathcal{A}_3 \in \{2.4, 3, 3.7, 4.4, 5.1\}$. Target four (which will be referred to as RT-04) is an example of a target with two-dimensional symmetry. For RT-04, the target is symmetric in its y-z coordinates. This is similar to a metal cylinder where its

[7] An actual sphere would have relaxation amplitudes that decrease as the relaxation frequency increases and the relaxations would be linearly spaced instead of logarithmically.

axis of rotation is in the x direction. The mathematical representation of the target is

$$\mathcal{M} = -f_{3.4}(\phi) \begin{bmatrix} 1 & 0 & 0 \\ 0 & 0 & 0 \\ 0 & 0 & 0 \end{bmatrix} - \sum_{k=\mathcal{A}_4^{YZ}} f_k(\phi) \begin{bmatrix} 0 & 0 & 0 \\ 0 & 1 & 0 \\ 0 & 0 & 1 \end{bmatrix} \tag{2.17}$$

where $\mathcal{A}_4^{YZ} \in \{2.7, 4.1, 4.7\}$. Realistic targets could look like metal objects in the shape of Fig. 2.3.

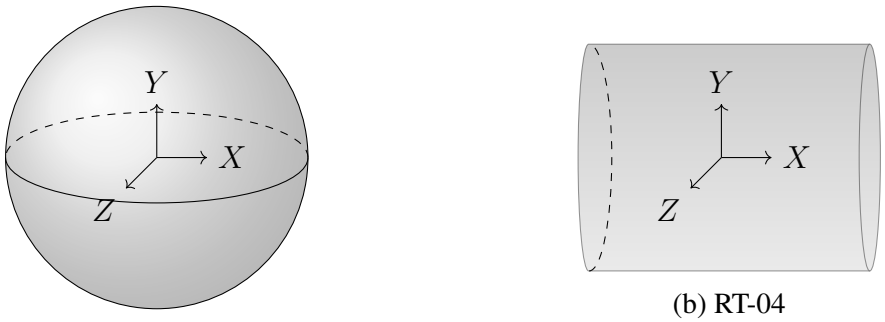

(a) RT-03

(b) RT-04

Figure 2.3: Possible physical shapes of degenerate reference targets. (a) is a rotationally symmetric target in all three dimensions. (b) is a rotationally symmetric target in the y-z dimensions.

Targets five and six are not connected to specific physical objects, but they are useful for analysis throughout this work. Both targets have the exact same relaxation frequencies as RT-03. The only difference is which coordinates the relaxations are active. Target five (RT-05) has all of its relaxation frequencies in the x dimension of the target. The mathematical representation of the target is

$$\mathcal{M} = -\sum_{k=\mathcal{A}_5^{X}} f_k(\phi) \begin{bmatrix} 1 & 0 & 0 \\ 0 & 0 & 0 \\ 0 & 0 & 0 \end{bmatrix} \tag{2.18}$$

where $\mathcal{A}_5^X \in \{2.4, 3, 3.7, 4.4, 5.1\}$. Target six (RT-06) has some of its relaxations in the x dimension and others in the y dimension of the target. The mathematical representation of

the target is

$$\boldsymbol{m} = -\sum_{k=\mathcal{A}_6^X} f_k(\phi) \begin{bmatrix} 1 & 0 & 0 \\ 0 & 0 & 0 \\ 0 & 0 & 0 \end{bmatrix} - \sum_{j=\mathcal{A}_6^Y} f_j(\phi) \begin{bmatrix} 0 & 0 & 0 \\ 0 & 1 & 0 \\ 0 & 0 & 0 \end{bmatrix} \tag{2.19}$$

where $\mathcal{A}_6^X \in \{3, 4.4\}$ and $\mathcal{A}_6^Y \in \{2.4, 3.7, 5.1\}$.

Targets seven and eight are two examples of targets that violate the ortho-point target assumption. These targets can be created by combining co-located wire coils of different sizes as shown in Fig. 2.4. Target seven (RT-07) can be made of two coils, one directed in the XX direction and the other directed 45° between the XX and YY direction. The mathematical representation of RT-07 is

$$\boldsymbol{m} = -f_{3.4}(\phi) \begin{bmatrix} 1 & 0 & 0 \\ 0 & 0 & 0 \\ 0 & 0 & 0 \end{bmatrix} - f_{4.1}(\phi) \begin{bmatrix} 1 & 1 & 0 \\ 1 & 1 & 0 \\ 0 & 0 & 0 \end{bmatrix}. \tag{2.20}$$

Target eight (RT-08) is a set of six co-located wire coils. Three of the coils are pointed orthogonal to each other in the x-y-z coordinates respectively. The other three are a set of orthogonal coils that have been rotated by 45° in each direction from the original x-y-z coordinates before being co-located with the first set of coils.[8] The mathematical represen-

[8]The coils are analyzed here as if they are not coupled together. In a physical system, the coils as shown in Fig. 2.4 may couple together sufficiently to make a target with ortho-point symmetry. However, it is always possible to shift the coils relative to each other to make them behave as described.

tation of the target is

$$\begin{aligned}\boldsymbol{m} = &- f_{2.4}(\phi)\begin{bmatrix}1&0&0\\0&0&0\\0&0&0\end{bmatrix} - f_{2.9}(\phi)\begin{bmatrix}0&0&0\\0&1&0\\0&0&0\end{bmatrix} - f_{3.5}(\phi)\begin{bmatrix}0&0&0\\0&0&0\\0&0&1\end{bmatrix} \\ &- f_{4.0}(\phi)\begin{bmatrix}1&1&0\\1&1&0\\0&0&0\end{bmatrix} - f_{4.5}(\phi)\begin{bmatrix}1&0&1\\0&0&0\\1&0&1\end{bmatrix} - f_{5.1}(\phi)\begin{bmatrix}0&0&0\\0&1&1\\0&1&1\end{bmatrix}.\end{aligned} \tag{2.21}$$

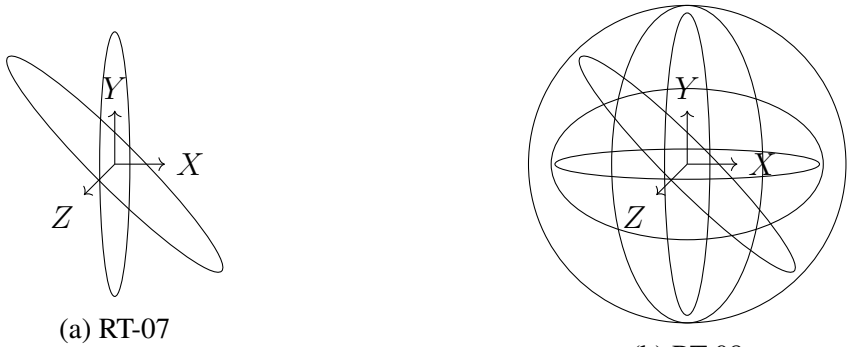

(a) RT-07

(b) RT-08

Figure 2.4: Physical shapes of reference targets that violate the ortho-point target assumption. (a) is the simplest target possible that breaks the ortho-point assumption. (b) is a target that breaks the ortho-point assumption and has a dipole active in each dimension.

Targets nine and ten are the same targets as previous reference targets, but they have different amplitudes that are not $\alpha_k \boldsymbol{m}_k \in \{0, 1\}$. Target nine (RT-09) is nearly identical to RT-02 except the amplitudes are not equal. The mathematical representation of the target is

$$\boldsymbol{m} = -f_{2.7}(\phi)\begin{bmatrix}1&0&0\\0&0&0\\0&0&0\end{bmatrix} - \frac{3}{4}f_{3.7}(\phi)\begin{bmatrix}0&0&0\\0&1&0\\0&0&0\end{bmatrix} - \frac{1}{2}f_{4.7}(\phi)\begin{bmatrix}0&0&0\\0&0&0\\0&0&1\end{bmatrix} \tag{2.22}$$

where it is noted that the y and z dimension no longer have an amplitude of 1. Target ten (RT-10) is nearly identical to RT-06 except the amplitudes are not equal. The mathematical

representation of the target is

$$\boldsymbol{m} = -\sum_{k=\mathcal{A}_{10}^{X}} f_k(\phi) \begin{bmatrix} 1 & 0 & 0 \\ 0 & 0 & 0 \\ 0 & 0 & 0 \end{bmatrix} - \sum_{j=\mathcal{A}_{10}^{Y}} f_j(\phi) \begin{bmatrix} 0 & 0 & 0 \\ 0 & 1 & 0 \\ 0 & 0 & 0 \end{bmatrix} \tag{2.23}$$

where the sets $\mathcal{A}_{10}^{X}$ and $\mathcal{A}_{10}^{Y}$ now contain pairs of values that control the amplitude and relaxation frequency. The sets are $\mathcal{A}_{10}^{X} \in \{(\frac{9}{10}, 3), (\frac{9}{20}, 4.4)\}$ and $\mathcal{A}_{10}^{Y} \in \{(1, 2.4), (\frac{3}{4}, 3.7), (\frac{1}{2}, 5.1)\}$.

CHAPTER 3

PREVIOUS FRAMEWORKS FOR EMI SENSORS

3.1 Joint Diagonalization

Some authors have proposed a framework based on multiple spatial measurements [6, 7, 8]. Starting from (2.1) using a single measurement parameter, it is straightforward to see that the magnetic polarizability is a 3×3 matrix that has at most a rank of three. This can be exploited if the model in (2.1) can be directly expanded into a matrix. In order to accomplish this, a specific measurement strategy can be planned. If a single receiver location is used, then a transmitter can be placed at N_T locations, $\boldsymbol{\ell_{TX}}$. This measurement design expands the component $\mathbf{h}_T$ into a matrix $\mathbf{H}_T \in \Re^{3\times N_T}$. This now expands the set of measurements into a vector representation given by

$$\mathbf{S}(\phi, \ell_{RX}, \boldsymbol{\ell_{TX}}) = \mathbf{h}_R(\ell_{RX} - \ell_M)^T \boldsymbol{\mathcal{M}}(\phi)\mathbf{H}_T(\boldsymbol{\ell_{TX}} - \ell_M). \tag{3.1}$$

The same expansion can be obtained by moving the receiver to a set of N_R receive locations, $\boldsymbol{\ell_{RX}}$, while keeping the transmitter location constant. If the sensor is designed such that every receiver in $\boldsymbol{\ell_{RX}}$ measures the target from every transmit location in $\boldsymbol{\ell_{TX}}$, then the measurements from each receive location can be concatenated next to each other such that

the data forms an $N_R \times N_T$ matrix modeled as

$$\mathbf{S}(\phi, \boldsymbol{\ell_{RX}}, \boldsymbol{\ell_{TX}}) = \begin{array}{|c|c|c|} \hline & & \\ & \boldsymbol{\mathcal{M}}(\phi) & \mathbf{H}_T(\boldsymbol{\ell_{TX}}) \\ \mathbf{H}_R(\boldsymbol{\ell_{RX}})^T & & \\ & & \\ \hline \end{array} \tag{3.2}$$

where the dependence on the target's location (ℓ_M) has been dropped for notational convenience. This is a low-rank matrix where the rank is equal to the rank of $\boldsymbol{\mathcal{M}}(\phi)$. The low-rank matrix can be recovered using a singular value decomposition (SVD) where the singular vectors contain the receiver and transmitter magnetic scenes respectively. The sensor can be designed in such a manner that the list of receiver and transmitter locations are equivalent ($\boldsymbol{\ell_{TX}} \equiv \boldsymbol{\ell_{RX}}$) and they have the same receive/transmit properties. If these highly specialized conditions are met, then the receiver and transmitter magnetic scenes will be the same ($\mathbf{H}_R = \mathbf{H}_T$), and an eigenvalue decomposition[1] can be used to extract the low-rank matrix. Assuming the target meets the ortho-point target assumption, the eigenvalue decomposition will also convert the data into the target's coordinate system such that

$$\text{Eig}\{\mathbf{S}(\phi, \boldsymbol{\ell_{RX}}, \boldsymbol{\ell_{TX}})\} = \vec{\mathbf{H}}_R(\boldsymbol{\ell_{RX}} - \ell_M)^T \vec{\boldsymbol{\Lambda}}(\phi) \vec{\mathbf{H}}_T(\boldsymbol{\ell_{TX}} - \ell_M) \tag{3.3}$$

where $\vec{\boldsymbol{\Lambda}}(\phi)$ is a 3×3 diagonal matrix.

This diagonalization process only works when a single measurement parameter is used. This means that only a single measurement frequency is used for a frequency-domain system, or a single time delay for a time-domain system. On the other hand, many systems

[1]For a frequency-domain sensor, the Autonne-Takagi factorization must be used for the complex-valued data.

collect multiple measurements for each relative location, $\mathbf{\Delta p}$. In order to jointly exploit the multiple measurement parameters, it can be noted that the magnetic scenes ($\vec{\mathbf{H}}_R$ and $\vec{\mathbf{H}}_T$) will not change because they are only dependent on the relative positions which are constant. If it is an ortho-point target such that (3.3) is true, then the rotation to the target's coodinate system is also consistent across measurements and the only changes occur in $\vec{\mathbf{\Lambda}}(\phi)$. Because of this, it is possible to better exploit the data by jointly estimating the diagonalization of the data. This is equivalent to modeling the signal as a tensor of size $M \times N_R \times N_T$ where M is the number of measurements taken at each position and each element in the tensor is calculated by

$$\mathbf{S}^{h,j,k}(\boldsymbol{\phi}, \boldsymbol{\ell_{RX}}, \boldsymbol{\ell_{TX}}) = \sum_{l=1}^{3} \vec{\mathbf{H}}_R^{j,l}(\boldsymbol{\ell_{RX}} - \ell_M)^T \vec{\mathbf{\Lambda}}^{h,l}(\boldsymbol{\phi}) \vec{\mathbf{H}}_T^{k,l}(\boldsymbol{\ell_{TX}} - \ell_M). \tag{3.4}$$

The superscripts h-j-k are the index for the element inside the three-dimensional data cube. The $\vec{\mathbf{H}}_R \in \Re^{3\times N_R}$ and $\vec{\mathbf{H}}_T \in \Re^{3\times N_T}$ matrices have been unchanged from (3.3). The $\vec{\mathbf{\Lambda}}(\boldsymbol{\phi})$ matrix of size $3\times M$ has been created by taking the diagonal elements for each measurement $\boldsymbol{\phi}_h$ and concatenating them into a matrix. This matrix will be real or complex valued depending on the type of EMI sensor.

This shows that the data cube can be represented by summing three rank-one tensors, where l indexes the rank-one tensors. This can be expanded to create a full three dimen-

sional data cube model that is described by

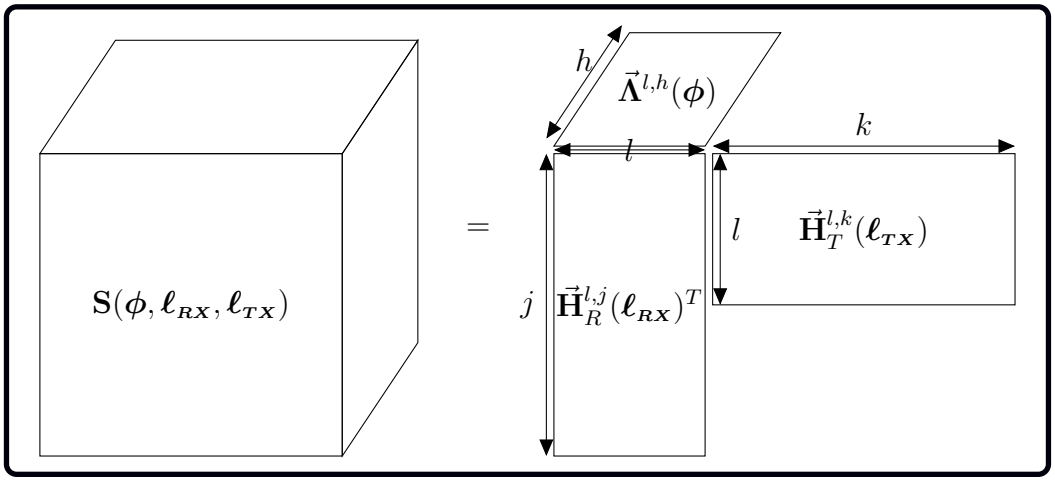

(3.5)

where the dimensions have been overlaid on the low-rank tensor model.

This joint diagonalization method is based on the ortho-point target assumption of EMI targets. It successfully separates the EMI data into two sections, position information and target information. However, it is extremely restrictive to the sensor design. Larger sensors, such as the TEMTADS system [9], can design a large array of EMI receivers and transmitters that are ideal for this method. Smaller hand-held EMI systems are unable to create such a restrictive data set because the transmitter and receiver move together. This means that hand-held systems are only able to measure the diagonal elements through (3.3) along the two position dimensions, and thus it is impossible to perform further diagonalization.

3.2 Discrete Spectrum of Relaxation Frequencies

Another area of recent EMI research has investigated the Discrete Spectrum of Relaxation Frequencies (DSRF) as a method to create a separable framework [10, 11, 12, 13, 14]. This work has primarily been focused on smaller, frequency-domain EMI systems including hand-held sensors. The DSRF is based on the extended physical model of the *magnetic polarizability* matrix as a sum of dipoles at the target location as was shown in (2.4) [2].

By inserting (2.4) back into (2.1) and rearranging the constant terms, the measurement

becomes

$$S(\phi, \Delta p) = -\sum_{k=0}^{K} \alpha_k f_k(\phi) g_k(\Delta p) \tag{3.6}$$

where $g_k(\Delta p) = \mathbf{h}_R(\Delta p)^T \boldsymbol{\mathcal{M}}_k \mathbf{h}_T(\Delta p)$. This model shows that the measurement specific data is separable from the position-dependent data. It can also be easily expanded for cases when the EMI sensor takes multiple (M) measurements at each location for multiple (N) locations. The measurements create a data matrix now, where the model of (3.6) can be expanded into

$$\boxed{\mathbf{S}(\boldsymbol{\phi}, \boldsymbol{\Delta p}) = -\sum_{k=0}^{K} \alpha_k \mathbf{f}_k(\boldsymbol{\phi}) \mathbf{g}_k(\boldsymbol{\Delta p})^T} \tag{3.7}$$

where $\mathbf{S}$ is a matrix of size $M \times N$ that is defined as a sum of rank-1 matrices, revealing that it has at most a rank of $K+1$. This formulation has provided some key insights, especially for frequency-domain systems.

The first insight from (3.7) is that there is a potential low-rank matrix model for multiple measurements based on the *magnetic polarizability* of the target. It is straightforward to see that $\text{rank}(\mathbf{S}) \leq K+1$ from the DSRF model. This means that the data will have a low rank when the target can be represented by only a few magnetic dipoles. Unfortunately, this is not a strong guarantee because previous work has shown that assuming only a few dipoles can lead to sub-optimal results for some targets [15], and it is a difficult problem to predict the correct number of expected dipole terms [16]. It is also known that some target models require a large number of magnetic dipoles, such as a metal sphere that is modeled by an infinite number of dipoles.

Another insight from this model is that frequency-domain systems can relax the signal processing from fitting complex data into a real-valued problem. When working with a frequency-domain sensor, $f_k(\omega) \in \mathfrak{C}$ is a complex value where the interaction between the primary field and the relaxation frequency is stored in the phase information. This creates a complex matrix $\mathbf{S}$. However, because $f_k(\omega)$ is the only complex term and no complex-

valued multiplications occur, the DSRF inversion can be solved by modeling the real and imaginary parts separately. This separation converts the problem back into real-valued data and also provides the extra benefit of effectively doubling the number of measurements from a frequency-domain system.

This model has limitations—the primary one being the accuracy of the inversion to fit this model. The $\mathbf{g}_k(\mathbf{\Delta p})$ vector is connected with a single relaxation frequency. This arises from the fact that $\mathbf{g}_k(\mathbf{\Delta p})$ contains the magnetic scene as well as the orientation information for each relaxation. As a result, there is a dependence in the processing chain where the location estimation can only be solved after the relaxation frequencies have been recovered. This requires the DSRF inversion to be highly accurate, but this inversion process is very sensitive to noise in the measurements. The DSRF recovery problem can be formulated as a sparse recovery problem from a given dictionary where the sparsity number is unknown. However, the sparse assumption is only approximate, e.g., some targets such as metal spheres are not actually sparse. In addition, the relaxation frequency vectors in a dense DSRF dictionary are highly colinear which further complicates the inversion process.

The nature of $\mathbf{g}_k(\mathbf{\Delta p})$ also forces the location estimator to jointly estimate the tensor information. This limitation led to estimating the tensor for each relaxation frequency separately with no clear method of combining tensors for improved performance [12].

Along with these limitations, frequency-domain sensors have traditionally relied on pre-filtering the data to remove strong interference created by the sensor [17]. All of these factors lead to a very sensitive processing framework where any errors that are introduced during the earlier stages affect the remaining processing chain, and all of the earlier stages are not trivial.

3.3 Least Squares

The final framework is based on a different perspective of (2.1). This perspective focuses on reshaping the measurement model into a linear product such that

$$\begin{aligned} S(\phi, \Delta p) &= \mathbf{h}_R^T(\Delta p)\boldsymbol{\mathcal{m}}(\phi)\mathbf{h}_T(\Delta p) = \begin{bmatrix} h_{RX} \\ h_{RY} \\ h_{RZ} \end{bmatrix}^T \begin{bmatrix} m_{XX} & m_{XY} & m_{XZ} \\ m_{YX} & m_{YY} & m_{YZ} \\ m_{ZX} & m_{ZY} & m_{ZZ} \end{bmatrix} \begin{bmatrix} h_{TX} \\ h_{TY} \\ h_{TZ} \end{bmatrix} \\ &= \mathbf{m}(\phi)^T\mathbf{h}(\Delta p) = \begin{bmatrix} m_{XX} \\ m_{YY} \\ m_{ZZ} \\ m_{XY} \\ m_{XZ} \\ m_{YZ} \end{bmatrix}^T \begin{bmatrix} h_{RX}h_{TX} \\ h_{RY}h_{TY} \\ h_{RZ}h_{TZ} \\ h_{RX}h_{TY} + h_{RY}h_{TX} \\ h_{RX}h_{TZ} + h_{RZ}h_{TX} \\ h_{RZ}h_{TY} + h_{RY}h_{TZ} \end{bmatrix} \end{aligned} \tag{3.8}$$

where the symmetric nature of the *magnetic polarizability* is exploited to reduce $\mathbf{m}(\phi)$ to only six terms. In this model, all of the separable terms are on different sides of the inner product.

Previous work has shown that if one side of the model is known and there are enough measurements, then it becomes an over-determined linear problem and a least-squares solution can be used [18, 19]. One approach has been to assume that the position information is known [18]. If the relative positions, $\mathbf{\Delta p}$, of more than six sensor locations are obtained, then a model for the magnetic scene can be formed into a matrix mapping such that

$$S^T(\phi, \mathbf{\Delta p}) = \mathbf{H}^T(\mathbf{\Delta p})\mathbf{m}(\phi) \tag{3.9}$$

where the *magnetic polarizability* for a specific measurement can be recovered using least squares. An extension to this framework is also provided for when the position is un-

known. By simulating different positions and using the remaining error from the least squares problem as the optimization metric, a grid search or gradient descent can be used to jointly estimate the position and *magnetic polarizability*.

This perspective has also been used in a similar manner after the DSRF inversion process [19]. This previous work uses a specific relaxation frequency found in the DSRF process and reshapes $g_k(\mathbf{\Delta p})$ as shown in 3.8 to isolate the magnetic scene and *tensor amplitude*. Convex optimization techniques are used to determine the location and target orientation by enumerating all possible combinations.

The linear model used in this framework can be advantageous. It is direct to see the separability of the model and the linear problem enables least-squares operations and other linear algebra techniques to be used. The main limitation of this model is that the framework does not take advantage of the separability of the data. Without knowing either the location or target information, the techniques attempt to jointly estimate both parameters. The other limitation is that neither approach provides a clear path to incorporate multiple measurements to improve the inversion estimate. Both techniques use only a single measurement (ϕ) to perform the inversion. There is not a direct path for extending this framework to incorporate the extra information jointly in the inversion process [12].

CHAPTER 4

LOW-RANK MODEL FOR EMI SENSORS

4.1 New Perspective

This chapter presents a new EMI processing framework that is capable of better exploiting the physical model of EMI targets. This novel framework is based on a new perspective of the EMI model developed by the author [20], which involves a low-rank model for EMI data that can be exploited by any sensor design. The low-rank model is obtained by using the reshaped bilinear model of (3.8) and combining it with the sum of dipoles target model used in (2.4). This arrives at a model for a single measurement given by

$$S(\phi, \Delta p) = -\sum_k \alpha_k f_k(\phi) \mathbf{m}_k^T \mathbf{h}(\Delta p). \tag{4.1}$$

This model can be directly extended for multiple locations and measurements by stacking each measurement into a new row and concatenating multiple locations into columns, just like the DSRF model. The data matrix for M measurements[1] at N locations can be written as

$$\mathbf{S}(\boldsymbol{\phi}, \boldsymbol{\Delta p}) = -\sum_k \alpha_k \mathbf{f}_k(\boldsymbol{\phi}) \mathbf{m}_k^T \mathbf{H}(\boldsymbol{\Delta p}) \tag{4.2}$$

where $\mathbf{S} \in \Re^{M \times N}$, $\mathbf{f}_k(\boldsymbol{\phi}) \in \Re^{M \times 1}$, $\mathbf{H}(\boldsymbol{\Delta p}) \in \Re^{6 \times N}$, and $\mathbf{m}_k \in \Re^{6 \times 1}$. The *tensor amplitude* can be defined as $-\alpha_k \mathbf{m}_k^T$, where it holds the strength and orientation of each dipole in the model. Using the *tensor amplitude* and writing the summation in matrix notation arrives at

$$\mathbf{S}(\boldsymbol{\phi}, \boldsymbol{\Delta p}) = \boxed{\mathbf{F}(\boldsymbol{\phi})} \boxed{\mathbf{G}^T} \boxed{\mathbf{H}(\boldsymbol{\Delta p})} \tag{4.3}$$

[1] For frequency-domain EMI systems, the real and imaginary parts of each measurement are treated as separate measurements. This means that only $M/2$ frequencies are needed.

where the columns of the matrix $\mathbf{F}(\boldsymbol{\phi}) \in \Re^{M \times K}$ are the relaxation terms $\mathbf{f}_k(\boldsymbol{\phi})$ and the rows of the matrix $\mathbf{G}^T \in \Re^{K \times 6}$ are the *tensor amplitudes*.

4.2 Low-Rank Insights

This new framework can also be used to predict the exact rank of the physical model for any target by taking a closer examination of each sub-matrix's rank in (4.3). By definition, the matrix $\mathbf{F}$ is made up of K column vectors $\mathbf{f}_k$. The $\mathbf{f}_k$ vectors will be linearly independent as long as each relaxation frequency is within the measurement range of the sensor and enough measurement samples are taken to separate them. As long as the $\mathbf{f}_k$ vectors remain linearly independent, then $\mathbf{F}$ will be full rank. The structure of $\mathbf{H}$ is completely driven by the magnetic scene of the sensor. As long as the sensor's design and operation path are selected in order to fully measure the target [11], then $\mathbf{H}$ will be full rank, i.e., $\text{rank}(\mathbf{H}) = 6$. This means that if the EMI sensor parameters are chosen appropriately to make both $\mathbf{F}$ and $\mathbf{H}$ full rank, any scenario where $\text{rank}(\mathbf{S}) < \min(K, 6)$ must be due to $\mathbf{G}$. It also can be noticed that if $\mathbf{G}$ is full rank, then $\text{rank}(\mathbf{G}) = \min(K, 6)$ because this will be the smallest dimension of $\mathbf{G}$. It follows that for an appropriately designed sensor it is true that $\text{rank}(\mathbf{S}) = \text{rank}(\mathbf{G})$. The matrix $\mathbf{G}$ can be decomposed into a set of linearly independent basis vectors and their associated weights as $\mathbf{G} = \boldsymbol{\Phi}\mathbf{W}$, where $\boldsymbol{\Phi} \in \Re^{6 \times R}$ is the matrix of linearly independent basis of $\mathbf{G}$ and $\mathbf{W} \in \Re^{R \times K}$ are the weights associated with each relaxation's tensor amplitude. By combining these observations, it is evident that $\text{rank}(\mathbf{S}) = R$, where the rank is determined by the number of linearly independent tensors of the target. Inserting the tensor basis vectors and weights into (4.3) creates a low-rank model which can be written in the following matrix form

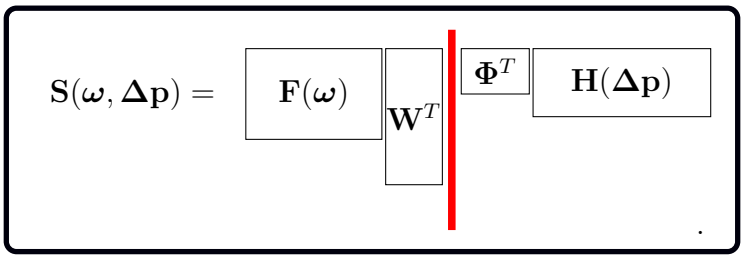

(4.4)

4.3 Ortho-Point Target Interpretation

For ortho-point targets, it was shown in (2.13) that the *magnetic polarizability* of a target is diagonal when rotated into the target's coordinate system. When this is possible, the low-rank model of (4.4) can be further described using the physical nature of the target. Starting with (2.13), it is useful to write the target as a sum of rank-one matrices such that

$$m = \vec{\mathbf{E}}\vec{\mathbf{\Lambda}}\vec{\mathbf{E}}^T = \sum_{j=1}^{3} \vec{\lambda}_j^{\vec{\mathbf{\Lambda}}} \vec{\mathbf{e}}_j \vec{\mathbf{e}}_j^T \tag{4.5}$$

where $\vec{\lambda}_j^{\vec{\mathbf{\Lambda}}}$ is the j^{th} diagonal value and $\vec{\mathbf{e}}_j \in \Re^{3\times 1}$ is the associated vector. It is desired to reshape (4.5) into a bilinear product as was done in (3.8), and it can be observed that the *magnetic polarizability* can be converted from a 3×3 symmetric matrix into a 6×1 vector. In order to achieve this, it is useful to note that the rank-one matrices of (4.5) can be vectorized as was done in (3.8) to obtain

$$\textit{s-vec}\{\vec{\mathbf{e}}_j \vec{\mathbf{e}}_j^T\} = \begin{bmatrix} \vec{e}_{j,1}\vec{e}_{j,1} & \vec{e}_{j,2}\vec{e}_{j,2} & \vec{e}_{j,3}\vec{e}_{j,3} & \vec{e}_{j,1}\vec{e}_{j,2} & \vec{e}_{j,1}\vec{e}_{j,3} & \vec{e}_{j,2}\vec{e}_{j,3} \end{bmatrix}^T \tag{4.6}$$

where *s-vec*$\{\square\}$ exploits the symmetry of $\vec{\mathbf{e}}_j\vec{\mathbf{e}}_j^T$ to ignore the last three components since they are redundant and creates a vector of only six terms. Using (4.6) in (4.5) arrives at

$$\textit{s-vec}\{\mathcal{M}\} = \begin{bmatrix} | & | & | \\ \mathbf{e}_1^{\mathfrak{s}} & \mathbf{e}_2^{\mathfrak{s}} & \mathbf{e}_3^{\mathfrak{s}} \\ | & | & | \end{bmatrix} \begin{bmatrix} \vec{\lambda}_1^{\vec{\mathbf{\Lambda}}} & \vec{\lambda}_2^{\vec{\mathbf{\Lambda}}} & \vec{\lambda}_3^{\vec{\mathbf{\Lambda}}} \end{bmatrix}^T = \vec{\mathbf{\Phi}}\vec{\boldsymbol{x}}_{\vec{\mathbf{\Lambda}}} \tag{4.7}$$

where $\vec{\mathbf{\Phi}} \in \Re^{6\times R}$ are the linearly independent directional tensor bases[2] that align with the target's coordinate system, $\vec{\boldsymbol{x}}_{\vec{\mathbf{\Lambda}}} \in \Re^{R_{\vec{\mathbf{\Lambda}}}\times 1}$ is a vector of the diagonal values in $\mathcal{M}$, $\mathbf{e}_j^{\mathfrak{s}} = \textit{s-vec}\{\vec{\mathbf{e}}_j\vec{\mathbf{e}}_j^T\} \in \Re^{6\times 1}$ is the reshaped column vector, and $R_{\vec{\mathbf{\Lambda}}} \leq 3$ is the number of non-zero diagonal values of $\mathcal{M}$.

There are some degenerate cases that have non-unique decompositions for (4.5), e.g., spheres, cylinders, and other symmetric targets. These cases arise because $\vec{\lambda}_j^{\vec{\mathbf{\Lambda}}}{=}\vec{\lambda}_i^{\vec{\mathbf{\Lambda}}}$ where $i{\neq}j$. Degenerate targets still have a classical tensor of rank 3, but they have fewer than 3 independent tensor components. Fortunately, the new vectorized tensors can easily represent these non-unique principal axes into a single, linearly independent tensor basis. This can be done by introducing a new matrix $\vec{\boldsymbol{D}}$. When the target is not degenerate, then $\vec{\boldsymbol{D}} = \boldsymbol{I}_R$ is the identity matrix the size of the rank of the target. If the target is degenerate, then $\vec{\boldsymbol{D}}$ combines the rotation vectors of the common diagonal terms and maps them to a single diagonal value. This can be accomplished with a heavily constrained $\vec{\boldsymbol{D}}$ matrix that only contains zeros and ones. For instance, a cylinder (e.g., RT-04) where there is a common diagonal value $\vec{\lambda}_d^{\vec{\mathbf{\Lambda}}}$ for the 2nd and 3rd diagonal value is represented by

$$\vec{\mathbf{\Phi}}\vec{\boldsymbol{x}}_{\vec{\mathbf{\Lambda}}} = \vec{\mathbf{\Phi}} \begin{bmatrix} 1 & 0 \\ 0 & 1 \\ 0 & 1 \end{bmatrix} \begin{bmatrix} \vec{\lambda}_1^{\vec{\mathbf{\Lambda}}} \\ \vec{\lambda}_d^{\vec{\mathbf{\Lambda}}} \end{bmatrix} = \vec{\mathbf{\Phi}}\vec{\boldsymbol{D}}\vec{\boldsymbol{x}} \tag{4.8}$$

[2]Note that there is no guarantee for $\vec{\mathbf{\Phi}}$ to have orthogonal column vectors like $\mathbf{\Phi}$ and $\vec{\mathbf{E}}$.

where $\vec{\boldsymbol{x}}$ only has the unique diagonal values and is denoted as such by dropping the $\vec{\boldsymbol{\Lambda}}$ subscript. This ability for the new vectorized tensor to treat standard point targets and degenerate targets in a uniform manner under the ortho-point target assumption further empowers it for processing EMI data.

The *magnetic polarizability* is the only term that is dependent on the measurement parameter ϕ. This means that $\vec{\boldsymbol{x}}(\phi)$ is the only matrix to change size when multiple measurements $\boldsymbol{\phi}$ are used together. Expanding the vectorized *magnetic polarizability* for multiple measurement parameters and multiple locations as was done in (4.3) becomes

$$\mathbf{S}(\boldsymbol{\phi}, \boldsymbol{\Delta}\mathbf{p}) = \boxed{\vec{\boldsymbol{X}}(\boldsymbol{\phi})} \boxed{\vec{\boldsymbol{D}}^T} \boxed{\vec{\boldsymbol{\Phi}}^T} \boxed{\mathbf{H}(\boldsymbol{\Delta}\mathbf{p})} \tag{4.9}$$

where the smallest rank of R always occurs between $\vec{\boldsymbol{X}}(\boldsymbol{\phi})$ and $\vec{\boldsymbol{D}}^T$ as denoted by the red line in (4.9).

If desired, each column of $\vec{\boldsymbol{X}}(\boldsymbol{\phi})$ can be represented using the sum of dipole model from (2.4). The result can be observed by expanding (4.2) with the physical model such that it becomes

$$\mathbf{S}(\boldsymbol{\phi}, \boldsymbol{\Delta}\mathbf{p}) = -\sum_j \sum_k \alpha_{j,k} \mathbf{f}_k(\boldsymbol{\phi}) \vec{\lambda}_j^{\vec{\boldsymbol{\Lambda}}} \left[\vec{\boldsymbol{D}}^T\right]_j \vec{\boldsymbol{\Phi}}^T \mathbf{H}(\boldsymbol{\Delta}\mathbf{p}) \tag{4.10}$$

where $\left[\vec{\boldsymbol{D}}^T\right]_j$ extracts the j$^{\text{th}}$ column of $\vec{\boldsymbol{D}}^T$ and a second sum has been added over each unique diagonal value of the *magnetic polarizability*. This shows that each column of $\left[\vec{\boldsymbol{X}}(\boldsymbol{\phi})\right]_j$ can be represented as a weighted sum of DSRF vectors $-\sum_k \mathbf{f}_k(\boldsymbol{\phi}) \alpha_{j,k} \vec{\lambda}_j^{\vec{\boldsymbol{\Lambda}}}$. Combining the weights into a matrix $\left[\vec{\mathbf{W}}\right]_{j,k} = -\alpha_{j,k} \vec{\lambda}_j^{\vec{\boldsymbol{\Lambda}}}$, the full physical model in terms of

the DSRF can be written as

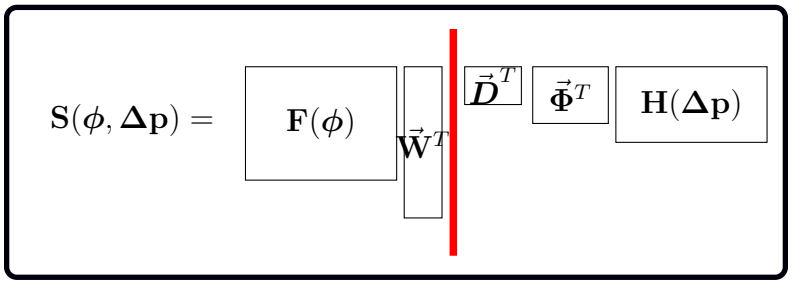

(4.11)

where the red line notes the location that drives the low-rank of R.

The connection of the low-rank model to the ortho-point target's physical model highlights further constraints for the rank. First, it provides a maximum rank for a single point target under the ortho-point target assumption. Any target that is small enough to be modeled as a point target and has its own target coordinate system will have at most three diagonal values for its *magnetic polarizability*. The low-rank physical model limits the $\text{rank}(\mathbf{S}) \leq 3$ because of the connection to these diagonal values for ortho-point targets. This is half of the maximum rank enforced by the matrix dimensionality of (4.3) for completely general point targets. If a target has a rank greater than three, then a point target model under the ortho-point target assumption is no longer valid. If this is the case, then a superposition of multiple ortho-point point targets can be used which simply becomes a summation of ortho-point point targets modeled by (4.11). These observations agree with [6]. Second, it provides a natural way to model all targets, including degenerate targets, using the low-rank model. A direct connection can now be made between the number of linearly independent tensors and the number of unique, non-zero diagonal values of the *magnetic polarizability*.

4.4 Reference Targets

It is useful to see how the new low-rank perspective is applied to actual targets. The targets RT-01 and RT-02 are straight forward. For RT-01, the ortho-point assumption low-rank

model of (4.11) is written as

$$\begin{aligned}\mathbf{S}(\boldsymbol{\phi},\boldsymbol{\Delta}\mathbf{p}) &= -\ f_{3.7}(\phi) \quad \begin{bmatrix}1\end{bmatrix} \quad \begin{bmatrix}1\end{bmatrix} \quad \boldsymbol{\mathfrak{e}}^{\mathfrak{s}}_{XX}{}^{T} \quad \mathbf{H}(\boldsymbol{\Delta}\mathbf{p}) \\ &= -\ \mathbf{F}(\boldsymbol{\phi}) \left(-\vec{\mathbf{W}}^{T}\right) \quad \vec{\boldsymbol{D}}^{T} \quad \vec{\boldsymbol{\Phi}}^{T} \quad \mathbf{H}(\boldsymbol{\Delta}\mathbf{p})\end{aligned} \tag{4.12}$$

which has a rank of one, where the negative sign is extracted from the $\vec{\mathbf{W}}$ term to make the detailed expansion have fewer signs throughout. RT-02 can be written as

$$\begin{aligned}\mathbf{S}(\boldsymbol{\phi},\boldsymbol{\Delta}\mathbf{p}) &= -\begin{bmatrix} f_{2.7}(\phi)^{T} \\ f_{3.7}(\phi)^{T} \\ f_{4.7}(\phi)^{T}\end{bmatrix}^{T} \begin{bmatrix}1&0&0\\0&1&0\\0&0&1\end{bmatrix} \begin{bmatrix}1&0&0\\0&1&0\\0&0&1\end{bmatrix} \begin{bmatrix}— & \boldsymbol{\mathfrak{e}}^{\mathfrak{s}}_{XX}{}^{T} & — \\ — & \boldsymbol{\mathfrak{e}}^{\mathfrak{s}}_{YY}{}^{T} & — \\ — & \boldsymbol{\mathfrak{e}}^{\mathfrak{s}}_{ZZ}{}^{T} & —\end{bmatrix} \mathbf{H}(\boldsymbol{\Delta}\mathbf{p}) \\ &= -\quad \mathbf{F}(\boldsymbol{\phi}) \qquad \left(-\vec{\mathbf{W}}^{T}\right) \qquad \vec{\boldsymbol{D}}^{T} \qquad\qquad \vec{\boldsymbol{\Phi}}^{T} \qquad\qquad \mathbf{H}(\boldsymbol{\Delta}\mathbf{p})\end{aligned} \tag{4.13}$$

which is a rank-three model.

It is useful to compare RT-01 and RT-02 to all of the previous frameworks. Both of these targets represent canonical target examples that are well described by the low-rank, DSRF, and joint diagonalization models as rank-one and rank-three targets, respectively. The least-squares model makes no claim of exploiting the target structure further than the model reshaping.

Targets RT-03 and RT-04 demonstrate the power of the new low-rank model by illustrating how it can represent degenerate targets. RT-03 can be written as

$$\begin{aligned}\mathbf{S}(\boldsymbol{\phi},\boldsymbol{\Delta}\mathbf{p}) &= -\left[\sum_{k=\mathcal{A}_3} f_k(\boldsymbol{\phi})\right] \begin{bmatrix}1\end{bmatrix} \quad \begin{bmatrix}1\\1\\1\end{bmatrix}^{T} \begin{bmatrix}— & \boldsymbol{\mathfrak{e}}^{\mathfrak{s}}_{XX}{}^{T} & — \\ — & \boldsymbol{\mathfrak{e}}^{\mathfrak{s}}_{YY}{}^{T} & — \\ — & \boldsymbol{\mathfrak{e}}^{\mathfrak{s}}_{ZZ}{}^{T} & —\end{bmatrix} \mathbf{H}(\boldsymbol{\Delta}\mathbf{p}) \\ &= -\qquad \mathbf{F}(\boldsymbol{\phi}) \ \left(-\vec{\mathbf{W}}^{T}\right) \ \vec{\boldsymbol{D}}^{T} \qquad\qquad \vec{\boldsymbol{\Phi}}^{T} \qquad\qquad \mathbf{H}(\boldsymbol{\Delta}\mathbf{p})\end{aligned} \tag{4.14}$$

which has a rank-one model. This is because there is only a single unique diagonal term in

the *magnetic polarizability*. Notice how the $\vec{\boldsymbol{D}}$ matrix combines all of the rotation vectors into a single vector that is a combination of all directions. This rank-one model is very different than what the DSRF and joint diagonalization model can predict. The DSRF model can only predict a rank of five because of the number of relaxation terms. Joint diagonalization predicts a rank-three tensor because there are three diagonal terms, although [6] notes that there is a further structure to the rank-three tensor that it does not immediately exploit. Only the low-rank model can fully exploit the structure of the target to create a rank-one model. RT-04 is another degenerate target. It can be modeled as

$$\begin{aligned}\mathbf{S}(\boldsymbol{\phi},\boldsymbol{\Delta}\mathbf{p}) &= -\begin{bmatrix} f_{3.4}(\phi)^T \\ \sum_{k=\mathcal{A}_4^{YZ}} f_k(\phi)^T \end{bmatrix}^T \begin{bmatrix} 1 & 0 \\ 0 & 1 \end{bmatrix} \begin{bmatrix} 1 & 0 \\ 0 & 1 \\ 0 & 1 \end{bmatrix}^T \begin{bmatrix} — & \mathfrak{e}^{\mathfrak{s}}_{XX}{}^T & — \\ — & \mathfrak{e}^{\mathfrak{s}}_{YY}{}^T & — \\ — & \mathfrak{e}^{\mathfrak{s}}_{ZZ}{}^T & — \end{bmatrix} \mathbf{H}(\boldsymbol{\Delta}\mathbf{p}) \\ &= - \quad \mathbf{F}(\boldsymbol{\phi}) \quad \left(-\vec{\mathbf{W}}^T\right) \quad \vec{\boldsymbol{D}}^T \quad \vec{\boldsymbol{\Phi}}^T \quad \mathbf{H}(\boldsymbol{\Delta}\mathbf{p}) \end{aligned} . \tag{4.15}$$

This shows that RT-04 is a rank-two target. One dimension is dedicated to the axis of rotation, XX, while the other dimension represents the combination of the symmetric directions, YY and ZZ. Again, the DSRF model predicts a rank of four due to the number of relaxations and the joint diagonalization predicts a rank of three due to the number of diagonal terms. These targets illustrate the new descriptive power of the low-rank model that was not available from any of the previous models.

RT-05 can be written in the new model as

$$\begin{aligned}\mathbf{S}(\boldsymbol{\phi},\boldsymbol{\Delta}\mathbf{p}) &= -\left[\sum_{k=\mathcal{A}_5} f_k(\boldsymbol{\phi})\right] \begin{bmatrix} 1 \end{bmatrix} \quad \begin{bmatrix} 1 \end{bmatrix}^T \mathfrak{e}^{\mathfrak{s}}_{XX}{}^T \ \mathbf{H}(\boldsymbol{\Delta}\mathbf{p}) \\ &= - \quad \mathbf{F}(\boldsymbol{\phi}) \ \left(-\vec{\mathbf{W}}^T\right) \ \vec{\boldsymbol{D}}^T \quad \vec{\boldsymbol{\Phi}}^T \quad \mathbf{H}(\boldsymbol{\Delta}\mathbf{p}) \end{aligned} \tag{4.16}$$

which is a rank-one target where RT-06 is a rank-two target modeled as

$$\begin{aligned}\mathbf{S}(\boldsymbol{\phi},\boldsymbol{\Delta}\mathbf{p}) &= -\begin{bmatrix}\sum_{k=\mathcal{A}_6^X} f_k(\phi)^T \\ \sum_{j=\mathcal{A}_6^Y} f_j(\phi)^T\end{bmatrix}^T \begin{bmatrix}1 & 0\\ 0 & 1\end{bmatrix}\begin{bmatrix}1 & 0\\ 0 & 1\end{bmatrix}^T \begin{bmatrix}— & \mathfrak{e}^{\mathfrak{s}}_{XX}{}^T & — \\ — & \mathfrak{e}^{\mathfrak{s}}_{YY}{}^T & —\end{bmatrix}\mathbf{H}(\boldsymbol{\Delta}\mathbf{p}) \\ &= - \quad \mathbf{F}(\boldsymbol{\phi}) \quad \left(-\vec{\mathbf{W}}^T\right) \quad \vec{\boldsymbol{D}}^T \quad \vec{\boldsymbol{\Phi}}^T \quad \mathbf{H}(\boldsymbol{\Delta}\mathbf{p})\end{aligned}. \tag{4.17}$$

The DSRF model would predict a rank of five for both of these targets because they have the exact same relaxations. The joint diagonalization model would correctly predict a rank one and two tensor, respectively, because of the number of nonzero diagonal terms.

Targets RT-07 and RT-08 violate the ortho-point assumption. This means that the joint diagonalization model cannot describe these targets accurately. It also means that the low-rank model must use the more general equation of (4.4) to describe the target. RT-07 can be modeled as

$$\begin{aligned}\mathbf{S}(\boldsymbol{\phi},\boldsymbol{\Delta}\mathbf{p}) &= -\begin{bmatrix}f_{3.4}(\phi)^T \\ f_{4.1}(\phi)^T\end{bmatrix}^T \begin{bmatrix}1 & 0\\ 0 & 2\end{bmatrix}\begin{bmatrix}1 & 0 & 0 & 0 & 0 & 0\\ \frac{1}{2} & \frac{1}{2} & 0 & \frac{1}{2} & 0 & 0\end{bmatrix}\vec{\mathbf{H}}(\boldsymbol{\Delta}\mathbf{p}) \\ &= - \quad \mathbf{F}(\boldsymbol{\phi}) \quad \left(-\mathbf{W}^T\right) \quad \boldsymbol{\Phi}^T \quad \vec{\mathbf{H}}(\boldsymbol{\Delta}\mathbf{p})\end{aligned} \tag{4.18}$$

which is a rank-two target. Because the target is not an ortho-point target, the linearly independent vectors are written out in (4.18). Also, the $\vec{\mathbf{H}}(\boldsymbol{\Delta}\mathbf{p})$ matrix is assumed to be aligned with the described model of (4.18). If an arbitrary $\mathbf{H}$ were used then $\boldsymbol{\Phi}$ would have different values, but the shape would remain the same. Normalization has been applied to the original directional vectors according to the description in Appendix A.1. This means the model uses the directional vector $\vec{\mathbf{e}}_2 = \left[\sqrt{2}/2, \sqrt{2}/2, 0\right]^T$ that is a normalized vector. This creates a vector *s-vec*$\{\vec{\mathbf{e}}_2\vec{\mathbf{e}}_2^T\}$ as shown in (4.6) that is then inserted as the second row of $\boldsymbol{\Phi}^T$ in (4.18). This target is correctly predicted as a rank-two target by the low-rank model. The DSRF model also predicts a rank of two because there are only two relaxations. The

joint diagonalization model is more complicated for this term. Because the target does not have a common axis, the two relaxations cannot be jointly diagonalized according to the model. Even though the target is rank two, it requires two separate rank-one point targets as the model.

Target RT-08 is a further extension of RT-07. It can be modeled as

$$\begin{aligned}\mathbf{S}(\boldsymbol{\phi},\boldsymbol{\Delta p}) &= -\begin{bmatrix} f_{2.4}(\phi)^T \\ f_{2.9}(\phi)^T \\ f_{3.5}(\phi)^T \\ f_{4.0}(\phi)^T \\ f_{4.5}(\phi)^T \\ f_{5.1}(\phi)^T \end{bmatrix}^T \begin{bmatrix} 1 & 0 & 0 & 0 & 0 & 0 \\ 0 & 1 & 0 & 0 & 0 & 0 \\ 0 & 0 & 1 & 0 & 0 & 0 \\ 0 & 0 & 0 & 2 & 0 & 0 \\ 0 & 0 & 0 & 0 & 2 & 0 \\ 0 & 0 & 0 & 0 & 0 & 2 \end{bmatrix} \begin{bmatrix} 1 & 0 & 0 & 0 & 0 & 0 \\ 0 & 1 & 0 & 0 & 0 & \\ 0 & 0 & 1 & 0 & 0 & 0 \\ \frac{1}{2} & \frac{1}{2} & 0 & \frac{1}{2} & 0 & 0 \\ \frac{1}{2} & 0 & \frac{1}{2} & 0 & \frac{1}{2} & 0 \\ 0 & \frac{1}{2} & \frac{1}{2} & 0 & 0 & \frac{1}{2} \end{bmatrix} \vec{\mathbf{H}}(\boldsymbol{\Delta p}) \\ &= - \quad \mathbf{F}(\boldsymbol{\phi}) \qquad \left(-\mathbf{W}^T\right) \qquad \boldsymbol{\Phi}^T \qquad \vec{\mathbf{H}}(\boldsymbol{\Delta p})\end{aligned} \tag{4.19}$$

which has a rank of six. This is the largest possible rank for a point target. The DSRF model predicts a rank of six for this target as well. Joint diagonalization requires modeling this as two rank-three tensors. However, this is only because the first three and last three relaxations are aligned with each other, respectively. It would be straightforward to create a target that would require more than two point targets for joint diagonalization to model.

Targets RT-09 and RT-10 are specifically designed to explore how amplitudes interact with the new low-rank model. Targets RT-01 through RT-08 all have unit amplitudes and the only terms that are not $\{0, 1\}$ are due to normalization of the directional vectors. The low-rank model also naturally handles different amplitudes between the different dipoles. This is accomplished through two main mechanisms. The first mechanism is exemplified

in RT-09 where each dimension has a different amplitude. It can be written as

$$\begin{aligned}\mathbf{S}(\boldsymbol{\phi},\boldsymbol{\Delta}\mathbf{p}) &= -\begin{bmatrix} f_{2.7}(\phi)^T \\ f_{3.7}(\phi)^T \\ f_{4.7}(\phi)^T \end{bmatrix}^T \begin{bmatrix} 1 & 0 & 0 \\ 0 & \frac{3}{4} & 0 \\ 0 & 0 & \frac{1}{2} \end{bmatrix} \begin{bmatrix} 1 & 0 & 0 \\ 0 & 1 & 0 \\ 0 & 0 & 1 \end{bmatrix} \begin{bmatrix} - & \mathfrak{e}^{\mathfrak{s}}_{XX}{}^T & - \\ - & \mathfrak{e}^{\mathfrak{s}}_{YY}{}^T & - \\ - & \mathfrak{e}^{\mathfrak{s}}_{ZZ}{}^T & - \end{bmatrix} \mathbf{H}(\boldsymbol{\Delta}\mathbf{p}) \\ &= - \quad \mathbf{F}(\boldsymbol{\phi}) \qquad \left(-\vec{\mathbf{W}}^T\right) \qquad \vec{\boldsymbol{D}}^T \qquad \vec{\boldsymbol{\Phi}}^T \qquad \mathbf{H}(\boldsymbol{\Delta}\mathbf{p}) \end{aligned} \tag{4.20}$$

which is a rank-three model that has a different value for each mapping in $\vec{\mathbf{W}}$. The second mechanism is that each relaxation frequency can have its own amplitude. Both of these mechanisms are combined in RT-10, which can be written as

$$\begin{aligned}\mathbf{S}(\boldsymbol{\phi},\boldsymbol{\Delta}\mathbf{p}) &= -\begin{bmatrix} \left(f_3 + \frac{1}{2}f_{4.4}\right)^T \\ \left(f_{2.4} + \frac{3}{4}f_{3.7} + \frac{1}{2}f_{5.1}\right)^T \end{bmatrix}^T \begin{bmatrix} \frac{9}{10} & 0 \\ 0 & 1 \end{bmatrix} \begin{bmatrix} 1 & 0 \\ 0 & 1 \end{bmatrix}^T \begin{bmatrix} - & \mathfrak{e}^{\mathfrak{s}}_{XX}{}^T & - \\ - & \mathfrak{e}^{\mathfrak{s}}_{YY}{}^T & - \end{bmatrix} \mathbf{H}(\boldsymbol{\Delta}\mathbf{p}) \\ &= - \quad \mathbf{F}(\boldsymbol{\phi}) \qquad \left(-\vec{\mathbf{W}}^T\right) \quad \vec{\boldsymbol{D}}^T \qquad \vec{\boldsymbol{\Phi}}^T \qquad \mathbf{H}(\boldsymbol{\Delta}\mathbf{p}) \end{aligned} \tag{4.21}$$

where the $\boldsymbol{\phi}$ dependence has been dropped to save space.

It should also be noted that there is no restriction that prevents non-degenerate targets from containing the same relaxation frequencies, and that when the same relaxation frequencies are present they can have different amplitudes. For instance, RT-10 could be slightly altered so that $f_{3.7}(\boldsymbol{\phi})$ was exchanged for a relaxation frequency of $f_3(\boldsymbol{\phi})$. This would create the model

$$\begin{aligned}\mathbf{S}(\boldsymbol{\phi},\boldsymbol{\Delta}\mathbf{p}) &= -\begin{bmatrix} \left(f_3 + \frac{1}{2}f_{4.4}\right)^T \\ \left(f_{2.4} + \frac{3}{4}f_{3} + \frac{1}{2}f_{5.1}\right)^T \end{bmatrix}^T \begin{bmatrix} \frac{9}{10} & 0 \\ 0 & 1 \end{bmatrix} \begin{bmatrix} 1 & 0 \\ 0 & 1 \end{bmatrix}^T \begin{bmatrix} - & \mathfrak{e}^{\mathfrak{s}}_{XX}{}^T & - \\ - & \mathfrak{e}^{\mathfrak{s}}_{YY}{}^T & - \end{bmatrix} \mathbf{H}(\boldsymbol{\Delta}\mathbf{p}) \\ &= - \quad \mathbf{F}(\boldsymbol{\phi}) \qquad \left(-\vec{\mathbf{W}}^T\right) \quad \vec{\boldsymbol{D}}^T \qquad \vec{\boldsymbol{\Phi}}^T \qquad \mathbf{H}(\boldsymbol{\Delta}\mathbf{p}) \end{aligned} \tag{4.22}$$

which has the same relaxation frequency of $f_3(\boldsymbol{\phi})$ in the x and y dimensions, while it is still not a degenerate target because the other relaxation frequencies are unique. Although (4.22) will not be used as a reference target, it is useful to point out that the low-rank model does extend to a large variety of targets that cover scenarios other than just the ones exemplified in the reference targets.

4.5 Comparison to Previous Frameworks

As demonstrated by the reference targets above, the new low-rank model has some very useful properties. The low-rank model now directly connects the rank of the matrix to the number of linearly independent tensors. For any arbitrary point target, it provides $\text{rank}(\mathbf{S}) = R \leq 6$. It has even further predictive properties for ortho-point targets. For ortho-point targets, it shows that the number of linearly independent tensors is the same as the number of non-unique diagonal terms of the *magnetic polarizability*, which must imply that $R \leq 3$. The DSRF model alone is not able to provide a maximum rank. The joint diagonalization model can only provide a tensor rank for ortho-point targets. The least-squares model can only predict a maximum rank of six due to matrix dimensions, but it has no insights into the physical nature of the target. Also, as shown by RT-03 and RT-04, the low-rank model is the only one that can successfully exploit the entire structure of degenerate EMI targets.

Another benefit of the low-rank model is the elegant processing structure implied by the model. This will be discussed further in regard to the new framework, but the new low-rank model allows well-proven linear algebra techniques such as the singular value decomposition (SVD) and least squares to be used. The low-rank model is able to exploit SVD techniques and diagonalization, but it does not have to expand to a three-dimensional data cube like the joint diagonalization model. The new framework allows least squares and matrix projection operators that are elegant like the least-squares model, except the data separability can still be exploited with the low-rank model. The DSRF recovery can

also still be extracted from the low-rank model, but it is no longer necessary to perform this difficult inversion problem prior to solving the other problems of interest such as localization.

The third benefit is that the low-rank model has no constraints on the type of EMI sensor. Nearly all EMI literature is written in reference to a specific EMI sensor design. At minimum, most works only focus on either a time-domain or frequency-domain EMI sensor and do not discuss if the results are transferable to the other type of sensor. Many works design algorithms for a specific EMI sensor design. The joint diagonalization framework is an example of a very custom framework designed for a specific sensor. Joint diagonalization was designed specifically for the TEMTADS EMI sensor which is a time-domain sensor that has a 5×5 grid of transmitter/receiver pairs [6, 9]. This enables joint diagonlization because the specialized data from TEMTADS creates a grid of 25×25 measurements between unique transmitter/receiver locations for a single data set. Although joint diagonalization is extendable to sensors of different grid sizes than 5×5, it enforces a sensor design with a grid of transmitter/receiver pairs which makes it essentially useless for hand-held sensors that do not have large sensor arrays. Joint Diagonalization is also only described in terms of a time-domain sensor. Other efforts, e.g. the DSRF framework, that are based on hand-held sensors are more generalizable; however, the DSRF has been created for frequency-domain sensors [10] and there has not been clear efforts to connect it with similar efforts for time-domain sensors [15, 16]. In contrast, the new low-rank model is developed to make it applicable to as many sensors as possible. It can exploit the spatial relationship of TEMTADS-like sensors while also being applicable to hand-held sensors. It is also designed against a generic measurement (ϕ) to help expedite reuse across the different EMI sensor types.

CHAPTER 5

NEW LOW-RANK PROCESSING FRAMEWORK FOR EMI SENSORS

The new low-rank model has been shown to accurately represent an EMI target. This work introduces a new signal processing framework that exploits the low-rank model. The framework focuses on a mathematical derivation for recovering a low-rank model of the signal. The singular value decomposition (SVD) is a well known mathematical tool for obtaining a low-rank approximation from measured data. The SVD is a powerful tool and has been proven to be the optimal approximation of a low-rank matrix [21]. The new framework builds upon the SVD and develops the capability to extract the physical properties of EMI targets from the measured matrix after using the SVD.

5.1 Connection to SVD

The general model for noisy measurements is

$$\boxed{\mathbf{M}(\boldsymbol{\phi}, \boldsymbol{\Delta}\mathbf{p}) = \mathbf{S}(\boldsymbol{\phi}, \boldsymbol{\Delta}\mathbf{p}) + \mathcal{E} = \mathbf{F}(\boldsymbol{\phi})\vec{\mathbf{W}}^T\vec{\boldsymbol{D}}^T\vec{\boldsymbol{\Phi}}^T\mathbf{H}(\boldsymbol{\Delta}\mathbf{p}) + \mathcal{E}} \tag{5.1}$$

where the measurement matrix $\mathbf{M} \in \Re^{M\times N}$ is modeled by a signal and noise model that only contains the target response[1]and $\mathcal{E}$ is a matrix of i.i.d. Gaussian noise where each sample is $\mathcal{N}(0, \sigma_\epsilon^2)$. For this derivation, the ortho-point model will be used from (4.11). The same derivation can be applied to the general EMI model if desired. In order for the recovery to work, the sensor must be designed in a way to allow the low-rank model to be accurate. This is done by ensuring that $\mathbf{F}$ and $\mathbf{H}$ are full-rank matrices. Based on [21], it is already known that the optimal method for recovering the low-rank information from the measurement is by taking the singular value decomposition (SVD). The SVD of $\mathbf{M}$ is taken

[1]This model is based on real data. For frequency-domain sensors, the real and imaginary parts have already been separated and $\mathbf{M} \in \Re^{2M\times N}$.

to both recover a low-rank approximation and also denoise the signal. The SVD operation creates

$$\mathbf{M}(\boldsymbol{\phi}, \boldsymbol{\Delta}\mathbf{p}) = \mathbf{U}_\mathbf{M}\boldsymbol{\Sigma}_\mathbf{M}\mathbf{V}_\mathbf{M}^T \tag{5.2}$$

where only the target's nonzero singular values need to be kept. Because the maximum rank of the target is known, only those singular values and associated vectors are needed. For this derivation, the largest three singular values are the most that need to be kept for ortho-point targets.[2] This means that $\mathbf{U}_\mathbf{M} \in \Re^{M\times R}$, $\boldsymbol{\Sigma}_\mathbf{M} \in \Re^{R\times R}$, $\mathbf{V}_\mathbf{M} \in \Re^{N\times R}$, and $R \leq 3$. The SVD can be chosen to correctly approximate the low-rank matrix, but it enforces properties on the created matrices that are usually undesirable in the model, such as $\boldsymbol{\Sigma}_\mathbf{M}$ is diagonal and $\mathbf{U}_\mathbf{M}$ and $\mathbf{V}_\mathbf{M}$ are both orthonormal. The new low-rank framework focuses on using the available information from the SVD to recover the physical low-rank model from the data. The recovery of the low-rank model is accomplished by noting that the matrix products on the two sides of (5.3) are equal except for a noise term (assumed small) that can be associated with the small singular values of the SVD.

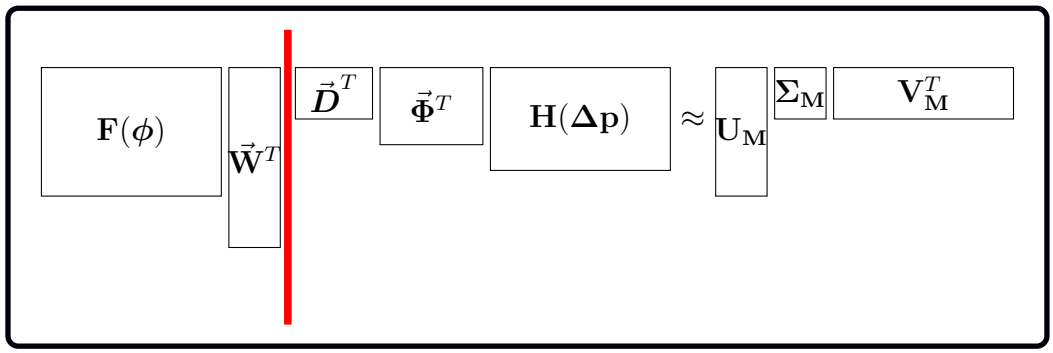

(5.3)

5.1.1 Aligning Subspaces

To simplify the discussion of recovering the low-rank model, it is useful to initially assume that $\mathbf{F}$ and $\mathbf{H}$ are known a priori. Based on the relationship in (5.3), $\mathbf{F}\vec{\mathbf{W}}^T$ and $\mathbf{U}_\mathbf{M}$ must span the same subspace, because both sides of (5.3) must have the same column space. The column space of the SVD is determined by $\mathbf{U}_\mathbf{M}$, while $\mathbf{F}\vec{\mathbf{W}}^T$ determines the column

[2] Six singular values are needed for a general EMI target.

space of the product on the left-hand side because they are the only matrices to the left of the minimum rank breaking point. This can actually be taken a step further because the column space of the left-hand side is determined by $\mathbf{F}$ since $\vec{\mathbf{W}}^T$ simply combines the columns of $\mathbf{F}$ in different ways.

The relationship between the column spaces can be derived more precisely through the following mathematical analysis. To obtain this connection, it is useful to investigate $\mathbf{M}\mathbf{M}^T$ which is a square $M \times M$ matrix which is symmetric and positive semidefinite. It is well known that the SVD of $\mathbf{M}$ is connected to the eigenvalue decomposition of $\mathbf{M}\mathbf{M}^T$ as follows:

$$\mathbf{M}\mathbf{M}^T = \mathbf{U}_\mathbf{M}\mathbf{\Sigma}_\mathbf{M}\mathbf{V}_\mathbf{M}^T\mathbf{V}_\mathbf{M}\mathbf{\Sigma}_\mathbf{M}\mathbf{U}_\mathbf{M}^T = \mathbf{U}_\mathbf{M}\mathbf{\Sigma}_\mathbf{M}^2\mathbf{U}_\mathbf{M}^T = \text{Eig}\{\mathbf{M}\mathbf{M}^T\}. \tag{5.4}$$

The $\mathbf{M}\mathbf{M}^T$ matrix can be analyzed in reference to (5.1) to obtain

$$\mathbf{M}\mathbf{M}^T = \mathbf{F}\vec{\mathbf{W}}^T \underbrace{\vec{\boldsymbol{D}}^T\vec{\mathbf{\Phi}}^T\mathbf{H}\mathbf{H}^T\vec{\mathbf{\Phi}}\vec{\boldsymbol{D}}}_{\text{matrix } \mathbf{B}_\mathbf{U} \succeq 0}\vec{\mathbf{W}}\mathbf{F}^T \tag{5.5}$$

where the noise term has been ignored. The symmetric matrix $\mathbf{B}_\mathbf{U}$ is positive semidefinite, so it has a square root $\mathbf{Q}_\mathbf{U}$ which is also symmetric, i.e., $\mathbf{Q}_\mathbf{U}^2 = \mathbf{B}_\mathbf{U} = \mathbf{Q}_\mathbf{U}\mathbf{Q}_\mathbf{U}^T$. One instance of $\mathbf{Q}_\mathbf{U}$ can be obtained from the eigendecomposition of $\mathbf{B}_\mathbf{U}$ by taking square roots of the nonnegative eigenvalues of $\mathbf{B}_\mathbf{U}$, but it is not unique. Any matrix of the form $\mathbf{Q}_\mathbf{U}\mathbf{R}$ is also a square root if $\mathbf{R}$ is unitary, because $\mathbf{Q}_\mathbf{U}\mathbf{R}\mathbf{R}^T\mathbf{Q}_\mathbf{U}^T = \mathbf{Q}_\mathbf{U}^2$ when $\mathbf{R}\mathbf{R}^T = \boldsymbol{I}$.

Now the square root of $\mathbf{M}\mathbf{M}^T = \mathbf{U}_\mathbf{M}\mathbf{\Sigma}_\mathbf{M}^2\mathbf{U}_\mathbf{M}^T$ in (5.4) is $\mathbf{U}_\mathbf{M}\mathbf{\Sigma}_\mathbf{M}$, while the square root of $\mathbf{M}\mathbf{M}^T$ in (5.5) is $\mathbf{F}\vec{\mathbf{W}}^T\mathbf{Q}_\mathbf{U}\mathbf{R}$, so the governing equation for the column spaces is

$$\mathbf{U}_\mathbf{M}\mathbf{\Sigma}_\mathbf{M} = \mathbf{F}\vec{\mathbf{W}}^T\mathbf{Q}_\mathbf{U}\mathbf{R} \tag{5.6}$$

The unitary matrix $\mathbf{R}$ can be a rotation or reflection, so it offers flexibility to obtain equality in (5.6). A new matrix $\mathbf{C}_\mathbf{U} \in \Re^{K \times R}$ can be defined that is equal to $\vec{\mathbf{W}}^T\mathbf{Q}_\mathbf{U}\mathbf{R}$ to create a

simplified connection between the column spaces of

$$\mathbf{U_M \Sigma_M} = \mathbf{F C_U} \tag{5.7}$$

where $\mathbf{C_U}$ can be thought of as a matrix responsible for orthogonalizing the columns of $\mathbf{F}$ and then weighting them accordingly.

The column space connection of (5.7) ignores the noise that was added to the measured data. The noise must be reintroduced into this relationship to arrive at

$$\boxed{\mathbf{U_M \Sigma_M} = \mathbf{F C_U} + \mathcal{E}_\mathbf{U}} \tag{5.8}$$

where it can still be assumed that $\mathcal{E}_\mathbf{U}$ is i.i.d $\mathcal{N}(0, \sigma_\epsilon^2)$. This measurement model is the well known least-squares problem

$$\min_{\mathbf{C_U}} \|\mathbf{U_M \Sigma_M} - \mathbf{F C_U}\|_F \tag{5.9}$$

where the expected minimum value is $\|\mathcal{E}_\mathbf{U}\|_F$. For the standard least-squares problem when no extra constraints are applied, the analytic solution can be achieved with

$$\boxed{\mathbf{C_U^{opt}} = \mathbf{F}^\dagger \mathbf{U_M \Sigma_M}} \tag{5.10}$$

where $\mathbf{F}^\dagger$ is the pseudo-inverse that is defined as $\mathbf{F}^\dagger = (\mathbf{F}^T\mathbf{F})^{-1}\mathbf{F}^T$. If there is no noise, we expect the least-squares error to be zero and have equality in (5.7).

Just like $\mathbf{F}$ and $\mathbf{U_M}$, $\mathbf{H}^T$ and $\mathbf{V_M}$ span the same subspace. This means that a noise model for aligning the row spaces becomes

$$\boxed{\mathbf{\Sigma_M V_M^T} = \mathbf{C_V^T H} + \mathcal{E}_\mathbf{V}} \tag{5.11}$$

and the above discussion applies for obtaining $\mathbf{C_V} \in \Re^{6\times R}$, also via least squares

$$\boxed{\begin{aligned} \min_{\mathbf{C_V}} \|\mathbf{\Sigma_M V_M}^T - \mathbf{C_V}^T\mathbf{H}\|_F \quad (5.12a) \\ (\mathbf{C_V}^{\text{opt}})^T = \mathbf{\Sigma_M V_M}^T\mathbf{H}^\ddagger, \quad (5.12b) \end{aligned}}$$

where $\mathbf{H}^\ddagger$ is the left pseudo-inverse of a matrix given by $\mathbf{H}^\ddagger = \mathbf{H}^T(\mathbf{H}\mathbf{H}^T)^{-1}$.

For all of these equations it has been assumed that the row and column subspaces are known *a priori*. This is not the case in practice and Sec. 5.2 discusses how the subspaces can be estimated from the singular values given different types of *a priori* information.

5.1.2 Recovering the Center Terms

Once the least-squares solution for the subspaces is found, it is possible to recover the center matrices $\vec{\mathbf{W}}^T\vec{\boldsymbol{D}}^T\vec{\mathbf{\Phi}}^T$. This is accomplished by inserting the relationships from (5.7) and (5.11) (when noise-free) into (5.3) to obtain

$$\begin{aligned} \mathbf{U_M\Sigma_M V_M}^T &= (\mathbf{U_M\Sigma_M})\mathbf{\Sigma_M}^{-1}(\mathbf{\Sigma_M V_M}^T) \quad (5.13a) \\ &= \mathbf{F}(\mathbf{C_U\Sigma_M}^{-1}\mathbf{C_V}^T)\mathbf{H} = \mathbf{F}\vec{\mathbf{W}}^T\vec{\boldsymbol{D}}^T\vec{\mathbf{\Phi}}^T\mathbf{H}. \quad (5.13b) \end{aligned}$$

From (5.13b) it becomes possible to recover the whole middle term as

$$\boxed{\vec{\mathbf{W}}^T\vec{\boldsymbol{D}}^T\vec{\mathbf{\Phi}}^T = \mathbf{C_U\Sigma_M}^{-1}\mathbf{C_V}^T.} \quad (5.14)$$

A different method for deriving (5.14) is to use the pseudo-inverses. Applying the pseudo-inverses of $\mathbf{F}$ and $\mathbf{H}$ to both sides arrives at

$$\begin{aligned} \vec{\mathbf{W}}^T\vec{\boldsymbol{D}}^T\vec{\mathbf{\Phi}}^T &= \mathbf{F}^\dagger\mathbf{U_M\Sigma_M V_M}^T\mathbf{H}^\ddagger \\ &= \left(\mathbf{F}^\dagger\mathbf{U_M\Sigma_M}\right)\mathbf{\Sigma_M}^{-1}\left(\mathbf{\Sigma_M V_M}^T\mathbf{H}^\ddagger\right) \quad (5.15) \\ &= \mathbf{C_U\Sigma_M}^{-1}\mathbf{C_V}^T \end{aligned}$$

which provides an alternative derivation of (5.14).

5.1.3 Selecting the Least-Squares Weighting Terms

At this point it is worth discussing a decision that was made above. In (5.7) it was implied that the singular vectors $\mathbf{U_M}$ should be weighted by the singular values $\mathbf{\Sigma_M}$. However, when this selection is made, it causes a weighting correction in (5.14) because the singular values have become squared. This decision is worth further discussion and justification. There are three natural choices for the weights

$$\min_{\mathbf{C_U}} \|\mathbf{U_M}\mathbf{\Sigma_M} - \mathbf{F}\mathbf{C_U}\|_2 \tag{5.16a}$$

$$\min_{\mathbf{C_U}} \|\mathbf{U_M}\mathbf{\Sigma_M}^{\frac{1}{2}} - \mathbf{F}\mathbf{C_U}\|_2 \tag{5.16b}$$

$$\min_{\mathbf{C_U}} \|\mathbf{U_M} - \mathbf{F}\mathbf{C_U}\|_2, \tag{5.16c}$$

where the singular values are weighted by different powers of the singular vectors. The (5.16b) weighting splits the singular values in half so each side of the SVD recovery contains equal weightings and (5.14) would not need a weighting correction term. The (5.16c) weighting removes any weighting influence and just focuses on the subspace alignment. Once aligned, the singular values would be applied in (5.14).

At first glance, all of the options in (5.16) seem valid. The (5.16a) was chosen due to the implications it has on the noise terms in (5.9). Appendix B discusses the maximum likelihood estimation of matrix recovery and shows that least squares is optimal under an i.i.d. Gaussian noise assumption. This means that the weighting needs to preserve the noise properties as i.i.d. from the original data. First, let it be assumed that the SVD of the signal term is known such that

$$\mathbf{F}\vec{\mathbf{W}}^T\vec{\boldsymbol{D}}^T\vec{\mathbf{\Phi}}^T\mathbf{H} = \mathbf{U_S}\mathbf{\Sigma_S}\mathbf{V_S}^T. \tag{5.17}$$

Now, the measurement model with noise can be written as

$$\mathbf{M} = \mathbf{U_M}\mathbf{\Sigma_M}\mathbf{V_M}^T = \mathbf{U_S}\mathbf{\Sigma_S}\mathbf{V_S}^T + \mathcal{E}. \tag{5.18}$$

The transformations of (5.18) to obtain the weightings of (5.16) become

$$\mathbf{U_M}\mathbf{\Sigma_M} = \mathbf{M}\mathbf{V_M} \tag{5.19a}$$

$$\mathbf{U_M}\mathbf{\Sigma_M}^{\frac{1}{2}} = \mathbf{M}\mathbf{V_M}\mathbf{\Sigma_M}^{-\frac{1}{2}} \tag{5.19b}$$

$$\mathbf{U_M} = \mathbf{M}\mathbf{V_M}\mathbf{\Sigma_M}^{-1}, \tag{5.19c}$$

respectively. Assuming high enough SNR, then $\mathbf{V_S}^T\mathbf{V_M} \cong \boldsymbol{I}$. The primary focus needs to be on the noise matrix though. Let $\mathbf{v}$ be any column vector from $\mathbf{V_M}$, which consists of multiple orthonormal vectors. Given a vector of random i.i.d. Gaussian noise samples, $\boldsymbol{\epsilon} \in \Re^{N\times 1}$, where each sample is drawn from the distribution $\mathcal{N}(0, \sigma_\epsilon^2)$, it can be easily shown that $\boldsymbol{\epsilon}^T\mathbf{v} \sim \mathcal{N}(0, \sigma_\epsilon^2)$ because $\|\mathbf{v}\|_2 = 1$. It can also be easily shown that because any two vectors from $\mathbf{V_M}$, $\mathbf{v}_i$ and $\mathbf{v}_j$, are orthogonal ($\mathbf{v}_i^T\mathbf{v}_j = 0$), then the new sample created from each vector will be independent ($\mathbf{v}_i^T\boldsymbol{\epsilon}$ and $\mathbf{v}_j^T\boldsymbol{\epsilon}$ are independent). Both of these constraints are true about all of the vectors within $\mathbf{V_M}$. This means that multiplying a noise vector by $\mathbf{V_M}$, $\boldsymbol{\epsilon}^T\mathbf{V_M}$, produces a new noise vector where each element is again i.i.d. $\mathcal{N}(0, \sigma_\epsilon^2)$. When $\mathbf{V_M}$ is applied to a matrix of i.i.d. $\mathcal{N}(0, \sigma_\epsilon^2)$ samples it will create

$$\mathcal{E}_\mathbf{U} = \mathcal{E}\mathbf{V_M} \tag{5.20}$$

where $\mathcal{E}_\mathbf{U} \in \Re^{M\times R}$ is a matrix of i.i.d. $\mathcal{N}(0, \sigma_\epsilon^2)$ samples. Using this new perspective on

the noise matrix, the noise terms of each weighting become

$$\mathcal{E}\mathbf{V}_{\mathbf{M}} = \mathcal{E}_{\mathbf{U}} \tag{5.21a}$$

$$\mathcal{E}\mathbf{V}_{\mathbf{M}}\boldsymbol{\Sigma}_{\mathbf{M}}^{-\frac{1}{2}} = \mathcal{E}_{\mathbf{U}}\boldsymbol{\Sigma}_{\mathbf{M}}^{-\frac{1}{2}} \tag{5.21b}$$

$$\mathcal{E}\mathbf{V}_{\mathbf{M}}\boldsymbol{\Sigma}_{\mathbf{M}}^{-1} = \mathcal{E}_{\mathbf{U}}\boldsymbol{\Sigma}_{\mathbf{M}}^{-1}, \tag{5.21c}$$

respectively. Based on the desire for i.i.d. noise, only the selected weighting of (5.16a) guarantees the noise remains undisturbed. In both of the other weighting schemes, the noise terms will have different variances because of the singular value weightings.

5.2 Recovering Model Subspaces

In order to obtain the low-rank model from the data, it was previously assumed that $\mathbf{F}$ and $\mathbf{H}$ were known a priori. In reality, obtaining valid matrices for $\mathbf{F}$ and $\mathbf{H}$ is the important problem of interest for recovering the model in (5.1). The benefit of recovering the low-rank model from the SVD is that it has completely decoupled the estimation of $\mathbf{F}$ and $\mathbf{H}$. The only joint estimation required occurs when obtaining $\vec{\mathbf{W}}^T\vec{\boldsymbol{D}}^T\vec{\boldsymbol{\Phi}}^T$. Separating these estimation problems better aligns with the model and allows for a more robust processing design. This enables the low-rank model to accurately estimate the location and estimate the target parameters for classification independently and only requires joint processing for determining the target's orientation. There are three general approaches for recovering these subspaces. The processing chain for the EMI model will primarily use the first two methods which are called subspace selection and sparse subspace creation, but the third technique of subspace projection is included here for completeness because this approach is generalizable to other applications. Appendix B provides further technical details that show these approaches are maximum likelihood estimators and discusses implementation trade-offs. The following sections serve as introductions to the subspace recovery techniques and further details for applying them to EMI data are provided in later chapters.

5.2.1 Subspace Selection Recovery

The subspace selection (SS) approach is the first recovery technique. SS is used when multiple options can be created from a model, but only a single option can be accurate. An example of this scenario is the position matrix $\mathbf{H}$. Using equations from the physical model, it is possible to simulate what $\mathbf{H}$ should be for any target location below the EMI sensor. By creating a discrete grid of locations and simulating $\mathbf{H}$ for each of the grid points, it is possible to generate a set $\boldsymbol{\mathcal{H}}$ of possible $\mathbf{H}$ matrices. Under the assumption that the EMI targets are physically separated such that the EMI sensor is only interacting with one target at a time, obtaining the correct $\mathbf{H}$ becomes a problem of selecting the best $\mathbf{H}$ from $\boldsymbol{\mathcal{H}}$.

In order to select the best fitting $\mathbf{H}$, it is natural to use (5.9) as a metric for how well each $\mathbf{H}$ fits. This is written as

$$\boxed{\min_{\boldsymbol{\mathcal{H}}} \min_{\mathbf{C}_{\mathbf{V}}^{i}} \|\mathbf{V}_{\mathbf{M}}\boldsymbol{\Sigma}_{\mathbf{M}} - \mathbf{H}_i\mathbf{C}_{\mathbf{V}}^{i}\|_F} \tag{5.22}$$

where $\mathbf{H}_i$ is one entry in $\boldsymbol{\mathcal{H}}$ and $\mathbf{C}_{\mathbf{V}}^{i}$ is the associated least-squares solution that best fits the data. In words, (5.22) fits $\mathbf{V}_{\mathbf{M}}\boldsymbol{\Sigma}_{\mathbf{M}}$ from the SVD in (5.2) to all possible $\mathbf{H}_i \in \boldsymbol{\mathcal{H}}$, and then selects the $\mathbf{H}_i$ that best aligns with the $\mathbf{V}_{\mathbf{M}}$ subspace.

5.2.2 Sparse Subspace Creation Recovery

The sparse subspace creation (SSC) approach is the second recovery technique. SSC is used when a sparse optimization problem can be designed with a dictionary to represent one of the subspaces. One example is the DSRF estimation of a target's signature response within the low-rank framework. The DSRF allows the left side of the EMI model to become

$$\mathbf{F}\vec{\mathbf{W}}^{T} = \mathbf{A}\vec{\mathbf{W}}_{\mathbf{A}}^{T} \tag{5.23}$$

where $\mathbf{A} \in \Re^{M \times Z}$ is an over-complete dictionary, i.e., $Z > M$, and $\vec{\mathbf{W}}_{\mathbf{A}} \in \Re^{Z \times R}$ is a matrix of weights that select a few of the column vectors from $\mathbf{A}$ to create $\mathbf{F}$. The matrix $\vec{\mathbf{W}}_{\mathbf{A}}^T$ is sparse because most of the rows are zero, and the nonzero rows correspond to the original values in $\vec{\mathbf{W}}^T$.[3] The matrix $\mathbf{A}$ is known from the physics of the EMI sensor. The model of (5.23) can be inserted into (5.7) to obtain

$$\mathbf{U_M \Sigma_M} = \mathbf{A}\vec{\mathbf{W}}_{\mathbf{A}}^T \mathbf{Q_U R} = \mathbf{A C}_{\vec{\mathbf{W}}} \tag{5.24}$$

where $\mathbf{C}_{\vec{\mathbf{W}}} = \vec{\mathbf{W}}_{\mathbf{A}}^T \mathbf{Q_U R}$. This connection between the SVD and sparse matrix optimization has been used in angle of arrival estimation for radio frequency systems [22]. The form of (5.24) is the same as the model used in [22] to derive the SOC optimization problem

$$\boxed{\min_{\mathbf{C}_{\vec{\mathbf{W}}}} \|\mathbf{U_M \Sigma_M} - \mathbf{A C}_{\vec{\mathbf{W}}}\|_F^2 + \lambda \|\mathbf{C}_{\vec{\mathbf{W}}}^{\ell_2}\|_1} \tag{5.25}$$

where $\|\square\|_1$ is the ℓ_1 norm, λ is a tuning parameter, and $\mathbf{C}_{\vec{\mathbf{W}}}^{\ell_2}$ is a vector containing the ℓ_2 norm of each row in $\mathbf{C}_{\vec{\mathbf{W}}}$. Other algorithms such as IAA [23] and M-FOCUSS [24] are also designed to solve problems such as (5.24).

It should be noted that SSC solves for $\mathbf{C}_{\vec{\mathbf{W}}}$ instead of $\mathbf{C_U}$. Solving for the center of the model again as was done in (5.13b) and (5.14) leads to

$$\mathbf{U_M \Sigma_M V_M^T} = \mathbf{A C}_{\vec{\mathbf{W}}} \mathbf{\Sigma_M^{-1} C_V^T H} = \mathbf{A}\vec{\mathbf{W}}_{\mathbf{A}}^T \vec{\boldsymbol{D}}^T \vec{\mathbf{\Phi}}^T \mathbf{H} \tag{5.26a}$$

$$\Rightarrow \ \vec{\mathbf{W}}_{\mathbf{A}}^T \vec{\boldsymbol{D}}^T \vec{\mathbf{\Phi}}^T = \mathbf{C}_{\vec{\mathbf{W}}} \mathbf{\Sigma_M^{-1} C_V^T} \tag{5.26b}$$

for the SSC approach. This center matrix is now a large sparse matrix of dimension $\Re^{Z \times 6}$, where each row is the *tensor amplitude* for a specific DSRF and most of the *tensor amplitudes* correspond to non-active relaxation frequencies and have a power of zero.

[3] This disregards the issue of sampling the relaxations which causes an off-grid artifact during recovery.

5.2.3 Subspace Projection Recovery

The subspace projection (SP) approach is the final recovery technique. SP can be used when the model subspace is created from an unknown linear combination of a larger subspace. This method is used throughout the EMI processing, but it is useful to explicitly state it. Consider a constrained general model of the form

$$\mathbf{S} = \mathbf{F}\mathbf{W}^T\mathbf{T} \tag{5.27}$$

where $\mathbf{W}^T \in \Re^{K\times R}$ is a generic center matrix and $\mathbf{T} \in \Re^{R\times N}$ is forced to have dimensions equal to the rank R. If the rank of the EMI data is known, and the matrices are forced to be the correct size, then it is necessary to replace $\mathbf{T}$ with a linear combination of a larger (known) subspace that can be written as

$$\mathbf{T}^T = \mathbf{H}^T\mathbf{\Phi} \tag{5.28}$$

where $\mathbf{H} \in \Re^{6\times N}$, $\mathbf{\Phi} \in \Re^{6\times R}$, and $6 > R$ when SP is used. Notice that this is inherently what has already occurred with the EMI processing above. Relaxing the model so that only the upper bound of the rank is known arrives at the general EMI target model of

$$\mathbf{S} = \mathbf{F}\mathbf{W}^T\mathbf{T} = \mathbf{F}\mathbf{W}^T\mathbf{\Phi}^T\mathbf{H} = \mathbf{F}\mathbf{G}^T\mathbf{H} \tag{5.29}$$

which is a different perspective from what was accomplished in (4.4). This is what allowed (5.12a) to solve for the rectangular matrix $\mathbf{C}_\mathbf{V}$ instead of the square matrix $\mathbf{B}_\mathbf{V}^{1/2}$. Although this does not change anything that has been discussed within the EMI context, it is used throughout the EMI processing. Using the SP technique does involve allowing some uncertainty into the model that causes a loss in processing performance, especially when recovering the center terms.

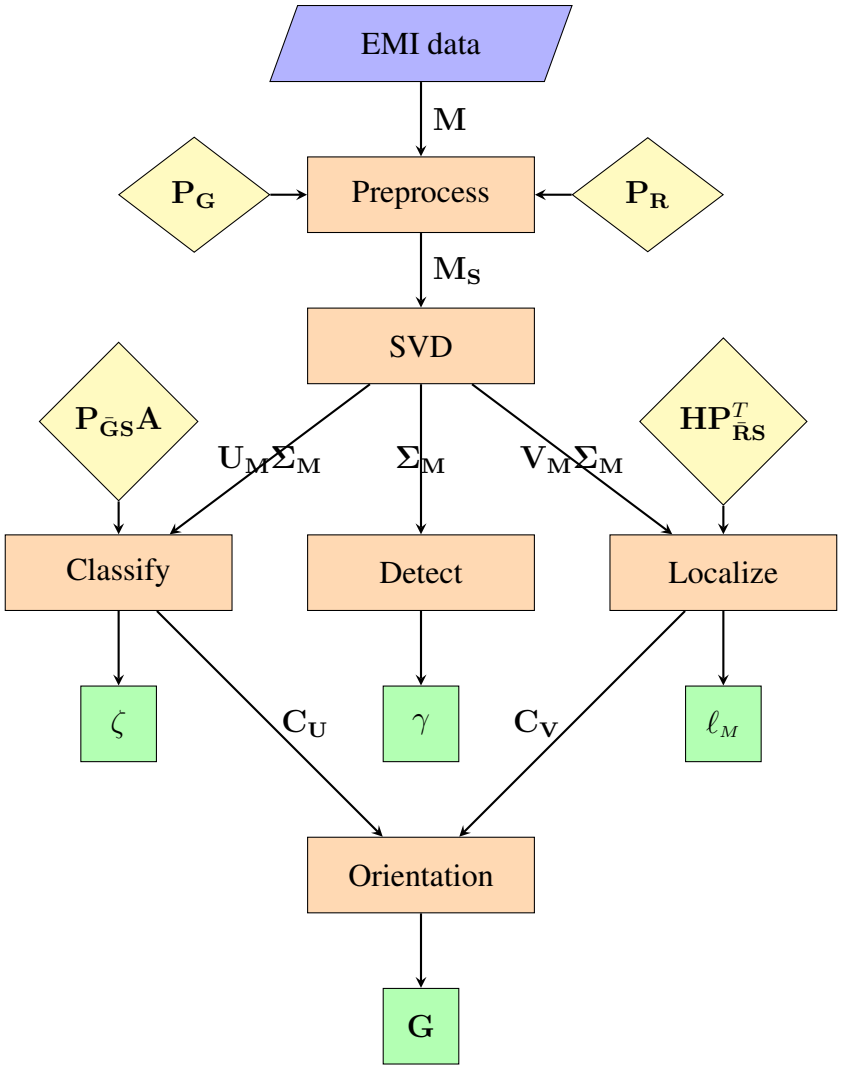

Figure 5.1: A flow graph of the new low-rank framework.

5.3 Defining the Framework

With the recovery techniques discussed above, all of these techniques can naturally be combined into an EMI processing framework. There are four objectives for an EMI processing framework: detection, classification, localization, and orientation. An ideal framework can recover all of this information in a robust and efficient manner. A new signal processing framework from the low-rank model is illustrated in Fig. 5.1. Not only does this framework achieve all four objectives, but it also provides a natural way to mitigate interference signals that are often measured by an EMI system.

The first operation on the measured data is to perform preprocessing on the raw data. This step is designed to remove known interference and produce a new matrix $\mathbf{M_S}$ that is designed to have only a signal and noise response where the signal-to-noise-ratio (SNR) is ideally higher than the raw data. The preprocessing stage will be discussed in detail in Ch. 6. Once the isolated signal is created, the SVD techniques that have been discussed are applied. The left singular vectors and singular values are used for target classification. This data can be used to extract the target's relaxation frequencies, which is discussed in Ch. 9. Chapter 10 shows that the low-rank model also leads to a natural method for classifying targets without needing to perform the DSRF inversion. This new method for target classification is independent of target location and orientation, which means that it has the same desirable benefits of the DSRF for classification but without a difficult inversion problem. The right singular values contain the location information and can use the SS recovery technique to determine the target's location. Once the location and target's features are recovered, the orientation of the target is determined by recovering the center matrix $\mathbf{G}$ of the signal model. This recovery is demonstrated in Ch. 11. Two other useful signal processing applications are studied within the low-rank framework. First, the process of detecting targets using EMI data is discussed in detail in Ch. 7. Secondly, Chapter 8 discusses automated rank estimation using established model order estimation techniques. All of these components together create a very streamlined and effective signal processing framework for EMI data.

The equations and variables that have been introduced throughout this chapter are re-used during the remainder of this thesis. For convenience, the primary equations are compiled in Table C.1 and the variables have been listed and defined in Table C.2. This is provided as a condensed resource for the reader.

5.4 SVD Considerations

An important consideration for the low-rank framework is the impacts of noise on the SVD. The robustness of the SVD for signal processing applications has been previously investigated [25]. Some of the key considerations are summarized here.

The error incurred by the singular values are limited to

$$\sqrt{\overline{(\sigma_{\mathbf{M}} - \sigma_{\mathbf{S}})}} \leq \frac{1}{\sqrt{M}} \|\mathcal{E}\|_F \tag{5.30}$$

where $\overline{\sigma_{\mathbf{M}} - \sigma_{\mathbf{S}}}$ is the average error of the singular values and M is the number of singular values.[4] This is a loose bound, and for EMI applications when the SNR $> 5\log(N)$ it is expected that the bound will be closer to $\frac{1}{\sqrt{MN}} \|\mathcal{E}\|_F$ which means that

$$\sqrt{\sigma_{\mathbf{M}} - \sigma_{\mathbf{S}}} \cong \sqrt{\sigma_{\epsilon}^2}. \tag{5.31}$$

For cases where the SNR is $\leq 5\log(N)$, the small singular values caused by the noise may start to interfere with the target and disturb the SVD.

The bound on the singular vectors depends on the assumption that the singular values of a group from $\mathbf{\Sigma_M}$ are separated from the other singular values. Because the EMI process is only interested in the strongest singular values, the primary separation of interest is

$$\min\{\mathbf{\Sigma_M}\} - \max\{\mathbf{\Sigma}_{\mathcal{E}}\} \geq \delta_{\sigma} \tag{5.32}$$

where $\mathbf{\Sigma}_{\mathcal{E}}$ are the remaining singular values from $\mathbf{M}$ after the strongest singular values have been extracted into $\mathbf{\Sigma_M}$. The canonical angle is the distance between two subspaces used in [25], which can be defined as

$$\|\mathbf{V_M} - \mathbf{V_S}\|_P = \|\boldsymbol{P}_{\mathbf{V_M}} - \boldsymbol{P}_{\mathbf{V_S}}\|_F \tag{5.33}$$

[4] Assuming that $M \leq N$

where $\boldsymbol{P}_{\square}$ is a projection matrix made out of the desired subspace. With these terms defined, the perturbation of the singular vectors is bounded by

$$\sqrt{\|\mathbf{V_M} - \mathbf{V_S}\|_P^2 + \|\mathbf{U_M} - \mathbf{U_S}\|_P^2} \leq \frac{1}{\delta_\sigma}\|\mathcal{E}\|_F \tag{5.34}$$

where this is known to be a loose bound but is used here for simplicity. This shows that there is a connection between how much noise is in the singular vectors and how large the SNR is when the SVD is taken.

5.5 Lab Results

Lab data was collected using the Georgia Tech (GT) EMI platform to measure various targets as they moved beneath the sensor in free space. The lab data contains multiple passes over a target, where the target was placed 7.5 cm below the EMI sensor. The system measures the response at 21 frequencies[5] and at $N = 200$ positions per pass. The data was processed to remove the sensor self-response and other background interference [26]. The resulting measured data was organized into a matrix as has been described previously. In order to verify the predictive model proposed by this work, the singular value decomposition (SVD) of the resulting matrix was taken. The singular values of the SVD should portray the rank of the matrix combined with the noise floor. The noise floor is expected to cause the small singular values to be roughly constant. The low-rank model is verified by showing that any singular values over six represent the noise floor. The number of singular values greater than the noise floor equals the rank of the signal matrix.

Figure 5.2 is a graph of the first ten singular values for four targets that, theoretically, are expected to have a single independent tensor. The targets consist of two aluminum spheres, a steel sphere, and a 22 gauge wire that has been formed into a single loop. The metal spheres have an infinite number of relaxations but only have a single independent

[5] In this frequency-domain system, the 21 complex-valued measurements become $M = 42$ because the real and imaginary parts are separated.

tensor – the identity tensor. The wire loop is expected to have a single relaxation frequency that is determined by the wire gauge and the loop size. The EMI system energizes the loop in the direction of the wire such that the single tensor component will be in a direction perpendicular to the plane of the loop. The singular values confirm the model and its theoretical expectations for these four targets as they only produce a rank-one matrix above the noise floor.

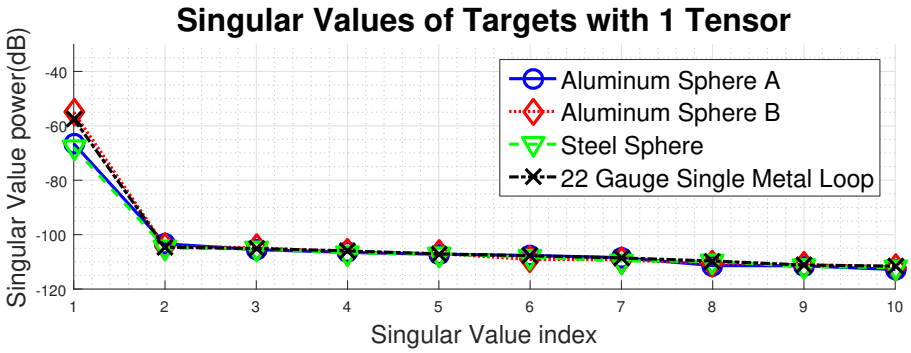

Figure 5.2: Singular values obtained from lab data for targets that are expected to be of rank-one.

Figure 5.3 is a graph of the first ten singular values for two targets that theoretically have two linearly independent tensors. Rotationally symmetric metal objects (such as nails and tacks) should have a tensor in the direction of the axis of symmetry and a second tensor that has equal components in directions perpendicular to the axis of symmetry. These targets also validate the low-rank model because there are only two singular values above the noise floor.

Figure 5.4 is a graph of the first ten singular values for two targets that are expected to have three linearly independent tensors. Both of these targets are created by orienting three different metal loops perpendicular to each other in a single target. This causes the composite target to have a single tensor along each primary axis. The singular values in Fig. 5.4 confirm that there are indeed three major tensor components.

In order to validate the signal model against the lab data, a three-loop target was simulated using reciprocity [3] and a sum of relaxations [2] model. The model is based on

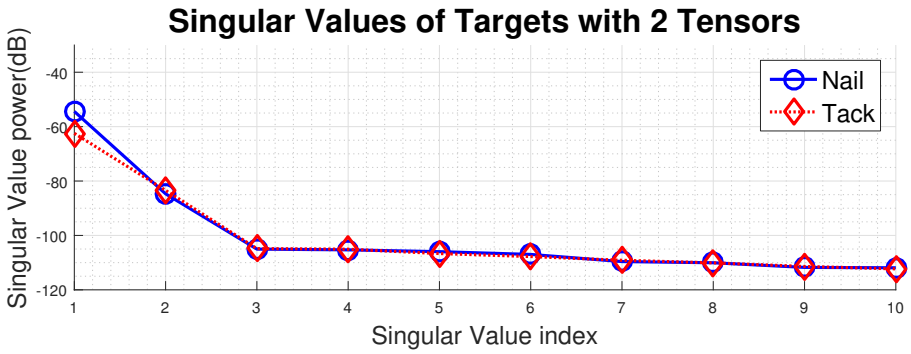

Figure 5.3: Singular values obtained from lab data for targets that are expected to be of rank-two.

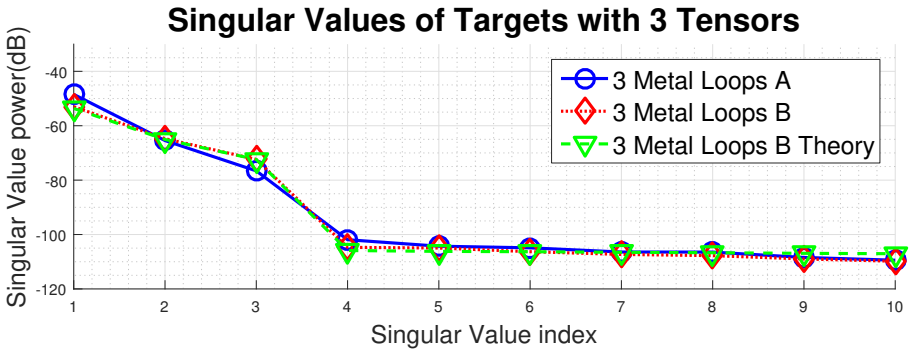

Figure 5.4: Singular values obtained from lab data for targets that are expected to be of rank-three. A simulation was run for the wire loop B target and the results align exactly with the measured data.

loop B in Fig. 5.4, which has metal loops built out of 22, 30, and 36 gauge copper wire. Random complex gaussian noise was added to the simulated data in order to replicate the noise floor present in the lab data. The singular values obtained from the simulation are in Fig. 5.4 along with the rank-three lab targets. As can be seen, the theoretical model aligns well with the lab data collected.

Lab data was also gathered for three targets of interest and presented in Fig. 5.5. These targets have more complicated physical structures and are made of various materials that contain differing amounts of ferrous materials. By using the low-rank model, it is possible to estimate the number of linearly independent tensors for each target. These physical parameters could now be used as added features for classification and identification.

These lab results confirmed two important facts. First, none of the targets produced a

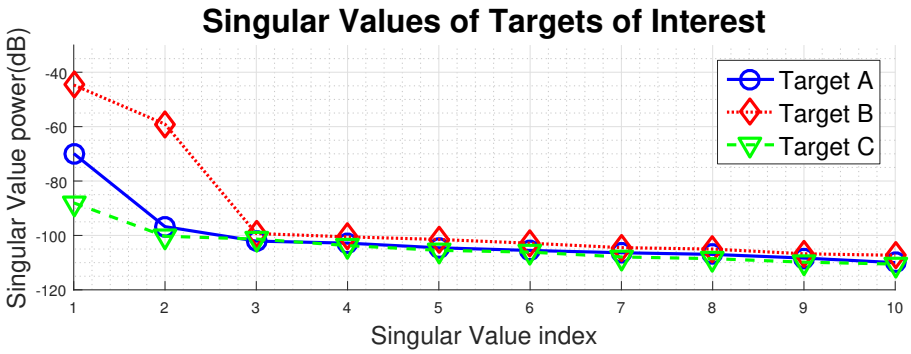

Figure 5.5: Singular values obtained from lab data for targets of interest.

signal matrix with rank higher than six. This is true for the complicated targets with unknown tensors or theoretical responses. An even stronger validation is that all measured targets had a rank less than four, which means that it is reasonable to assume all of these targets are also modeled as ortho-point targets. Secondly, the ability of the low-rank model to predict the rank of the signal matrix becomes evident. The predictive capability is a powerful property for allowing the physical design to be mapped directly to the measurement's rank. It also could allow one to map measurements from an unknown target into physical constraints of the target's shape and design.

It is useful to confirm that the SVD has successfully compressed the target's information. This is necessary in order for any further processing to exploit the compressed, denoised data instead of the raw data. The singular vectors of the simulated target and lab data are presented in Figs. 5.6a and 5.6b, respectively. The left singular vectors have real and imaginary parts since they are from a frequency-domain sensor and contain the information in $\mathbf{F}$ and $\mathbf{W}$. The position singular vectors contain the information in $\mathbf{\Phi}$ and $\mathbf{H}$. Figures 5.6a and 5.6b clearly show that the simulated and lab data contain the same information in the first three singular vectors. The fourth and greater singular vectors contain noise terms for both types of singular vectors. It is clear that the simulated data contains random noise in both the frequency and position singular vectors. However, for the measured data, it is interesting to note that the stronger noise terms are concentrated in the lower frequency measurements, and only the position vectors appear to be random noise. This is believed

to be a result of low-frequency interference near the lab during the measurements.

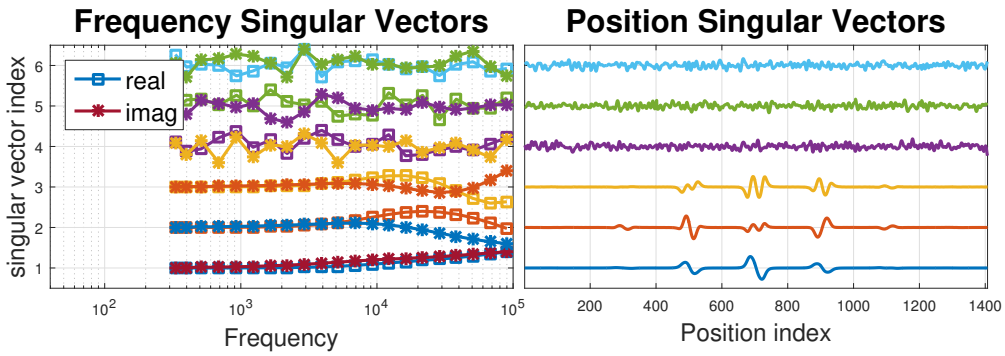

(a)

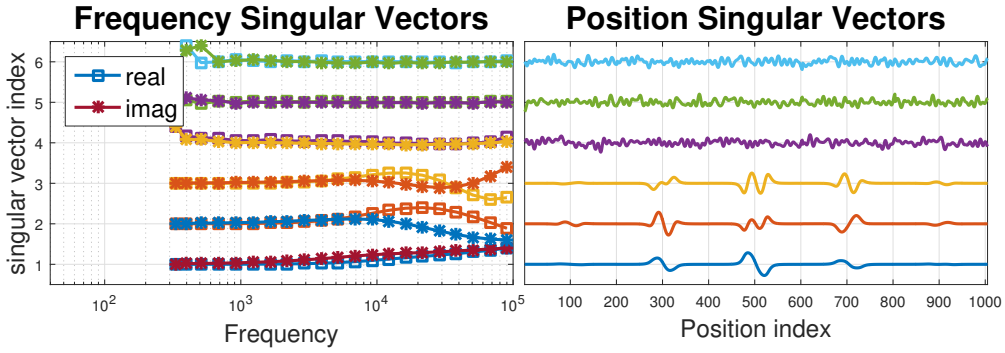

(b)

Figure 5.6: Singular vectors obtained from (a) simulated data and (b) lab data for a three-loop target.

5.6 Reference Targets

The reference targets were simulated and their SVD computed to provide further intuition for the low-rank signal processing framework. In order to simulate the reference targets, a sensor type and measurement locations had to be selected. For this thesis, the GT EMI frequency-domain sensor has been used as the sensor type. It measures magnitude and phase at 21 frequencies that span 300Hz to 90MHz and are roughly equally log-spaced. A scan path was chosen as shown in Fig. 5.18 where a single transmitter/receiver pair is moved along nine scans in the Y dimension. Each scan contains a measurement every 5mm in the X dimension, and a scan is taken every 5cm in the Y dimension. This is designed to mimic a hand-held system, but the scan path is overly sampled to reduce the chance of

being blind to any target orientations.

Using these parameters, the reference target measurements were simulated and an SVD was calculated. The results are shown in Figs. 5.7 – 5.16. The singular values confirm the true rank that was already discussed for the reference targets. There was a minimal amount of random Gaussian noise applied to the measurements to illustrate the flat noise singular values and the random nature of the singular vectors for the values that no longer contain target information. The singular vectors contain that target information as was shown above. The first notable fact about both sides of the singular vectors is that the vector is smooth when it contains target information. Once the index becomes larger than the target rank, the spatial response in the right singular values and the real and imaginary components in the left singular values take on a random value nature.

The right singular vectors contain the spatial information on the orientation. For most of the targets, the orientation aligns with the X-Y-Z coordinate dimensions. It can be seen that each of the nine passes over the target by the sensor is recognizable by the repeated nature of the vectors every 121 samples. The X and Z directed targets have the strongest spatial response in the middle of the vector when the sensor measured directly over the target. The Y directed components are nulled when the sensor passes directly over the target and grow in strength as the sensor is more offset. This is caused by the sensor design and the use of a quadrupole receiver that nulls the EMI response when directly over the sensor in the desired measurement direction.

The right singular vectors contain the target response information. The real and imaginary parts should move smoothly across frequency, and they will typically cross at least once in the vector. Figure 5.17 provides a different visualization of these singular vectors. The Argand diagram plots the frequency response as the tip of a vector defined by the real and imaginary parts, and parameterized by frequency. Within an Argand diagram, target responses will mostly take a circular shape around the origin or be sums of circles. Once the index is higher than the target's rank the left singular vectors also display erratic values.

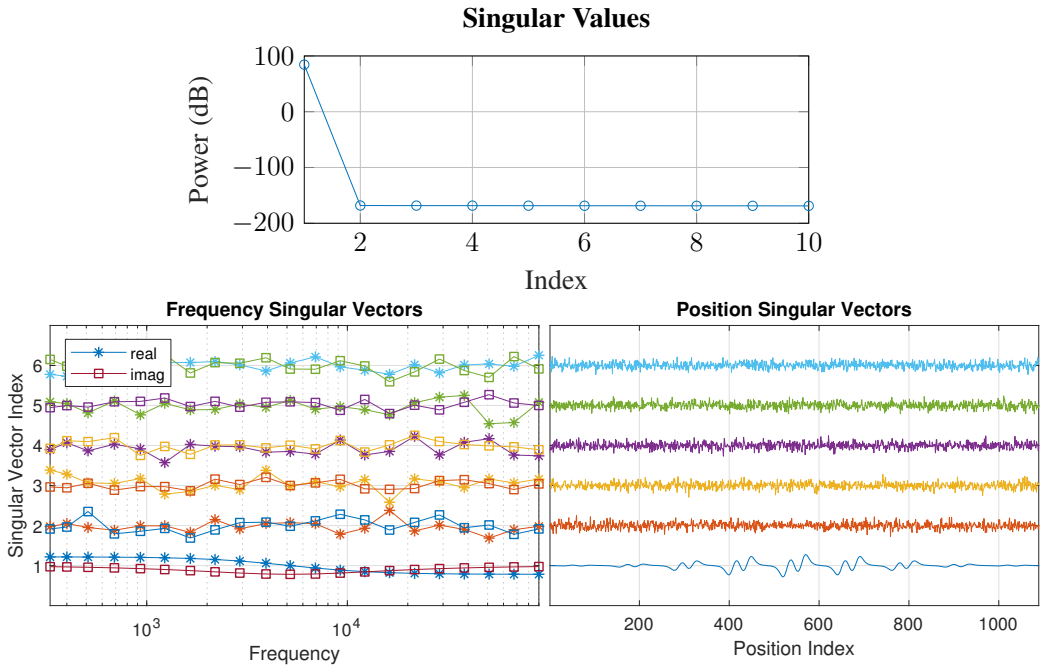

Figure 5.7: The singular values and associated singular vectors for RT-01. Argand diagrams of left singular vectors are provided in Fig. 5.17.

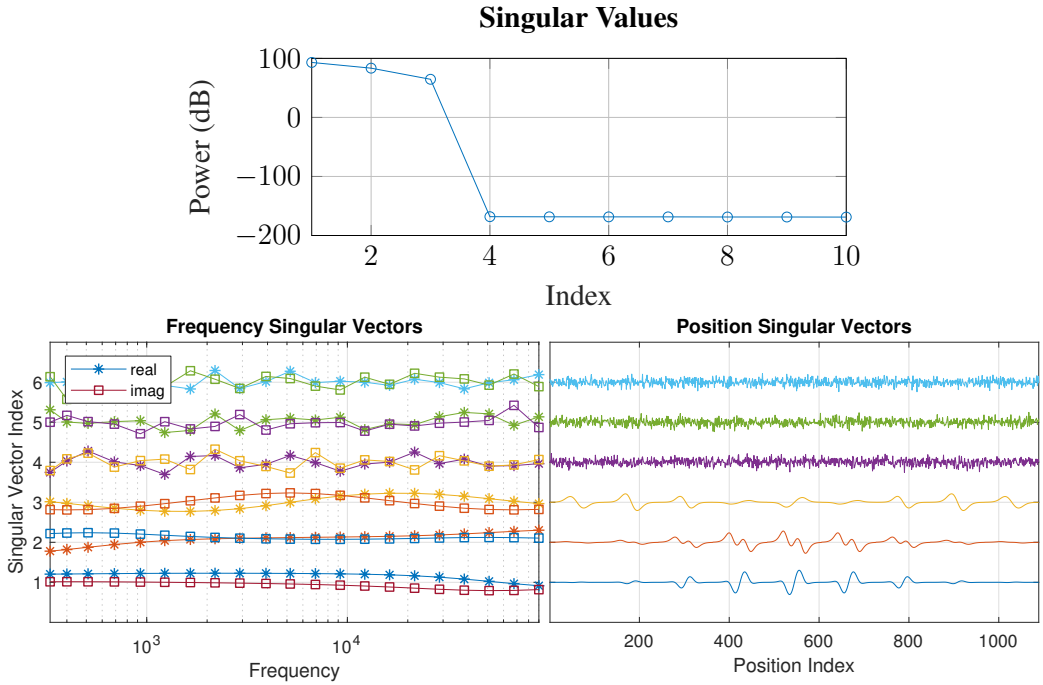

Figure 5.8: The singular values and associated singular vectors for RT-02. Argand diagrams of left singular vectors are provided in Fig. 5.17.

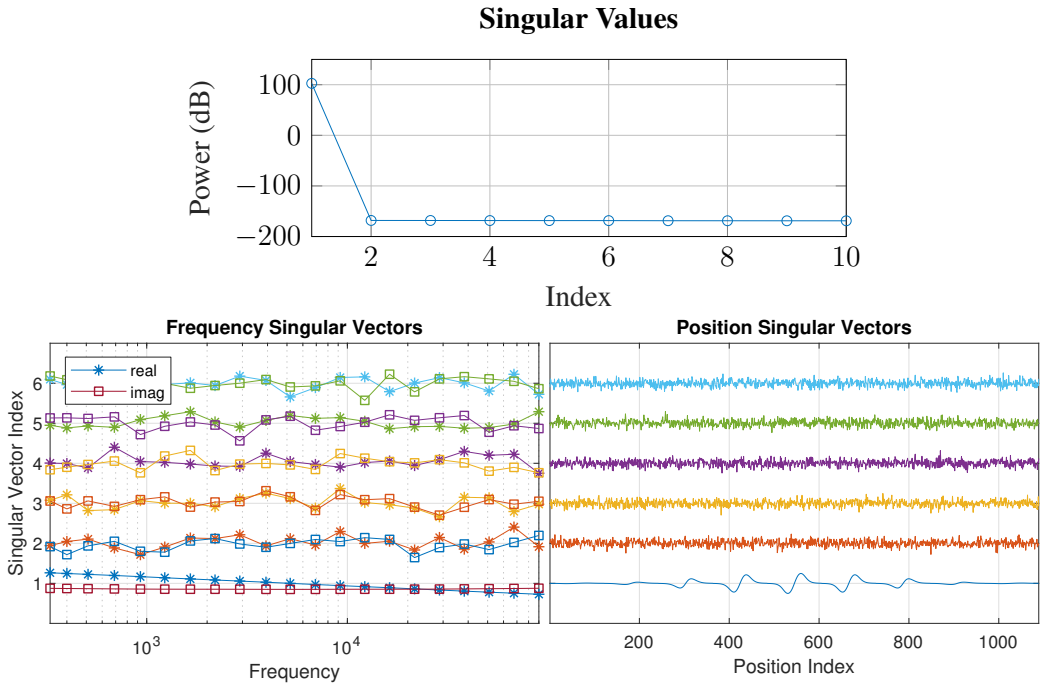

Figure 5.9: The singular values and associated singular vectors for RT-03. Argand diagrams of left singular vectors are provided in Fig. 5.17.

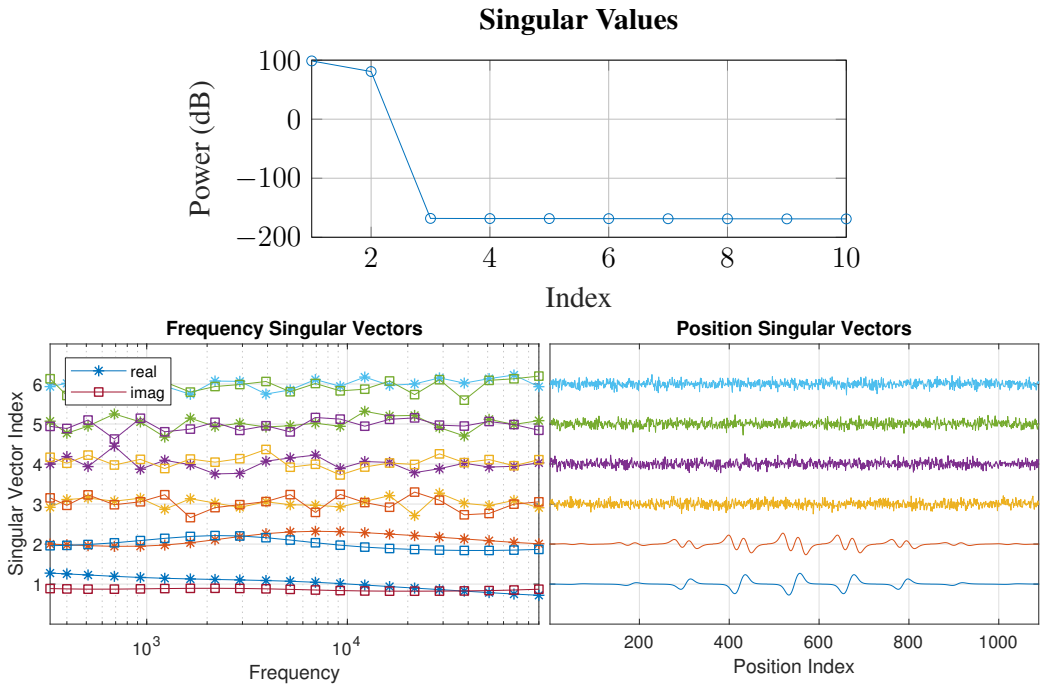

Figure 5.10: The singular values and associated singular vectors for RT-04. Argand diagrams of left singular vectors are provided in Fig. 5.17.

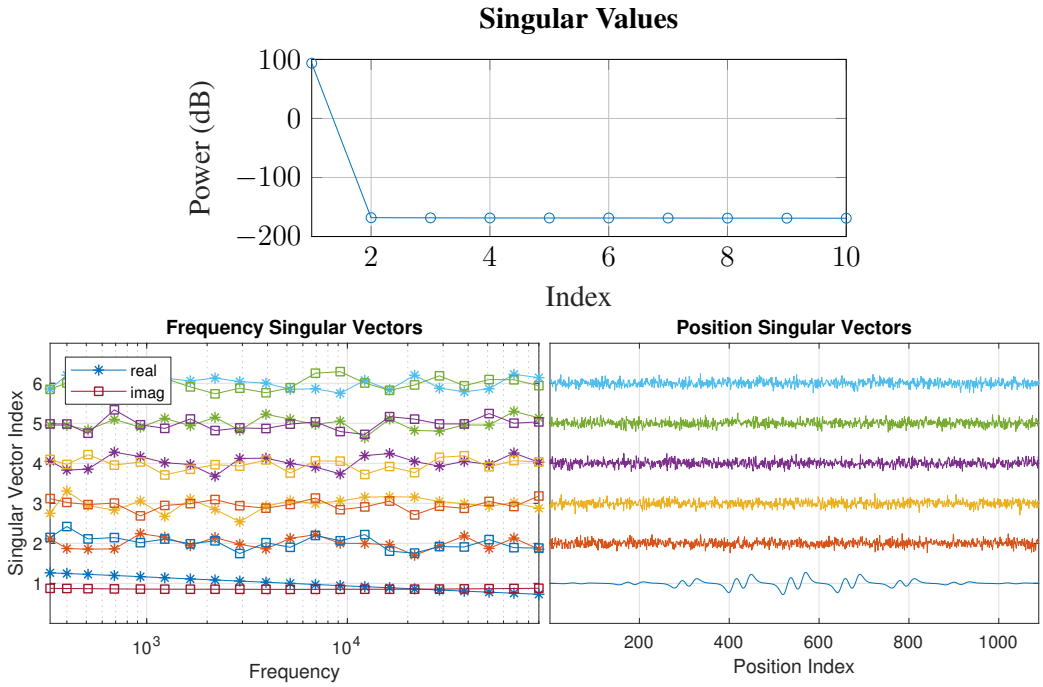

Figure 5.11: The singular values and associated singular vectors for RT-05. Argand diagrams of left singular vectors are provided in Fig. 5.17.

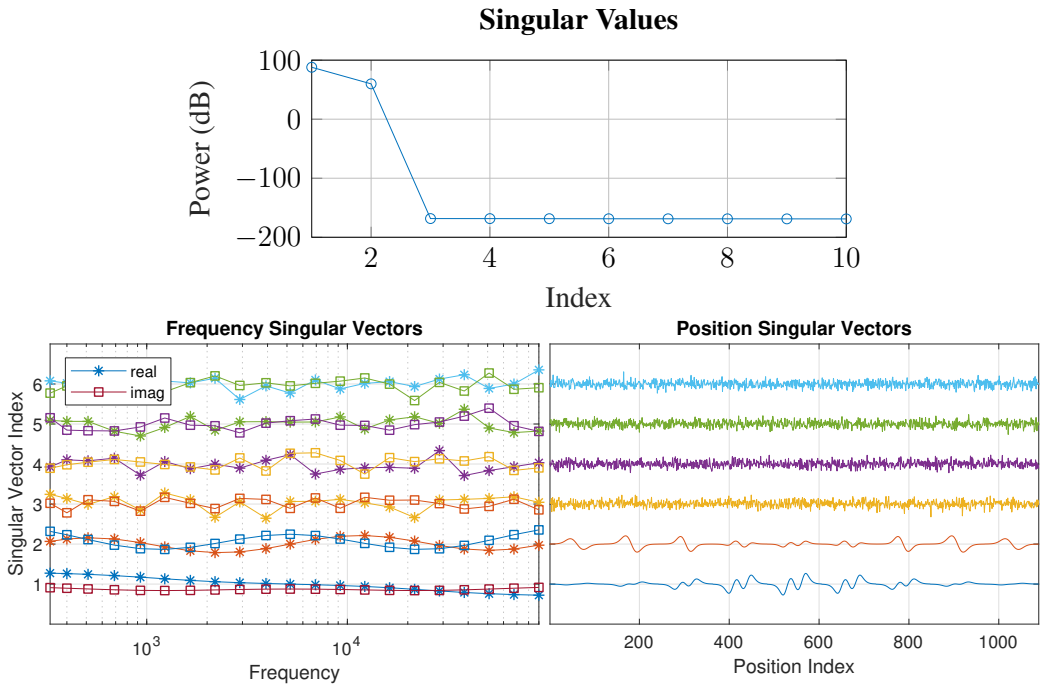

Figure 5.12: The singular values and associated singular vectors for RT-06. Argand diagrams of left singular vectors are provided in Fig. 5.17.

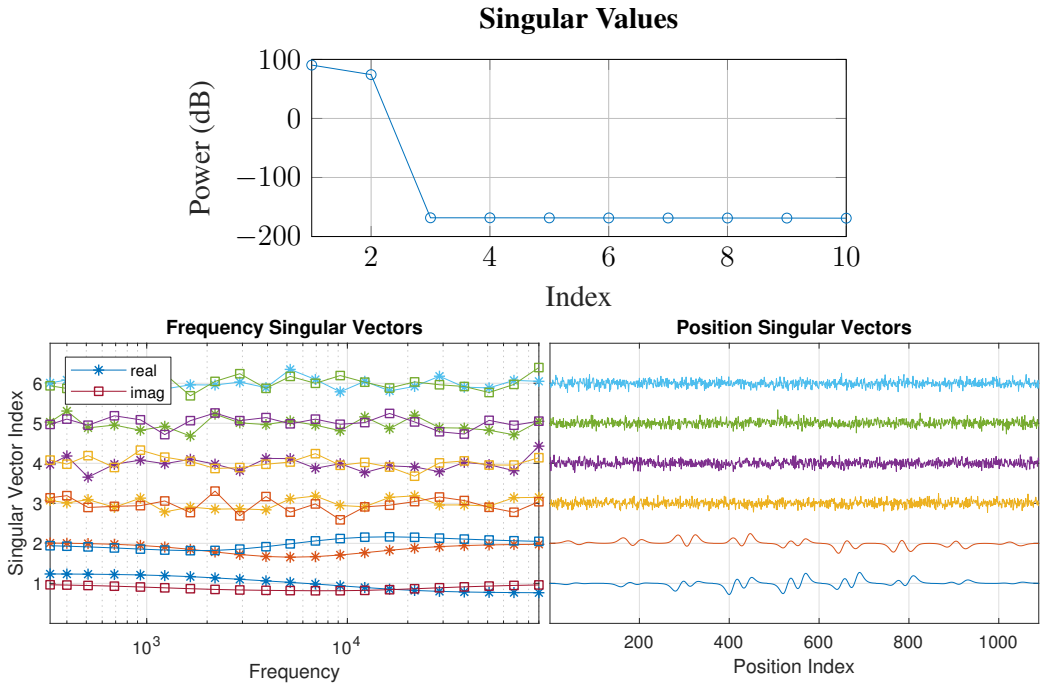

Figure 5.13: The singular values and associated singular vectors for RT-07. Argand diagrams of left singular vectors are provided in Fig. 5.17.

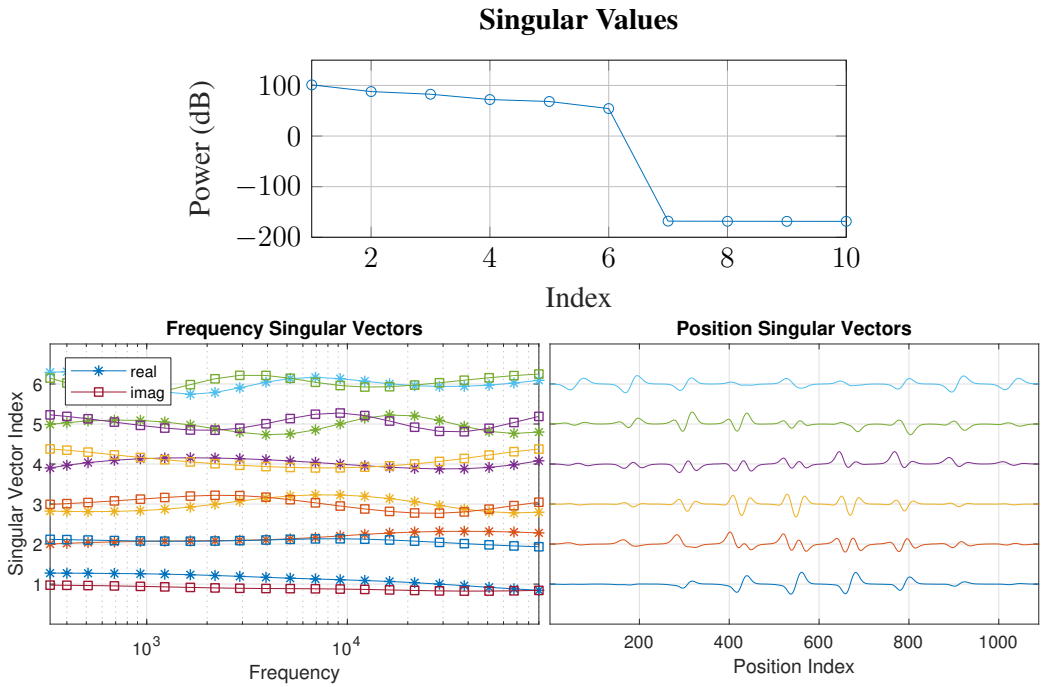

Figure 5.14: The singular values and associated singular vectors for RT-08. Argand diagrams of left singular vectors are provided in Fig. 5.17.

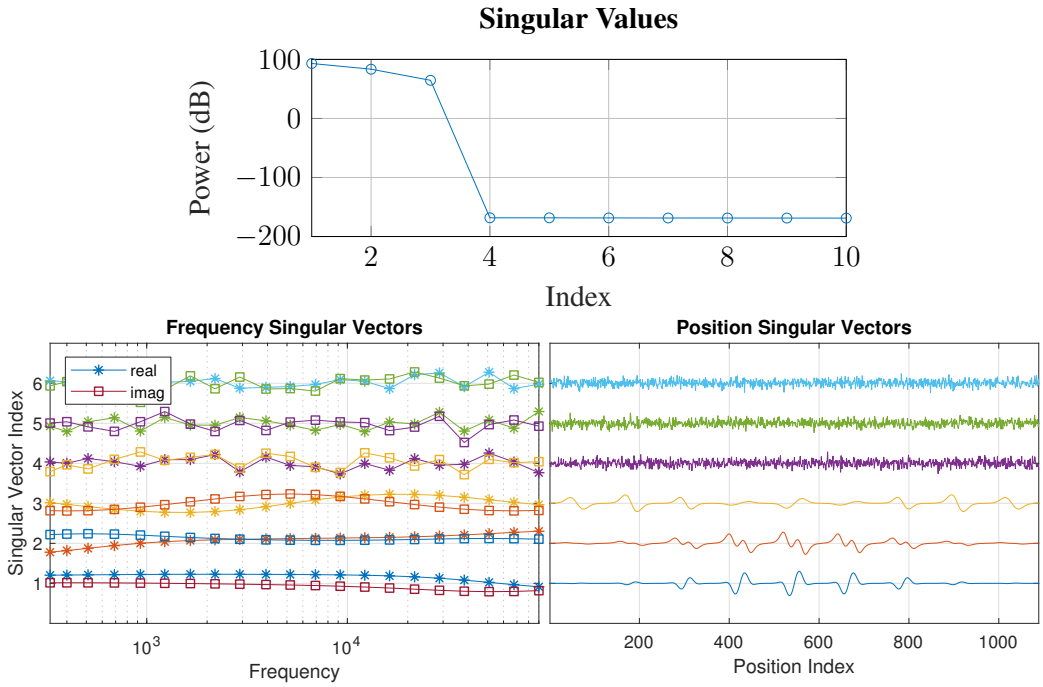

Figure 5.15: The singular values and associated singular vectors for RT-09. Argand diagrams of left singular vectors are provided in Fig. 5.17.

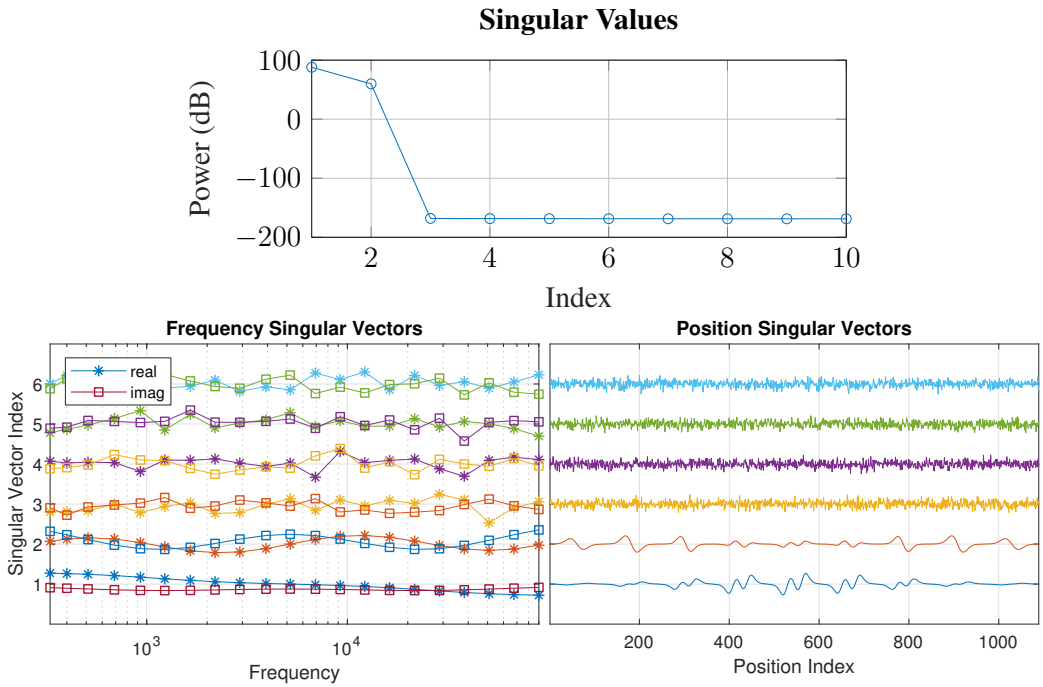

Figure 5.16: The singular values and associated singular vectors for RT-10. Argand diagrams of left singular vectors are provided in Fig. 5.17.

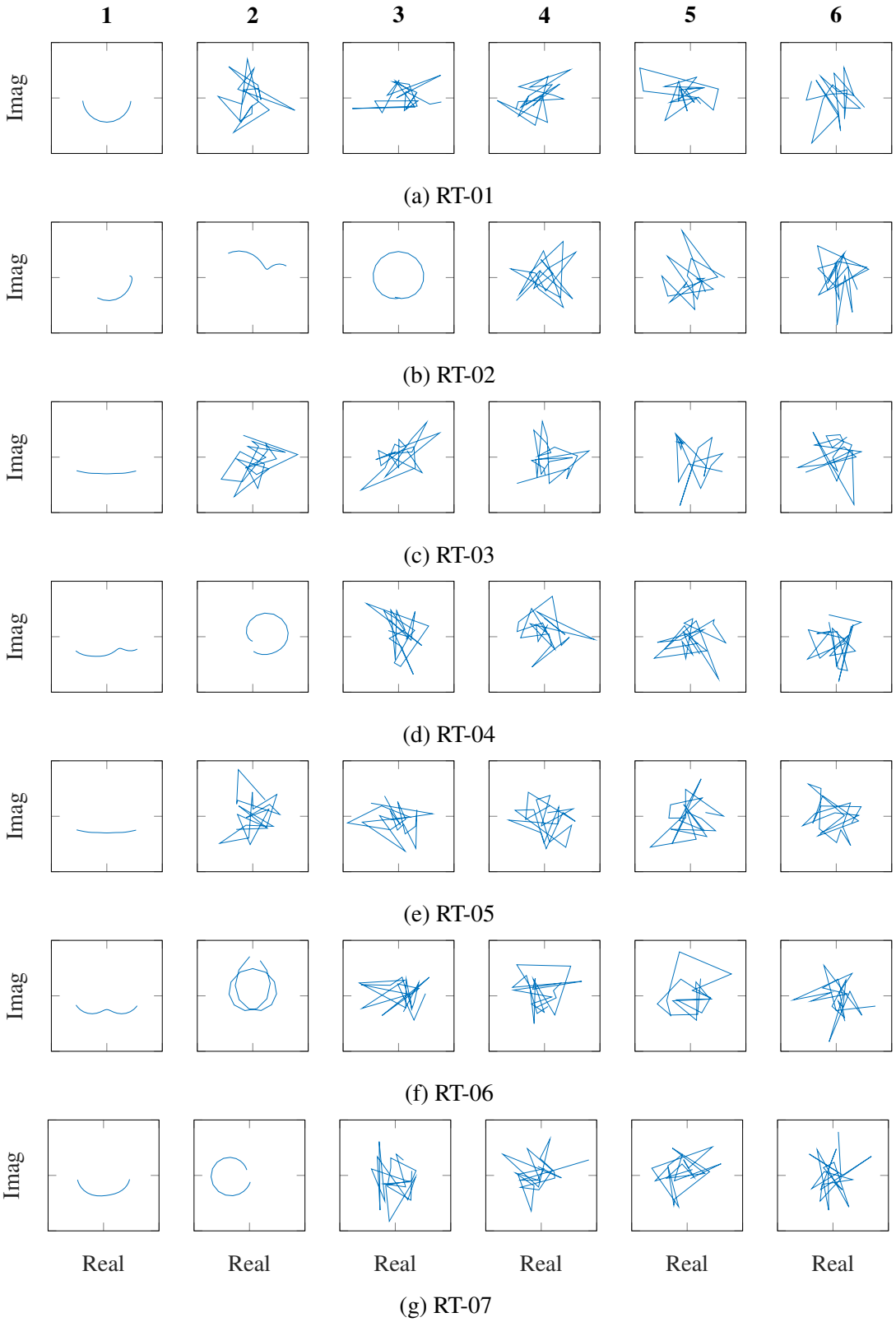

(a) RT-01

(b) RT-02

(c) RT-03

(d) RT-04

(e) RT-05

(f) RT-06

(g) RT-07

Figure 5.17: The left singular vectors of the reference targets plotted as Argand diagrams.

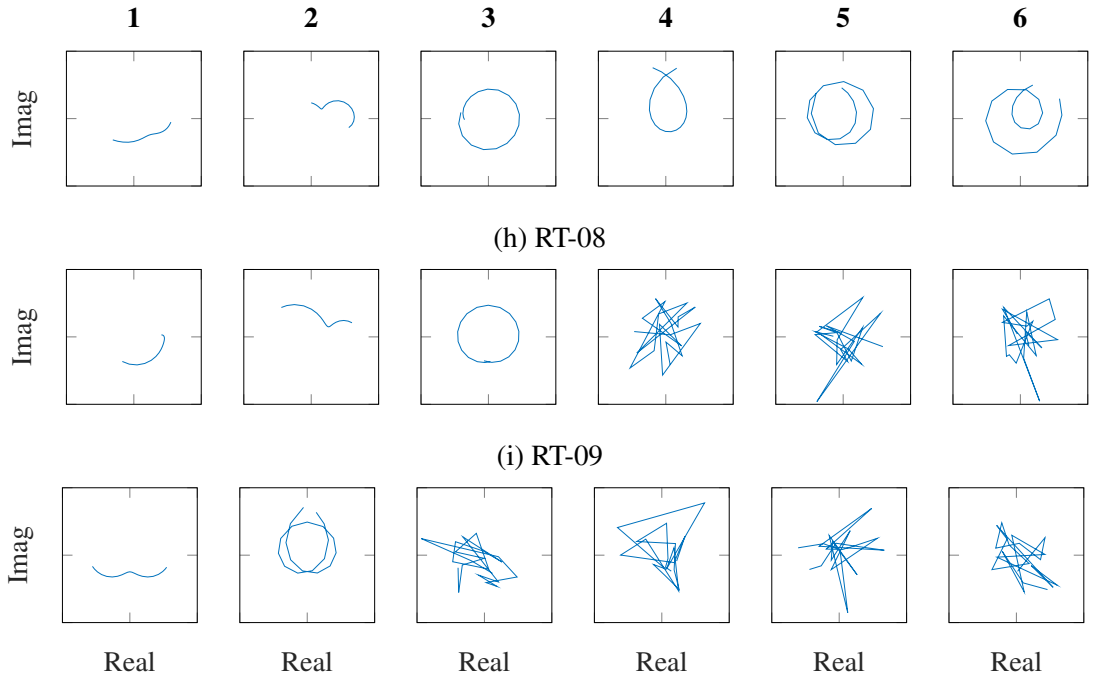

(h) RT-08

(i) RT-09

(j) RT-10

Figure 5.17: The left singular vectors of the reference targets plotted as Argand diagrams (cont.).

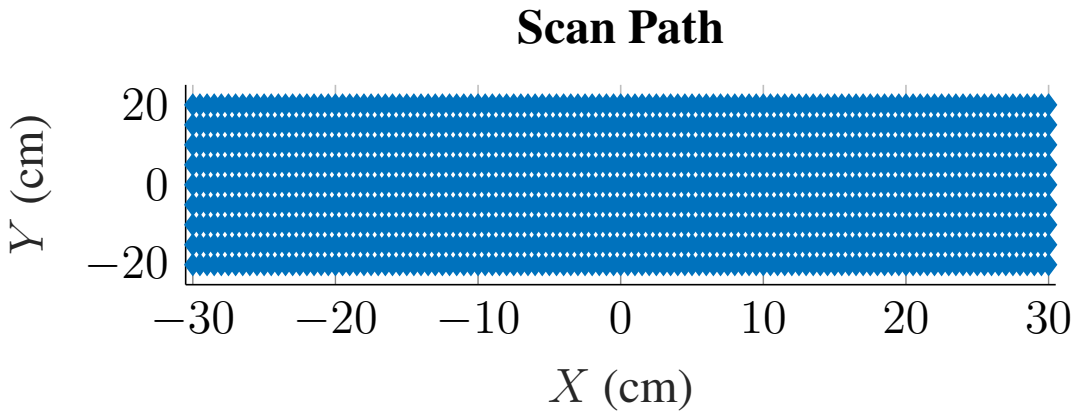

Figure 5.18: Sensor scan path used for simulating the reference targets. There are 121 equally spaced measurements along the X dimension for each scan and nine equally spaced scans along the Y dimension.

Part II

Application of the Low-Rank EMI Framework

CHAPTER 6

PREPROCESS EMI DATA

6.1 Measurement Matrix Model

In order to delve into the new preprocessing framework [26], it is useful to review the physical model of the EMI data including known interferences that are expected to be measured. This thesis will provide a detailed derivation for frequency-domain systems as this corresponds to the available simulated and sensor collected data; however, it is straightforward to extend these techniques to time-domain systems. A frequency-domain EMI system takes a complex measurement, $\tilde{m}(\omega, \Delta p)$, at a specific operating frequency, ω, and at a specific location of the sensor, Δp. Each measurement taken by the sensor contains four primary sources: the response from a target, $\tilde{s}$, the magnetic response of the soil, $\tilde{g}$, the self response from the sensor, $\tilde{r}$, and a random noise term that can be approximated as a complex Gaussian random value, $\tilde{\epsilon} \sim \mathcal{CN}(0, 2\sigma_\epsilon^2)$. The sensor measurement is modeled as

$$\tilde{m}(\omega, \Delta p) = \tilde{s}(\omega, \Delta p) + \tilde{g}(\omega, \Delta p) + \tilde{r}(\omega, \Delta p) + \tilde{\epsilon}. \tag{6.1}$$

Recent work [26, 20] has shown that the target response can be modeled as a low-rank matrix when multiple frequencies and positions are processed jointly. This leads to creating a measurement matrix for further processing by grouping M frequencies, $\boldsymbol{\omega}$, along the columns of a matrix and N positions, $\boldsymbol{\Delta p}$, along the rows to create $\tilde{\mathbf{M}}(\boldsymbol{\omega}, \boldsymbol{\Delta p}) = [\tilde{m}(\boldsymbol{\omega}_i, \boldsymbol{\Delta p}_j)]_{i,j}$ where $\tilde{\mathbf{M}} \in \mathfrak{C}^{M \times N}$. The matrix model can then be written as

$$\tilde{\mathbf{M}}(\boldsymbol{\omega}, \boldsymbol{\Delta p}) = \tilde{\mathbf{S}}(\boldsymbol{\omega}, \boldsymbol{\Delta p}) + \tilde{\mathbf{G}}(\boldsymbol{\omega}, \boldsymbol{\Delta p}) + \tilde{\mathbf{R}}(\boldsymbol{\omega}, \boldsymbol{\Delta p}) + \tilde{\mathcal{E}} \tag{6.2}$$

where it is assumed that each noise term in $\tilde{\mathcal{E}}$ is an i.i.d. complex noise measurement. Fi-

nally, because the received signal only has a single complex component [20], the measured data can be split into the real and imaginary components to be processed jointly across frequencies. This expansion can be written as

$$\mathbf{M}(\boldsymbol{\omega}, \boldsymbol{\Delta}\mathbf{p}) = \begin{bmatrix} \Re\{\tilde{\mathbf{M}}(\boldsymbol{\omega}, \boldsymbol{\Delta}\mathbf{p})\} \\ \Im\{\tilde{\mathbf{M}}(\boldsymbol{\omega}, \boldsymbol{\Delta}\mathbf{p})\} \end{bmatrix} \tag{6.3}$$

where $\mathbf{M} \in \Re^{2M \times N}$ is the new real-valued measurement matrix. The model for the real-valued measurements become

$$\boxed{\mathbf{M}(\boldsymbol{\omega}, \boldsymbol{\Delta}\mathbf{p}) = \mathbf{S}(\boldsymbol{\omega}, \boldsymbol{\Delta}\mathbf{p}) + \mathbf{G}(\boldsymbol{\omega}, \boldsymbol{\Delta}\mathbf{p}) + \mathbf{R}(\boldsymbol{\omega}, \boldsymbol{\Delta}\mathbf{p}) + \mathcal{E}} \tag{6.4}$$

where each term has been separated as in (6.3).

As this work is focused on exploiting the new filterless preprocessing scheme [26] that uses projection matrices on $\mathbf{M}$, it is necessary to further investigate the matrix components. The target response has been discussed in previous work [20], and the low-rank model for a target will be used for this work to model $\mathbf{S}$. The elements of the noise matrix $\mathcal{E}$ are assumed to be drawn from i.i.d. $\mathcal{N}(0, \sigma_\epsilon^2)$ distributions. The remaining two components are discussed below and can be regarded as interference signals because they are always present in the measurements and interfere with the desired target response.

6.1.1 Self Response Matrix

The self-response $\tilde{r}(\omega, \Delta p)$ is an artifact from the transmitter coil and receiver coils of the EMI system coupling together. Given a specific operating frequency, this coupling is expected to be relatively constant over multiple positions because the sensor platform moves as a unit and should have a relatively steady response. This allows the self response to be modeled over multiple positions as $\tilde{\boldsymbol{r}}(\omega, \boldsymbol{\Delta}\mathbf{p}) = \tilde{r}(\omega)\mathbf{1}^T$, where $\mathbf{1} \in \Re^{N \times 1}$ is a vector of 1's. Each operating frequency can have a different coupling response, and the phase of

the coupling response is also unknown. Because of this, each operating frequency's real and imaginary part is assumed unknown and the self-response matrix is modeled as

$$\boxed{\mathbf{R}(\boldsymbol{\omega}, \boldsymbol{\Delta}\mathbf{p}) = \boldsymbol{r}(\boldsymbol{\omega})\mathbf{1}^T} \tag{6.5}$$

where $\boldsymbol{r} \in \Re^{2M \times 1}$ is an unknown vector of the system coupling responses.

It should be noted that the constant coupling response is an approximation. As long as the drift is small enough for the sensor and the window of position values, N, is short enough, then this approximation is expected to be true. However, if either of these conditions is not met, then it may require the self response position model to be expanded into a more sophisticated model such as a linear model $\tilde{\boldsymbol{r}}(\omega, \boldsymbol{\Delta}\mathbf{p}) = b + m\boldsymbol{\Delta}\mathbf{p}$, or even a more sophisticated modeling mechanism (e.g., Taylor expansion).

In an EMI system, the self response is partially mitigated in the hardware design by nulling the coupling between the coils in the system. Even with hardware nulling, the self response of the system is often several magnitudes greater than the average target response as will be evident in the results below. Because nulling is not sufficient, the remaining part of the self response must be mitigated using processing. Several types of filters have been investigated for mitigating the effects of the self response, and, generally, a single filter that is constrained to be zero mean has been used [17, 14, 27], although multiple filters constrained to be zero mean have also been used [12].

6.1.2 Soil Matrix

The soil response has been studied previously in [28] where an empirical model for the soil response was found. The soil response is mostly contained in a two-dimensional subspace within the operating frequency dimension. This allows the soil response to be described as

$$\tilde{g}(\omega, \Delta p) = \begin{bmatrix} 1 & \log(\frac{\omega}{\omega_c}) + \frac{j\pi}{2} \end{bmatrix} \begin{bmatrix} \xi_1(\Delta p) \\ \xi_2(\Delta p) \end{bmatrix} \tag{6.6}$$

where $\xi_1(\Delta p)$ and $\xi_2(\Delta p)$ are the strengths of the soil response in these dimensions at a given position. These strengths will be dependent on the properties of the soil at each position as well as the geometry of the EMI sensor. In order to be as general as possible, this work will model only the mean and variance of this soil strength function. This is equivalent to modeling the strength terms as Gaussian distributions such that $\xi_1(\Delta p) \sim \mathcal{N}(g_1, \sigma_g^2)$ and $\xi_2(\Delta p) \sim \mathcal{N}(g_2, \sigma_g^2)$. If the frequency model of the soil is expanded into a matrix and the real and imaginary parts are separated as in (6.3), then the soil matrix can be modeled as

$$\boxed{\mathbf{G}(\boldsymbol{\omega}, \boldsymbol{\Delta p}) = \boldsymbol{\Psi}(\boldsymbol{\omega})\boldsymbol{\Xi}^T} \tag{6.7}$$

where $\boldsymbol{\Psi} \in \Re^{2M \times 2}$ and $\boldsymbol{\Xi} \in \Re^{N \times 2}$.

6.1.3 Data Corroboration

In order to validate the measurement model, data was processed to illustrate the model [28]. The data at the beginning of the first lane was used to validate the measurement model. A matrix of data from the beginning of the lane was used because it will not have a target response and should only contain the other three terms: the self response, soil response, and random noise. The models for the self response and soil response predict that the data matrix should have a rank of three or less because the self response is rank one and the soil response is rank two. Because of the low-rank nature of these interference responses, a singular value decomposition (SVD) can be used to determine whether the data is accurately modeled with rank three or less. The remaining noise term is expected to make the data matrix full rank where the rest of the singular values are roughly equal. These results are shown in Fig. 6.1 along with the singular values of the data after the interference has been

removed with projection operators.

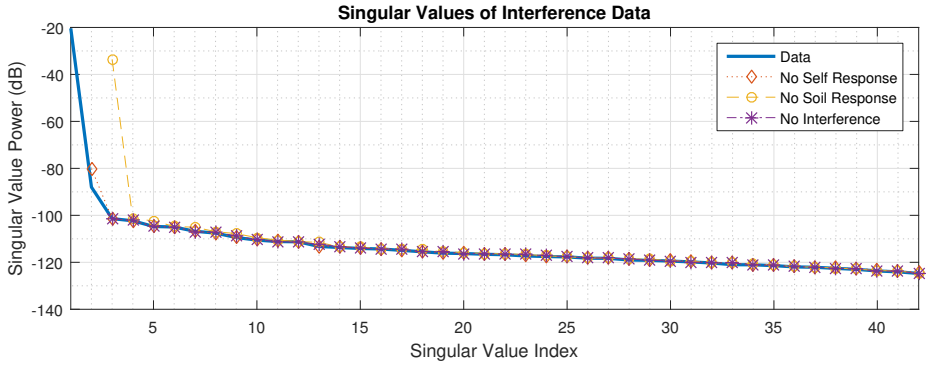

Figure 6.1: The singular values of a measured data matrix that does not contain any targets. The accuracy of the measurement model is shown by the singular values that remain after the soil and self response are removed.

The singular values of the data show that there is a single strong response in the raw data followed by another weaker response around -87 dB. The remaining singular values appear to be due to the noise floor. The self response is mostly mitigated when a constant term in the spatial domain is removed, which clearly lowers the first singular value. The second singular value increases slightly from this operation because the soil response that does not overlap with the constant spatial term is forced into this singular value. The soil response is mostly mitigated by projecting the data away from the soil model, so the singular values are also shown when only the soil response is removed. Although the soil response accounts for some of the interference, it is obvious that there is still a strong interferer remaining which corresponds to the self response according to the model. Finally, both the self and soil responses are removed, and the singular values align exactly with the original data's noise floor where the strongest singular values from the interference have been removed. This suggests that the measurement model fits the measured data accurately. It is interesting to note that the two interference terms overlap significantly and only appear to have a total rank of two.

6.2 Projections

6.2.1 Portioning Out the Measurement Matrix

In order to best exploit EMI data, it is desirable to isolate the target response. Improved target isolation should translate into greater achievable processing gains. Previous work [26] has proposed using a filterless preprocessing scheme to isolate the target signal. This strategy uses two orthonormal projection matrices: $\mathbf{P_R}$ and $\mathbf{P_G}$. $\mathbf{P_R}$ is a projection matrix applied to the position dimension and is responsible for isolating the self response into a low-dimensional subspace, leaving a useful subspace where the target signal is isolated from the self response. Ideally, $\mathbf{P_R}$ will have three portions and is described as

$$\mathbf{P_R} = \begin{bmatrix} \mathbf{P_{RR}} \\ \mathbf{P_{\bar{R}S}} \\ \mathbf{P_{\bar{R}\mathcal{E}}} \end{bmatrix} \tag{6.8}$$

where $\mathbf{P_{RR}}$ is a lower-dimensional mapping that isolates the self response, $\mathbf{P_{\bar{R}S}}$ is a lower-dimensional mapping that extracts the target response that is orthogonal to the self response, and $\mathbf{P_{\bar{R}\mathcal{E}}}$ maps the remaining space that does not contain the self response or the target response. These three mappings must be orthogonal to each other and create the square projection matrix $\mathbf{P_R}$. For the ground response $\mathbf{P_G}$ performs the same function as $\mathbf{P_R}$ except on the measurement dimension, which means it creates a low-dimensional soil subspace as well as a subspace with the target isolated from the soil in the measurement dimension. Ideally, $\mathbf{P_G}$ also has three portions and is described as

$$\mathbf{P_G} = \begin{bmatrix} \mathbf{P_{\bar{G}S}} \\ \mathbf{P_{\bar{G}\mathcal{E}}} \\ \mathbf{P_{GG}} \end{bmatrix} \tag{6.9}$$

where $\mathbf{P}_{\bar{\mathbf{G}}\mathbf{S}}$ is a lower-dimensional mapping that isolates the soil response, $\mathbf{P}_{\bar{\mathbf{G}}\mathcal{E}}$ is a lower dimensional mapping that extracts the target response that is orthogonal to the soil response, and $\mathbf{P}_{\mathbf{GG}}$ maps the remaining space that does not contain the soil response or the target response. These three mappings must be orthogonal to each other and create the square projection matrix $\mathbf{P}_{\mathbf{G}}$. These projection matrices are applied to the measurements $\mathbf{M}$ to obtain the decomposition

$$\begin{aligned}\mathbf{P}_{\mathbf{G}}\mathbf{M}\mathbf{P}_{\bar{\mathbf{R}}}^{T} &= \mathbf{P}_{\mathbf{G}}\begin{bmatrix}\mathbf{M}\mathbf{P}_{\mathbf{R}\mathbf{R}}^{T} & \mathbf{M}\mathbf{P}_{\bar{\mathbf{R}}\mathbf{S}}^{T} & \mathbf{M}\mathbf{P}_{\bar{\mathbf{R}}\mathcal{E}}^{T}\end{bmatrix} \\ &= \begin{bmatrix}\mathbf{P}_{\bar{\mathbf{G}}\mathbf{S}}\mathbf{M}\mathbf{P}_{\mathbf{R}\mathbf{R}}^{T} & \mathbf{P}_{\bar{\mathbf{G}}\mathbf{S}}\mathbf{M}\mathbf{P}_{\bar{\mathbf{R}}\mathbf{S}}^{T} & \mathbf{P}_{\bar{\mathbf{G}}\mathbf{S}}\mathbf{M}\mathbf{P}_{\bar{\mathbf{R}}\mathcal{E}}^{T} \\ \mathbf{P}_{\bar{\mathbf{G}}\mathcal{E}}\mathbf{M}\mathbf{P}_{\mathbf{R}\mathbf{R}}^{T} & \mathbf{P}_{\bar{\mathbf{G}}\mathcal{E}}\mathbf{M}\mathbf{P}_{\bar{\mathbf{R}}\mathbf{S}}^{T} & \mathbf{P}_{\bar{\mathbf{G}}\mathcal{E}}\mathbf{M}\mathbf{P}_{\bar{\mathbf{R}}\mathcal{E}}^{T} \\ \mathbf{P}_{\mathbf{G}\mathbf{G}}\mathbf{M}\mathbf{P}_{\mathbf{R}\mathbf{R}}^{T} & \mathbf{P}_{\mathbf{G}\mathbf{G}}\mathbf{M}\mathbf{P}_{\bar{\mathbf{R}}\mathbf{S}}^{T} & \mathbf{P}_{\mathbf{G}\mathbf{G}}\mathbf{M}\mathbf{P}_{\bar{\mathbf{R}}\mathcal{E}}^{T}\end{bmatrix}\end{aligned} \tag{6.10}$$

that creates nine subblocks from the original data matrix. The matrix subblocks are shown in Figure 6.2 where variables have been given to each subblock that represents the data held within it. Previously, $\mathbf{M}_{\bar{\mathbf{G}}\mathbf{S}}^{\bar{\mathbf{R}}\mathbf{S}}$ was the only block used because the target signal has high SNR and is isolated from both the soil and self response [26]. This work will investigate each measurement block to develop a further understanding of how the data can best be exploited. In order to investigate the nine data blocks, it is necessary to first elaborate on the projection matrices used.

6.2.2 Creating $\mathbf{P}_{\mathbf{G}}$

The first projection matrix that will be investigated is $\mathbf{P}_{\mathbf{G}}$. The creation of the projection matrix $\mathbf{P}_{\mathbf{G}}$ is based on earlier work for computing the Discrete Spectrum of Relaxation Frequencies (DSRF)[29]. Previous work took advantage of the terms in $\mathbf{M}$ that are known to be dependent on the operating frequencies. Two terms, the soil and the target response, have known frequency dependencies. As described in (6.6), the soil has a two-dimensional model in the operating frequency domain. The target signal also has an operating frequency dependence that varies between targets, but the DSRF model[30] allows it to be represented

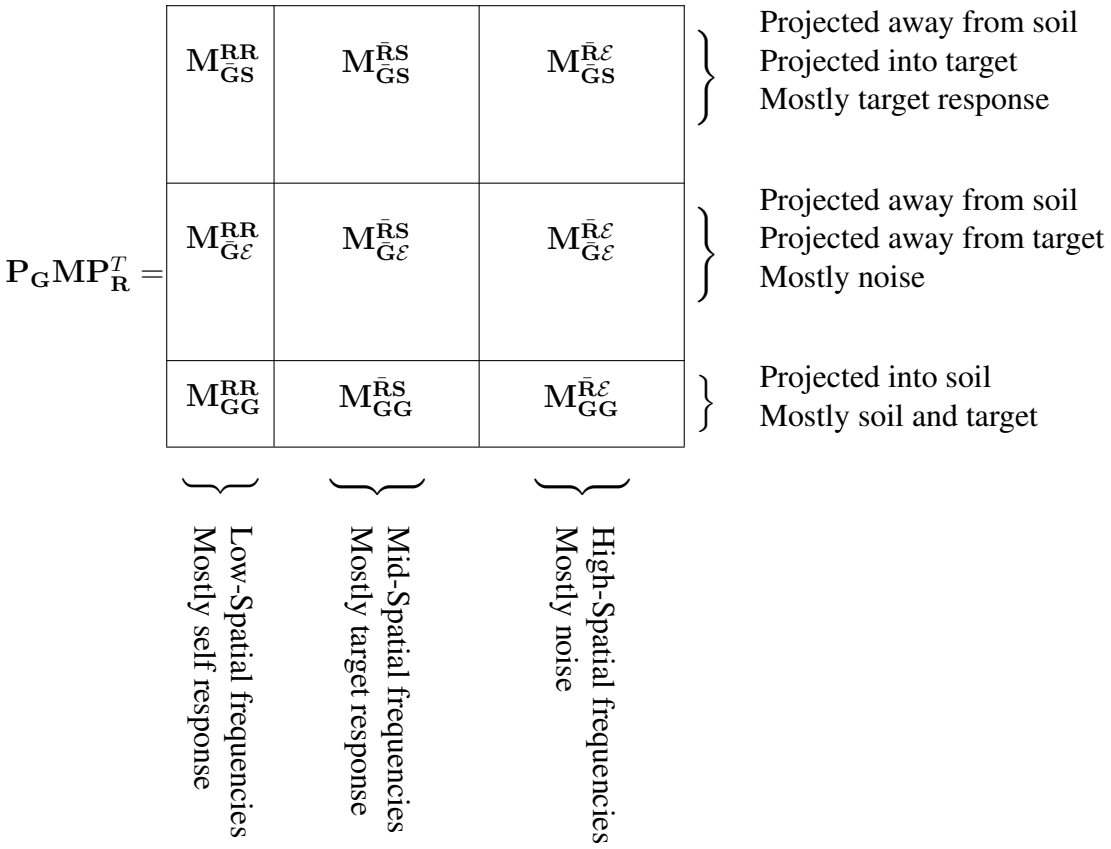

(6.11)

Figure 6.2: Orthogonal projections for soil and self response applied to raw measurements $\mathbf{M}$.

by a sparse selection of the DSRF dictionary $\mathbf{A}$. The DSRF dictionary $\mathbf{A}$ contains templates for multiple possible relaxation frequencies $\boldsymbol{\zeta}$ that a target may have. Each element of $\mathbf{A}$ is defined as

$$\tilde{a}(\omega, \zeta) = \frac{j\omega/\zeta}{1 + j\omega/\zeta} \tag{6.12}$$

which serves as a mapping from a target's relaxation frequency to a EMI system's measurement frequency. The dictionary $\mathbf{A}$ is created by selecting a set of possible discrete relaxation frequencies, $\boldsymbol{\zeta}$, and mapping them to the EMI measurement frequencies, $\boldsymbol{\omega}$. This creates a complex-valued matrix that is separated as in (6.3) to create a real-valued matrix. Often $\boldsymbol{\zeta}$ is chosen as 100 equally logarithmically-spaced frequencies from just below the

minimum operating frequency to just above the maximum operating frequency. Previously it was shown that by combining the dictionary $\mathbf{A}$ with the knowledge of the soil model, a set of projected operating frequency measurements could be created that were isolated from the soil[29]. This is accomplished through a two-step process. First, a projection matrix into the soil subspace is created in the standard manner as $\mathbf{P_{GG}} = \mathbf{\Psi}(\mathbf{\Psi}^T\mathbf{\Psi})^{-1}\mathbf{\Psi}^T$. This allows $\mathbf{A}$ to be defined as

$$\mathbf{A} = \mathbf{P_{GG}}\mathbf{A} + \mathbf{P}^{\perp}_{\mathbf{GG}}\mathbf{A} \tag{6.13}$$

where $\mathbf{P}^{\perp}_{\mathbf{GG}} = \mathbf{I} - \mathbf{P_{GG}}$ is the projection into the space orthogonal of the soil projection matrix. The second stage is to apply a singular value decomposition (SVD) to both terms in (6.13) which arrives at

$$\mathbf{A} = \mathbf{U}^{\mathbf{A}}_{\mathbf{G}}\mathbf{\Sigma}^{\mathbf{A}}_{\mathbf{G}}{\mathbf{V}^{\mathbf{A}}_{\mathbf{G}}}^T + \mathbf{U}^{\mathbf{A}}_{\bar{\mathbf{G}}}\mathbf{\Sigma}^{\mathbf{A}}_{\bar{\mathbf{G}}}{\mathbf{V}^{\mathbf{A}}_{\bar{\mathbf{G}}}}^T. \tag{6.14}$$

The singular values of the dictionary perpendicular to the soil, $\mathbf{P}^{\perp}_{\mathbf{GG}}\mathbf{A}$, can be used to estimate how much weaker the target signal will be in each of the projected frequency terms. A maximum target SNR requirement can be selected for the system which allows a singular value threshold, $\lambda_{\mathbf{G}\mathcal{E}}$, to be selected. If the terms in $\mathbf{\Sigma}^{\mathbf{A}}_{\bar{\mathbf{G}}}$ are normalized by the strongest singular value, then any term below $\lambda_{\mathbf{G}\mathcal{E}}$ can be ignored when reconstructing the data. The reconstructed signal will have a new "noise term" that will be roughly $\lambda_{\mathbf{G}\mathcal{E}}$ smaller than the target response. Using this threshold to separate the singular value terms of $\mathbf{P}^{\perp}_{\mathbf{GG}}\mathbf{A}$, the DSRF dictionary can be represented as

$$\mathbf{A} = \begin{bmatrix} \mathbf{U}^{\mathbf{A}}_{\bar{\mathbf{G}}\mathbf{S}} & \mathbf{U}^{\mathbf{A}}_{\bar{\mathbf{G}}\mathcal{E}} & \mathbf{U}^{\mathbf{A}}_{\mathbf{G}} \end{bmatrix} \begin{bmatrix} \mathbf{\Sigma}^{\mathbf{A}}_{\bar{\mathbf{G}}\mathbf{S}} & 0 & 0 \\ 0 & \mathbf{\Sigma}^{\mathbf{A}}_{\bar{\mathbf{G}}\mathcal{E}} & 0 \\ 0 & 0 & \mathbf{\Sigma}^{\mathbf{A}}_{\mathbf{G}} \end{bmatrix} \begin{bmatrix} {\mathbf{V}^{\mathbf{A}}_{\bar{\mathbf{G}}\mathbf{S}}}^T \\ {\mathbf{V}^{\mathbf{A}}_{\bar{\mathbf{G}}\mathcal{E}}}^T \\ {\mathbf{V}^{\mathbf{A}}_{\mathbf{G}}}^T \end{bmatrix} \tag{6.15}$$

where $\mathbf{U}_{\bar{\mathbf{G}}}^{\mathbf{A}}\mathbf{\Sigma}_{\bar{\mathbf{G}}}^{\mathbf{A}}\mathbf{V}_{\bar{\mathbf{G}}}^{\mathbf{A}}{}^{T} = \mathbf{U}_{\bar{\mathbf{G}}\mathbf{S}}^{\mathbf{A}}\mathbf{\Sigma}_{\bar{\mathbf{G}}\mathbf{S}}^{\mathbf{A}}\mathbf{V}_{\bar{\mathbf{G}}\mathbf{S}}^{\mathbf{A}}{}^{T} + \mathbf{U}_{\bar{\mathbf{G}}\mathcal{E}}^{\mathbf{A}}\mathbf{\Sigma}_{\bar{\mathbf{G}}\mathcal{E}}^{\mathbf{A}}\mathbf{V}_{\bar{\mathbf{G}}\mathcal{E}}^{\mathbf{A}}{}^{T}$ has been decomposed into a target response and a noise response and the addition of all three terms has been rewritten as a combination of three low-rank matrices. This decomposition looks like a SVD, but it is worth noting that this is not a direct SVD of $\mathbf{A}$ because $\mathbf{V}_{\mathbf{G}}^{\mathbf{A}}{}^{T}\mathbf{V}_{\bar{\mathbf{G}}\mathbf{S}}^{\mathbf{A}} \neq 0$ and $\mathbf{V}_{\mathbf{G}}^{\mathbf{A}}{}^{T}\mathbf{V}_{\bar{\mathbf{G}}\mathcal{E}}^{\mathbf{A}} \neq 0$.

The decomposition of $\mathbf{A}$ in (6.15) is useful because the desired orthonormal matrix $\mathbf{P}_{\mathbf{G}}$ can now be defined as

$$\mathbf{P}_{\mathbf{G}} = \begin{bmatrix} \mathbf{P}_{\bar{\mathbf{G}}\mathbf{S}} \\ \mathbf{P}_{\bar{\mathbf{G}}\mathcal{E}} \\ \mathbf{P}_{\mathbf{G}\mathbf{G}} \end{bmatrix} = \begin{bmatrix} \mathbf{U}_{\bar{\mathbf{G}}\mathbf{S}}^{\mathbf{A}} & \mathbf{U}_{\bar{\mathbf{G}}\mathcal{E}}^{\mathbf{A}} & \mathbf{U}_{\mathbf{G}}^{\mathbf{A}} \end{bmatrix}^{T}. \tag{6.16}$$

For notational clarification, even though $\mathbf{P}_{\mathbf{G}\mathbf{G}} = \mathbf{U}_{\mathbf{G}}^{\mathbf{A}}$ is not guaranteed, they are guaranteed to span the same subspace and be orthonormal, so from a projection operator stance they are equivalent.

The frequency projection matrix, $\mathbf{P}_{\mathbf{G}}$, can be calculated off-line prior to the measurements as long as the soil subspace is known. The only necessary tuning parameter is choosing $\lambda_{\mathbf{G}\mathcal{E}}$. Fig 6.3 shows the singular values from realistic DSRF dictionaries for determining $\lambda_{\mathbf{G}\mathcal{E}}$. These plots assume that a EMI system was designed to span the frequency range from 330 Hz to 90 kHz. The system measures 7, 14, 21, or 28 equally log-spaced frequencies in this range respectively. The DSRF dictionary is then created by using 100 equally log-spaced relaxation frequencies from 44 Hz to 667 kHz (roughly 0.87 decades beyond the measured frequencies). These design parameters are used for (9.1)-(6.15), and the singular values are shown in Fig. 6.3. It is also of interest to know how much of the target response is expected to be lost to the soil subspace. In order to illustrate the target loss, the singular values of the original dictionary before projecting away from the soil subspace are also shown in Fig. 6.3.

It is interesting to note that the number of measurement frequencies has little impact

on the shape of the singular values. However, more measurement frequencies make a larger range of singular values. This enables a lower threshold $\lambda_{\mathbf{G}\mathcal{E}}$ to be chosen while still leaving a reasonable size noise subspace for future operations. This work uses data from a Georgia Tech frequency-domain EMI system that uses the same operating characteristics with 21 measurement frequencies. This work selected 100 dB as the cutoff threshold $\lambda_{\mathbf{G}\mathcal{E}}$, which translates into having 21 projected frequency measurements in the signal subspace, 19 measurements in the noise subspace, and 2 measurements in the soil subspace. This threshold was also chosen because it is expected that further EMI processing should be able to exploit targets in 100 dB SNR or lower, so the information lost due to this threshold should be insignificant.

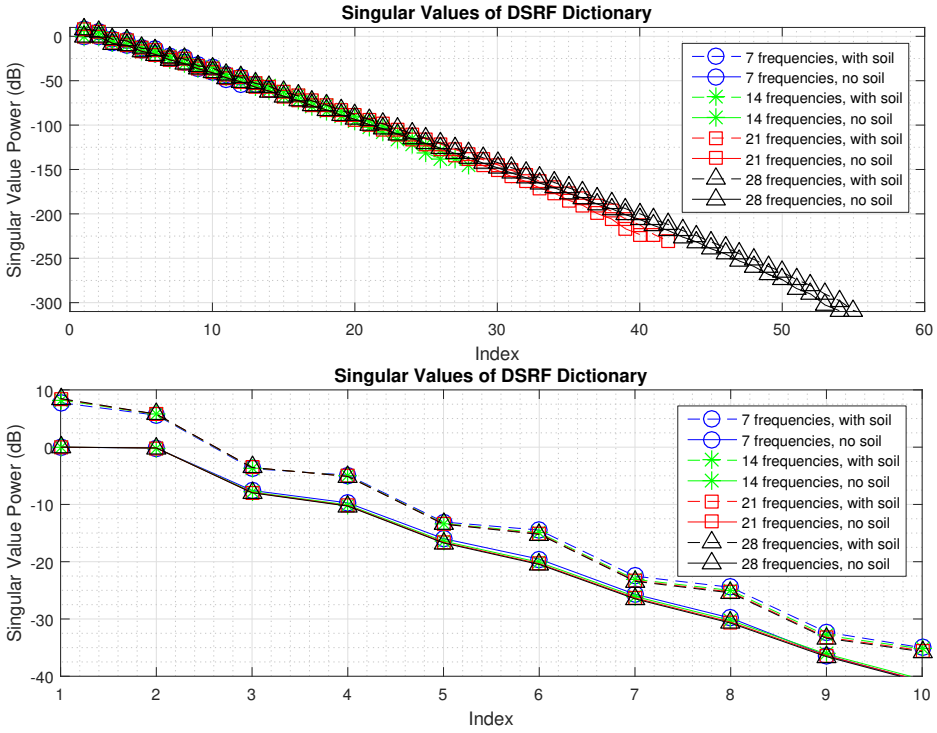

Figure 6.3: The singular values from the DSRF dictionary before (top) and after (bottom) the dictionary has been projected away from the soil subspace.

As can be seen in Fig. 6.3, the largest singular value of $\mathbf{P}^{\perp}_{\mathbf{GG}}\mathbf{A}$ is 8.5 dB smaller than the largest singular value of the original dictionary $\mathbf{A}$. This means that the largest response of a target in measured data will decrease by roughly 8.5 dB when projecting the target

away from the soil response. This significant drop motivates a later discussion on how this data can be potentially recovered. It should be noted however that this is only the energy drop from the strongest component. Figure 6.4 shows the ratio of the total power in the DSRF dictionary after it has been isolated from the soil to the total power of the original dictionary. Mathematically this was calculated as $\delta_g = \|\mathbf{P}^{\perp}_{\mathbf{GG}}\mathbf{A}\|_F^2 / \|\mathbf{A}\|_F^2$.

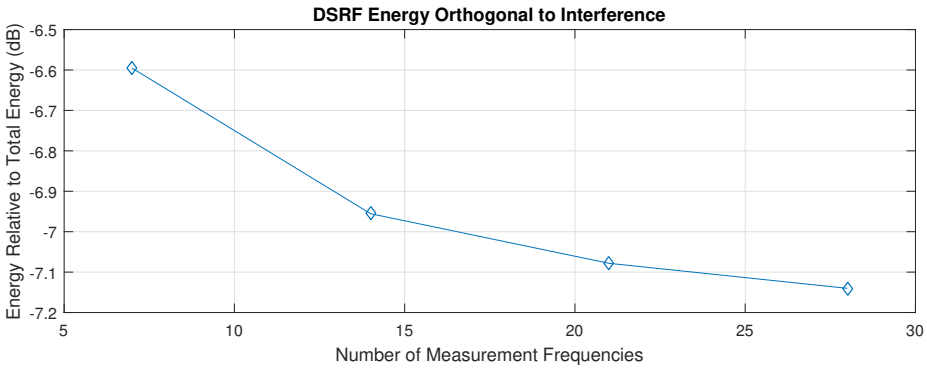

Figure 6.4: The ratio of the DSRF dictionary after being isolated from the soil compared to the total power.

6.2.3 Creating $\mathbf{P_R}$

The spatial domain projection matrix, $\mathbf{P_R}$, must also be created. The current $\mathbf{P_R}$ matrix is inspired by previous frequency-domain EMI filters. An elegant and highly effective non-adaptive filter for frequency-domain EMI sensors with a quadrupole receiver is the sine filter. The sine filter is a rough approximation of the target response as it passes under the receiver. Fig. 6.5 shows how the sine filter is designed to mimic the spatial dimension of a target response as it passes under the positive and then negatively polarized receiver. The traditional sine filter is usually tuned to the spatial wavelength of the system.

The most direct extension of the sine filter into a projection matrix is to use a Discrete Fourier Transform (DFT). This is intuitively the same as using a filter bank of multiple sine filters. The DFT is effective, but previous work has migrated to using the Discrete Cosine Transform (DCT) matrix[27, 26] for two reasons. The first reason is that the DCT is more robust when the target is on the edge of the spatial window. The second reason is

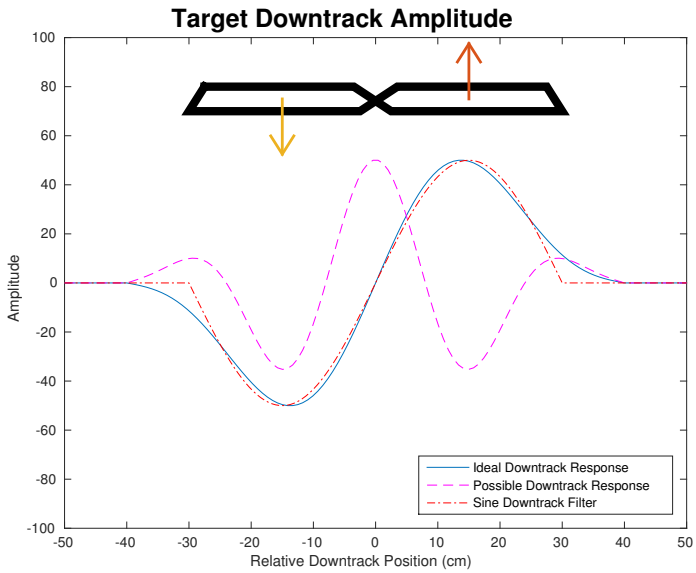

Figure 6.5: An illustration of how the sine filter is an approximate matched filter to a target response when using a quadrupole receiver.

that the DFT would convert the real-valued matrix back into complex-values, but the DCT projects the measured data into a new real-valued matrix. Keeping the data as real-valued is beneficial when it comes to quickly and easily operating on the data in future stages, such as the DSRF recovery problem.

In order to show the difference between the DCT and DFT as a projection matrix, Fig. 6.6 illustrates both projections being used on a simulated target. Fig. 6.6a is a target of rank two that is centered directly under the sensor. The measurements are projected into the DFT (Fig. 6.6c) and DCT (Fig. 6.6d) domains respectively. The target's spatial response is then reconstructed by only using the terms orthogonal to the DC term and with a spatial wavelength larger than 5 cm. The reconstructed spatial response is plotted again in Fig. 6.6a to show that it is an accurate representation of the data. The same process was performed on the same simulated target when it was shifted to the edge of the measurement matrix. Fig. 6.6b shows that the reconstructed DFT data no longer accurately represents the signal because the DFT forces the samples on the edges to converge so the signal is continuous when circularly shifted in the window. The DCT projection is designed so that it does not enforce this edge artifact and thus can reconstruct the measured data. A few

observations can be taken from Fig. 6.6d and 6.6c. First, the target's spatial response is mostly contained in terms with a wavelength longer than 5 cm. Second, the DCT contains less target response in the shorter wavelengths than the DFT. Finally, both the DCT and DFT greatly increase the target's power in the short wavelengths when the target is on the edge of the measurement matrix.

Both the DFT and DCT satisfy the constraints needed for $\mathbf{P_R}$. Both projections have a subspace that holds the constant (DC) component, and all other elements are orthogonal to the constant component (zero-mean). The longer wavelengths (lower spatial frequencies) can also be used to isolate the drift component of the self response if desired. It is also useful to point out that the target response should lie within a subset of the possible wavelengths (spatial frequencies) due to the physical design of the quadrupole receiver. Because of this, any extremely short wavelength patterns (high spatial frequencies) can be assumed to not have any target response and thus only contain the noise term. This allows the self-response projection matrix to be defined as

$$\mathbf{P_R} = \begin{bmatrix} \mathbf{P_{RR}} \\ \mathbf{P_{\bar{R}S}} \\ \mathbf{P_{\bar{R}\mathcal{E}}} \end{bmatrix} = \begin{bmatrix} \boldsymbol{\mathcal{D}}_L \\ \boldsymbol{\mathcal{D}}_M \\ \boldsymbol{\mathcal{D}}_S \end{bmatrix} = \boldsymbol{\mathcal{D}} \tag{6.17}$$

where $\boldsymbol{\mathcal{D}}_L$ contains the long spatial wavelengths that contain the self response, $\boldsymbol{\mathcal{D}}_M$ contain the expected spatial wavelengths for targets, and $\boldsymbol{\mathcal{D}}_S$ are the short spatial wavelengths that are expected to be noise. The wavelengths (spatial frequencies) to separate these subspaces are selected based on the receiver design.

6.3 Measurement Matrix Blocks

With the detailed description of the preprocessing stages for the frequency-domain EMI framework provided in Section 6.2.1, it is possible to investigate each of the sub-matrix

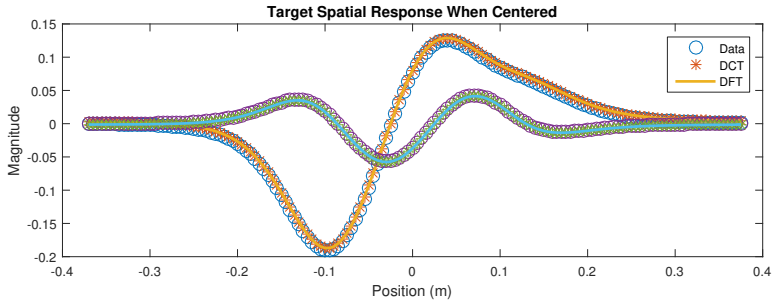

(a)

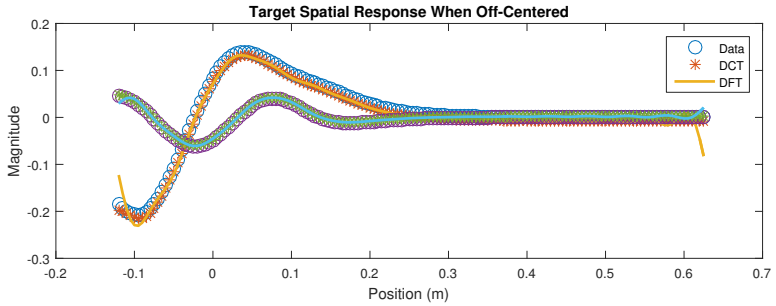

(b)

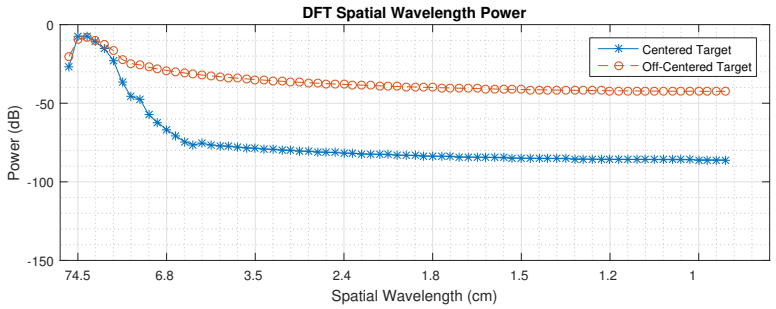

(c)

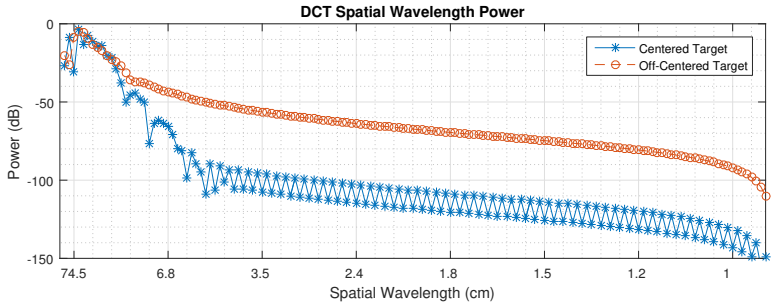

(d)

Figure 6.6: These plots show how well the DFT and DCT matrices can be used to isolate the spatial dimension of a target response. A target's spatial response was simulated and then reconstructed from a small subspace of the DFT and DCT matrices in (a) and (b). The power from the simulated target in the projected DFT and DCT domain are shown in (c) and (d) respectively.

data blocks shown in Fig. 6.2. Each data block is inspected below to create a mathematical formulation for what data is expected to be present. The mathematical model is paired with results from data obtained using the Georgia Tech frequency-domain EMI system[28]. The data has been processed by creating data matrices that span roughly 75 cm. This creates a data matrix that is roughly the size $\mathbf{M} \in \Re^{42\times 175}$, where the number of spatial samples can vary slightly for each lane. The data matrix is preprocessed using $\lambda_{\mathbf{G}\mathcal{E}} = 100$dB and a minimum spatial wavelength of 5 cm. Each data block is shown for all 26 lanes collected with the sensor. The locations of metallic targets have been labeled with a filled circle and non-metallic targets are labeled with an empty diamond. In a few areas of the collected data, the target response was strong enough to significantly increase the sensor voltage. These strong targets potentially violate the assumptions of the model because they can overwhelm the sensor and cause model inaccuracies. Because these strong targets potentially violate the model, they have been circled in red as a warning that the results are potentially misleading. A discussion of how each data block can be used to improve processing is also included with the results.

6.3.1 Investigating $\mathbf{M}_{\bar{\mathbf{G}}\mathbf{S}}^{\mathbf{R}\mathbf{R}}$

The data block $\mathbf{M}_{\bar{\mathbf{G}}\mathbf{S}}^{\mathbf{R}\mathbf{R}}$ is designed to contain the overlap of the self response and the target response that is orthogonal from the ground. This is expressed mathematically as

$$\mathbf{P}_{\bar{\mathbf{G}}\mathbf{S}}\mathbf{M}\mathbf{P}_{\mathbf{R}\mathbf{R}}^{T} = \cancelto{\epsilon}{\mathbf{P}_{\bar{\mathbf{G}}\mathbf{S}}\mathbf{S}\mathbf{P}_{\mathbf{R}\mathbf{R}}^{T}} + \cancelto{0}{\mathbf{P}_{\bar{\mathbf{G}}\mathbf{S}}\mathbf{G}\mathbf{P}_{\mathbf{R}\mathbf{R}}^{T}} + \mathbf{P}_{\bar{\mathbf{G}}\mathbf{S}}\mathbf{R}\mathbf{P}_{\mathbf{R}\mathbf{R}}^{T} + \mathbf{P}_{\bar{\mathbf{G}}\mathbf{S}}\mathcal{E}\mathbf{P}_{\mathbf{R}\mathbf{R}}^{T} \tag{6.18}$$

where it is noted that both the target response and soil response are expected to be negligible in this data block. The soil response should be completely removed because $\mathbf{P}_{\bar{\mathbf{G}}\mathbf{S}}$ was designed such that $\mathbf{P}_{\bar{\mathbf{G}}\mathbf{S}}\mathbf{G} \rightarrow \mathbf{0}$. The target response is expected to be some small value, ϵ, because of the design of the EMI system. By using a quadrupole receiver, the target should change signs while passing below the receiver and have a zero-mean effect on the received

measurements. Ideally, this indicates that $\mathbf{SP}_{\mathbf{RR}}^{T} \rightarrow \epsilon$; however, the target response will leak into $\mathbf{M}_{\bar{\mathbf{GS}}}^{\mathbf{RR}}$ when a) the sensor is tilted which skews the response making it no longer zero mean, b) the target is on the edge of the data matrix, $\mathbf{M}$, so it only contains part of the target response which is not zero mean, and c) the target has a tensor component that does not create a zero mean response. Other EMI sensors may not have a zero-mean response in normal operation and will always leak into $\mathbf{M}_{\bar{\mathbf{GS}}}^{\mathbf{RR}}$.

Because the self response is expected to be the dominating term, this block is a useful metric in estimating how strong the coupling is between the transmitter and receiver. This can be used as a metric to test the design of the platform or for any other purpose where the self response is needed. When creating this block from the measured data, it was $\mathbf{M}_{\bar{\mathbf{GS}}}^{\mathbf{RR}} \in \Re^{21\times 1}$. Fig. 6.7 shows this data block's average power per sample across all of the measured lanes. As can be seen, the metric remains constant around an average power of -50dB across nearly all of the measurements. Only a few stronger targets distort this metric, mainly when they are on the edge of the data matrix which causes an increase in target leakage from $\mathbf{P}_{\mathbf{G}}$.

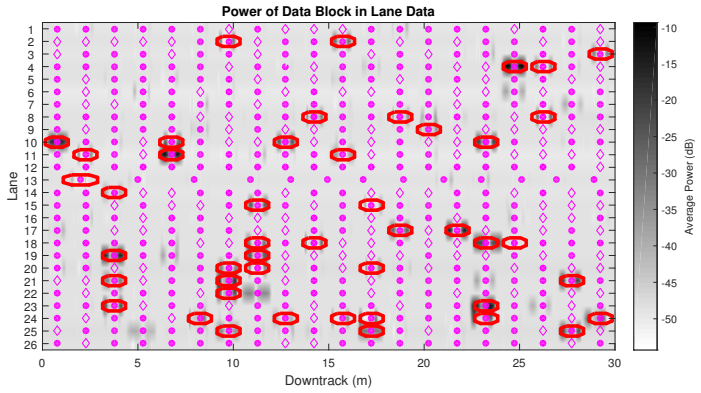

Figure 6.7: Average power of the $\mathbf{M}_{\bar{\mathbf{GS}}}^{\mathbf{RR}}$ data block from measured EMI data. This data block has low spatial frequencies and is orthogonal from the soil subspace while aligning with the target's DSRF. This data is expected to be dominated by the self response. Filled circles are metallic targets, empty diamonds are locations absent of metallic targets, and red circles are strong targets that potentially overwhelmed the sensor.

6.3.2 Investigating $\mathbf{M}_{\bar{\mathbf{G}}\mathbf{S}}^{\bar{\mathbf{R}}\mathbf{S}}$

The data block $\mathbf{M}_{\bar{\mathbf{G}}\mathbf{S}}^{\bar{\mathbf{R}}\mathbf{S}}$ is designed to contain the target response when it is orthogonal to both the ground and self response. This is expressed mathematically as

$$\mathbf{P}_{\bar{\mathbf{G}}\mathbf{S}}\mathbf{M}\mathbf{P}_{\bar{\mathbf{R}}\mathbf{S}}^{T} = \mathbf{P}_{\bar{\mathbf{G}}\mathbf{S}}\mathbf{S}\mathbf{P}_{\bar{\mathbf{R}}\mathbf{S}}^{T} + \cancelto{0}{\mathbf{P}_{\bar{\mathbf{G}}\mathbf{S}}\mathbf{G}\mathbf{P}_{\bar{\mathbf{R}}\mathbf{S}}^{T}} + \cancelto{0}{\mathbf{P}_{\bar{\mathbf{G}}\mathbf{S}}\mathbf{R}\mathbf{P}_{\bar{\mathbf{R}}\mathbf{S}}^{T}} + \mathbf{P}_{\bar{\mathbf{G}}\mathbf{S}}\mathcal{E}\mathbf{P}_{\bar{\mathbf{R}}\mathbf{S}}^{T} \tag{6.19}$$

where it is noted that both the self response and soil response are expected to be negligible in this data block. The soil response should be completely removed again because of the design of $\mathbf{P}_{\bar{\mathbf{G}}\mathbf{S}}$. The self response should also be completely removed because the design of $\mathbf{P}_{\bar{\mathbf{R}}\mathbf{S}}$ causes $\mathbf{R}\mathbf{P}_{\bar{\mathbf{R}}\mathbf{S}}^{T} \rightarrow 0$. This leaves only the target information and noise in $\mathbf{M}_{\bar{\mathbf{G}}\mathbf{S}}^{\bar{\mathbf{R}}\mathbf{S}}$. It is useful to define this projected data block as $\mathbf{M}_{\mathbf{S}} = \mathbf{P}_{\bar{\mathbf{G}}\mathbf{S}}\mathbf{M}\mathbf{P}_{\bar{\mathbf{R}}\mathbf{S}}^{T}$, the target response in this data block as $\mathbf{S}_{\mathbf{S}} = \mathbf{P}_{\bar{\mathbf{G}}\mathbf{S}}\mathbf{S}\mathbf{P}_{\mathbf{R}\mathbf{R}}^{T}$, and the noise matrix in $\mathbf{M}_{\bar{\mathbf{G}}\mathbf{S}}^{\bar{\mathbf{R}}\mathbf{S}}$ as $\mathcal{E}_{\mathbf{S}} = \mathbf{P}_{\bar{\mathbf{G}}\mathbf{S}}\mathcal{E}\mathbf{P}_{\bar{\mathbf{R}}\mathbf{S}}^{T}$ because they are of primary interest for future processing.

The average power of $\mathbf{M}_{\mathbf{S}}$ is shown in Fig. 6.8, were it had a size of roughly $\mathbf{M}_{\mathbf{S}} \in \Re^{21\times 29}$. The targets in the measured data correspond to an increase in average power as the model predicts. Also, it can be noted that the noise floor of the EMI sensor has been reduced to an average power of -130dB.

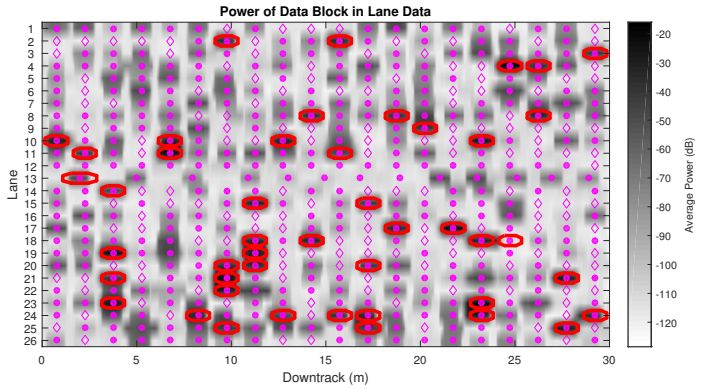

Figure 6.8: Average power of the $\mathbf{M}_{\bar{\mathbf{G}}\mathbf{S}}^{\bar{\mathbf{R}}\mathbf{S}}$ data block from measured EMI data. This data block has the middle spatial frequencies and is orthogonal from the soil subspace while aligning with the target's DSRF. This data is expected to be dominated by the target response. Filled circles are metallic targets, empty diamonds are locations absent of metallic targets, and red circles are strong targets that potentially overwhelmed the sensor.

It is insightful to elaborate on the effect of the projection matrices on $\mathcal{E}$ at this point to describe the resulting signal-to-noise ratio (SNR) of the data block $\mathbf{M_S}$. Let $\mathbf{p}$ be any vector in a projection matrix. For this example, assume $\mathbf{p} \in \Re^{2M \times 1}$ is a row-vector from $\mathbf{P_G}$ that has been rotated into a column-vector. Given a vector of random i.i.d. Gaussian noise samples, $\boldsymbol{\epsilon} \in \Re^{2M \times 1}$, where each sample is drawn from the distribution $\mathcal{N}(0, \sigma_\epsilon^2)$, it can be easily shown that $\mathbf{p}^T \boldsymbol{\epsilon} \sim \mathcal{N}(0, \sigma_\epsilon^2)$ as long as $\|\mathbf{p}\|_2 = 1$. It can also be easily shown that as long as two projection vectors, $\mathbf{p}_i$ and $\mathbf{p}_j$, are orthogonal ($\mathbf{p}_i^T \mathbf{p}_j = 0$), then the new sample created from each projection vector will be independent ($\mathbf{p}_i^T \boldsymbol{\epsilon}$ and $\mathbf{p}_j^T \boldsymbol{\epsilon}$ are independent). Both of these constraints are true about all of the vectors within a projection matrix. This means that multiplying a noise vector by a projection matrix, $\mathbf{P}_{\bar{\mathbf{G}}\mathbf{S}} \boldsymbol{\epsilon}$, produces a new noise vector where each element is again i.i.d. $\mathcal{N}(0, \sigma_\epsilon^2)$. When the projection operator is applied to a matrix of i.i.d. samples it will create a new matrix of i.i.d. samples, $\mathbf{P}_{\bar{\mathbf{G}}\mathbf{S}} \mathcal{E} \in \Re^{O \times N}$. This procedure is repeated for the projection matrix on the other side to create a new noise matrix $\mathcal{E}_\mathbf{S} \in \Re^{O \times P}$ where each element is i.i.d. $\mathcal{N}(0, \sigma_\epsilon^2)$.

In order to discuss SNR, it is necessary to define the power metric. The power of a matrix will be defined as the squared Frobenius norm (the sum of each element squared). The average power of a matrix will be defined as the power divided by the number of elements in the matrix. Under these definitions, it is straightforward to calculate the expected power of the two noise matrices as $E\left[\|\mathcal{E}\|_F^2\right] = 2MN\sigma_\epsilon^2$ and $E\left[\|\mathcal{E}_\mathbf{S}\|_F^2\right] = OP\sigma_\epsilon^2$. This shows that the projections have reduced the expected noise power by a factor of $\frac{OP}{2MN}$ in $\mathcal{E}_\mathbf{S}$. Unlike the expected noise power, the signal power should be roughly unchanged except for the signal power that was projected into the soil subspace. This means that the signal power should be $\|\mathbf{S_S}\|_F^2 \approx (1 - \delta_g)\|\mathbf{S}\|_F^2$. By combining these observations, it is possible to define the SNR change from only the signal and noise terms through the projection operators as

$$\boxed{E\left[\frac{\|\mathbf{S_S}\|_F^2}{\|\mathcal{E}_\mathbf{S}\|_F^2}\right] = (1 - \delta_g)\frac{2MN}{OP} E\left[\frac{\|\mathbf{S}\|_F^2}{\|\mathcal{E}\|_F^2}\right]} \tag{6.20}$$

where inserting the dimensions of the data produce $\frac{2MN}{OP} = \frac{42 \cdot 175}{21 \cdot 29} \approx 12$. This shows that the data block $\mathbf{M_S}$ can potentially have a SNR boost over the raw measurements $\mathbf{M}$ while also being isolated from interference signals.[1]

The data block $\mathbf{M_S}$ can be processed for further SNR improvement. Previous work has shown that the target response matrix $\mathbf{S}$ is low-rank, where it has a maximum rank of three for an ortho-point target and six for a general point target.[20] The target's low-rank nature will also be true in $\mathbf{S_S}$ as the projections cannot increase the rank of the matrix. The target's low-rank can be exploited by taking a singular value decomposition (SVD) of the data block[26]

$$\mathbf{M_S} = \mathbf{U}_{\mathbf{M_S}} \mathbf{\Sigma}_{\mathbf{M_S}} {\mathbf{V}_{\mathbf{M_S}}}^T. \tag{6.21}$$

The target response will be contained in three singular values or less.[2] Ideal i.i.d. Gaussian noise will spread out evenly through all of the singular values. As long as the singular values of the target are larger than the noise, then they will be contained in the largest predicted singular values of $\mathbf{\Sigma}_{\mathbf{M_S}}$. This allows $\mathbf{M_S}$ to be further separated into two subblocks

$$\begin{aligned} \mathbf{M_S} &= \begin{bmatrix} \mathbf{U}_{\mathbf{S}}^{\mathbf{M_S}} & \mathbf{U}_{\mathcal{E}}^{\mathbf{M_S}} \end{bmatrix} \begin{bmatrix} \mathbf{\Sigma}_{\mathbf{S}}^{\mathbf{M_S}} & 0 \\ 0 & \mathbf{\Sigma}_{\mathcal{E}}^{\mathbf{M_S}} \end{bmatrix} \begin{bmatrix} {\mathbf{V}_{\mathbf{S}}^{\mathbf{M_S}}}^T \\ {\mathbf{V}_{\mathcal{E}}^{\mathbf{M_S}}}^T \end{bmatrix} \\ &= \mathbf{U}_{\mathbf{S}}^{\mathbf{M_S}} \mathbf{\Sigma}_{\mathbf{S}}^{\mathbf{M_S}} {\mathbf{V}_{\mathbf{S}}^{\mathbf{M_S}}}^T + \mathbf{U}_{\mathcal{E}}^{\mathbf{M_S}} \mathbf{\Sigma}_{\mathcal{E}}^{\mathbf{M_S}} {\mathbf{V}_{\mathcal{E}}^{\mathbf{M_S}}}^T \end{aligned} \tag{6.22}$$

by isolating the contents of the three largest singular values from the rest of the singular values in $\mathbf{M_S}$.

The low-rank target signal isolation was performed on the EMI lane data. The only change was that the strongest six singular values were used for the targets to account for general targets that are not ortho-point targets. Figure 6.9 shows the average power of the

[1] It is also possible to perform these calculations on the average power, where it is seen that the expected average power for the noise remains unchanged at σ_ϵ^2, but the target average power increases by the amount in (6.20).

[2] This uses an ortho-point target assumption. Six singular values could be used for general targets if desired.

increased SNR signal within $\mathbf{\Sigma_S^{M_S}}$. Notice that the target response is minimally impacted by the operation. It should be noted that when a target is not present, the noise is only slightly decreased by the SVD because the strongest noise still remains. When a target is present, the above SNR discussion should hold true. Fig. 6.10 shows the average power of the noise removed from $\mathbf{M_S}$ in the singular values of $\mathbf{\Sigma_\mathcal{E}^{M_S}}$. Notice that the remaining noise power is minimally correlated to when a target is present. Also, it is relatively constant at a low noise floor of roughly -130dB.

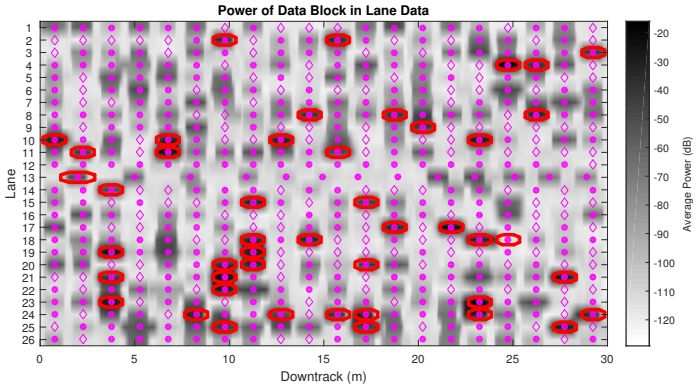

Figure 6.9: Average power of the $\mathbf{\Sigma_S^{M_S}}$ data block from measured EMI data. This data block contains the low-rank approximation of $\mathbf{M_{\bar{G}S}^{\bar{R}S}}$ and is expected to further isolate the target response. Filled circles are metallic targets, empty diamonds are locations absent of metallic targets, and red circles are strong targets that potentially overwhelmed the sensor.

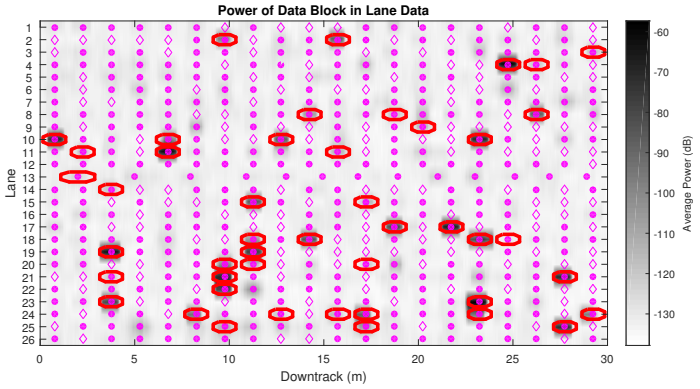

Figure 6.10: Average power of the $\mathbf{\Sigma_\mathcal{E}^{M_S}}$ data block from measured EMI data. This data block contains the remaining power of $\mathbf{M_{\bar{G}S}^{\bar{R}S}}$ after the low-rank approximation and is expected to contain only noise. Filled circles are metallic targets, empty diamonds are locations absent of metallic targets, and red circles are strong targets that potentially overwhelmed the sensor.

This process of further isolating the signal within $\mathbf{M_S}$ will further increase the SNR as long as the signal was originally strong enough for the SVD operation to isolate it into the largest singular vectors. The SNR increase can be calculated by exploiting the relationship between the Frobenius norm and singular values. By definition, the squared Frobenius norm is equivalent to the sum of the squared singular values of the matrix. This means that the expected power of the noise under an i.i.d. Gaussian assumption for the data block can also be described as

$$E\left[\|\mathcal{E}_{\mathbf{S}}\|_F^2\right] = OP\sigma_\epsilon^2 = \min\{O,P\} \cdot \lambda_{\mathcal{E}}^{\mathbf{M_S}} \tag{6.23}$$

where $\lambda_{\mathcal{E}}^{\mathbf{M_S}}\mathbf{I}$ are the singular values of $\mathcal{E}_{\mathbf{S}}$. When the subblocks of $\mathbf{M_S}$ are created, only three singular values remain. This means that the expected noise power becomes $(3\sigma_\epsilon^2) \cdot \max\{O,P\}$.[3] Because the target response is fully contained in the low-rank approximation, the final SNR becomes

$$\begin{aligned}\text{SNR}\left(\mathbf{U}_{\mathbf{S}}^{\mathbf{M_S}}\mathbf{\Sigma}_{\mathbf{S}}^{\mathbf{M_S}}\mathbf{V}_{\mathbf{S}}^{\mathbf{M_S}\,T}\right) =& \frac{\min\{O,P\}}{3}(1-\delta_g)\frac{2MN}{OP}E\left[\frac{\|\mathbf{S}\|_F^2}{\|\mathcal{E}\|_F^2}\right] \\ =& (1-\delta_g)\frac{2MN}{3\cdot\max\{O,P\}}E\left[\frac{\|\mathbf{S}\|_F^2}{\|\mathcal{E}\|_F^2}\right]\end{aligned} \tag{6.24}$$

where the dimensions for this data collection can be inserted to arrive at $\frac{2MN}{3\cdot\max\{O,P\}} = \frac{42\cdot175}{3\cdot29} \approx 84.5$.

6.3.3 Investigating $\mathbf{M}_{\mathbf{GS}}^{\bar{\mathbf{R}}\mathcal{E}}$

The data block $\mathbf{M}_{\mathbf{GS}}^{\bar{\mathbf{R}}\mathcal{E}}$ is designed to contain short spatial wavelength (high frequency) noise terms found in the spatial dimension that overlap with the target response orthogonal from

[3] This comes from the fact that $\lambda_{\mathcal{E}}^{\mathbf{M_S}} = \sigma_\epsilon^2 \cdot \max\{O,P\}$ based on (6.23) and there remain three singular values.

the ground. This is expressed mathematically as $\mathbf{M}_{\bar{\mathbf{G}}\mathbf{S}}^{\bar{\mathbf{R}}\mathcal{E}}$

$$\mathbf{P}_{\bar{\mathbf{G}}\mathbf{S}}\mathbf{M}\mathbf{P}_{\bar{\mathbf{R}}\mathcal{E}}^{T} = \cancel{\mathbf{P}_{\bar{\mathbf{G}}\mathbf{S}}\mathbf{S}\mathbf{P}_{\bar{\mathbf{R}}\mathcal{E}}^{T}}^{\epsilon} + \cancel{\mathbf{P}_{\bar{\mathbf{G}}\mathbf{S}}\mathbf{G}\mathbf{P}_{\bar{\mathbf{R}}\mathcal{E}}^{T}}^{0} + \cancel{\mathbf{P}_{\bar{\mathbf{G}}\mathbf{S}}\mathbf{R}\mathbf{P}_{\bar{\mathbf{R}}\mathcal{E}}^{T}}^{0} + \mathbf{P}_{\bar{\mathbf{G}}\mathbf{S}}\mathcal{E}\mathbf{P}_{\bar{\mathbf{R}}\mathcal{E}}^{T} \tag{6.25}$$

where it is noted that all terms except the noise matrix are expected to be negligible in this data block. The soil response should be completely removed because $\mathbf{P}_{\bar{\mathbf{G}}\mathbf{S}}$ was designed such that $\mathbf{P}_{\bar{\mathbf{G}}\mathbf{S}}\mathbf{G} \rightarrow \mathbf{0}$. The target response is expected to be some small value, ϵ, because of the design of the EMI system. By using a quadrupole receiver, the target should remain the same sign for shorter spatial wavelengths because the transmitter-receiver polarity will remain constant. Because of this, any sign variation in the response on this short of a spatial span is unlikely to be derived from that target. This means that $\mathbf{S}\mathbf{P}_{\bar{\mathbf{R}}\mathcal{E}}^{T} \rightarrow \epsilon$. Finally, because of the design of $\mathbf{P}_{\bar{\mathbf{R}}\mathcal{E}}$, the self response should be completely removed such that $\mathbf{R}\mathbf{P}_{\bar{\mathbf{R}}\mathcal{E}}^{T} \rightarrow \mathbf{0}$.

The dominating remaining term in this data block is the noise. This provides an area for the system's noise floor to be calculated. It is possible that this noise floor estimation can be corrupted by ϵ when a target is present. Various factors could cause the target response to leak into this data block. These errors could arise from factors such as: $\mathbf{P}_{\mathbf{R}}$ not being an accurate model (such as the edge effects of the filter), motion artifacts from the sensor, or sampling offset in real data since the measurements are not taken on an ideal equally-spaced grid of locations.

The average power of $\mathbf{M}_{\bar{\mathbf{G}}\mathbf{S}}^{\bar{\mathbf{R}}\mathcal{E}}$ from the EMI lane data is shown in Fig. 6.11. Notice that strong targets often bleed over into this data block, especially when they are on the edge of the data matrix where $\mathbf{P}_{\mathbf{G}}$ does not isolate the target as well (as shown in 6.6d). Aside from the stronger targets, the noise floor remains fairly constant at roughly -135dB.

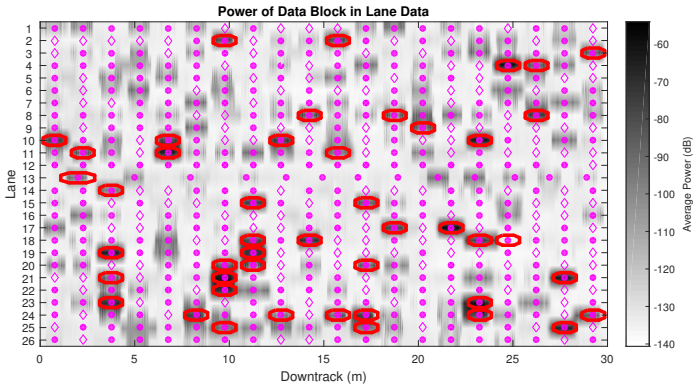

Figure 6.11: Average power of the $\mathbf{M}_{\bar{\mathbf{G}}\mathbf{S}}^{\bar{\mathbf{R}}\mathcal{E}}$ data block from measured EMI data. This data block has the high spatial frequencies and is orthogonal from the soil subspace while aligning with the target's DSRF. This data is expected to be dominated by the noise, but strong targets can bleed into this data block due to positional error artifacts. Filled circles are metallic targets, empty diamonds are locations absent of metallic targets, and red circles are strong targets that potentially overwhelmed the sensor.

6.3.4 Investigating $\mathbf{M}_{\bar{\mathbf{G}}\mathcal{E}}^{\mathbf{RR}}$

The data block $\mathbf{M}_{\bar{\mathbf{G}}\mathcal{E}}^{\mathbf{RR}}$ is designed to contain the self response of the system when it overlaps with minimal distortion from the target and is orthogonal from the soil response. This is expressed mathematically as

$$\mathbf{P}_{\bar{\mathbf{G}}\mathcal{E}}\mathbf{M}\mathbf{P}_{\mathbf{RR}}^{T} = \cancel{\mathbf{P}_{\bar{\mathbf{G}}\mathcal{E}}\mathbf{S}\mathbf{P}_{\mathbf{RR}}^{T}}^{\epsilon\lambda_{\mathbf{G}\mathcal{E}}} + \cancel{\mathbf{P}_{\bar{\mathbf{G}}\mathcal{E}}\mathbf{G}\mathbf{P}_{\mathbf{RR}}^{T}}^{0} + \mathbf{P}_{\bar{\mathbf{G}}\mathcal{E}}\mathbf{R}\mathbf{P}_{\mathbf{RR}}^{T} + \mathbf{P}_{\bar{\mathbf{G}}\mathcal{E}}\mathcal{E}\mathbf{P}_{\mathbf{RR}}^{T} \tag{6.26}$$

where the target response and soil response are expected to be negligible in this data block. The soil response should be removed because $\mathbf{P}_{\bar{\mathbf{G}}\mathcal{E}}\mathbf{G} \rightarrow \mathbf{0}$. The target response is expected to be an extremely small value, $\epsilon\lambda_{\mathbf{G}\mathcal{E}}$. This is because the target will be removed for two reasons. First, the target will be removed from the spatial dimension as discussed previously such that $\mathbf{S}\mathbf{P}_{\mathbf{RR}}^{T} \rightarrow \epsilon$. Secondly, the target will be removed due to the measurement frequency projection. This is because $\mathbf{P}_{\bar{\mathbf{G}}\mathcal{E}}$ has been designed in such a way that $\mathbf{P}_{\bar{\mathbf{G}}\mathcal{E}}\mathbf{S} \rightarrow \lambda_{\mathbf{G}\mathcal{E}}$, where $\lambda_{\mathbf{G}\mathcal{E}}$ has been pre-selected as a small term. When both of these projections operate on $\mathbf{S}$, the resulting effect is that $\mathbf{P}_{\bar{\mathbf{G}}\mathcal{E}}\mathbf{S}\mathbf{P}_{\mathbf{RR}}^{T} \rightarrow \epsilon\lambda_{\mathbf{G}\mathcal{E}}$.

The self response of the system is the dominating term in this data block. It also has

the minimal amount of corruption from other sources when compared to all the other data blocks. This creates the ideal data to calculate the strength of the system self response.

Fig. 6.12 shows the average power of this data block in the lane data, where the size is $\mathbf{M}_{\bar{\mathbf{G}}\mathcal{E}}^{\mathbf{RR}} \in \Re^{19\times 1}$. As can be seen, the average power does not correlate with targets except for the edges of strong targets when $\mathbf{P}_{\mathbf{G}}$ does not isolate it well. The data also shows that very little of the self response energy actually is contained in this data block. This is not too surprising as the self response can be modeled as the eddy currents induced in the platform and thus should also be decreased by $\mathbf{P}_{\bar{\mathbf{G}}\mathcal{E}}\mathbf{R} \rightarrow \lambda_{\mathbf{G}\mathcal{E}}$. Even though this means that the self response may not be estimated well here, it does serve as an ideal place to test the system calibration. This is because if the system is not calibrated well between measurement frequencies, then the DSRF model used for $\mathbf{P}_{\mathbf{G}}$ will no longer be valid and the self response will bleed into this data block. This provides evidence that the measured data was well calibrated since the average power is roughly -100 dB, which is $\lambda_{\mathbf{G}\mathcal{E}}$ lower than the 0 dB strength self response that will be seen in Fig. 6.15. This both provides an indicator for when the sensor's calibration is failing and potentially provides a method to adaptively calibrate the system.

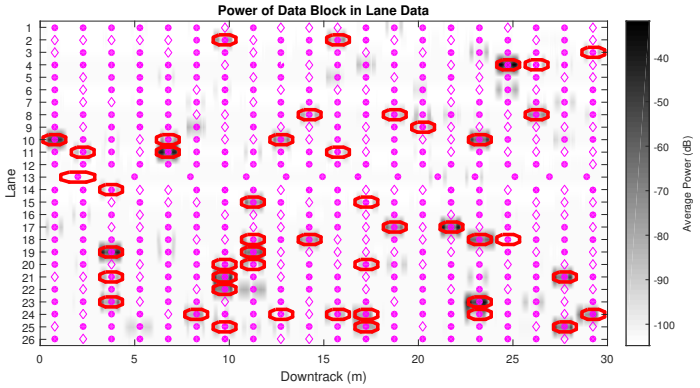

Figure 6.12: Average power of the $\mathbf{M}_{\bar{\mathbf{G}}\mathcal{E}}^{\mathbf{RR}}$ data block from measured EMI data. This data block has the low spatial frequencies and is orthogonal from the soil subspace but does not align with the target's DSRF. This data is expected to be dominated by the self response. Filled circles are metallic targets, empty diamonds are locations absent of metallic targets, and red circles are strong targets that potentially overwhelmed the sensor.

6.3.5 Investigating $\mathbf{M}_{\bar{\mathbf{G}}\mathcal{E}}^{\bar{\mathbf{R}}\mathbf{S}}$

The data block $\mathbf{M}_{\bar{\mathbf{G}}\mathcal{E}}^{\bar{\mathbf{R}}\mathbf{S}}$ is designed to be isolated from both the self response and soil response and only have the minimal amount of target response. This is expressed mathematically as

$$\mathbf{P}_{\bar{\mathbf{G}}\mathcal{E}}\mathbf{M}\mathbf{P}_{\bar{\mathbf{R}}\mathbf{S}}^{T} = \cancel{\mathbf{P}_{\bar{\mathbf{G}}\mathcal{E}}\mathbf{S}\mathbf{P}_{\bar{\mathbf{R}}\mathbf{S}}^{T}}^{\lambda_{\mathbf{G}\mathcal{E}}} + \cancel{\mathbf{P}_{\bar{\mathbf{G}}\mathcal{E}}\mathbf{G}\mathbf{P}_{\bar{\mathbf{R}}\mathbf{S}}^{T}}^{0} + \cancel{\mathbf{P}_{\bar{\mathbf{G}}\mathcal{E}}\mathbf{R}\mathbf{P}_{\bar{\mathbf{R}}\mathbf{S}}^{T}}^{0} + \mathbf{P}_{\bar{\mathbf{G}}\mathcal{E}}\mathcal{E}\mathbf{P}_{\bar{\mathbf{R}}\mathbf{S}}^{T} \tag{6.27}$$

where the target response, soil response, and self response are expected to be negligible in this data block. Both the self response and soil response will be removed from the data block due to the design of the projection matrices such that $\mathbf{P}_{\bar{\mathbf{G}}\mathcal{E}}\mathbf{G} \rightarrow \mathbf{0}$ and $\mathbf{R}\mathbf{P}_{\bar{\mathbf{R}}\mathbf{S}}^{T} \rightarrow \mathbf{0}$. The target response is expected to be a small value that is roughly $\lambda_{\mathbf{G}\mathcal{E}}$ smaller than the target response. This is due to the cutoff threshold chosen when creating $\mathbf{P}_{\bar{\mathbf{G}}\mathcal{E}}$, where the target will be diminished by $\lambda_{\mathbf{G}\mathcal{E}}$.

This creates a data block that is most likely dominated by noise. This is another useful data block for estimating the noise power. The only factor other than noise is when strong targets are present in the measurements. If a target is $\lambda_{\mathbf{G}\mathcal{E}}$ stronger than the noise, then the target's energy will begin to bleed into this data block. Otherwise, the noise should dominate the target response and give accurate noise power estimations.

The lane data for the average power of $\mathbf{M}_{\bar{\mathbf{G}}\mathcal{E}}^{\bar{\mathbf{R}}\mathbf{S}}$ is shown in Fig. 6.13 where $\mathbf{M}_{\bar{\mathbf{G}}\mathcal{E}}^{\bar{\mathbf{R}}\mathbf{S}} \in \Re^{19\times 29}$ is the rough dimension depending on the number of spatial samples. As predicted, most of the measurements estimate a noise floor of roughly -130dB for the sensor. When a strong target is present, this estimate is distorted by the target bleeding into this data block, but this power is heavily reduced from the target's total power.

6.3.6 Investigating $\mathbf{M}_{\bar{\mathbf{G}}\mathcal{E}}^{\bar{\mathbf{R}}\mathcal{E}}$

The data block $\mathbf{M}_{\bar{\mathbf{G}}\mathcal{E}}^{\bar{\mathbf{R}}\mathcal{E}}$ is designed to solely contain noise that is orthogonal from the self response and soil response and the target response has minimal contribution. This is ex-

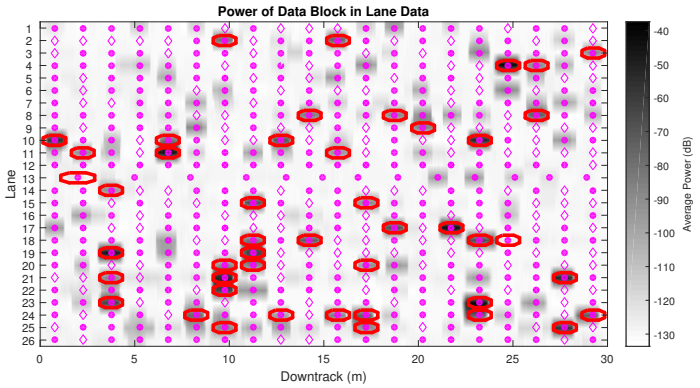

Figure 6.13: Average power of the $\mathbf{M}^{\bar{\mathbf{R}}\mathbf{S}}_{\bar{\mathbf{G}}\mathcal{E}}$ data block from measured EMI data. This data block has the middle spatial frequencies and is orthogonal from the soil subspace but does not align with the target's DSRF. This data is expected to be dominated by noise, but can have strong target's bleed into it. Filled circles are metallic targets, empty diamonds are locations absent of metallic targets, and red circles are strong targets that potentially overwhelmed the sensor.

pressed mathematically as

$$\mathbf{P}_{\bar{\mathbf{G}}\mathcal{E}}\mathbf{M}\mathbf{P}^{T}_{\bar{\mathbf{R}}\mathcal{E}} = \cancelto{\epsilon\lambda_{\mathbf{G}\mathcal{E}}}{\mathbf{P}_{\bar{\mathbf{G}}\mathcal{E}}\mathbf{S}\mathbf{P}^{T}_{\bar{\mathbf{R}}\mathcal{E}}} + \cancelto{0}{\mathbf{P}_{\bar{\mathbf{G}}\mathcal{E}}\mathbf{G}\mathbf{P}^{T}_{\bar{\mathbf{R}}\mathcal{E}}} + \cancelto{0}{\mathbf{P}_{\bar{\mathbf{G}}\mathcal{E}}\mathbf{R}\mathbf{P}^{T}_{\bar{\mathbf{R}}\mathcal{E}}} + \mathbf{P}_{\bar{\mathbf{G}}\mathcal{E}}\mathcal{E}\mathbf{P}^{T}_{\bar{\mathbf{R}}\mathcal{E}} \tag{6.28}$$

where all sources but the noise term are negligible. The soil and self response are removed by their associated projection operators, $\mathbf{P}_{\bar{\mathbf{G}}\mathcal{E}}\mathbf{G} \rightarrow \mathbf{0}$ and $\mathbf{R}\mathbf{P}^{T}_{\bar{\mathbf{R}}\mathcal{E}} \rightarrow \mathbf{0}$. The target is expected to be an extremely small value that is $\epsilon\lambda_{\mathbf{G}\mathcal{E}}$ smaller than the total target energy. As discussed above, this is due to $\mathbf{P}_{\bar{\mathbf{G}}\mathcal{E}}$ causing the target to be reduced to $\mathbf{P}_{\bar{\mathbf{G}}\mathcal{E}}\mathbf{S} \rightarrow \lambda_{\mathbf{G}\mathcal{E}}$ and the $\mathbf{P}_{\bar{\mathbf{R}}\mathcal{E}}$ reducing the target to $\mathbf{S}\mathbf{P}^{T}_{\bar{\mathbf{R}}\mathcal{E}} \rightarrow \epsilon$.

This is the ideal data block to estimate the noise power. The data is isolated from both the soil and self response interferers. It also contains the least amount of target response out of all of the data blocks.

The average power of $\mathbf{M}^{\bar{\mathbf{R}}\mathcal{E}}_{\bar{\mathbf{G}}\mathcal{E}} \in \Re^{19\times 144}$ is shown in Fig. 6.14. This noise power estimate is more stable than any other data block (compare to Fig. 6.11 and 6.13). It shows that the noise floor of the EMI system is close to -140dB. It has minimal power that bleeds in from strong targets. Even when targets do bleed in, the power is extremely reduced where it is less than -100dB except for the targets that overwhelm the sensor. It is also worth

noting that this data block has roughly 2500 noise samples, so the estimated noise power is expected to be fairly reliable from this data block.

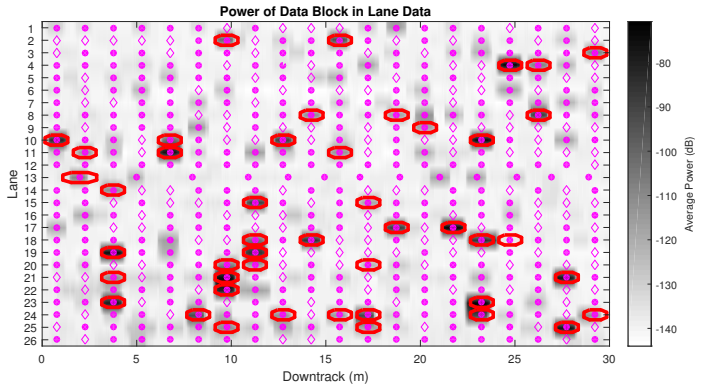

Figure 6.14: Average power of the $\mathbf{M}^{\bar{\mathbf{R}}\mathcal{E}}_{\bar{\mathbf{G}}\mathcal{E}}$ data block from measured EMI data. This data block has the high spatial frequencies and is orthogonal from the soil subspace but does not align with the target's DSRF. This data is expected to be dominated by noise. Filled circles are metallic targets, empty diamonds are locations absent of metallic targets, and red circles are strong targets that potentially overwhelmed the sensor.

6.3.7 Investigating $\mathbf{M}^{\mathbf{RR}}_{\mathbf{GG}}$

The data block $\mathbf{M}^{\mathbf{RR}}_{\mathbf{GG}}$ is designed to contain the overlap of the soil response and self response in the measurements. This is expressed mathematically as

$$\mathbf{P_{GG}MP^{T}_{RR}} = \cancel{\mathbf{P_{GG}SP^{T}_{RR}}}^{\epsilon} + \mathbf{P_{GG}GP^{T}_{RR}} + \mathbf{P_{GG}RP^{T}_{RR}} + \mathbf{P_{GG}}\mathcal{E}\mathbf{P^{T}_{RR}}. \tag{6.29}$$

This data block is going to be heavily dominated by the interference components of the measurements. The self response, as mentioned before, can be orders of magnitude stronger than the target. As was seen in Fig. 6.1, a large portion of the self response overlaps with the soil response and thus is expected to reside in this data block.

Also, a large portion of the soil response resides here as well. Assuming the non-zero mean noise model of $\boldsymbol{\Xi}$, the constant term across positions will estimate the mean of both these distributions, g_1 and g_2, and place the energy in this data block. The combination of these interferences is expected to overwhelm the target when present. On the other hand,

the quadrupole design of the receiver should cause $\mathbf{SP}_{\mathbf{RR}}^{T} \rightarrow \epsilon$ because the target should change signs as the quadrupole receiver passes over it. This means that very little target information is expected to be in this block. When solely interested in the target response, this block will have little value. However, if it is desired to extract information about either the soil response's average value or the strength of the self response then it can become useful.

Fig. 6.15 shows the average power for $\mathbf{M}_{\mathbf{GG}}^{\mathbf{RR}} \in \Re^{2\times 1}$ across all of the lanes. Comparing the average power of $\mathbf{M}_{\mathbf{GG}}^{\mathbf{RR}}$ to all other data blocks, it is clear that a majority of the measured power resides here. The power remains relatively stable at -25dB.

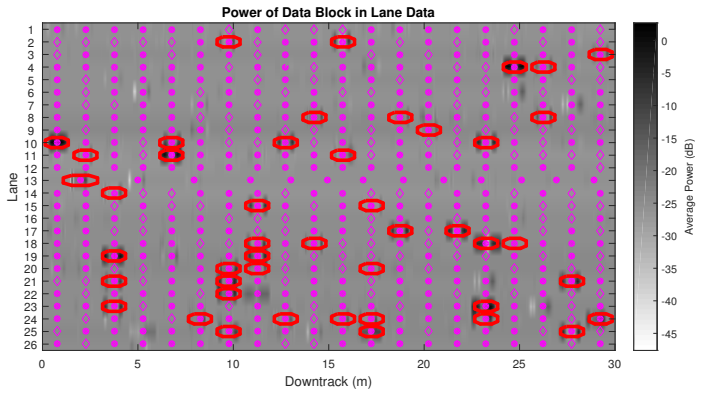

Figure 6.15: Average power of the $\mathbf{M}_{\mathbf{GG}}^{\mathbf{RR}}$ data block from measured EMI data. This data block has the low spatial frequencies and contains the soil subspace. This data is expected to be dominated by the self response and soil response. Filled circles are metallic targets, empty diamonds are locations absent of metallic targets, and red circles are strong targets that potentially overwhelmed the sensor.

6.3.8 Investigating $\mathbf{M}_{\mathbf{GG}}^{\bar{\mathbf{R}}\mathbf{S}}$

The data block $\mathbf{M}_{\mathbf{GG}}^{\bar{\mathbf{R}}\mathbf{S}}$ is designed to contain the soil response that overlaps the target response but is orthogonal from the self response. This is expressed mathematically as

$$\mathbf{P}_{\mathbf{GG}}\mathbf{M}\mathbf{P}_{\bar{\mathbf{R}}\mathbf{S}}^{T} = \mathbf{P}_{\mathbf{GG}}\mathbf{S}\mathbf{P}_{\bar{\mathbf{R}}\mathbf{S}}^{T} + \mathbf{P}_{\mathbf{GG}}\mathbf{G}\mathbf{P}_{\bar{\mathbf{R}}\mathbf{S}}^{T} + \cancelto{0}{\mathbf{P}_{\mathbf{GG}}\mathbf{R}\mathbf{P}_{\bar{\mathbf{R}}\mathbf{S}}^{T}} + \mathbf{P}_{\mathbf{GG}}\mathcal{E}\mathbf{P}_{\bar{\mathbf{R}}\mathbf{S}}^{T} \tag{6.30}$$

where the self response of the system has been removed because $\mathbf{P}_{\bar{\mathbf{R}}\mathbf{S}}$ has been designed so $\mathbf{R}\mathbf{P}_{\bar{\mathbf{R}}\mathbf{S}}^{T} \rightarrow \mathbf{0}$. As was shown in Section 6.2.2, the target response overlaps the soil subspace through the projection $\mathbf{P}_{\mathbf{GG}}\mathbf{S}$. The position projection operator $\mathbf{P}_{\bar{\mathbf{R}}\mathbf{S}}$ is also designed to extract any variation that corresponds to an object below the transmitter. This means that $\mathbf{M}_{\mathbf{GG}}^{\bar{\mathbf{R}}\mathbf{S}}$ is expected to have a large amount of target information. Unfortunately this data is also strongly corrupted by the soil response. Depending on the permeability of the soil, the soil response can drastically reduce the amount of information that can be extracted from this data and can easily dominate many targets.

This data block is also potentially very interesting because it provides the opportunity to detect voids beneath the soil. This is because it concentrates the soil response into a small data block that also is extracting variations the size of the sensor. If a void exists beneath the ground, this would create an absence of the soil response. This absence would appear in the spatial domain very similar to a target response, and thus get highlighted in this data block. It is the author's belief that metrics from this data block could be used to detect such voids within the soil, especially in areas with a strong soil response.

The average power of $\mathbf{M}_{\mathbf{GG}}^{\bar{\mathbf{R}}\mathbf{S}} \in \Re^{2\times 29}$ is shown in Fig. 6.16. Many of the targets are still detectable in this data block, but the noise floor is noticeably higher than $\mathbf{M}_{\bar{\mathbf{G}}\mathbf{S}}^{\bar{\mathbf{R}}\mathbf{S}}$. The noise and interference floor has been increased to roughly -80dB for this data block due to the soil response. The increase in the noise and interference floor of around 50dB compared to $\mathbf{M}_{\bar{\mathbf{G}}\mathbf{S}}^{\bar{\mathbf{R}}\mathbf{S}}$ illustrates that the target power of roughly 7.1dB that is lost when using $\mathbf{P}_{\mathbf{G}}$ to isolate the target from the soil response is recouped from the interference isolation. However, it is still desirable to extract the target power contained in this data block as well.

In order to exploit the target data in $\mathbf{M}_{\mathbf{GG}}^{\bar{\mathbf{R}}\mathbf{S}}$, it is ideal to further isolate it from the soil response. From the SVD of $\mathbf{M}_{\bar{\mathbf{G}}\mathbf{S}}^{\bar{\mathbf{R}}\mathbf{S}}$, the spatial response of the target is contained in $\mathbf{V}_{\mathbf{S}}^{\mathbf{M_S}}$. As long as the target is strong enough in $\mathbf{M}_{\bar{\mathbf{G}}\mathbf{S}}^{\bar{\mathbf{R}}\mathbf{S}}$ to be isolated in the strongest three singular values, then the spatial response of the target is described by $\mathbf{V}_{\mathbf{S}}^{\mathbf{M_S}^{T}}\mathbf{P}_{\bar{\mathbf{R}}\mathbf{S}}$. Using this knowledge, it is possible to isolate the data in $\mathbf{M}_{\mathbf{GG}}^{\bar{\mathbf{R}}\mathbf{S}}$ that corresponds to the target's

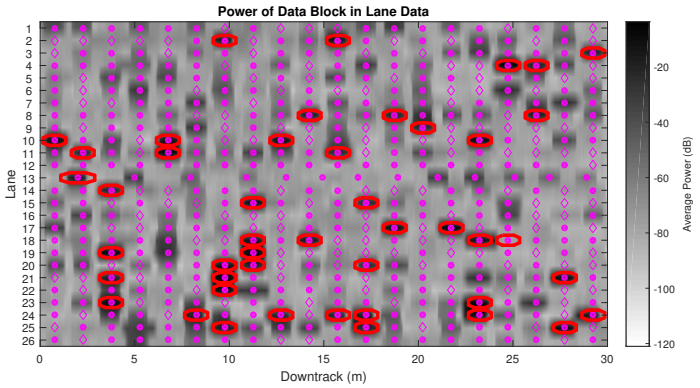

Figure 6.16: Average power of the $\mathbf{M}_{\mathbf{GG}}^{\bar{\mathbf{R}}\mathbf{S}}$ data block from measured EMI data. This data block has the middle spatial frequencies and contains the soil subspace. This data is expected to be a mixture of the target response and soil response. Filled circles are metallic targets, empty diamonds are locations absent of metallic targets, and red circles are strong targets that potentially overwhelmed the sensor.

spatial response by creating an adaptive matched subspace filter bank. This is accomplished by creating the spatial signal projection matrix $\mathbf{P_S} = \mathbf{V}_{\mathbf{S}}^{\mathbf{M_S}}(\mathbf{V}_{\mathbf{S}}^{\mathbf{M_S}^T}\mathbf{V}_{\mathbf{S}}^{\mathbf{M_S}})^{-1}\mathbf{V}_{\mathbf{S}}^{\mathbf{M_S}^T}$. The data block can then be separated into two subblocks

$$\boxed{\mathbf{M}_{\mathbf{GG}}^{\bar{\mathbf{R}}\mathbf{S}} = \mathbf{M}_{\mathbf{GG}}^{\bar{\mathbf{R}}\mathbf{S}}\mathbf{P}_{\mathbf{S}}^{T} + \mathbf{M}_{\mathbf{GG}}^{\bar{\mathbf{R}}\mathbf{S}}\mathbf{P}_{\mathbf{S}}^{\perp^T}} \tag{6.31}$$

where $\mathbf{P}_{\mathbf{S}}^{\perp} = \mathbf{I} - \mathbf{P_S}$ is the projection operator orthogonal to $\mathbf{P_S}$. The target response should be contained in $\mathbf{M}_{\mathbf{GG}}^{\bar{\mathbf{R}}\mathbf{S}}\mathbf{P}_{\mathbf{S}}^{T}$ and the soil response power will be decreased by a factor of $\frac{3}{P}$ under the Gaussian soil assumption. The remaining subblock $\mathbf{M}_{\mathbf{GG}}^{\bar{\mathbf{R}}\mathbf{S}}\mathbf{P}_{\mathbf{S}}^{\perp^T}$ should have minimal target response and be dominated by the soil response.

The average power of the target and noise subblocks of $\mathbf{M}_{\mathbf{GG}}^{\bar{\mathbf{R}}\mathbf{S}}$ are shown in Fig. 6.17 and 6.18 respectively. It can be seen that the power of a target remains mostly unchanged in $\mathbf{M}_{\mathbf{GG}}^{\bar{\mathbf{R}}\mathbf{S}}\mathbf{P}_{\mathbf{S}}^{T}$ compared to $\mathbf{M}_{\mathbf{GG}}^{\bar{\mathbf{R}}\mathbf{S}}$ and the interference floor is slightly reduced. It is also compelling that Fig. 6.18 is fairly constant and minimally correlates to the presence of a target. This shows that the target response has been further isolated from the soil response. This process also provides a data subblock that can be used to obtain an accurate estimate of the noise and interference floor.

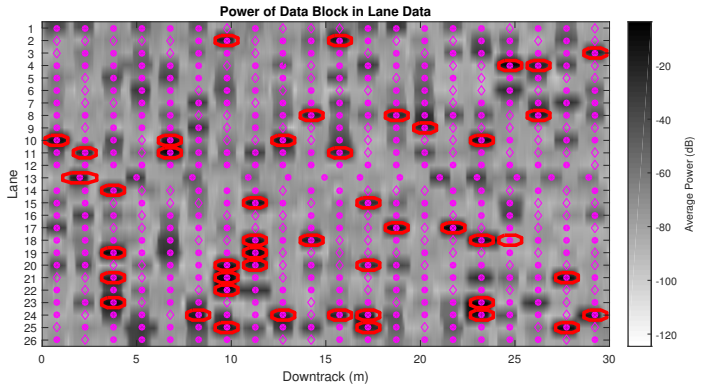

Figure 6.17: Average power of the $\mathbf{M}_{\mathbf{GG}}^{\bar{\mathbf{R}}\mathbf{S}}\mathbf{P}_{\mathbf{S}}^{T}$ data block from measured EMI data. This data block has the power in $\mathbf{M}_{\mathbf{GG}}^{\bar{\mathbf{R}}\mathbf{S}}$ that aligns with the measured spatial response of the target. This data is expected to contain the self response where the soil response has been reduced. Filled circles are metallic targets, empty diamonds are locations absent of metallic targets, and red circles are strong targets that potentially overwhelmed the sensor.

6.3.9 Investigating $\mathbf{M}_{\mathbf{GG}}^{\bar{\mathbf{R}}\mathcal{E}}$

The data block $\mathbf{M}_{\mathbf{GG}}^{\bar{\mathbf{R}}\mathcal{E}}$ is designed to contain the soil response that is orthogonal to the self response and contains minimal target energy. This is expressed mathematically as

$$\mathbf{P}_{\mathbf{GG}}\mathbf{M}\mathbf{P}_{\bar{\mathbf{R}}\mathcal{E}}^{T} = \cancel{\mathbf{P}_{\mathbf{GG}}\mathbf{S}\mathbf{P}_{\bar{\mathbf{R}}\mathcal{E}}^{T}}^{\epsilon} + \mathbf{P}_{\mathbf{GG}}\mathbf{G}\mathbf{P}_{\bar{\mathbf{R}}\mathcal{E}}^{T} + \cancel{\mathbf{P}_{\mathbf{GG}}\mathbf{R}\mathbf{P}_{\bar{\mathbf{R}}\mathcal{E}}^{T}}^{0} + \mathbf{P}_{\mathbf{GG}}\mathcal{E}\mathbf{P}_{\bar{\mathbf{R}}\mathcal{E}}^{T} \tag{6.32}$$

where there is minimal impact from the target response and self response. The self response is again removed because $\mathbf{R}\mathbf{P}_{\bar{\mathbf{R}}\mathcal{E}}^{T} \rightarrow \mathbf{0}$. The target response is diminished to some small number due to the position projection matrix because $\mathbf{S}\mathbf{P}_{\bar{\mathbf{R}}\mathcal{E}}^{T} \rightarrow \epsilon$.

This creates an ideal data block for estimating the variance of the soil response. Because the mean of the soil response has been removed (since it is contained in $\mathbf{M}_{\mathbf{GG}}^{\mathbf{RR}}$), the strongest component in this data block is expected to be the soil's variation. The data block also contains the noise component, but it is expected that the soil response is stronger than the system noise level and will thus dominate these measurements. Alternatively, the combination of the soil response and noise response can be thought of as an interference level in the data block $\mathbf{M}_{\mathbf{GG}}^{\bar{\mathbf{R}}\mathbf{S}}$. This allows the interference floor to be estimated to further enable processing on $\mathbf{M}_{\mathbf{GG}}^{\bar{\mathbf{R}}\mathbf{S}}$. Also, this provides ideal data for testing how strong the soil response

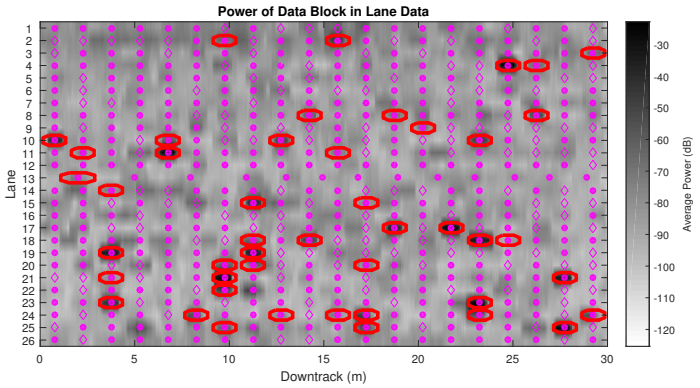

Figure 6.18: Average power of the $\mathbf{M}_{\mathbf{GG}}^{\bar{\mathbf{R}}\mathbf{S}}\mathbf{P}_{\mathbf{S}}^{\perp^T}$ data block from measured EMI data. This data block has the power in $\mathbf{M}_{\mathbf{GG}}^{\bar{\mathbf{R}}\mathbf{S}}$ that does not align with the measured spatial response of the target. This data is expected to be dominated by the soil response. Filled circles are metallic targets, empty diamonds are locations absent of metallic targets, and red circles are strong targets that potentially overwhelmed the sensor.

is in a specific area, regardless of the presence or absence of a target. If the interference level in this data block is compared to a noise data block, such as $\mathbf{M}_{\mathbf{G}\mathcal{E}}^{\bar{\mathbf{R}}\mathcal{E}}$, then it is possible to estimate how much stronger the soil response variation is from the noise variation. This information could be used to determine if it is better to project the target data away from the soil interference for processing and take the target response decrease $\lambda_{\mathbf{G}\mathcal{E}}$, or if the soil response is weak enough that $\mathbf{M}_{\mathbf{GS}}^{\bar{\mathbf{R}}\mathbf{S}}$ and $\mathbf{M}_{\mathbf{GG}}^{\bar{\mathbf{R}}\mathbf{S}}$ should be processed together. Estimating the interference level can also allow for the measurements in $\mathbf{M}_{\mathbf{GS}}^{\bar{\mathbf{R}}\mathbf{S}}$ and $\mathbf{M}_{\mathbf{GG}}^{\bar{\mathbf{R}}\mathbf{S}}$ to be properly whitened so processing can correctly extract information from $\mathbf{M}_{\mathbf{GS}}^{\bar{\mathbf{R}}\mathbf{S}}$ and $\mathbf{M}_{\mathbf{GG}}^{\bar{\mathbf{R}}\mathbf{S}}$ jointly from any data regardless of the soil response's strength.

Fig. 6.19 shows the average power of $\mathbf{M}_{\mathbf{GG}}^{\bar{\mathbf{R}}\mathcal{E}} \in \Re^{2\times 144}$ through the lanes. Strong targets bleed into this data block due to $\mathbf{P}_{\mathbf{R}}$. Otherwise, this data block is fairly consistent and provides an opportunity to estimate the interference plus noise level.

6.4 Reference Targets

The above conversations detail each subblock of the preprocessed EMI data. The results from the collected lane data confirm that the preprocessing successfully exploits measured EMI data as expected. In order to gain a better understanding of exactly how the pre-

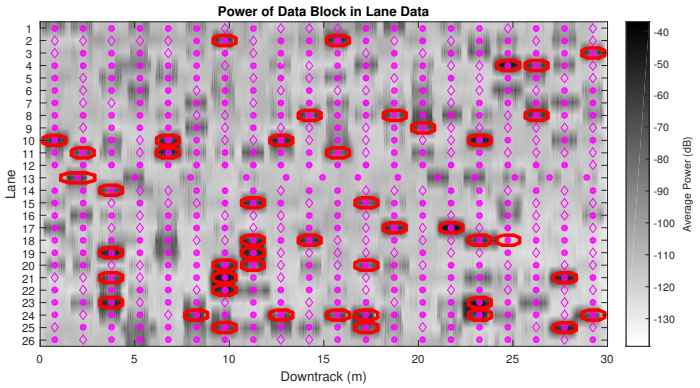

Figure 6.19: Average power of the $\mathbf{M}_{\mathbf{GG}}^{\bar{\mathbf{R}}\mathcal{E}}$ data block from measured EMI data. This data block has the high spatial frequencies and contains the soil subspace. This data is expected to be dominated by the soil response. Filled circles are metallic targets, empty diamonds are locations absent of metallic targets, and red circles are strong targets that potentially overwhelmed the sensor.

processing effects the signal, it is helpful to return to the simulated reference targets to investigate the effects of the preprocessing. The simulated targets were generated using the procedure described in Section 5.6.

For the reference targets, it is more effective to show the different subblock powers in relation to each other for a specific target. Figure 6.20 labels the different subblocks after preprocessing as was introduced in (6.11). On top of the basic nine subblocks from preprocessing, four sub-divided blocks are also contained in the power relations and are denoted by they're relevant matrices. The $\mathbf{M}_{\bar{\mathbf{G}}\mathbf{S}}^{\bar{\mathbf{R}}\mathbf{S}}$ subblock is split into a signal ($\mathbf{\Sigma}_{\mathbf{S}}^{\mathbf{M_S}}$) and noise ($\mathbf{\Sigma}_{\mathcal{E}}^{\mathbf{M_S}}$) component based on the low-rank nature of the target as shown in (6.22). Likewise, $\mathbf{M}_{\mathbf{GG}}^{\bar{\mathbf{R}}\mathbf{S}}$ is split into a signal ($\mathbf{P_S}$) and noise ($\mathbf{P}_{\mathbf{S}}^{\perp}$) component by using the SVD of $\mathbf{M}_{\bar{\mathbf{G}}\mathbf{S}}^{\bar{\mathbf{R}}\mathbf{S}}$ to create an adaptive spatial filter as shown in (6.31).

Performing the preprocessing on the simulated reference targets is slightly different than the lane data. Because the data collection path for the simulated targets involves multiple passes over the target at different y locations, the preprocessing must take this into account. To achieve this, the spatial projection matrix ($\mathbf{P_R}$) is applied to each pass. The results of each projected measurement pass can then be concatenated as new columns into the same projected measurement matrix. For a sensor that passes over the target three

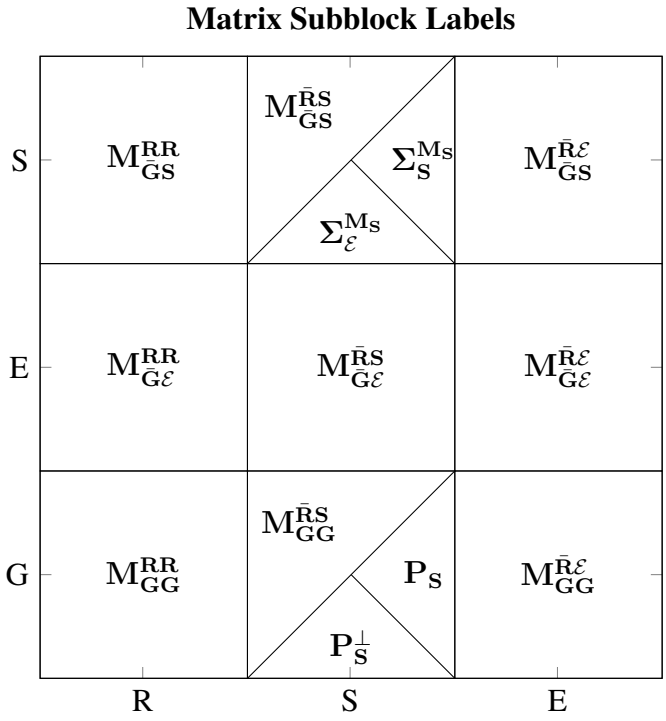

Figure 6.20: Labels for the matrix subblocks that are created when performing preprocessing stages on a single EMI target measurement matrix.

times, this is written as

$$\mathbf{P_G}\begin{bmatrix}\mathbf{M}_1\mathbf{P}_{\mathbf{R}}^T & \mathbf{M}_2\mathbf{P}_{\mathbf{R}}^T & \mathbf{M}_3\mathbf{P}_{\mathbf{R}}^T\end{bmatrix} \tag{6.33}$$

where $\mathbf{M}_x$ is the x$^{\text{th}}$ pass of the sensor. This preprocessing change must be used because the spatial projection is based on relative samples for a single pass by utilizing the spatial frequencies. The edges where each pass starts and ends are undesirable artifacts that are ignored, but the multiple passes can be processed together as different locations ($\mathbf{\Delta p}$) in a single target measurement matrix after the spatial filters are applied separately.

The first important test is to explore how an i.i.d. noise matrix is processed. A matrix the same size as the reference targets was created, where each sample contains an i.i.d. $\mathcal{N}(0, \sigma_\epsilon^2)$ that has a variance of 50dB. The preprocessing is applied to this matrix and the results are shown in Fig. 6.21. As can be seen, the noise distributes evenly between all of the sections and they are within 2dB of the correct power. It is also expected that the $\mathbf{\Sigma}^{\mathbf{M_S}}_{\mathbf{S}}$ created block is slightly stronger because the SVD is forcing it to only keep the strongest

noise in the $\mathbf{M}_{\bar{\mathbf{G}}\mathbf{S}}^{\bar{\mathbf{R}}\mathbf{S}}$ block. Note that these images show the element-wise average power. This means that the power (using Frobenius norm) is taken for each subblock and then this power is divided by the number of elements in the subblock to estimate the average power of each element. If the subblock power is desired then the average element power can be multiplied by the number of elements per subblock that is shown in Fig. 6.22.

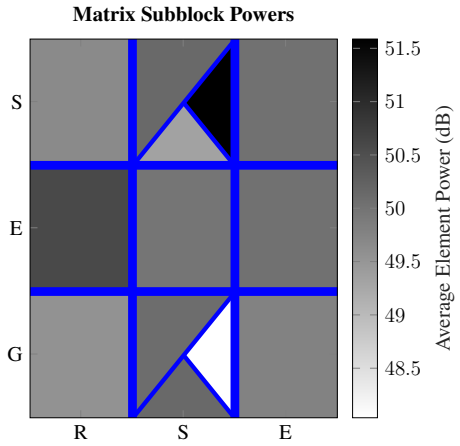

Figure 6.21: The average element-wise power after the preprocessing is applied to a noise matrix.

The preprocessing has been applied to the reference targets. Each reference target was created with an SNR of 50dB.[4] The noise is created as i.i.d. $\mathcal{N}(0,1)$ and the target response was scaled accordingly for the desired SNR. The results are shown in Fig. 6.23. As expected,nearly all of the signal power is distributed into the signal subblocks $\mathbf{M}_{\bar{\mathbf{G}}\mathbf{S}}^{\bar{\mathbf{R}}\mathbf{S}}$ and $\mathbf{\Sigma}_{\mathbf{S}}^{\mathbf{M_S}}$ and into the soil/interferes subblocks $\mathbf{M}_{\mathbf{GG}}^{\bar{\mathbf{R}}\mathbf{S}}$ and $\mathbf{P}_{\mathbf{S}}$. For these targets, an unusually large portion of the target's signature are contained in the soil/interferes subblocks. This effect is somewhat exaggerated for the reference targets as their frequency response looks more like soil than typical targets[5]. It is interesting to note that none of the reference targets actually have a zero-mean spatial response. They all lose energy to the self response subblocks. Based on (6.20), the predicted SNR of $\mathbf{M}_{\bar{\mathbf{G}}\mathbf{S}}^{\bar{\mathbf{R}}\mathbf{S}}$ should be 62dB.[6] All of the reference targets

[4]The same SNR can be interpreted as the relative Frobenius norms or the average element SNR because they are mathematically equivalent.

[5]The soil can be modeled as a uniform distribution with respect to log frequency of equal strength relaxations so the targets with equal strength relaxations look somewhat like the soil.

[6]The dimensions of the data are $M = 42$, $N = 4347$), $O = 21$, and $P = 207$. The estimated soil target

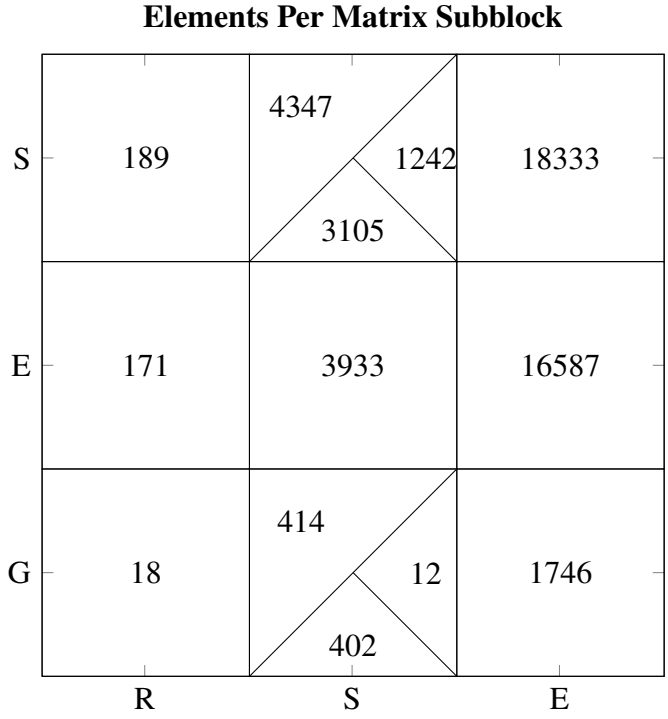

Figure 6.22: The number of elements in each subblock after preprocessing the reference targets.

increase the SNR in $\mathbf{M}_{\mathbf{\bar{G}S}}^{\mathbf{\bar{R}S}}$ to > 50dB, but none of them reach the predicted SNR of 62dB. This is not surprising with the extra power being in the self response and more than average power overlapping with the soil response. The predicted SNR of $\mathbf{\Sigma}_{\mathbf{S}}^{\mathbf{M_S}}$ is 67.5dB based on (6.24), which is 5.5dB stronger than $\mathbf{M}_{\mathbf{\bar{G}S}}^{\mathbf{\bar{R}S}}$.[7] This 5.5dB SNR increase is observed in all of the reference targets. It is also obvious in these results that the adaptive spatial filter in the $\mathbf{P_S}$ subblock are very effective at consolidating the target response in $\mathbf{M}_{\mathbf{GG}}^{\mathbf{\bar{R}S}}$.

The results in Fig. 6.23 show that the preprocessing does indeed increase the SNR. However, it does not highlight why it is worth isolating the interferers, but it does show that significant amounts of the target's signal is lost due to these isolations. These simulated targets are unrealistic in that they do not have any interference present, so to make the simulated measurements more realistic the interference can be added. The reference targets

drop of $\delta_g \approx -7.1$dB from Fig. 6.4 is used.

[7]The six largest singular values were kept because some of the reference targets represent general EMI targets.

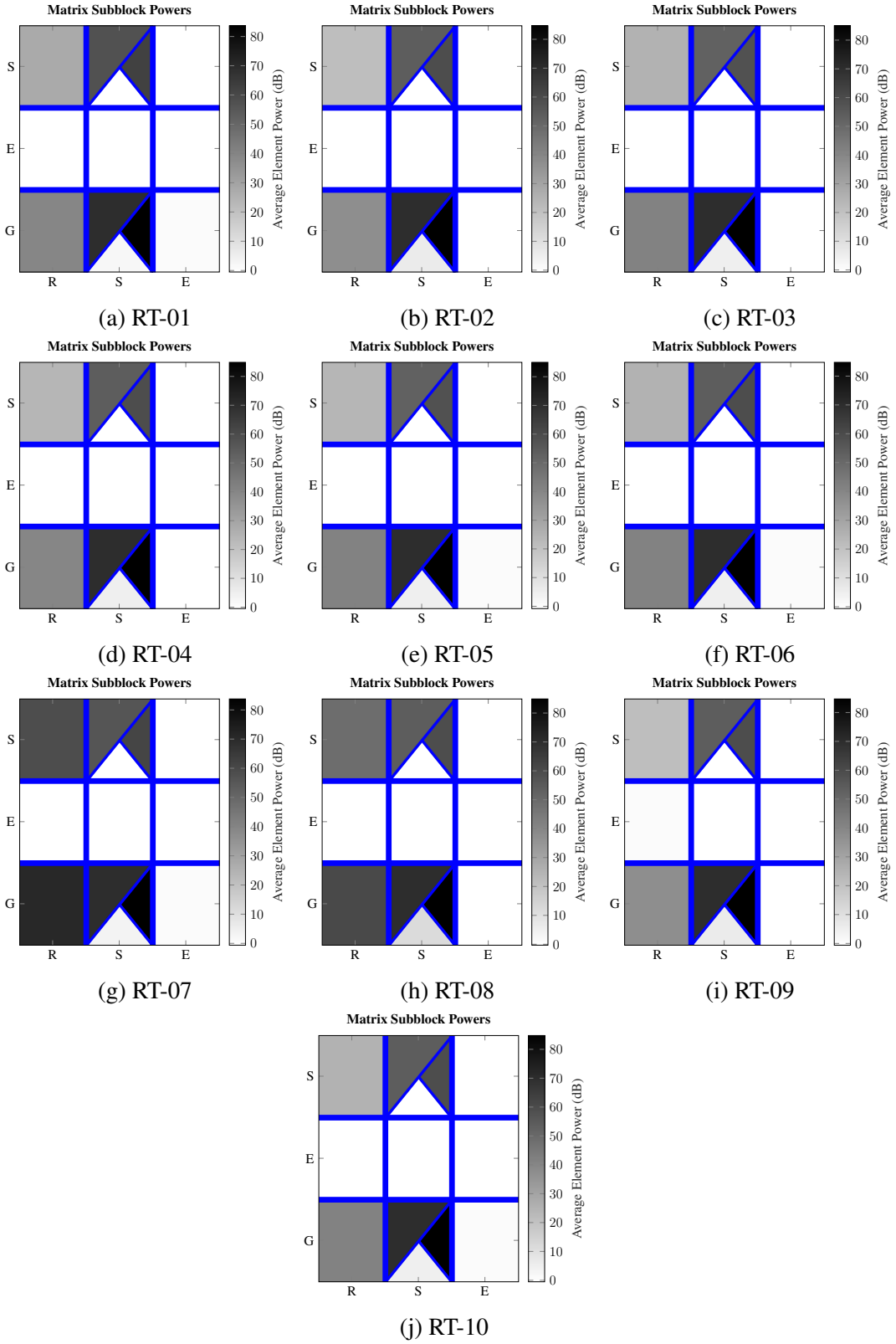

(a) RT-01 (b) RT-02 (c) RT-03

(d) RT-04 (e) RT-05 (f) RT-06

(g) RT-07 (h) RT-08 (i) RT-09

(j) RT-10

Figure 6.23: Reference targets' preprocessing results with random noise at 50dB SNR.

were kept at 50dB SNR, but simulated soil was added at a signal-to-soil-ratio of 20dB and a simulated self response was add at a signal-to-self-response-ratio of -30dB. These numbers are fairly representative of an EMI system as the preprocessed lane data presented above showed the soil power being 30dB stronger than the noise floor and the self response is expected to be much larger than the target response. Again, the noise was modeled as i.i.d. $\mathcal{N}(0,1)$ and every other response was scaled accordingly. The results of the preprocessing are shown in Fig. 6.24. Notice that the four subblocks that are isolated from the interferers have remained unchanged. The energy in the self-response subblocks is now dominated by the self-response interference in the measured signal, and the energy from the signal is no longer discernible. The soil subblocks new have a higher noise floor that can be modeled as the combination of the soil and noise power. This can be seen in $\mathbf{M}_{\mathbf{GG}}^{\bar{\mathbf{R}}\mathcal{E}}$, where the interference-noise floor becomes just over 40dB because it has been consolidated in the lower dimension sub-space. Even though there is a large amount of target response in $\mathbf{M}_{\mathbf{GG}}^{\bar{\mathbf{R}}\mathbf{S}}$, it now has to compete with a much higher interference-noise floor and only has a signal-to-interference-noise-ratio (SINR) of 25dB. This shows why it is useful to create the $\mathbf{M}_{\mathbf{GS}}^{\bar{\mathbf{R}}\mathbf{S}}$ subblock that still maintains the SNR of over 50dB. It is also worth pointing out that the $\mathbf{P_S}$ subblock remains effective in continuing to extract the target response that is mixed with the soil by increasing the SINR to 40dB.

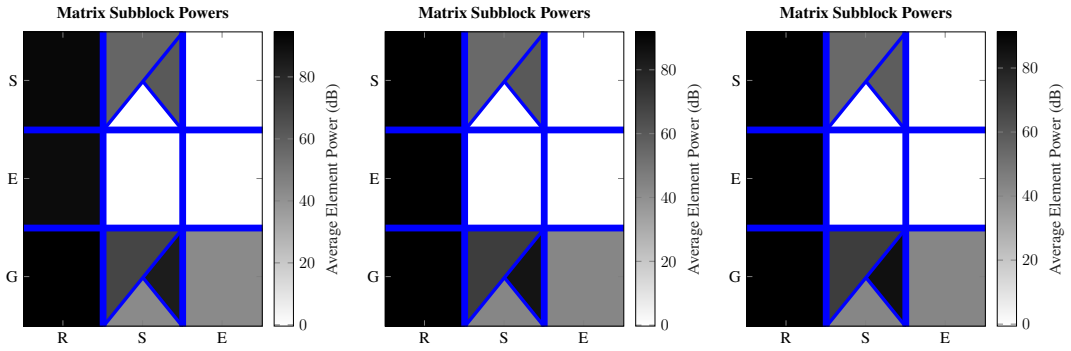

(a) RT-01 (b) RT-02 (c) RT-03

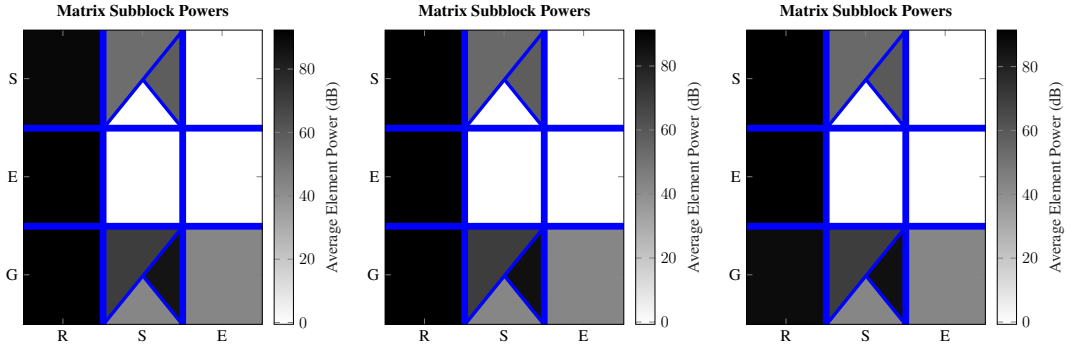

(d) RT-04 (e) RT-05 (f) RT-06

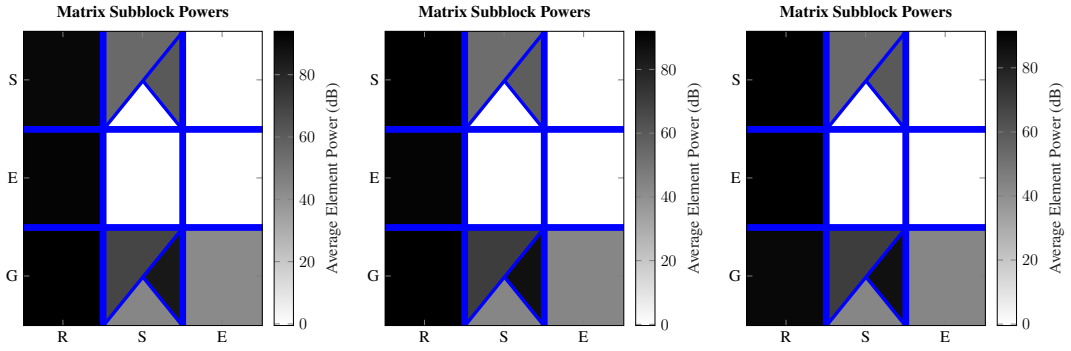

(g) RT-07 (h) RT-08 (i) RT-09

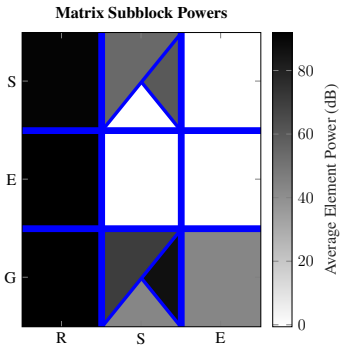

(j) RT-10

Figure 6.24: Reference targets' preprocessing results at 50dB SNR with Signal-Soil ratio at 20dB and Signal-Self Response ratio at -20dB.

CHAPTER 7
DETECTION

The first stage of any processing framework is to detect the presence of a target. A target detection method can serve as a prescreener for an EMI device to reduce the processing requirements of the system. The goal of the detector is to create an accurate method for detecting the presence of a target quickly and with minimal computation. Once a target is detected, then further processing can classify and localize the target. Because the detection stage of the EMI system is primarily a prescreener to reduce processing, this work will focus on a variety of options that require differing degrees of computation and compare the resulting performance. This investigation is meant to allow future systems to make an educated trade-off between performance and computation.

7.1 Matched Subspace and Constant False Alarm Rate Detection

Detection is a well studied problem. In order to address the EMI detection problem, the matched subspace detector (MSD) and constant false alarm rate detector (CFAR) developed by Scharf will be used [31]. These detectors create the uniformly most powerful invariant (UMPI) detector in Gaussian noise with a known covariance structure by defining a signal and noise subspace. It will be shown that the MSD and CFAR detector can be applied directly to the EMI data to provide the UMPI optimal detector.

7.1.1 Background

In [31], Scharf provides theoretical proofs that state how to make the UMPI detection system for detecting a signal with multivariate Gaussian distributed noise with a covariance structure that is known but contains an unknown scaling factor, which can be written as $\mathcal{N}(0, \sigma^2 \boldsymbol{K}_\epsilon)$ where $\boldsymbol{K}_\epsilon$ is the known covariance structure and σ^2 is an unknown scaling

constant. For ease of explanation, this work borrows the notation from [32] to describe the MSD and CFAR detection methods. The fundamental approach of these works assume that the measurements, $\boldsymbol{y}$, can be projected in such a way to create

$$\mathbf{z} = \begin{bmatrix} \mathbf{z}_1 \\ \\ \mathbf{z}_2 \end{bmatrix} = \begin{bmatrix} \boldsymbol{\nu} \\ \\ 0 \end{bmatrix} + \epsilon \tag{7.1}$$

where $\mathbf{z}_1$ contains all of the signal content, denoted as $\boldsymbol{\nu}$, plus a random Gaussian noise term, denoted as ϵ, and $\mathbf{z}_2$ contains only the Gaussian noise term. This is done by pre-whitening the noise of the measurements through the operation $\boldsymbol{K}_{\epsilon}^{-\frac{1}{2}}\boldsymbol{y}$, where $\boldsymbol{K}_{\epsilon}$ is the covariance structure of the noise term. After the noise whitening is performed, a subspace projection must be found to create $\mathbf{z} = \boldsymbol{P}_d^T\boldsymbol{y}$.

Once $\mathbf{z}$ has been formulated, the values for the associated detection methods can be described as

$$\text{MSD)} \quad \gamma = \|\mathbf{z}_1\|_2^2 \tag{7.2a}$$

$$\text{CFAR)} \quad \gamma = \frac{\|\mathbf{z}_1\|_2^2}{\|\mathbf{z}_2\|_2^2} \tag{7.2b}$$

where γ is then compared against a trained threshold value in order to determine if a target is present. If these values are greater than the threshold, then it corresponds to a detection. The MSD is the best detection metric when the noise covariance structure and scaling value are known and the CFAR metric is the optimal discriminator for when the covariance structure is known but the scaling can change.

7.1.2 Application to EMI Data

In order for this detection theory to be used in the new framework, it is useful to point out that the Frobenius norm of a matrix is equivalent to reshaping the matrix into a vector and

taking the ℓ_2 norm. This allows (7.2) to be rewritten as

$$\text{MSD)} \quad \gamma = \|\mathbf{Z}_1\|_F^2 \tag{7.3a}$$

$$\text{CFAR)} \quad \gamma = \frac{\|\mathbf{Z}_1\|_F^2}{\|\mathbf{Z}_2\|_F^2} \tag{7.3b}$$

where $\mathbf{Z}_1$ is a matrix containing the signal and noise, and $\mathbf{Z}_2$ is a matrix containing only noise. With the new detection metrics of (7.3), it becomes clear how UMPI detection is performed in the new framework. By defining the signal matrix and a noise matrix, (7.3) can be directly applied to create either CFAR or MSD detection values.

It is possible to directly use the data blocks of the EMI data shown in (6.11) to define a variety of signal and noise matrices. There exist four possible data blocks to use for $\mathbf{Z}_1$. These MSD detectors will be defined as

$$\boxed{\begin{aligned} \gamma_{\mathbf{S}} &= \|\mathbf{M}_{\mathbf{S}}\|_F^2 && (7.4a)\\ \gamma_{\mathbf{G}} &= \|\mathbf{M}_{\mathbf{GG}}^{\bar{\mathbf{R}}\mathbf{S}}\|_F^2 && (7.4b)\\ \gamma_{\mathbf{\Sigma S}} &= \|\mathbf{\Sigma}_{\mathbf{S}}^{\mathbf{M_S}}\|_F^2 && (7.4c)\\ \gamma_{\mathbf{\Sigma G}} &= \|\mathbf{M}_{\mathbf{GG}}^{\bar{\mathbf{R}}\mathbf{S}}\mathbf{P}_{\mathbf{S}}^T\|_F^2 && (7.4d) \end{aligned}}$$

where $\gamma_{\mathbf{G}}$ uses the signal that overlaps with the soil response, $\gamma_{\mathbf{S}}$ uses the isolated signal data block, $\gamma_{\mathbf{\Sigma S}}$ uses the signal power after it has been further condensed into the singular values, and $\gamma_{\mathbf{\Sigma G}}$ uses the signal that has been condensed in the soil response from the SVD information.

Each MSD has one or more corresponding CFAR metrics. The MSD metrics from the soil data blocks have fewer CFAR options. This is because there are limited data blocks to use that contain both the noise and soil response necessary to properly form the CFAR

metric. The $\gamma_{\mathbf{G}}$ metric only has one corresponding CFAR metric that is defined as

$$\boxed{\gamma_{\mathcal{E}}^{\mathbf{G}} = \frac{\|\mathbf{M}_{\mathbf{GG}}^{\bar{\mathbf{R}}\mathbf{S}}\|_F^2}{\|\mathbf{M}_{\mathbf{GG}}^{\bar{\mathbf{R}}\mathcal{E}}\|_F^2}} \tag{7.5}$$

where $\mathbf{M}_{\mathbf{GG}}^{\bar{\mathbf{R}}\mathcal{E}}$ is used as the noise subspace. The $\gamma_{\mathbf{\Sigma G}}$ has three possible methods for creating a noise matrix. These options create the three CFAR metrics

$$\boxed{\begin{aligned}
\gamma_{\mathcal{E}}^{\mathbf{\Sigma G}} &= \frac{\|\mathbf{M}_{\mathbf{GG}}^{\bar{\mathbf{R}}\mathbf{S}}\mathbf{P}_{\mathbf{S}}^{T}\|_F^2}{\|\mathbf{M}_{\mathbf{GG}}^{\bar{\mathbf{R}}\mathcal{E}}\|_F^2} && \text{(7.6a)}\\
\gamma_{\mathbf{\Sigma}\mathcal{E}}^{\mathbf{\Sigma G}} &= \frac{\|\mathbf{M}_{\mathbf{GG}}^{\bar{\mathbf{R}}\mathbf{S}}\mathbf{P}_{\mathbf{S}}^{T}\|_F^2}{\|\mathbf{M}_{\mathbf{GG}}^{\bar{\mathbf{R}}\mathbf{S}}\mathbf{P}_{\mathbf{S}}^{\perp T}\|_F^2} && \text{(7.6b)}\\
\gamma_{\mathbf{\Pi}}^{\mathbf{\Sigma G}} &= \frac{\|\mathbf{M}_{\mathbf{GG}}^{\bar{\mathbf{R}}\mathbf{S}}\mathbf{P}_{\mathbf{S}}^{T}\|_F^2}{\|\mathbf{M}_{\mathbf{GG}}^{\bar{\mathbf{R}}\mathcal{E}}\|_F^2 + \|\mathbf{M}_{\mathbf{GG}}^{\bar{\mathbf{R}}\mathbf{S}}\mathbf{P}_{\mathbf{S}}^{\perp T}\|_F^2} && \text{(7.6c)}
\end{aligned}}$$

where the soil and noise blocks are found by using the data block ($\mathbf{M}_{\mathbf{GG}}^{\bar{\mathbf{R}}\mathcal{E}}$), the signal that does not align with the target's spatial response from the SVD ($\mathbf{M}_{\mathbf{GG}}^{\bar{\mathbf{R}}\mathbf{S}}\mathbf{P}_{\mathbf{S}}^{\perp T}$), or a combination of the two soil plus noise blocks.

It is possible to build CFAR detectors from the $\gamma_{\mathbf{S}}$ and $\gamma_{\mathbf{\Sigma S}}$ MSD detectors as well. Both of these metrics are expected to only have the noise term. Based on the data blocks created in (6.11), there are many more options for creating $\mathbf{Z}_2$ for the CFAR detector. This is because $\mathbf{M}_{\bar{\mathbf{G}}\mathcal{E}}^{\bar{\mathbf{R}}\mathcal{E}}$, $\mathbf{M}_{\bar{\mathbf{G}}\mathbf{S}}^{\bar{\mathbf{R}}\mathcal{E}}$, and $\mathbf{M}_{\bar{\mathbf{G}}\mathcal{E}}^{\bar{\mathbf{R}}\mathbf{S}}$ are all possible options. It is also possible to use any combination of these noise blocks for $\mathbf{Z}_2$. This effort will limit the combinatorial options to focus on using each noise block separately and then a single test case using all of the

options. The CFAR detectors are defined as

$$\gamma_{\mathcal{E}}^{\mathbf{S}} = \frac{\|\mathbf{M}_{\bar{\mathbf{G}}\mathbf{S}}^{\bar{\mathbf{R}}\mathbf{S}}\|_F^2}{\|\mathbf{M}_{\bar{\mathbf{G}}\mathcal{E}}^{\bar{\mathbf{R}}\mathcal{E}}\|_F^2} \tag{7.7a}$$

$$\gamma_{\mathbf{G}\mathcal{E}}^{\mathbf{S}} = \frac{\|\mathbf{M}_{\bar{\mathbf{G}}\mathbf{S}}^{\bar{\mathbf{R}}\mathbf{S}}\|_F^2}{\|\mathbf{M}_{\bar{\mathbf{G}}\mathcal{E}}^{\bar{\mathbf{R}}\mathbf{S}}\|_F^2} \tag{7.7b}$$

$$\gamma_{\mathbf{R}\mathcal{E}}^{\mathbf{S}} = \frac{\|\mathbf{M}_{\bar{\mathbf{G}}\mathbf{S}}^{\bar{\mathbf{R}}\mathbf{S}}\|_F^2}{\|\mathbf{M}_{\bar{\mathbf{G}}\mathbf{S}}^{\bar{\mathbf{R}}\mathcal{E}}\|_F^2} \tag{7.7c}$$

$$\gamma_{\mathbf{\Pi}}^{\mathbf{S}} = \frac{\|\mathbf{M}_{\bar{\mathbf{G}}\mathbf{S}}^{\bar{\mathbf{R}}\mathbf{S}}\|_F^2}{\|\mathbf{M}_{\bar{\mathbf{G}}\mathcal{E}}^{\bar{\mathbf{R}}\mathcal{E}}\|_F^2 + \|\mathbf{M}_{\bar{\mathbf{G}}\mathcal{E}}^{\bar{\mathbf{R}}\mathbf{S}}\|_F^2 + \|\mathbf{M}_{\bar{\mathbf{G}}\mathbf{S}}^{\bar{\mathbf{R}}\mathcal{E}}\|_F^2} \tag{7.7d}$$

for the $\gamma_{\mathbf{S}}$ metric. The same subset of CFAR detectors can be used for $\gamma_{\mathbf{\Sigma S}}$ to create

$$\gamma_{\mathcal{E}}^{\mathbf{\Sigma S}} = \frac{\|\mathbf{\Sigma}_{\mathbf{S}}^{\mathbf{M_S}}\|_F^2}{\|\mathbf{M}_{\bar{\mathbf{G}}\mathcal{E}}^{\bar{\mathbf{R}}\mathcal{E}}\|_F^2} \tag{7.8a}$$

$$\gamma_{\mathbf{G}\mathcal{E}}^{\mathbf{\Sigma S}} = \frac{\|\mathbf{\Sigma}_{\mathbf{S}}^{\mathbf{M_S}}\|_F^2}{\|\mathbf{M}_{\bar{\mathbf{G}}\mathcal{E}}^{\bar{\mathbf{R}}\mathbf{S}}\|_F^2} \tag{7.8b}$$

$$\gamma_{\mathbf{R}\mathcal{E}}^{\mathbf{\Sigma S}} = \frac{\|\mathbf{\Sigma}_{\mathbf{S}}^{\mathbf{M_S}}\|_F^2}{\|\mathbf{M}_{\bar{\mathbf{G}}\mathbf{S}}^{\bar{\mathbf{R}}\mathcal{E}}\|_F^2} \tag{7.8c}$$

$$\gamma_{\mathbf{\Sigma}\mathcal{E}}^{\mathbf{\Sigma S}} = \frac{\|\mathbf{\Sigma}_{\mathbf{S}}^{\mathbf{M_S}}\|_F^2}{\|\mathbf{\Sigma}_{\mathcal{E}}^{\mathbf{M_S}}\|_F^2} \tag{7.8d}$$

$$\gamma_{\mathbf{\Pi}}^{\mathbf{\Sigma S}} = \frac{\|\mathbf{\Sigma}_{\mathbf{S}}^{\mathbf{M_S}}\|_F^2}{\|\mathbf{M}_{\bar{\mathbf{G}}\mathcal{E}}^{\bar{\mathbf{R}}\mathcal{E}}\|_F^2 + \|\mathbf{M}_{\bar{\mathbf{G}}\mathcal{E}}^{\bar{\mathbf{R}}\mathbf{S}}\|_F^2 + \|\mathbf{M}_{\bar{\mathbf{G}}\mathbf{S}}^{\bar{\mathbf{R}}\mathcal{E}}\|_F^2 + \|\mathbf{\Sigma}_{\mathcal{E}}^{\mathbf{M_S}}\|_F^2} \tag{7.8e}$$

where the extra noise block $\mathbf{\Sigma}_{\mathcal{E}}^{\mathbf{M_S}}$ is available from the noise singular values.

7.1.3 Results on EMI Data

All of the detection metrics introduced above have been tested against the lane data collected by the Georgia Tech frequency-domain EMI system[28]. In all of the lane plots, filled in circles represent a location where a target was buried for the sensor to measure and empty diamonds are locations where no target is present. The MSD detection metrics are shown in Fig. 7.1. The CFAR detection metrics for $\gamma_{\mathbf{G}}$ are shown in Fig. 7.2. The CFAR

detection metrics for $\gamma_{\mathbf{S}}$ are shown in Fig. 7.3. The CFAR detection metrics for $\gamma_{\mathbf{\Sigma G}}$ are shown in Fig. 7.4. The CFAR detection metrics for $\gamma_{\mathbf{\Sigma S}}$ are shown in Fig. 7.5.

In order to illustrate how well these detection metrics performed, receiver operating characteristic (ROC) curves have been created from the lane data to quantify the detection performance. The area under the ROC curve is shown in the legend to provide a single number that can be used to compare detection performance. An area of one under the ROC curve corresponds to perfect detection, so the larger the area the better the detection performance results. The MSD detection ROC curves are shown in Fig. 7.6. Notice that $\gamma_{\mathbf{S}}$ and $\gamma_{\mathbf{\Sigma S}}$ both are nearly equivalent and provide improved detection performance over $\mathbf{M}_{\mathbf{GG}}^{\bar{\mathbf{R}}\mathbf{S}}$ based detection methods. This is predictable because $\mathbf{M}_{\mathbf{\bar{G}S}}^{\bar{\mathbf{R}}\mathbf{S}}$ was shown to have better SINR properties in Chap. 6.

The ROC curves for the CFAR metrics are shown in Fig. 7.7. Comparing the MSD ROC curves to the respective CFAR curves is enlightening. The MSD curves outperform the CFAR curves in almost all cases. The theory states that MSD is the optimal detection if the noise is consistent, but CFAR will be optimal if the noise power varies and is unknown. The lane data that is measured is from the same time and location and the noise appears to be very consistent across measurements. This causes the MSD to outperform CFAR in a number of metrics; however, the CFAR metric provides a consistent threshold that enables it to more optimally tune the detection threshold across multiple measurements and data sets. This is expected to produce improved results from CFAR metrics for EMI devices in practice when the detection is performed in real-time and the threshold must be tuned beforehand. It is a good sign that transitioning from the MSD to CFAR detector has minimal impact on the detection performance. It is also noteworthy that the CFAR detection metrics using $\mathbf{M}_{\mathbf{GG}}^{\bar{\mathbf{R}}\mathbf{S}}$ are much closer and can even outperform the MSD detectors. This indicates that although the noise floor is consistent across this dataset, the soil varies slightly within the same dataset.

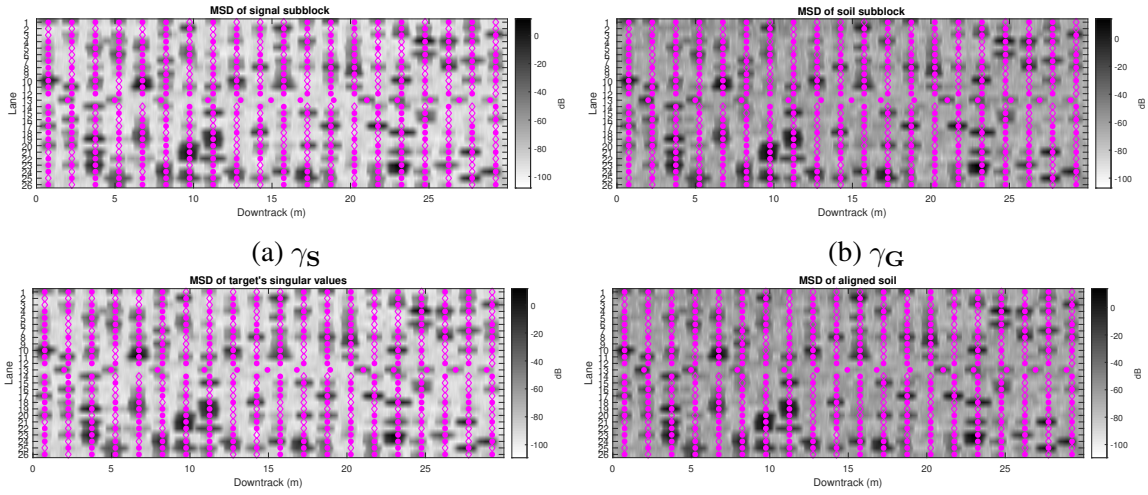

(a) $\gamma_{\mathbf{S}}$ (b) $\gamma_{\mathbf{G}}$

(c) $\gamma_{\mathbf{\Sigma S}}$ (d) $\gamma_{\mathbf{\Sigma G}}$

Figure 7.1: MSD metrics for data collected with the GT EMI system.

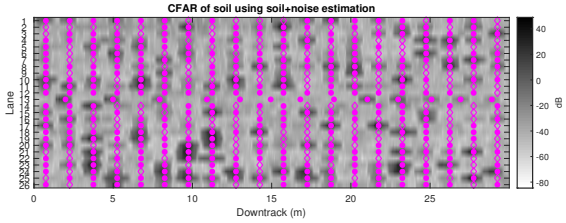

(a) $\gamma_{\mathcal{E}}^{\mathbf{G}}$

Figure 7.2: CFAR metrics from the $\gamma_{\mathbf{G}}$ MSD metric for data collected with the GT EMI system.

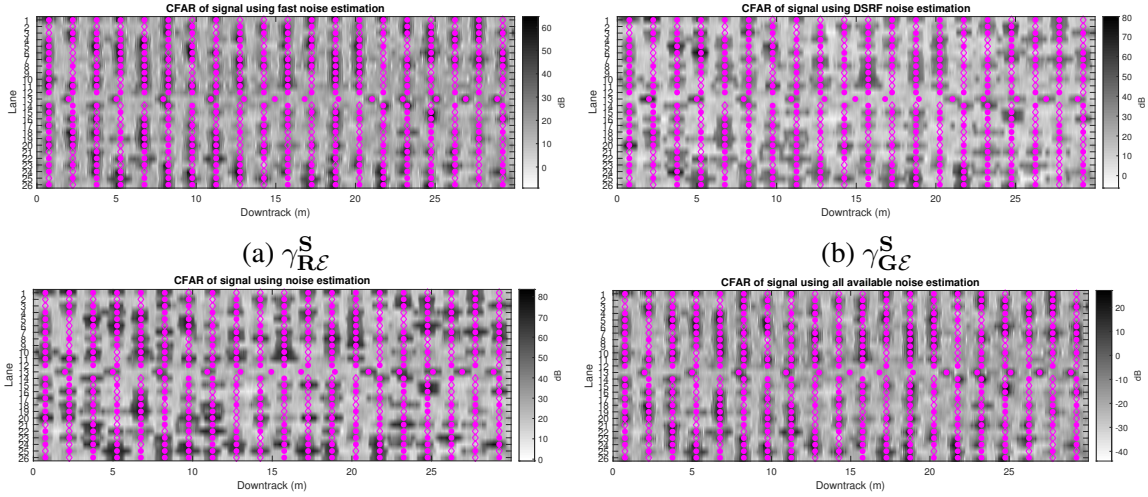

(a) $\gamma_{\mathbf{R}\mathcal{E}}^{\mathbf{S}}$ (b) $\gamma_{\mathbf{G}\mathcal{E}}^{\mathbf{S}}$

(c) $\gamma_{\mathcal{E}}^{\mathbf{S}}$ (d) $\gamma_{\mathbf{\Pi}}^{\mathbf{S}}$

Figure 7.3: CFAR metrics from the $\gamma_{\mathbf{S}}$ MSD metric for data collected with the GT EMI system.

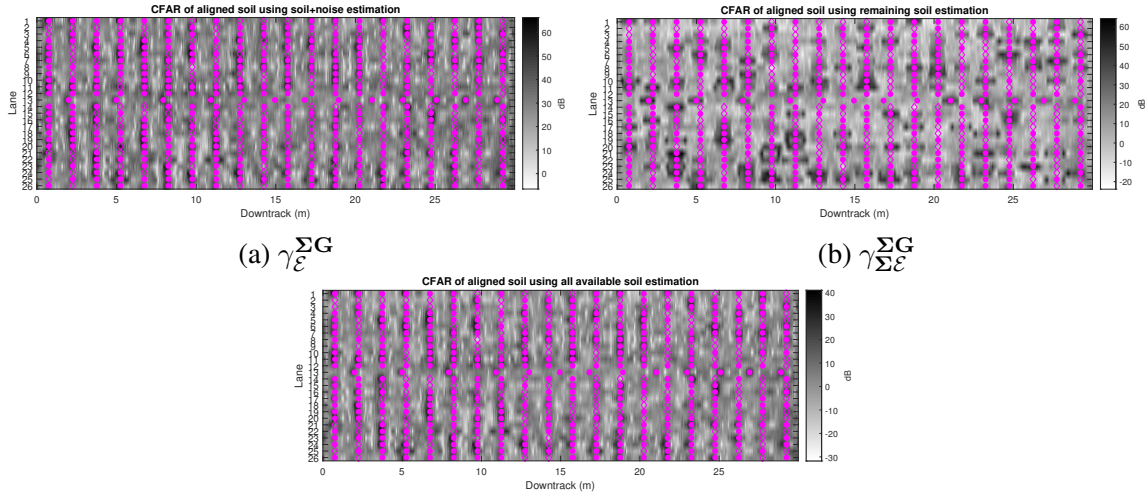

(a) $\gamma_{\mathcal{E}}^{\mathbf{\Sigma G}}$ (b) $\gamma_{\mathbf{\Sigma}\mathcal{E}}^{\mathbf{\Sigma G}}$

(c) $\gamma_{\mathbf{\Pi}}^{\mathbf{\Sigma G}}$

Figure 7.4: CFAR metrics from the $\gamma_{\mathbf{\Sigma G}}$ MSD metric for data collected with the GT EMI system.

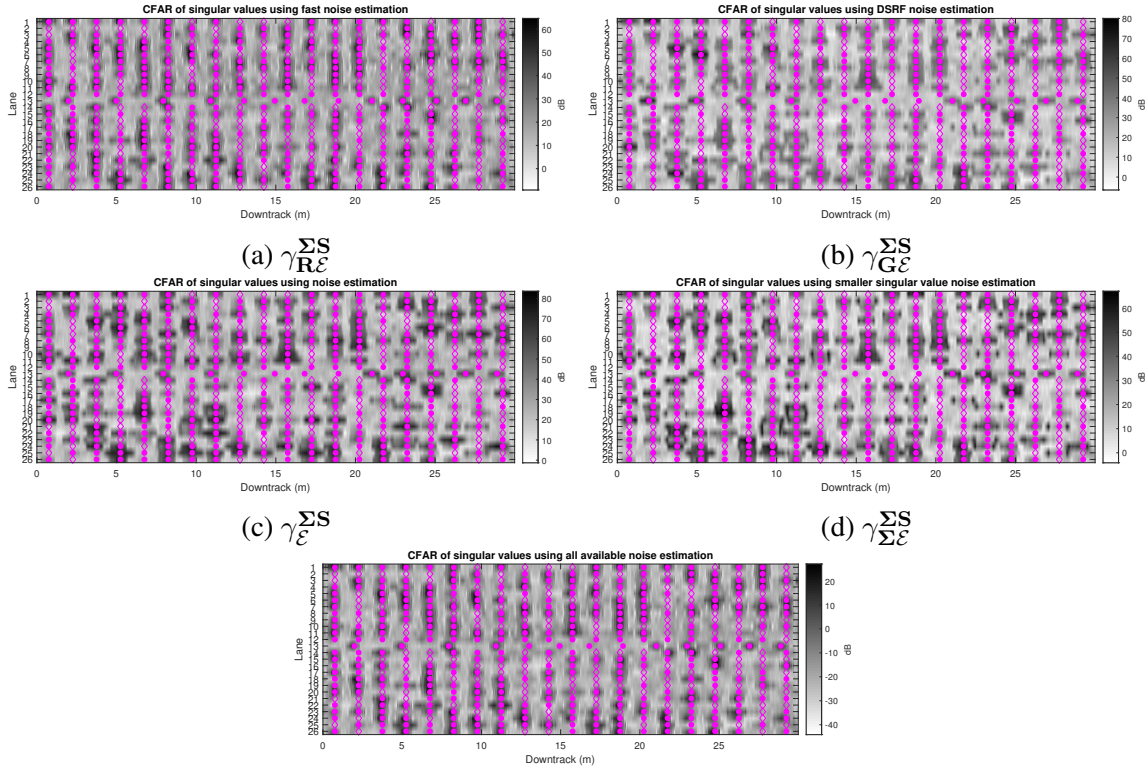

(a) $\gamma_{\mathbf{R}\mathcal{E}}^{\mathbf{\Sigma S}}$ (b) $\gamma_{\mathbf{G}\mathcal{E}}^{\mathbf{\Sigma S}}$

(c) $\gamma_{\mathcal{E}}^{\mathbf{\Sigma S}}$ (d) $\gamma_{\mathbf{\Sigma}\mathcal{E}}^{\mathbf{\Sigma S}}$

(e) $\gamma_{\mathbf{\Pi}}^{\mathbf{\Sigma S}}$

Figure 7.5: CFAR metrics from the $\gamma_{\mathbf{\Sigma S}}$ MSD metric for data collected with the GT EMI system.

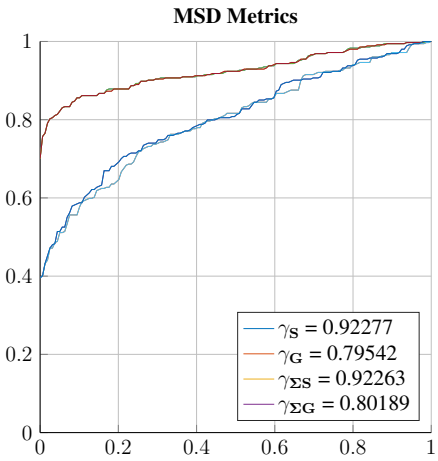

Figure 7.6: ROC curves for MSD detection on data collected with the GT EMI system.

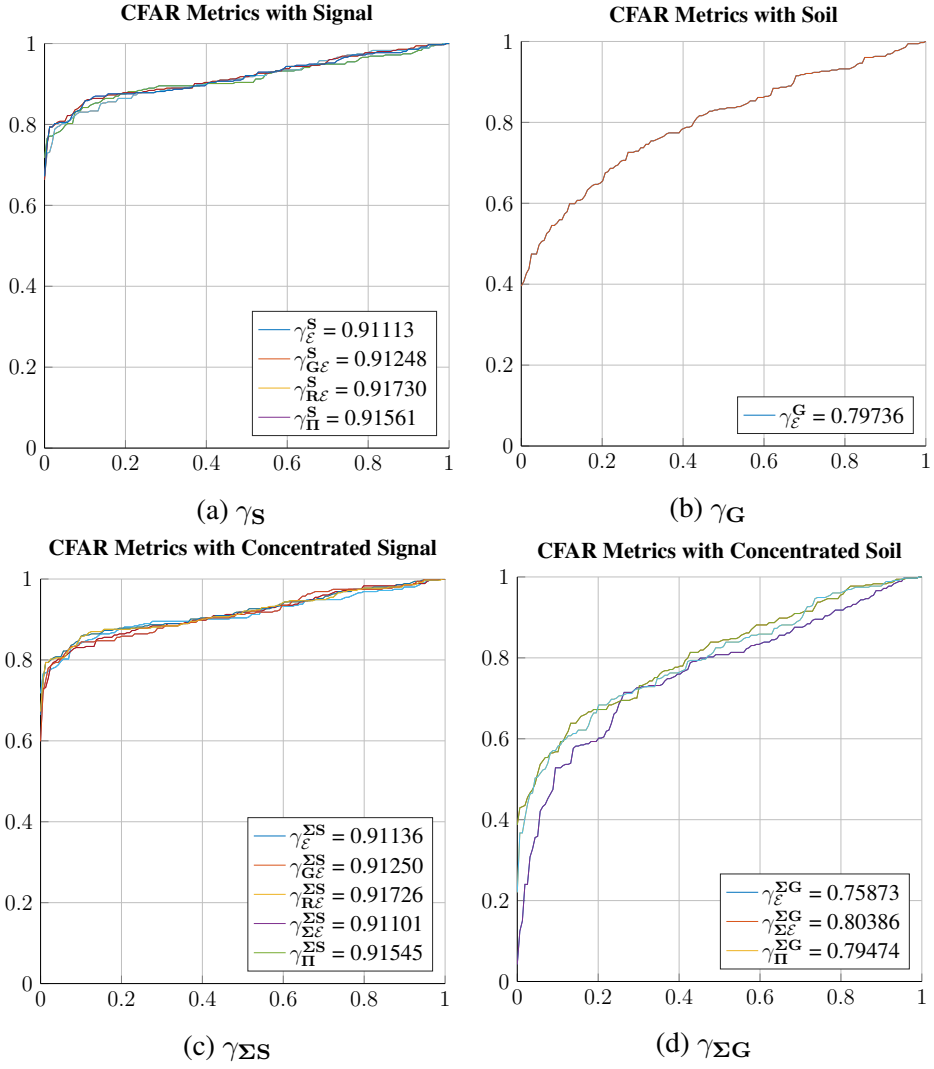

(a) $\gamma_{\mathbf{S}}$ (b) $\gamma_{\mathbf{G}}$

(c) $\gamma_{\mathbf{\Sigma S}}$ (d) $\gamma_{\mathbf{\Sigma G}}$

Figure 7.7: ROC curves for CFAR detection on data collected with the GT EMI system.

7.2 Joint Detection Strategies

The above detection methods work well, but they are not able to use all of the information in one detection metric. Ideally the detection would use both the signal power isolated from the soil and the signal power mixed with the soil response to make a decision. This will allow it to detect targets that have a soil like response (such as a sphere made out of led) while also exploiting other targets' power that is separable from the soil.

7.2.1 Examining EMI Detection Model

For this to optimally work, the detection metric must adaptively weight the importance of the two subblocks. This can be accomplished by taking a look at the models for the subblocks. It is possible to define a model for a single element of $\mathbf{M}_{\bar{\mathbf{G}}\mathbf{S}}^{\bar{\mathbf{R}}\mathbf{S}}$ as

$$\left[\mathbf{M}_{\bar{\mathbf{G}}\mathbf{S}}^{\bar{\mathbf{R}}\mathbf{S}}\right]_{i,j} = \mu_{\mathbf{S}} s + \epsilon \tag{7.9}$$

as was shown in (6.19) where $\epsilon \sim \mathcal{N}(0, \sigma_\epsilon^2)$ has the same distribution but the signal is now $\mu_{\mathbf{S}}$ stronger due to the preprocessing. Likewise, a model can be defined for a single element of $\mathbf{M}_{\mathbf{G}\mathbf{G}}^{\bar{\mathbf{R}}\mathbf{S}}$ as

$$\left[\mathbf{M}_{\mathbf{G}\mathbf{G}}^{\bar{\mathbf{R}}\mathbf{S}}\right]_{i,j} = \mu_{\mathbf{G}} s + g + \epsilon \tag{7.10}$$

as was shown in (6.30) where ϵ has the same distribution, the signal is now $\mu_{\mathbf{G}}$ stronger due to the preprocessing, and $g \sim \mathcal{N}(0, \sigma_g^2)$ because the preprocessing has removed the mean of the soil response but the variance has remained due to the projection matrices aligning with $\mathbf{\Psi}$.

A deterministic model can be used based on these models. By assuming that s, $\mu_{\mathbf{S}}$, and

$\mu_{\mathbf{G}}$ are fixed but unknown values, it is possible to define the signal vector as

$$\mathbf{z_{JS}} = \begin{bmatrix} \text{vec}\left\{\mathbf{M}_{\bar{\mathbf{G}}\mathbf{S}}^{\bar{\mathbf{R}}\mathbf{S}}\right\} \\ \text{vec}\left\{\mathbf{M}_{\mathbf{GG}}^{\bar{\mathbf{R}}\mathbf{S}}\right\} \end{bmatrix} \tag{7.11a}$$

$$\mathbf{z_{J\Sigma}} = \begin{bmatrix} \text{vec}\left\{\mathbf{\Sigma}_{\mathbf{S}}^{\mathbf{M_S}}\right\} \\ \text{vec}\left\{\mathbf{M}_{\mathbf{GG}}^{\bar{\mathbf{R}}\mathbf{S}}\mathbf{P}_{\mathbf{S}}^{T}\right\} \end{bmatrix} \tag{7.11b}$$

respectively for the subblocks and the low-rank projected subblocks, where the matrices have been reshaped into a single large vector. The covariance matrix for the detection vector is

$$\boldsymbol{R}_{\mathbf{G}\mathcal{E}} = E\left[\mathbf{z}\mathbf{z}^T\right] = \begin{bmatrix} \sigma_\epsilon^2 \boldsymbol{I} & 0 \\ 0 & \sigma_{g\epsilon}^2 \boldsymbol{I} \end{bmatrix} \tag{7.12}$$

where $\sigma_{g\epsilon}^2 = \sigma_g^2 + \sigma_\epsilon^2$ and the size of the identity matrices correspond to the number of elements in the respective subblocks of $\mathbf{z_{JS}}$ and $\mathbf{z_{J\Sigma}}$. The explicit covariance matrix of (7.12) is obtained when the noise and soil response are assumed independent, each noise sample from the original measurement $\mathbf{M}$ is assumed independent, and the soil response terms ξ_1 and ξ_2 are assumed independent of each other and independent over position (Δp). The first two independence assumptions are expected to be valid. The soil independence is a simplifying assumption. In reality, it is unclear if ξ_1 and ξ_2 are independent at a single location, and there is no expectation for the soil to be independent across position.[1]

Using this model, the covariance is known exactly. When there is no unknown scalar on the covariance, the MSD is optimal[31]. These detection metrics can be defined as

$$\gamma_{\mathbf{JS}} = \mathbf{z}_{\mathbf{JS}}^T \boldsymbol{R}_{\mathbf{G}\mathcal{E}}^{-1} \mathbf{z}_{\mathbf{JS}} = \frac{1}{\sigma_\epsilon^2}\|\mathbf{M_S}\|_F + \frac{1}{\sigma_{g\epsilon}^2}\|\mathbf{M}_{\mathbf{GG}}^{\bar{\mathbf{R}}\mathbf{S}}\|_F \tag{7.13a}$$

$$\gamma_{\mathbf{J\Sigma}} = \mathbf{z}_{\mathbf{J\Sigma}}^T \boldsymbol{R}_{\mathbf{G}\mathcal{E}}^{-1} \mathbf{z}_{\mathbf{J\Sigma}} = \frac{1}{\sigma_\epsilon^2}\|\mathbf{\Sigma}_{\mathbf{S}}^{\mathbf{M_S}}\|_F + \frac{1}{\sigma_{g\epsilon}^2}\|\mathbf{M}_{\mathbf{GG}}^{\bar{\mathbf{R}}\mathbf{S}}\mathbf{P}_{\mathbf{S}}^T\|_F \tag{7.13b}$$

[1] Incorporating this dependence across position and tracking it through the preprocessing may be able to provide improved results in the future.

Subblock of Interest	Best CFAR Metric	Variance Subblock
$\mathbf{M}_{\mathbf{GS}}^{\bar{\mathbf{R}}\mathbf{S}}$	$\gamma_{\mathbf{R}\mathcal{E}}^{\mathbf{S}}$	$\mathbf{M}_{\mathbf{GS}}^{\bar{\mathbf{R}}\mathcal{E}}$
$\mathbf{M}_{\mathbf{GG}}^{\bar{\mathbf{R}}\mathbf{S}}$	$\gamma_{\mathcal{E}}^{\mathbf{G}}$	$\mathbf{M}_{\mathbf{GG}}^{\bar{\mathbf{R}}\mathcal{E}}$
$\mathbf{\Sigma}_{\mathbf{S}}^{\mathbf{M_S}}$	$\gamma_{\mathbf{R}\mathcal{E}}^{\mathbf{\Sigma S}}$	$\mathbf{M}_{\mathbf{GS}}^{\bar{\mathbf{R}}\mathcal{E}}$
$\mathbf{M}_{\mathbf{GG}}^{\bar{\mathbf{R}}\mathbf{S}}\mathbf{P}_{\mathbf{S}}^{T}$	$\gamma_{\mathbf{\Sigma}\mathcal{E}}^{\mathbf{\Sigma G}}$	$\mathbf{M}_{\mathbf{GG}}^{\bar{\mathbf{R}}\mathbf{S}}\mathbf{P}_{\mathbf{S}}^{\perp T}$

Table 7.1: Best variance estimate subblocks used for the joint detection based on the CFAR results.

where they are a weighted sum of the Frobenius norms of the subblocks. The weights correspond to the noise variances σ_ϵ^2 and $\sigma_{g\epsilon}^2$. Fortunately, the noise subblocks can be used to estimate these terms. Because all of the noise subblocks are zero mean with the corresponding variance on each term, the variance is estimated by finding the average of each term squared (e.g. $\sigma_\epsilon^2 \approx \frac{1}{\text{number}\left\{\mathbf{M}_{\mathbf{G}\mathcal{E}}^{\bar{\mathbf{R}}\mathcal{E}}\right\}}\|\mathbf{M}_{\mathbf{G}\mathcal{E}}^{\bar{\mathbf{R}}\mathcal{E}}\|_F^2$ and $\sigma_{g\epsilon}^2 \approx \frac{1}{\text{number}\left\{\mathbf{M}_{\mathbf{GG}}^{\bar{\mathbf{R}}\mathcal{E}}\right\}}\|\mathbf{M}_{\mathbf{GG}}^{\bar{\mathbf{R}}\mathcal{E}}\|_F^2$).

7.2.2 Results on EMI data

The joint detection metrics have been tested against the same lane data collected by the Georgia Tech frequency-domain EMI system as above[28]. For estimating the σ_ϵ^2 and $\sigma_{g\epsilon}^2$, there are multiple subblocks that can be used for each detection method. Instead of using a more exhaustive test for the joint detection, the best performing subblocks were used from Sec. 7.1.3 to estimate the needed variances. From Fig. 7.7, the CFAR metric that performed best can be assumed to provide the best variance estimate. Using this assumption, Table 7.1 shows the subblocks that are selected to estimate the needed variances.

Using these joint detection methods, the results on the lane data are shown in Fig. 7.8. The ROC curves are in Fig. 7.9. Notice that the ROC curves in Fig. 7.9 are minimally impacted from combining the $\mathbf{M}_{\mathbf{GS}}^{\bar{\mathbf{R}}\mathbf{S}}$ and $\mathbf{M}_{\mathbf{GG}}^{\bar{\mathbf{R}}\mathbf{S}}$ information. This is arguably because all of the targets in the lane data are successfully detected with just the $\mathbf{M}_{\mathbf{GS}}^{\bar{\mathbf{R}}\mathbf{S}}$ information and the joint detection method is successfully weighting the two metrics appropriately.

The joint detection metric allows the detection to automatically trade between the relevant information of the target appropriately while minimally impacting the detection results when only one metric is needed.

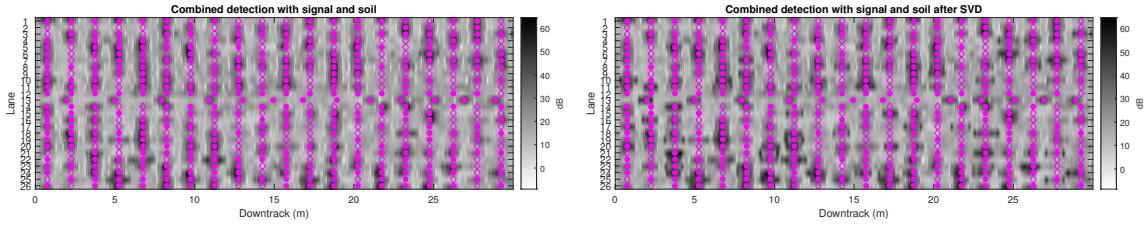

(a) $\gamma_{\mathbf{JS}}$ (b) $\gamma_{\mathbf{J\Sigma}}$

Figure 7.8: Joint detection metrics for data collected with the GT EMI system.

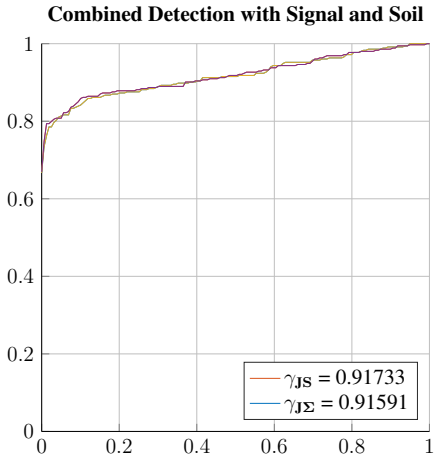

Figure 7.9: ROC curves for joint detection on data collected with the GT EMI system.

CHAPTER 8

RANK ESTIMATION

Model-order estimation is a well-studied problem within signal processing. The need to estimate the number of terms required arises in a variety of problems including estimating the number of signals arriving at an array, the number of sinusoidal components in a noisy measurement, and the size of an autoregressive moving average model. There are a variety of techniques used to solve these problems [33].

Within the low-rank framework for EMI data, model-order estimation is used to identify the rank of the measurement matrix in noise. Once the rank is obtained, it can be used for two primary purposes. First, it can be used to determine if the rank is above six which means that there is more than a point target present.[1] Determining the number of targets present in the measurements is clearly important as the low-rank framework currently assumes it is processing only a single target. It should be possible to expand it to multiple targets in the future, but this requires further research. Second, the estimated rank will indicate how many linearly independent tensors are present in the target. The rank of the target has clear indications to physical limitations on the target that could be used for target classification to a limited extent.

Knowing the rank can also be used to inform further processing. The SVD is limited to the largest singular values. Most of the further signal processing only uses knowledge of the maximum rank and limits the SVD matrices to $\mathbf{U_M} \in \Re^{M\times 6}$,$\mathbf{\Sigma_M} \in \Re^{6\times 6}$, and $\mathbf{V_M} \in \Re^{N\times 6}$; however, if the rank is estimate then the SVD can be limited to the appropriate $\mathbf{U_M} \in \Re^{M\times R}$,$\mathbf{\Sigma_M} \in \Re^{R\times R}$, and $\mathbf{V_M} \in \Re^{N\times R}$. Reducing the matrix sizes reduces the noise while maintaining all of the target information, so it is expected to provide improved processing performance. However, this is limited by how accurately the rank can

[1] Or to check for a rank over three to determine if a single ortho-point target assumption is invalid

be estimated. A better understanding of the applications of this trade-off should be studied. This chapter only focuses on demonstrating the ability to automatically estimate the target's rank.

8.1 Model Order Estimation

This chapter focuses on the information criterion methods for performing model-order estimation, specifically Akaike Information Criterion (AIC) and Bayesian Information Criterion (BIC) model-order selection [33]. This chapter specifically used the model-order estimation description from [34] for implementation.[2] The model-order estimation problem in literature is based on processing the eigenvalues of a covariance matrix, but the EMI singular values can be directly related as shown in (5.4). It is desirable to have a full-rank covariance matrix, so assuming that $M \leq N$,[3] then the eigenvalues of the covariance matrix $\mathbf{\Lambda_M}$ are equal to $\mathbf{\Sigma_\Lambda^2}$ given the relationship

$$\text{Eig}\{\mathbf{M}\mathbf{M}^T\} = \text{Eig}\{\mathbf{U_\Lambda}\mathbf{\Sigma_\Lambda}\mathbf{V_\Lambda^T}\mathbf{V_\Lambda}\mathbf{\Sigma_\Lambda}\mathbf{U_\Lambda^T}\} = \mathbf{U_\Lambda}\mathbf{\Sigma_\Lambda^2}\mathbf{U_\Lambda^T} \tag{8.1}$$

where $\mathbf{U_\Lambda}$, $\mathbf{\Sigma_\Lambda}$, and $\mathbf{V_\Lambda}$ are the original SVD matrices of the measurements before truncation.

The information criterion methods are based on combining the maximum likelihood estimator with an Occam's razor term that prefers simpler models over more complicated models. To apply these techniques to EMI data, first the loglikelihood term must be defined. For the rank of a matrix using the singular values, the loglikelihood is written as

$$\mathcal{L}\left\{\mathbf{\Lambda_M}\right\} = N(M-R)\ln\left[\frac{\left(\prod_{i=R+1}^{M}\sigma_{\mathbf{M}i}^2\right)^{\frac{1}{M-R}}}{\frac{1}{M-R}\sum_{i=R+1}^{M}\sigma_{\mathbf{M}i}^2}\right] \tag{8.2}$$

where $\sigma_{\mathbf{M}}$ are the singular values of $\mathbf{M}$ in descending order and the loglikelihood is the

[2] [34] uses the name minimum description length, but the algorithm is equivalent to BIC.

[3] If $N < M$, then $\mathbf{M}^T\mathbf{M}$ can be used and only the dimensions need to be adjusted in the calculations.

scaled ratio of the product of extra singular values divided by the sum of extra singular values. Using this loglikelihood, the difference in AIC and BIC are the Occum's razor terms

$$\text{AIC} = -\mathcal{L}\left\{\mathbf{\Lambda_M}\right\} + R(2M - R + 1) \tag{8.3a}$$

$$\text{BIC} = -\mathcal{L}\left\{\mathbf{\Lambda_M}\right\} + \frac{1}{2}R(2M - R + 1)\ln(N) \tag{8.3b}$$

that enforce the simplicity of the model, where BIC has a $1/2\ln(N)$ stronger term. The optimal model order from each of these metrics is the rank that produces the smallest value. In general, AIC predicts a slightly larger rank [34] and BIC is expected to provide superior performance [33].

For simplicity, this derivation was shown for the full measurement matrix. In practice the SVD is only performed on the $\mathbf{M_S}$ matrix that is created from the preprocessing. Everything is directly transferable to $\mathbf{M_S}$, where the dimensions just need to be updated accordingly.

8.2 Simulated Results

Monte Carlo simulations were performed and the error of the rank-estimation techniques are shown in Fig. 8.1. The simulation created a random ortho-point target that had a random rank between one and three and a random number of relaxation frequencies between two and ten. The simulated targets were generated using the procedure described in Section 5.6 and preprocessing was applied to the resulting measurements as described in Ch. 6. The simulations used 100 random targets and each target was tested at every SNR.

Based on these results, it can be seen that BIC is superior for higher SNR targets. It can exactly detect the rank above 20dB SNR. However, BIC's performance degrades faster than AIC as the SNR decreases. Unfortunately, both algorithms struggle at 0dB and below. At 0dB, a blind guess of rank 2 would perform just as well if not better because the rank can only be in the set $\{1, 2, 3\}$ so it would have a maximum error of one.

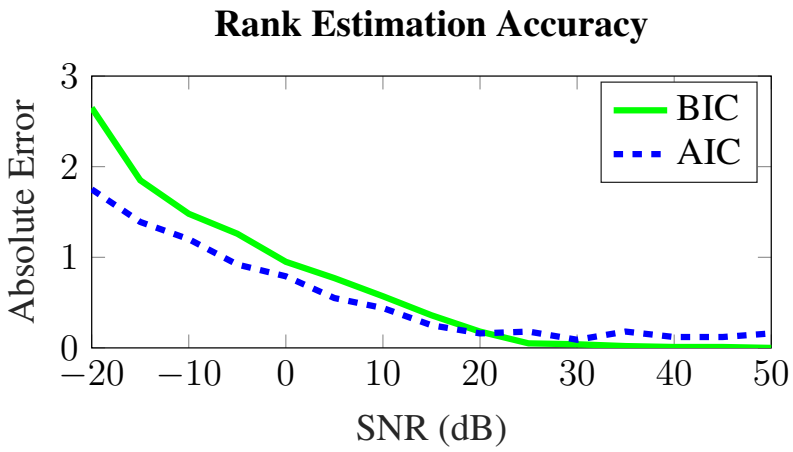

Figure 8.1: Monte Carlo simulations to determine rank estimation performance vs. SNR.

8.3 Reference Targets

To better understand these rank-estimation techniques, the methods were applied to the reference targets in Fig. 8.2. The reference targets were generated using the procedure described in Section 5.6 and preprocessing was applied to the resulting measurements as described in Ch. 6. These reference targets had an SNR of 50dB. The curves show both the AIC and BIC metrics across all possible rank options of $\mathbf{M_S}$. The preprocessing stage leaves 21 singular values, which allows the estimation of a rank in the range $[0, 20]$. As can be seen, the curves have very large metrics for ranks that are smaller than the target's rank because the model does not accurately represent the data. Once the true rank is reach, the sharp decline in the metric ends and in most cases there is a knee point into a gradual increase. The gradual increase at larger ranks is due to the Occum's razor term that limits the complexity of the model. As can be seen in the graphs, BIC's penalty term is stronger and thus increases the metric faster at larger ranks. The lowest value for each term is marked on the plots. This corresponds to the measured rank of the target from each method. Both methods perform well for the reference targets, as is expected at 50dB SNR. It is interesting to note that AIC over-estimates the rank of RT-02 and RT-08, but BIC correctly predicts the rank of all the reference targets. This agrees with the results in Fig. 8.1 where BIC

converges to zero error for high SNR faster than AIC. In both of these reference targets, AIC only over-estimates the rank by one and there does appear to be a knee point at the correct rank, but the lowest value was just past the knee point. It is plausible that a knee point algorithm could be created to improve the AIC results, but this seems unnecessary when BIC already performs well.

8.4 Research Opportunities

An opportunity for further research exists in applying these rank-estimation techniques to actual data obtained from an EMI sensor. Initial work was performed on measured lane data from the GT EMI frequency-domain sensor [28]. Unfortunately the rank-estimation failed and always predicted a rank much greater than six. It is the author's belief that this is because there is another colored noise source being measured that has been unaccounted for in the preprocessing. This aligns with the results in Fig. 8.3, where the singular values from all of the locations in the first lane were grouped and the median value was calculated to approximate the singular value of the noise response.[4] As can be seen, the smaller singular values do not flatten as expected for i.i.d. Gaussian noise. This invalidates the rank estimation assumptions, and it will potentially impact other processing stages that also assume i.i.d. Gaussian noise. Determining this extra colored noise source or creating an adaptive noise whitening method could further increase processing performance on EMI data.

[4]The median should treat targets as outliers because there are more noise measurements than target across the lane.

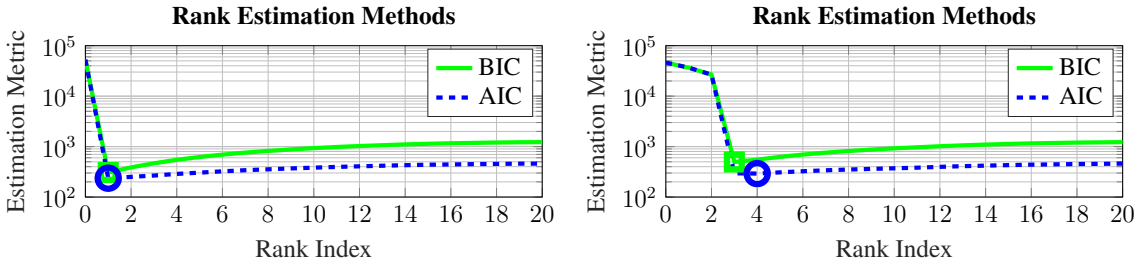

(a) Reference target 01

(b) Reference target 02

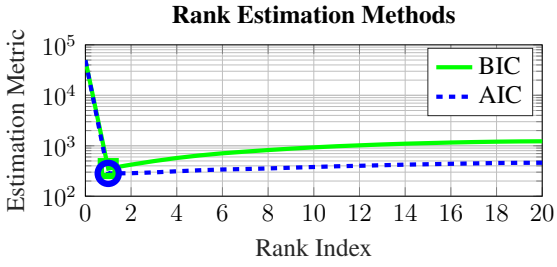

(c) Reference target 03

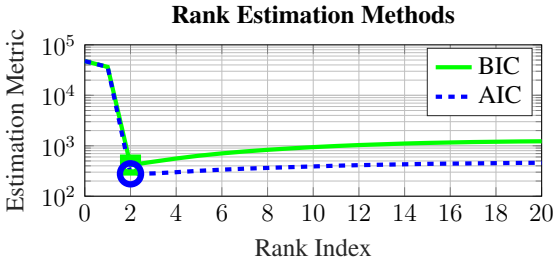

(d) Reference target 04

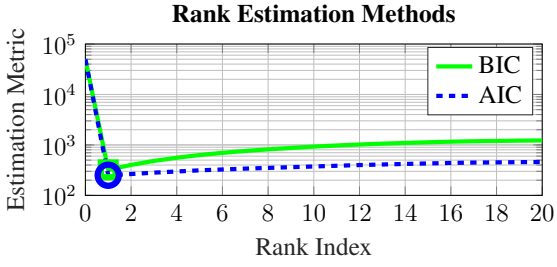

(e) Reference target 05

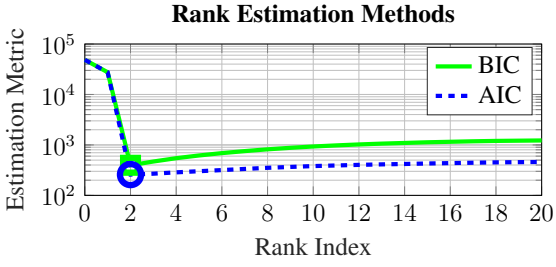

(f) Reference target 06

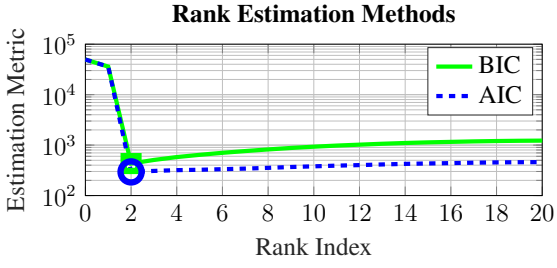

(g) Reference target 07

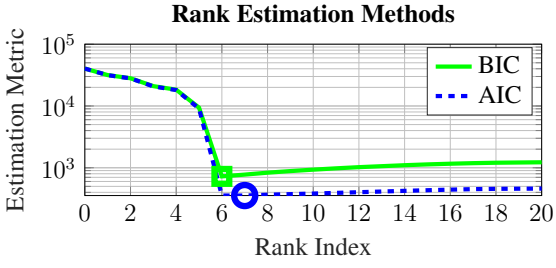

(h) Reference target 08

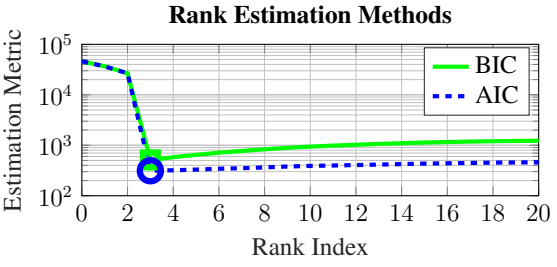

(i) Reference target 09

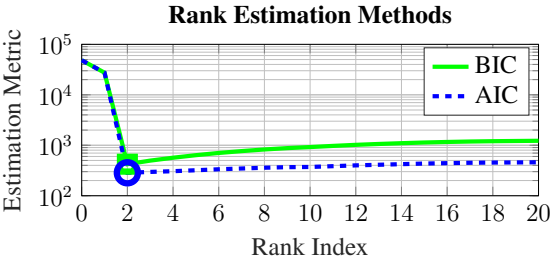

(j) Reference target 10

Figure 8.2: Rank estimation curves and predicted rank for reference targets at 50dB SNR.

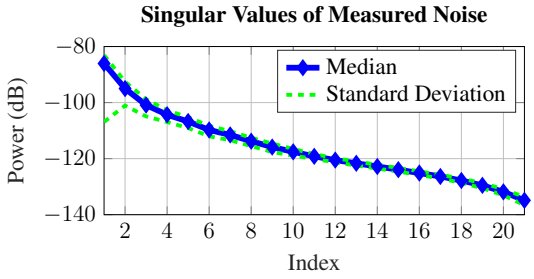

Figure 8.3: Singular values of the median noise response from data collected with the GT EMI sensor.

CHAPTER 9
RECOVERING THE DISCRETE SPECTRUM OF RELAXATION FREQUENCIES

The discrete spectrum of relaxation frequencies (DSRF) has been previously shown as a useful tool for EMI classification. This is because the relaxation frequencies of a target remain constant regardless of the target location or orientation. Such a feature encapsulates inherent information about the properties of the target and can allow it to be distinguished from other targets. Previous works have developed DSRF recovery from EMI data to perform target classification [10, 13, 5]. As it has been a useful tool for EMI classification previously, it is important to demonstrate that the low-rank model also enables DSRF extraction. It should be noted, that not only does the low-rank framework enable DSRF extraction, but it provides further insight and more information from the inversion process. Take RT-02 for an example; it was shown earlier that all of the target information can be illustrated as shown in Fig. 9.1 where the relaxations and their connections to specific orientations completely describe the targets *magnetic polarizability*. The objective of DSRF recovery has been to recover both the number of relaxations in the target and the relaxation frequencies. Essentially, this corresponds to finding all active relaxations ζ in a target and using this information for classification. For RT-02, the DSRF would ideally provide the three relaxation frequencies $(f_{2.7}, f_{3.7}, f_{4.7})$ and the power of each column vector associated with these frequencies.

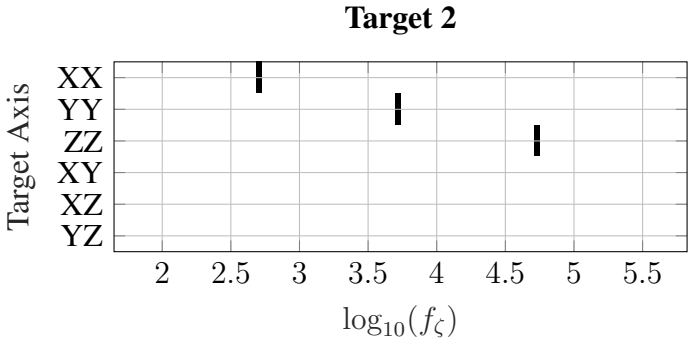

Figure 9.1: RT-02's relaxation frequency representation.

9.1 Defining the DSRF Problem

An EMI target has a physical model that determines the relationship between a relaxation frequency ζ and a measurement frequency ω.[1] This dependence can be defined as

$$\tilde{a}(\omega, \zeta) = \frac{1 - j\omega/\zeta_k}{1 + j\omega/\zeta_k} \tag{9.1}$$

when using the *allpass* model of (2.7) which will cause all of the components to have unit amplitude. It has been shown that this relationship can be used to create a sparse recovery problem by over-sampling the ζ components to create a dictionary $\tilde{\mathbf{A}}$ [10]. Typically $\boldsymbol{\zeta}$ is chosen as 100 equally logarithmically-spaced frequencies from just below the minimum operating frequency to just above the maximum operating frequency. The $\boldsymbol{\zeta}$ are then mapped to the measurements $\boldsymbol{\omega}$. With complex-valued data, the real and imaginary parts are separated as shown in (6.3) to create the final DSRF dictionary $\mathbf{A} \in \Re^{2M \times Z}$.

For a single location measurement, the problem can be stated as a direct ℓ_1 sparse recovery problem written as

$$\min_{\boldsymbol{x}} \|\mathbf{S}(\boldsymbol{\phi}, \Delta p) - \mathbf{A}\boldsymbol{x}\|_2^2 + \lambda \|\boldsymbol{x}\|_1. \tag{9.2}$$

[1] DSRF inversion has primarily been performed using frequency-domain sensors, but the process could be applied to time-domain data using (2.6)

The low-rank model indicates that the sparse recovery is applied to the left singular vectors of the measurements and must be extended to multiple measurements for targets that are greater than rank-one to create

$$\min_{\mathbf{C}_{\vec{\mathbf{W}}}} \|\mathbf{U}_{\mathbf{M}}\mathbf{\Sigma}_{\mathbf{M}} - \mathbf{A}\mathbf{C}_{\vec{\mathbf{W}}}\|_F^2 + \lambda\|\mathbf{C}_{\vec{\mathbf{W}}}^{\ell_2}\|_1 \tag{9.3}$$

which is the SSC problem shown before in (5.25).

For the low-rank framework, the singular vectors do not correspond directly to the original measured data. After the preprocessing, the measurement frequency dimension (and thus the left singular vectors) have been multiplied by the projection matrix $\mathbf{P}_{\bar{\mathbf{G}}\mathbf{S}}$ in the creation of $\mathbf{M}_{\mathbf{S}}$. This means that the sparse recovery method becomes

$$\min_{\mathbf{C}_{\vec{\mathbf{W}}}} \|\mathbf{U}_{\mathbf{M}}\mathbf{\Sigma}_{\mathbf{M}} - \mathbf{A}_{\boldsymbol{P}}\mathbf{C}_{\vec{\mathbf{W}}}\|_F^2 + \lambda\|\mathbf{C}_{\vec{\mathbf{W}}}^{\ell_2}\|_1 \tag{9.4}$$

where $\mathbf{A}_{\boldsymbol{P}} = \mathbf{P}_{\bar{\mathbf{G}}\mathbf{S}}\mathbf{A} \in \Re^{O\times Z}$ is the projected DSRF dictionary. Using the preprocessing, the estimated noise floor can also be used to inform λ if desired [35].

9.2 DSRF Inversion Challenges

Sparse recovery techniques have been used on a variety of applications with favorable results. The performance of these sparse recovery techniques is limited by the difficulty of the DSRF problem. The primary issue in the DSRF problem comes from the fact that the DSRF dictionary is highly correlated. This is shown in Fig. 9.2 where the correlation between each column vector of $\mathbf{A}$ with the others is shown. This $\mathbf{A}$ was designed for the GT EMI frequency-domain sensor that measures 21 frequencies from 300Hz to 90MHz and 100 relaxation frequencies were used. This creates the dictionary $\mathbf{A} \in \Re^{42\times 100}$. As can be seen in the correlation, many of the columns are highly similar which makes the inversion difficult.

It is useful to compare the DSRF inversion to a similar problem to understand the inher-

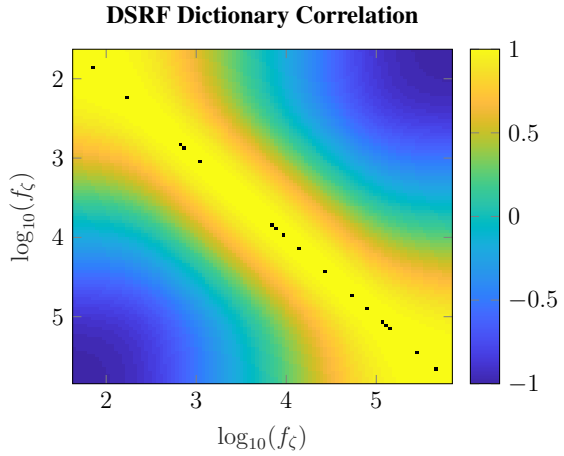

Figure 9.2: Dictionary correlation of the DSRF matrix $\mathbf{A} \in \Re^{42\times100}$.

ent difficulties of the model. The direction of arrival (DOA) for array processing is a well studied application for sparse recovery. To create a comparable reference, a DOA dictionary was created for for a uniform linear array (ULA) with 21 receivers using $\lambda/2$ spacing. The angular space was equally sampled into 100 possible directions. The resulting dictionary correlation is shown in Fig. 9.3. As can be seen, the columns are much less correlated than the DSRF matrix.

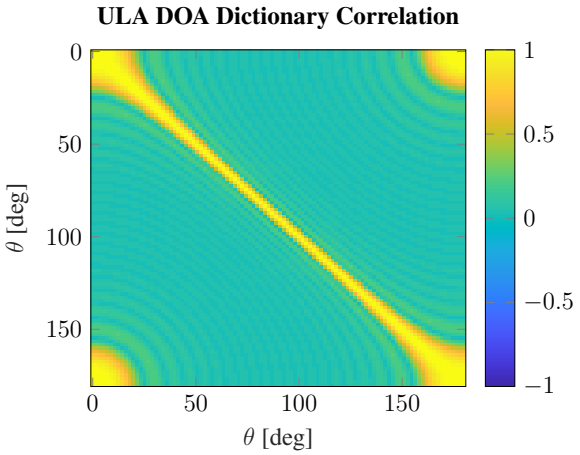

Figure 9.3: Dictionary correlation of a uniform linear array for estimating direction of arrival.

Previously researched DSRF inversions used a dictionary similar to that in Fig. 9.2, but under the low-rank framework, the projected dictionary $\mathbf{A}_{\boldsymbol{P}}$ must now be used. The pro-

jected dictionary becomes $\mathbf{A_P} \in \Re^{O\times 100}$, where it now has roughly half the measurements for inversion. Initially one would expect the reduction of measurements would hinder the performance of sparse recovery. However, based on how the projection matrix is formed by using $\mathbf{A}$ in (6.16), the correlation properties of the columns in $\mathbf{A_P}$ are actually improved as can be seen in Fig. 9.4. This helps counterbalance the loss in measurements used.

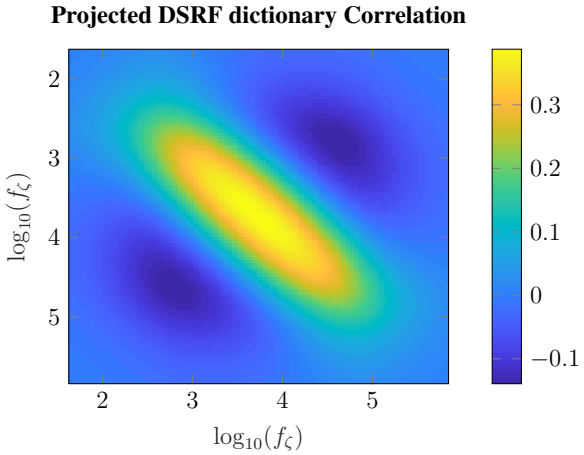

Figure 9.4: Dictionary correlation of the projected DSRF matrix $\mathbf{A_P} \in \Re^{O\times 100}$.

The projection operator on the DSRF dictionary caused the elements to no longer be normalized. As can be seen in Fig. 9.4, the relaxation frequencies in the middle have retained a stronger sensitivity while the edges have decreased in power. For inversion purposes, many inversion algorithms expect the dictionary to have normalized columns. This means that each column vector should have a unit norm equal to one. Normalizing the projected DSRF dictionary creates the new correlations as shown in Fig. 9.5.

The properties of the projected DSRF is still not as nice as the DOA inversion problem for a ULA. This leads to a perspective that the DSRF inversion problem can be viewed as a similar DOA problem where the array geometry is designed poorly in detecting the DOA. Using this perspective, it is possible to compare standard DOA algorithms. Three standard beamforming algorithms are applied to the DSRF inversion problem. The first is a traditional delay-and-sum (DS) beamformer, which projects the measurements from the measurement space to the DSRF space [36]. The second is the well-known MUSIC

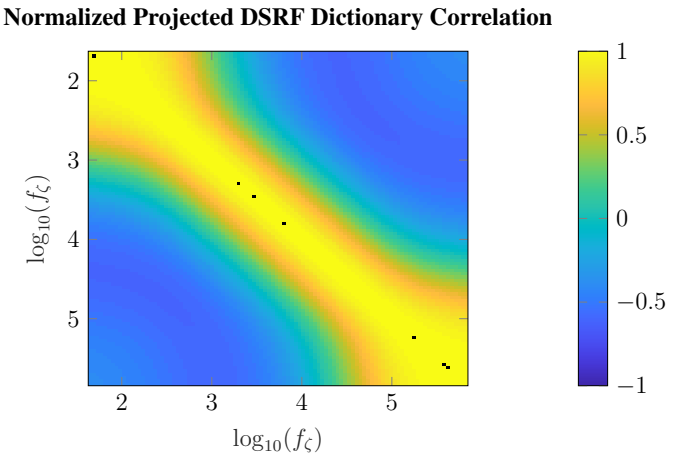

Figure 9.5: Dictionary correlation of the projected DSRF matrix after the columns have been normalized.

algorithm [37]. The final algorithm is matching pursuit (MP) [38]. This is a representative greedy sparse recovery algorithm. Greedy recovery algorithms sequentially find the DSRF contained in the data.

To simplify the problem and highlight the difficulty of the DSRF problem, a few simple cases were run without any noise while the exact rank was provided to MUSIC and MP. Fictional targets were synthesized with three-dimensional symmetry.[2] This causes the target to be rotationally invariant, which means that the target location and orientation will have no impact on the DSRF inversion problem. Also, all relaxation frequencies in the target are chosen to be an exact relaxation in the DSRF dictionary so that there are no off-grid artifacts in the inversion process.

The first target has a single relaxation frequency. The classical DOA algorithms were applied to this target using both the regular DSRF dictionary $\mathbf{A}$ and the normalized projected matrix $\mathbf{A}_{\boldsymbol{P}}$. The results are shown in Fig. 9.6. For this very specialized target, it can be seen that classical DOA algorithms work effectively for DSRF inversion.

Significant DSRF inversion challenges are demonstrated as soon as a target has more than one relaxation frequency. The same target was used as before, except two relaxations were included in the target. Both relaxations in the new target have equal power. This

[2]This creates a degenerate sphere-like target similar to RT-03.

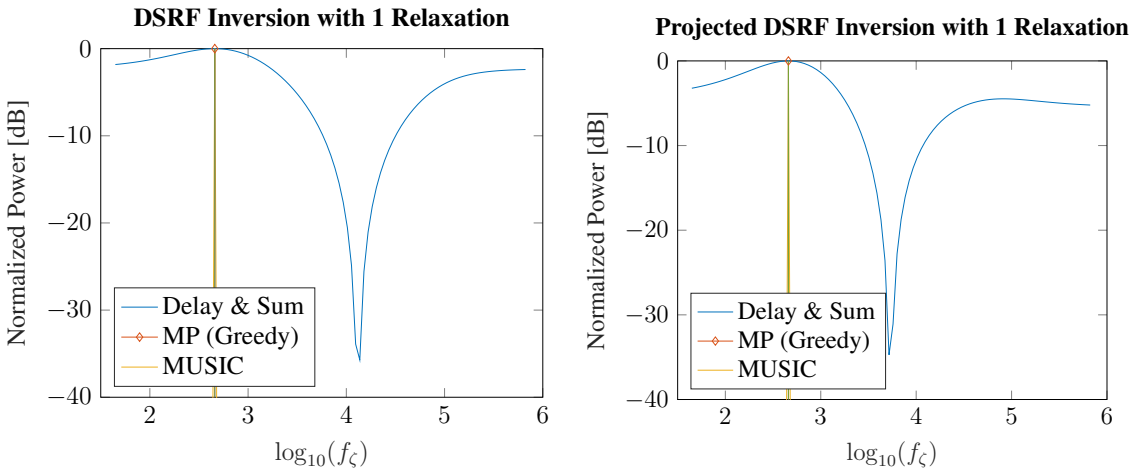

Figure 9.6: Applying classical DOA estimation techniques to a simplified EMI target with one relaxation.

creates a target that still has only a rank-one tensor model, but now has two relaxation frequencies. The same inversion techniques were applied and are shown in Fig. 9.7. Along with these classical DOA methods, nonnegative least squares (NNLSQ) was used to recover the relaxation frequencies. This is motivated by the fact that NNLSQ has been shown to work well for the DSRF inversion problem, but only in the event that all of the relaxations have the same sign [10, 14]. This sign restriction was enforced in this simulation, and will be discussed in more detail later. The results can be seen in Fig. 9.7.

As can be seen in the two relaxation example, many of the standard algorithms are ill-suited for the DSRF inversion problem. The effects of the highly correlated dictionary elements are made evident in the DSRF dictionary. When the two relaxations are combined in the data, they merge and look like a different relaxation frequency in the middle. Both the DS and MP methods using $\mathbf{A}$ indicate that the data appears to have a relaxation frequency in the middle at roughly $10^{3.7}$Hz. When using a greedy algorithm for sparse recovery, this "combined" relaxation in the middle is selected first and there is no way to remove the incorrect estimation. It is interesting to point out that using the projected dictionary helps remove this problem. Figure 9.7 (right) shows that by using the projected measurements, both the DS and MP algorithms obtain a dramatic improvement even though they have

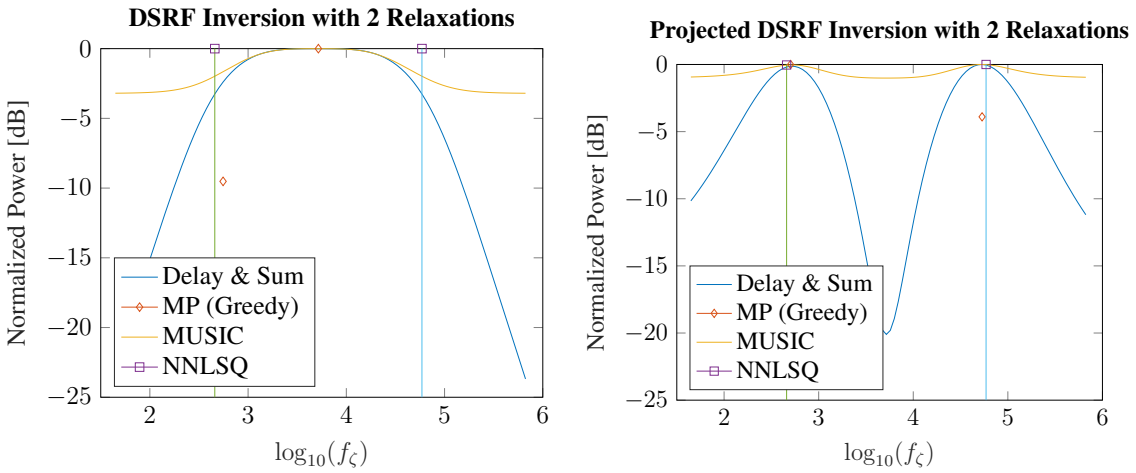

Figure 9.7: Applying classical DOA estimation techniques to a simplified EMI target with two relaxations.

half the observation samples to estimate the inversion. The projected DSRF dictionary is not able to completely remove the correlation between the two relaxations though, so it can be observed that the DS and MP algorithms are still shifted slightly inwards towards the center. Also, the MP algorithm finds the second relaxation to have much lower power than the first. This is also due to the relaxations being correlated, so the first relaxation found by MP steals power from the second relaxation. The MUSIC algorithm works very poorly with both dictionaries, because MUSIC works with the null space of the covariance. Null space algorithms assume that when multiple signals are present, the different signals are independent in the other dimension (e.g., the signals are independent in time for DOA problems) which causes the rank of the resulting covariance to equal the number of signals being found in the DOA. This assumption is not true for the EMI problem and the DSRF inversion because the spatial dimensions for relaxation frequencies can be identical, as shown in this example. This is similar to the multi-path problem for DOA estimation, which is known to cause issues with MUSIC algorithms without further extensions [39]. As can be seen, the NNLSQ inversion method works extremely well for the DSRF recovery process in both cases.

9.3 DSRF Inversion Algorithms

Based on the difficulties of the DSRF inversion problem, greedy algorithms are not expected to perform well and it is necessary to use a sparse inversion algorithm that jointly estimates all of the relaxation frequencies. With the low-rank framework, it is also necessary to use algorithms that can process multiple measurements. This chapter investigates three published sparse solvers: least angle regression (LARS) [40], iterative adaptive approach (IAA) [23], and multiple measurement version of focal underdetermined system solver (FOCUSS) [24]. These algorithms represent a subset of possible methods for providing a sparse solver. LARS is an efficient single measurement joint sparse recovery algorithm that computes each measurement's inverse independently. FOCUSS is a sparse recovery algorithm that has been shown to compute (9.3) while also optimizing over λ. IAA is a sparse recovery algorithm that has no hyper-parameters such as λ required to perform the inversion.

A fourth method was created by the author to explicitly exploit the properties of the EMI data. The new solver is based on the superior results of NNLSQ on EMI data when the sign conditions are met. The new solver is called nonnegative rotational least squares (NRLS) and has similarities with nonnegative matrix factorization (NMF) [41]. The new NRLS solver is discussed in the next section.

9.3.1 Nonnegative Rotational Least-Squares Solver

The NRLS inversion method is designed to exploit the low-rank EMI model. Starting at (5.6), which states that the left singular vectors are modeled as

$$\mathbf{U_M}\mathbf{\Sigma_M} = \mathbf{F}\vec{\mathbf{W}}^T\mathbf{Q_U}\mathbf{R} \tag{9.5}$$

where $\mathbf{Q}_\mathbf{U}^2 = \vec{\boldsymbol{D}}^T \vec{\boldsymbol{\Phi}}^T \mathbf{H}\mathbf{H}^T \vec{\boldsymbol{\Phi}} \vec{\boldsymbol{D}}$. This relationship is expanded to the underdetermined problem

$$\mathbf{U}_\mathbf{M}\boldsymbol{\Sigma}_\mathbf{M} = \mathbf{A}\vec{\mathbf{W}}_\mathbf{A}^T \mathbf{Q}_\mathbf{U}\mathbf{R} \tag{9.6}$$

where all of the other sparse techniques estimate $\vec{\mathbf{W}}_\mathbf{A}^T \mathbf{Q}_\mathbf{U}\mathbf{R}$ as a single matrix. Based on the model, $\mathbf{Q}_\mathbf{U}$ is known to be a square, symmetric, PSD matrix. This means that an eigenvalue decomposition can be found such that $\mathbf{Q}_\mathbf{U} = \mathbf{R}_{\boldsymbol{QU}} \boldsymbol{\Lambda}_{\boldsymbol{QU}} \mathbf{R}_{\boldsymbol{QU}}^T$, which can be inserted in (9.6) to obtain

$$\mathbf{U}_\mathbf{M}\boldsymbol{\Sigma}_\mathbf{M} = \mathbf{A}\vec{\mathbf{W}}_\mathbf{A}^T \mathbf{R}_{\boldsymbol{QU}} \boldsymbol{\Lambda}_{\boldsymbol{QU}} \mathbf{R} \tag{9.7}$$

where $\mathbf{R}_{\boldsymbol{QU}}^T \mathbf{R}$ is still an arbitrary orthonormal unitary matrix and can be renamed $\mathbf{R}$.

This model leads to the unconstrained least-squares problem

$$\min_{\vec{\mathbf{W}}_\mathbf{A}, \mathbf{R}_{\boldsymbol{QU}}, \boldsymbol{\Lambda}_{\boldsymbol{QU}}, \mathbf{R}} \|\mathbf{U}_\mathbf{M}\boldsymbol{\Sigma}_\mathbf{M} - \mathbf{A}\vec{\mathbf{W}}_\mathbf{A}^T \mathbf{R}_{\boldsymbol{QU}} \boldsymbol{\Lambda}_{\boldsymbol{QU}} \mathbf{R}\|_F^2 \tag{9.8}$$

that must be solved to minimize the Frobenius norm of the error between the two matrices. This is an underdetermined problem, so constraints must be added to restrict the solution space. Instead of applying sparsity constraints, the goal is to create other matrix restrictions such as nonnegativity that have proven useful with NNLSQ and also tend to create sparse solutions.

The first constraint comes from applying the ortho-point target assumption. Referring back to (4.11), the matrix $\vec{\mathbf{W}}_\mathbf{A}$ either has zeros or the values from $\vec{\mathbf{W}}$. It was shown that the elements of $\vec{\mathbf{W}}$ are $\left[\vec{\mathbf{W}}\right]_{j,k} = -\alpha_{j,k}\vec{\lambda}_j^{\vec{\boldsymbol{\Lambda}}}$, where $\alpha \in \Re_+$ by definition, and $\vec{\lambda}_j^{\vec{\boldsymbol{\Lambda}}} \geq 0$ because they are the eigenvalues of $\boldsymbol{\mathcal{m}}$ which is known to be PSD. This means that $\vec{\mathbf{W}}_\mathbf{A} \in \Re_-$ must be non-positive, so $-\vec{\mathbf{W}}_\mathbf{A}$ must be a nonnegative matrix. This leads to the constrained

optimization problem

$$\min_{\vec{\mathbf{W}}_\mathbf{A},\mathbf{R}_{\boldsymbol{QU}},\boldsymbol{\Lambda}_{\boldsymbol{QU}},\mathbf{R}} \|\mathbf{U}_\mathbf{M}\boldsymbol{\Sigma}_\mathbf{M} + \mathbf{A}(-\vec{\mathbf{W}}_\mathbf{A}^T)\mathbf{R}_{\boldsymbol{QU}}\boldsymbol{\Lambda}_{\boldsymbol{QU}}\mathbf{R}\|_F^2 \quad \text{s.t. } -\vec{\mathbf{W}}_\mathbf{A} \geq 0 \tag{9.9}$$

where the nonnegative constraint is element-wise.

A second constraint is derived from making a simplifying assumption. If it is assumed that an ideal[3] EMI sensor is used, then the strength of the target will not change based on rotation. This means that $\boldsymbol{\Lambda}_{\boldsymbol{QU}} = \lambda_{\boldsymbol{QU}}\boldsymbol{I}$, where $\lambda_{\boldsymbol{QU}} > 0$ because it is PSD. Using this assumption, $\lambda_{\boldsymbol{QU}} \in \Re_+$ is a positive scalar that can be moved in the least-squares equation to create

$$\min_{\vec{\mathbf{W}}_\mathbf{A},\mathbf{R}_{\boldsymbol{QU}},\boldsymbol{\Lambda}_{\boldsymbol{QU}},\lambda_{\boldsymbol{QU}},\mathbf{R}} \|\mathbf{U}_\mathbf{M}\boldsymbol{\Sigma}_\mathbf{M} + \mathbf{A}(-\lambda_{\boldsymbol{QU}}\vec{\mathbf{W}}_\mathbf{A}^T)\mathbf{R}_{\boldsymbol{QU}}\mathbf{R}\|_F^2. \tag{9.10}$$

This can be concisely written by defining $\vec{\boldsymbol{W}}_{\boldsymbol{Q}\mathbf{A}} = -\lambda_{\boldsymbol{QU}}\vec{\mathbf{W}}_\mathbf{A} \geq 0$ and noting that $-\mathbf{R}_{\boldsymbol{QU}}\mathbf{R}$ is still an arbitrary orthonormal unitary matrix that can be renamed to $\mathbf{R}$. Combining these new variables into (9.9) and adding the orthonormal unitary constraint creates

$$\boxed{\begin{aligned}\min_{\vec{\boldsymbol{W}}_{\boldsymbol{Q}\mathbf{A}},\mathbf{R}} &\|\mathbf{U}_\mathbf{M}\boldsymbol{\Sigma}_\mathbf{M} - \mathbf{A}\vec{\boldsymbol{W}}_{\boldsymbol{Q}\mathbf{A}}^T\mathbf{R}\|_F^2 \\ &\text{s.t. } \vec{\boldsymbol{W}}_{\boldsymbol{Q}\mathbf{A}} \geq 0 \\ &\text{s.t. } \mathbf{R}\mathbf{R}^T = \boldsymbol{I}\end{aligned}} \tag{9.11}$$

which is the new constrained optimization problem for NRLS.

Solving (9.11) is a non-convex problem that is similar to the solution discussed in Appendix B. In this case, it is useful to look at specific models. For the EMI problem, it is known that $R \leq 3$ under the ortho-point assumption. It is possible to make specialized solvers for these cases. When $R = 1$, then $\mathbf{R}$ is limited to the set $\{1, -1\}$. This problem can be solved by testing all possible $\mathbf{R}$ options in (9.11) and selecting the $\mathbf{R}$ that minimizes

[3] Ideal in this case means that the EMI sensor has equal sensitivity in all directions.

the error. Once $\mathbf{R}$ is fixed, (9.11) simply becomes a NNLSQ problem. There are fast algorithms that can be used to solve a nonnegative least-squares problem for a single vector. This effort used Matlab's provided *lsqnonneg* function and simply ran it twice for the two $\mathbf{R}$ cases. Also, note that for rank-one targets, the ideal sensor assumption is not required because $\mathbf{Q_U}$ is a scalar value.

When solving for targets with $R \in \{2, 3\}$, it is no longer practical to evaluate every unitary matrix possible for $\mathbf{R}$. Instead, a binary search method was used for the rotation angle. Again, once the binary search has selected the potential $\mathbf{R}$ terms to evaluate, then (9.11) becomes a NNLSQ problem. However, now the NNLSQ problem is for multiple vectors. This effort used the block pivot method from [42].

9.4 Inversion Results on Simulated Data

Simulations were run to test which DSRF inversion method is most effective. One hundred targets were simulated for each run. Each target contains from two to six relaxation frequencies in the target. The relaxation frequencies lie directly on the DSRF recovery matrix to avoid causing any distortions from off-grid estimation. Each relaxation frequency was given a magnitude of one. The simulated targets were generated using the procedure described in Section 5.6. Each target was then combined with noise before preprocessing to create various levels of SNR. The SNR is defined as the ratio of the squared Frobenius norm of the target to the squared Frobenius norm of the noise. This corresponds to an average SNR per sample taken by the EMI system. Preprocessing was then applied to the data and the DSRF inversion is calculated for each of the inversion techniques: LARS, IAA, FOCUSS, and NRLS. An earth mover's distance (EMD) was calculated in order to test the effectiveness of each method. This was accomplished by taking the average power obtained by the inversion process at each relaxation frequency. Then the "truth" measurement was obtained by selecting the known relaxation frequencies and performing least-squares optimization to solve for the magnitudes. This needed to be done to account for any magnitude

changes caused by the measurement pattern, sensitivity of the EMI system, and preprocessing stages that can cause changes to the magnitudes. Least-squares optimization at the known relaxation frequencies should recover the altered magnitudes. The power from the truth recovery was then calculated in the same manner as the recovered DSRFs. Because both powers are nonnegative, a standard EMD can be calculated between the two vectors. The sum of the powers for each vector was normalized to one before taking the EMD. The resulting EMD distance was then normalized so that if a single relaxation was found, the EMD corresponds to the error in decades of the recovered relaxation.

The first test simulated targets that have a single independent tensor. This means that the measured data is rank-one, and the DSRF inversion is applied to a single singular vector. The results are shown in Fig. 9.8. NRLS consistently performs the best. This is expected because it uses the extra physical knowledge of the targets. Note that LARS is able to work at lower SNRs. This is due to the fact that LARS is designed for single vectors, so it should recover the best answer that an ℓ_1 minimization recovery can achieve. IAA works poorly because it does not restrict the answer to a sparse solution.

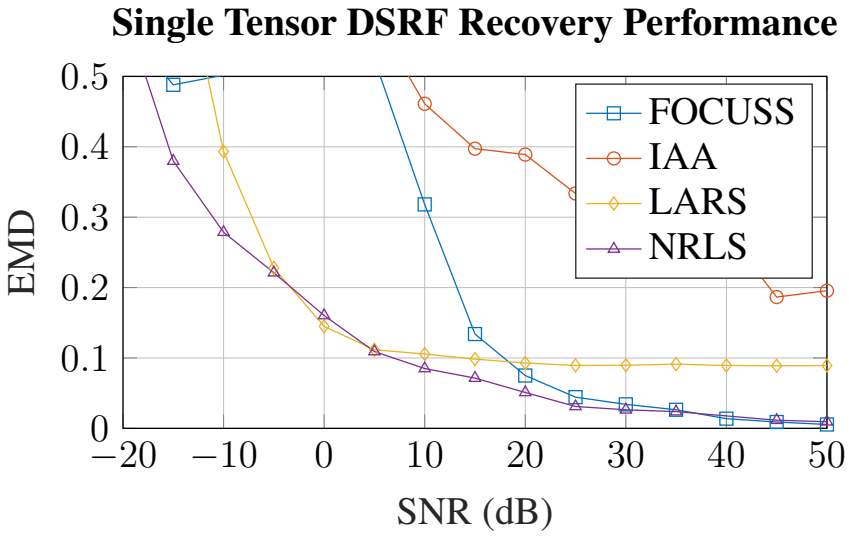

Figure 9.8: DSRF inversion for targets with a single tensor.

The second test simulated targets that have two independent tensors. This means that

the measured data is rank-two, and the DSRF inversion is applied to the two corresponding singular vectors. The results are shown in Fig. 9.9. NRLS again performs the best overall. LARS begins to struggle at lower SNRs because it is unable to combine the measurements across the two singular vectors. Alternatively, FOCUSS improves its performance because it can exploit the multiple vectors. IAA still shows poor performance for these targets.

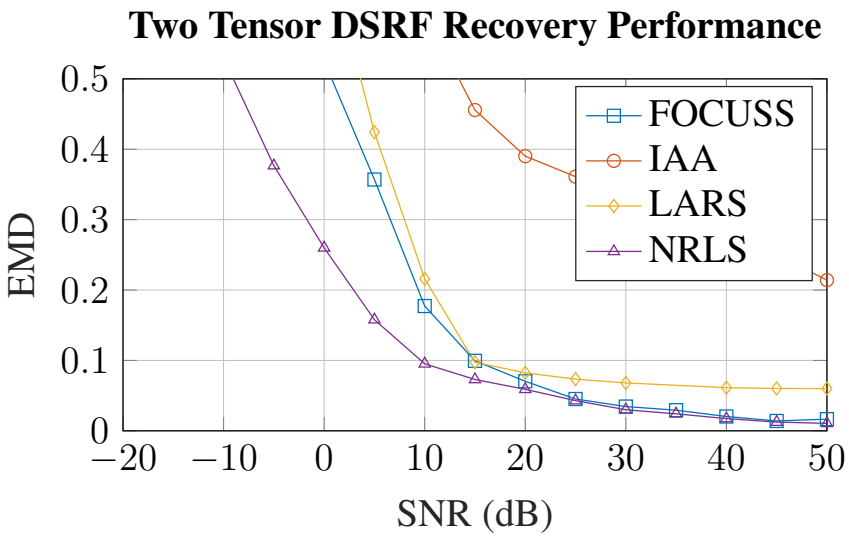

Figure 9.9: DSRF inversion for targets with two tensors.

The results in Figs. 9.8 and 9.9 showed the performance of the DSRF recovery algorithms from Monte Carlo simulations. The DSRF recovery was also applied to RT-05 and RT-06. These targets contain the same relaxation frequencies, and the only difference is that RT-05 is rank-one and RT-06 is rank-two. The results of all four inversion techniques applied at different SNR levels are shown in Figs. 9.10 and 9.11, respectively.

Each one of these results shows the true relaxation frequency with a vertical dotted line, the recovered "truth" DSRF in blue boxes that were obtained by applying least squares to the known relaxation frequency terms, and the recovered DSRF from the algorithm in a red stem plot with diamonds. All of the magnitudes have been normalized so the strongest relaxation frequency is equal to one. A plot is made for each algorithm so the recovery performance is clearly visible. Each plot also shows the measured EMD metric. As can be

seen, any EMD metric above 0.1 decades is not close enough to the actual relaxations for reliable classification from the results.

One observation that can be made from these results is how the "truth" result changes with SNR. At the low SNRs (e.g., -20dB), even the truth results are not perfect due to the noise level that has been added. At the high SNR, it is interesting to compare the "truth" results for RT-05 and RT-06. The Y components of RT-06 have dropped by nearly 20dB, which is a result of the EMI measurement scheme and target orientation.[4]

These plots also provide insights into the different recovery algorithms' performance. It becomes clear that IAA does not enforce a strong sparsity condition on the results. NRLS and FOCUSS consistently provide sparse solutions even at low SNRs, but as the SNR decreases the relaxation selection performance degrades. The LARS algorithm relaxes the sparsity constraint as the SNR decreases.

[4]Section 10.3.2 discusses the impact of a non-ideal EMI sensor, which contributes to the dependence on target orientation

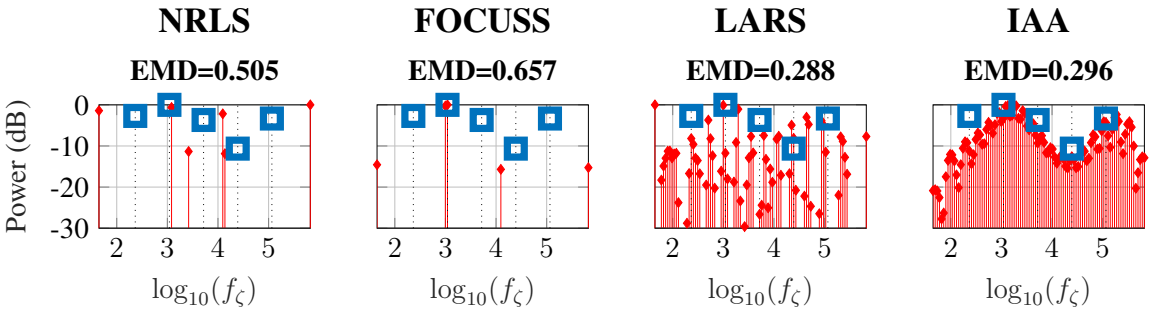

(a) Inversion results with -20dB SNR.

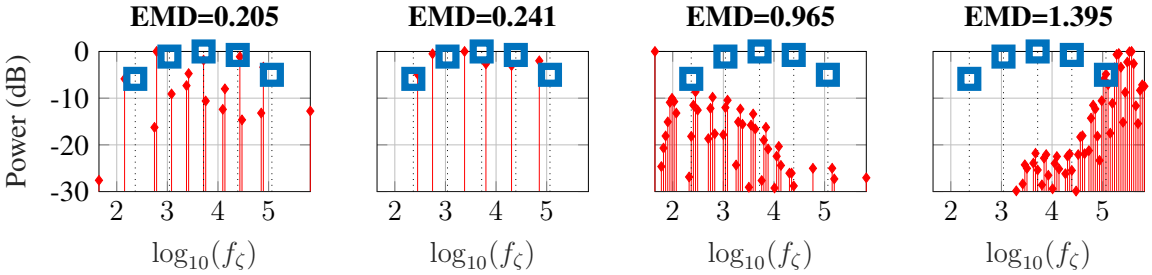

(b) Inversion results with 0dB SNR.

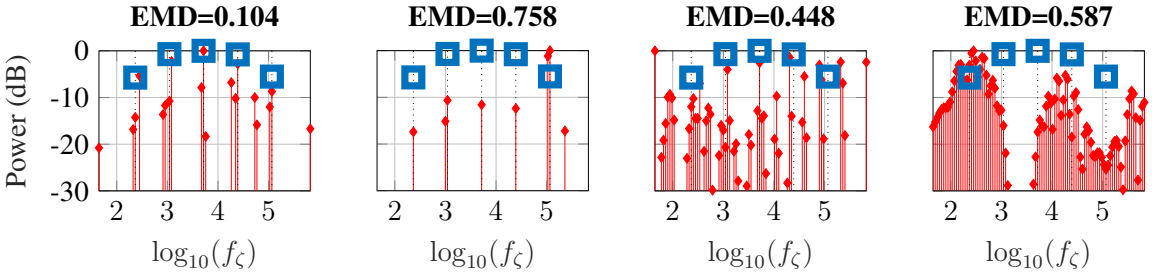

(c) Inversion results with 20dB SNR.

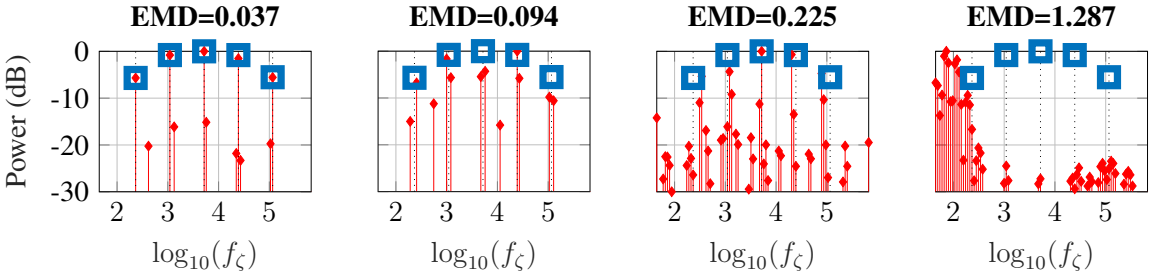

(d) Inversion results with 40dB SNR.

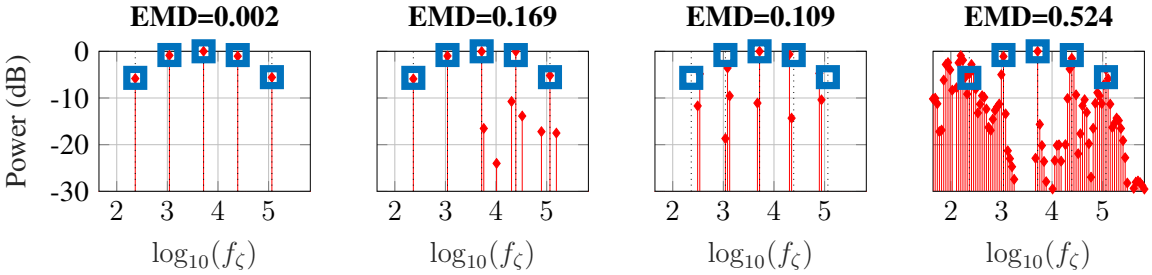

(e) Inversion results with 60dB SNR.

Figure 9.10: DSRF inversion comparison across SNR and algorithms for RT-05.

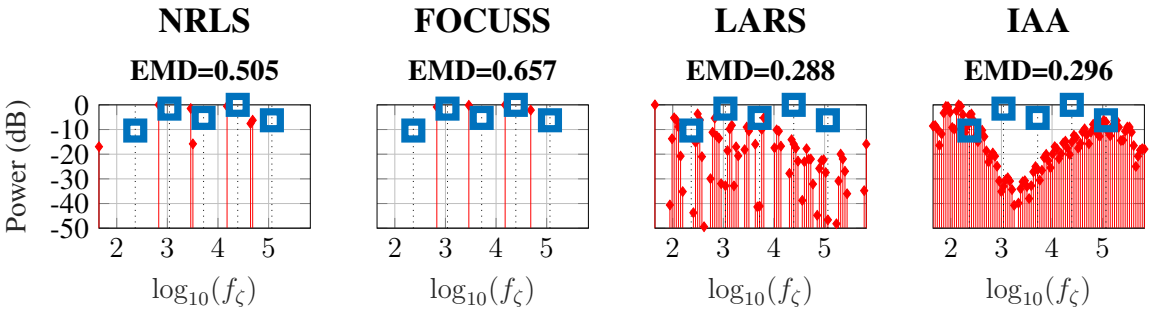

(a) Inversion results with -20dB SNR.

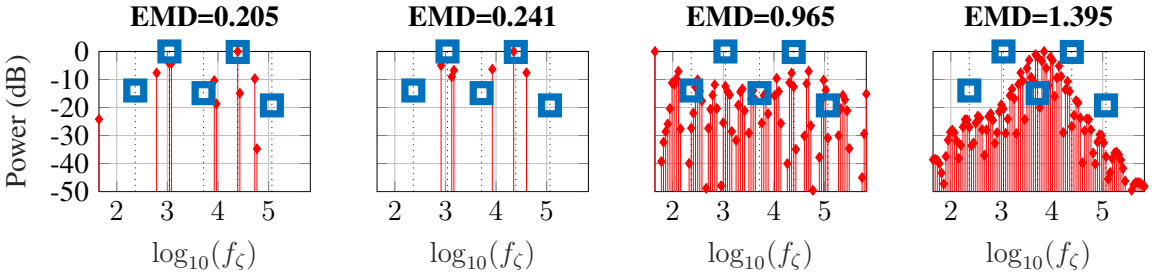

(b) Inversion results with 0dB SNR.

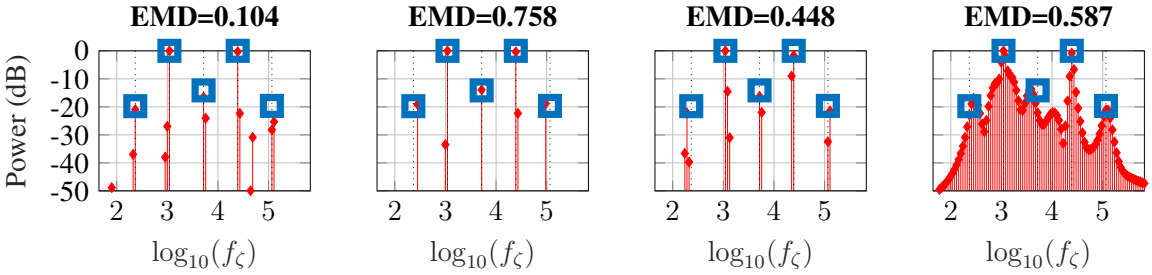

(c) Inversion results with 20dB SNR.

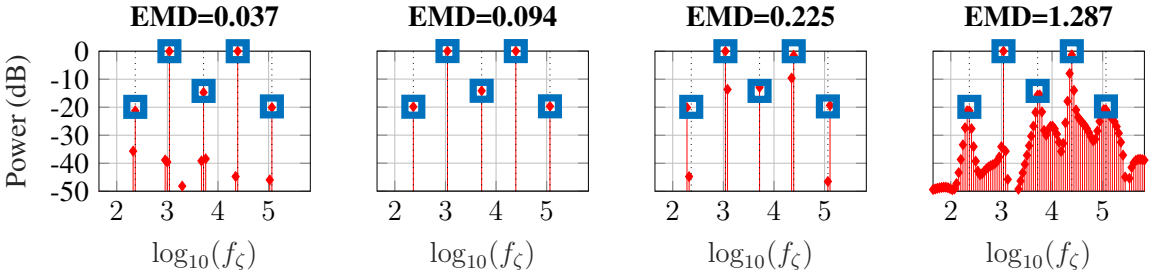

(d) Inversion results with 40dB SNR.

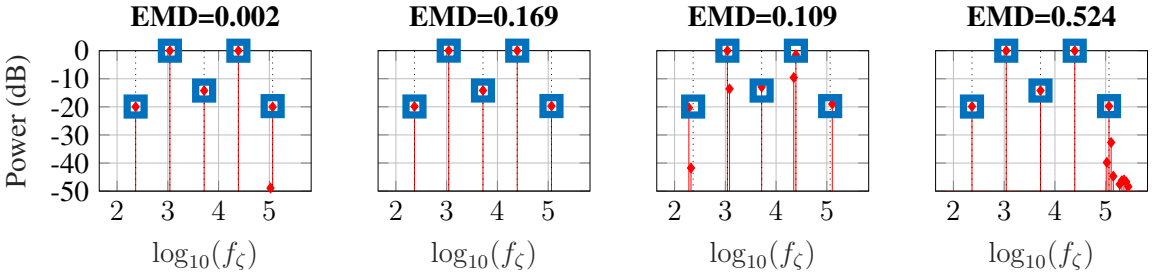

(e) Inversion results with 60dB SNR.

Figure 9.11: DSRF inversion comparison across SNR and algorithms for RT-06.

CHAPTER 10

CLASSIFYING TARGETS WITH EMI DATA

The new low-rank model provides insights into a new method for classifying EMI targets. Just like the DSRF inversion, the main goal of any classifier is to create a set of features that can separate EMI targets in an accurate manner. Ideally, the classifying process can operate in an efficient manner and is agnostic to the targets location and orientation. The DSRF has been used previously as it represents target specific features. This chapter will investigate the left singular values of the low-rank model as a new possible set of features for target classification.

10.1 New Target Features

The new set of features under investigation are derived from the matrix $\vec{\boldsymbol{X}}(\boldsymbol{\phi})$ in (4.9). Each column of $\vec{\boldsymbol{X}}(\boldsymbol{\phi})$ represents a weighted sum of DSRF vectors $-\sum_k \mathbf{f}_k(\boldsymbol{\phi})\alpha_{j,k}\vec{\lambda}_j^{\vec{\mathbf{\Lambda}}}$ for each unique directional tensor and there are R column vectors which is the number independent tensors for the target. This means that the matrix $\vec{\boldsymbol{X}}(\boldsymbol{\phi})$ concisely compresses the target information of the DSRF, their respective amplitudes, and the number of independent tensors. This matrix only contains target information and is not dependent on the target's location or orientation other than the rank of the target R, which is a target feature that can be used for classification.

The new low-rank framework efficiently isolates $\vec{\boldsymbol{X}}(\boldsymbol{\phi})$. The relationship of (5.3) can be described in terms of $\vec{\boldsymbol{X}}(\boldsymbol{\phi})$ as

$$\vec{\boldsymbol{X}}(\boldsymbol{\phi}) \;\big|\; \vec{\boldsymbol{D}}^T \; \vec{\boldsymbol{\Phi}}^T \; \mathbf{H}(\boldsymbol{\Delta}\mathbf{p}) \approx \mathbf{U}_{\mathbf{M}} \; \boldsymbol{\Sigma}_{\mathbf{M}} \; \mathbf{V}_{\mathbf{M}}^T \tag{10.1}$$

where $\vec{\boldsymbol{X}} = \mathbf{F}\vec{\mathbf{W}}^T$. Using this relationship, (5.6) can be re-written as

$$\mathbf{U_M}\mathbf{\Sigma_M} = \vec{\boldsymbol{X}}\mathbf{B}_{\mathbf{U}}^{1/2}. \tag{10.2}$$

where $\mathbf{B}_{\mathbf{U}}^{1/2} = \mathbf{Q_U R} \in \Re^{R\times R}$ is an arbitrary square matrix. This means that the target classification problem is achieved by classifying the left singular vectors of a measured target against known targets, where there is an unknown weighting and rotation matrix applied to the subspaces.

10.2 Comparing Target Singular Vectors

In order to classify targets using the left singular vectors, a distance metric must be chosen between subspaces. Once a distance metric is chosen, then the SS technique can be used to classify targets. The classification process becomes

$$\min_{\boldsymbol{\mathcal{X}}} \textit{dist}\{\mathbf{U_M}\mathbf{\Sigma_M}, \vec{\boldsymbol{X}}_i\} \tag{10.3}$$

where $\boldsymbol{\mathcal{X}}$ is a set of all targets of interest and $\textit{dist}\{X, Y\}$ is a distance metric between two subspaces. The first natural distance is the canonical angle distance of (5.33). This is a measurement between two subspaces. Appendix B develops an equivalent distance in (B.7) based on maximum likelihood estimation (MLE), this distance is a scaled version of the canonical distance [25]. For the target classification problem, this distance would be

$$\min_{\boldsymbol{\mathcal{X}}} \|\boldsymbol{P}_{\mathbf{U}}{}^{\perp} - \boldsymbol{P}_{\vec{\boldsymbol{X}}_i}{}^{\perp}\|_F \tag{10.4}$$

where the projection matrix is only dependent on the $\mathbf{U_M}$ matrix and does not use the singular values.

If it is assumed that the rank is predicted in advance, then (10.4) could be used to calculate the distance between the two subspaces. If the rank is not calculated, then the subspaces

must be larger than necessary and undesired noise is introduced into the distance. It is desirable to use a distance that uses the singular values to weight the importance of singular vectors. This is achieved by returning to the model and developing more constraints on the model. Returning to (10.2), but replacing the $\mathbf{Q}_{\mathbf{U}}$ matrix with its eigenvalue decomposition as was done in (9.7) becomes

$$\mathbf{U}_{\mathbf{M}}\boldsymbol{\Sigma}_{\mathbf{M}} = \vec{\boldsymbol{X}}\mathbf{R}_{\boldsymbol{QU}}\boldsymbol{\Lambda}_{\boldsymbol{QU}}\mathbf{R}. \tag{10.5}$$

Using the ideal EMI sensor assumption, the relationship between the data becomes

$$\mathbf{U}_{\mathbf{M}}\boldsymbol{\Sigma}_{\mathbf{M}} = \lambda_{\boldsymbol{QU}}\vec{\boldsymbol{X}}\mathbf{R} \tag{10.6}$$

where the constant eigenvalue can be moved as desired. Enforcing the constraints that $\mathbf{B}_{\mathbf{U}}^{1/2}$ is only an orthonormal unitary matrix and a constant scaling factor arrives at the new distance

$$\boxed{\min_{\boldsymbol{\mathcal{X}}} \min_{\mathbf{R},\lambda_{\boldsymbol{QU}}} \|\mathbf{U}_{\mathbf{M}}\boldsymbol{\Sigma}_{\mathbf{M}} - \lambda_{\boldsymbol{QU}}\vec{\boldsymbol{X}}\mathbf{R}\|_F^2} \tag{10.7}$$

which has a straight forward implementation as shown in App. B.3.

10.3 Target Classification Simulations

The reference targets were used to test the classification performance with one minor change. RT-03 and RT-05 have the exact same relaxation frequencies and are both rank-one targets. This means that the left singular vectors are the exact same and cannot be classified in this manner. This forced the simulations to modify the reference targets as shown in Fig. 10.1.

A similarity matrix between the modified reference targets is shown in Fig. 10.2 using the distance measure from (10.7). For all of these classification results, the reference targets were generated using the procedure described in Section 5.6 and preprocessing was applied

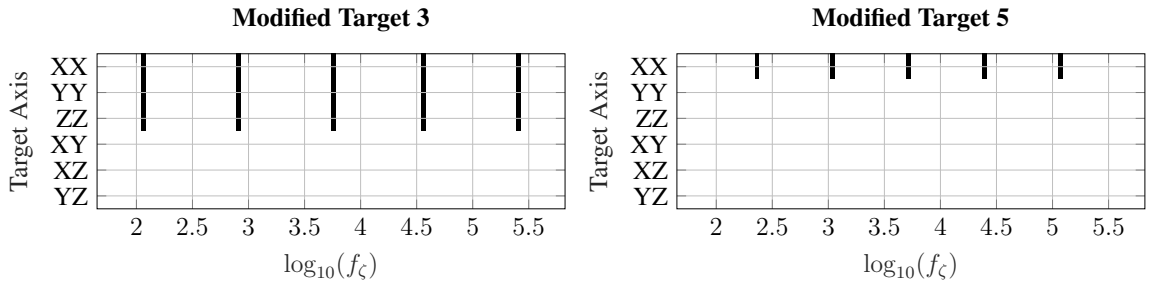

Figure 10.1: Modified reference targets' relaxation frequency representations for classification.

to the resulting measurements as described in Ch. 6. The similarity matrix between the reference targets after preprocessing is shown in Fig. 10.3.

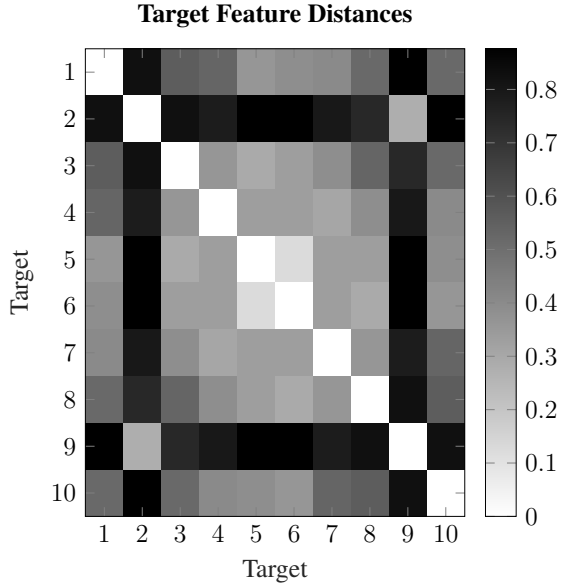

Figure 10.2: Similarity matrix between reference targets.

As can be seen in Figures 10.2 and 10.3, many of the reference targets are very similar. This was done by design because the reference targets are examples that are meant to be very similar. For instance, RT-02 and RT-09 are nearly identical because the only difference is in the amplitudes which change by less than 3dB. The classification results are useful, but expected to be overly pessimistic. Also, the reference targets are defined as completely general targets where $R \leq 6$, but the distance matrix (10.7) was designed assuming ortho-point targets. For these reasons, a set of ten ortho-point targets where created that had a

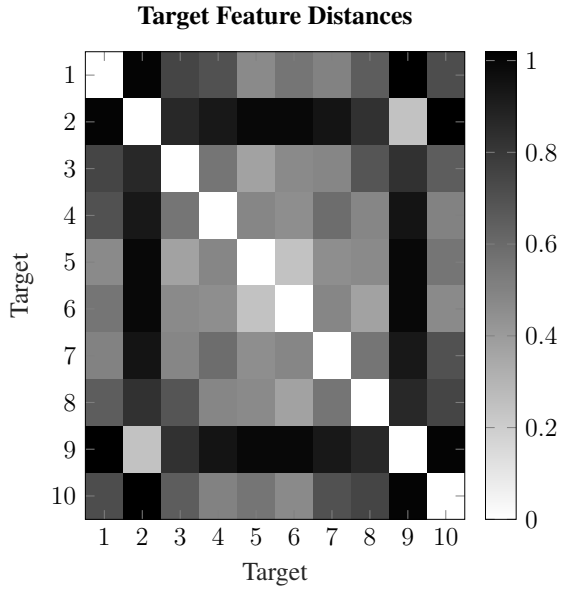

Figure 10.3: Similarity matrix between reference targets after applying preprocessing.

random number of relaxations in the range $K \in [2, 10]$ and the relaxations were randomly placed in a spatial direction. The randomly generated targets are shown in Fig. 10.4. The random targets' similarity matrix for both before and after preprocessing are shown in Fig. 10.5. The reference targets use all six singular values and vectors for classification in (10.7) while the simulated ortho-point targets only use three singular values and vectors.

10.3.1 Classification Results

Classification performance was tested by creating an ideal response and using these to classify the targets at different SNRs and rotations. The ideal target was created by applying the preprocessing stages to the noiseless targets and storing the obtained $\mathbf{U_M \Sigma_M}$ after the singular values were normalized such that the largest singular value equaled one. For the ideal response, a target was placed at a pitch-yaw-roll of 0° respectively.[1] For each SNR, the reference targets were rotated to all combinations of the angles $\varphi \in [-180, 180]$ in steps of 60°, $\theta \in [0, 180]$ in steps of 60°, and $\psi \in [-180, 180]$ in steps of 60°. Each target rotation was generated with a new instance of noise. This means that each target

[1] See (A.1a) for the definition of pitch-yaw-roll angles.

was simulated with 196 different noise variations and orientations for each SNR. These variations were run for all ten targets, creating a Monte Carlo of 1,960 classification results for each SNR. The results of the Monte Carlo classification tests are shown in Fig. 10.6.

Based on the results in Fig. 10.6, the classification consistently performs once it reaches 30dB SNR. Unfortunately it does not reach 100% and confuses the same amount of targets. The minimum expected classification performance is reached at 0dB SNR when the classification is roughly 10%, the same as a random guess between ten targets.

It is useful to investigate the confusion matrix of the classification results at different SNR levels. This provides intuition on which targets are most easily classified and why the classification reaches a plateau. The confusion matrices for the reference targets are shown in Fig. 10.7 and the simulated targets are shown in Fig. 10.8. The most interesting observation is that the SNR plateau is not caused by a few targets getting confused but rather by multiple targets having a few mis-classifications typically with a less complicated target of lower rank.

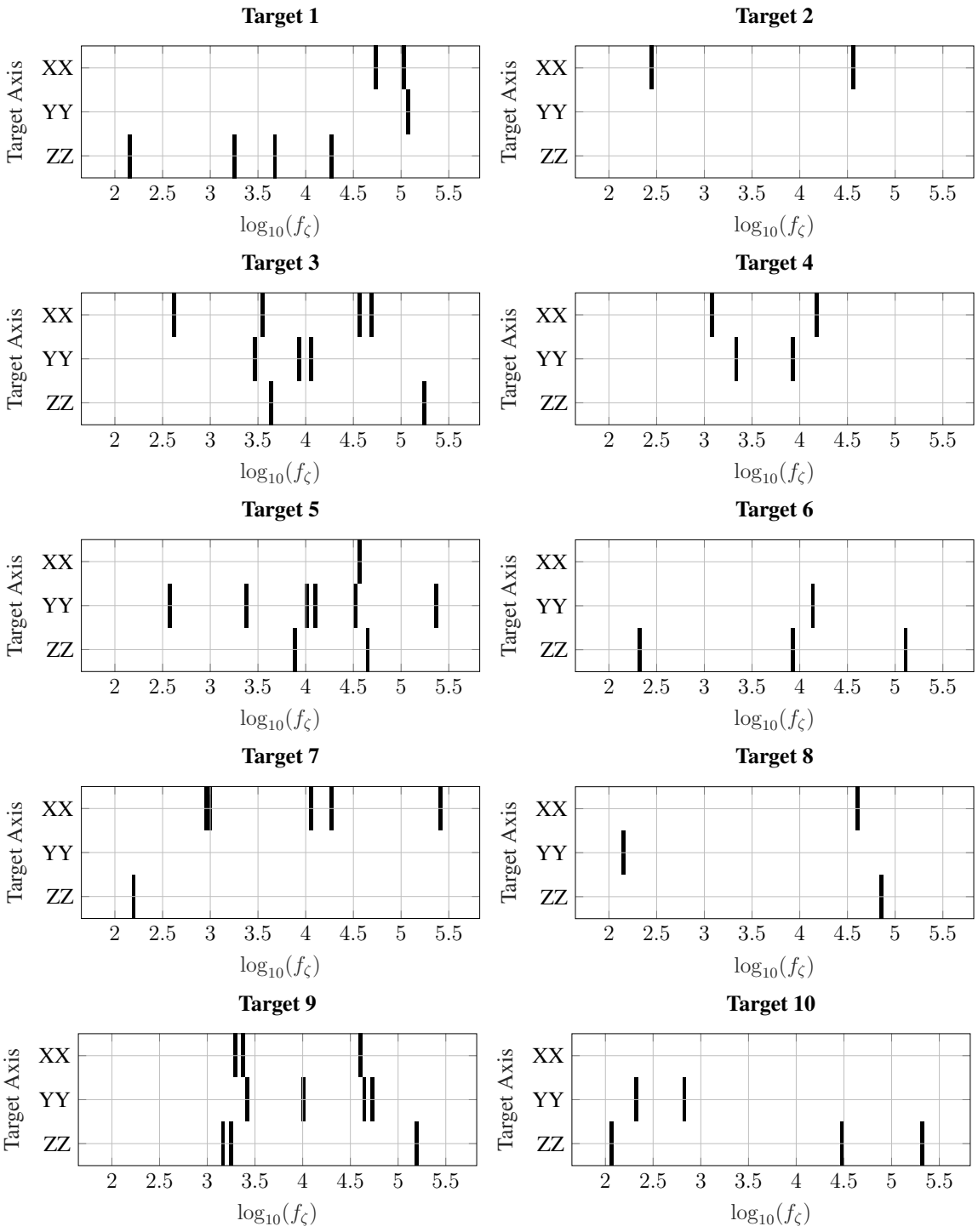

Figure 10.4: Simulated targets' relaxation frequency representations.

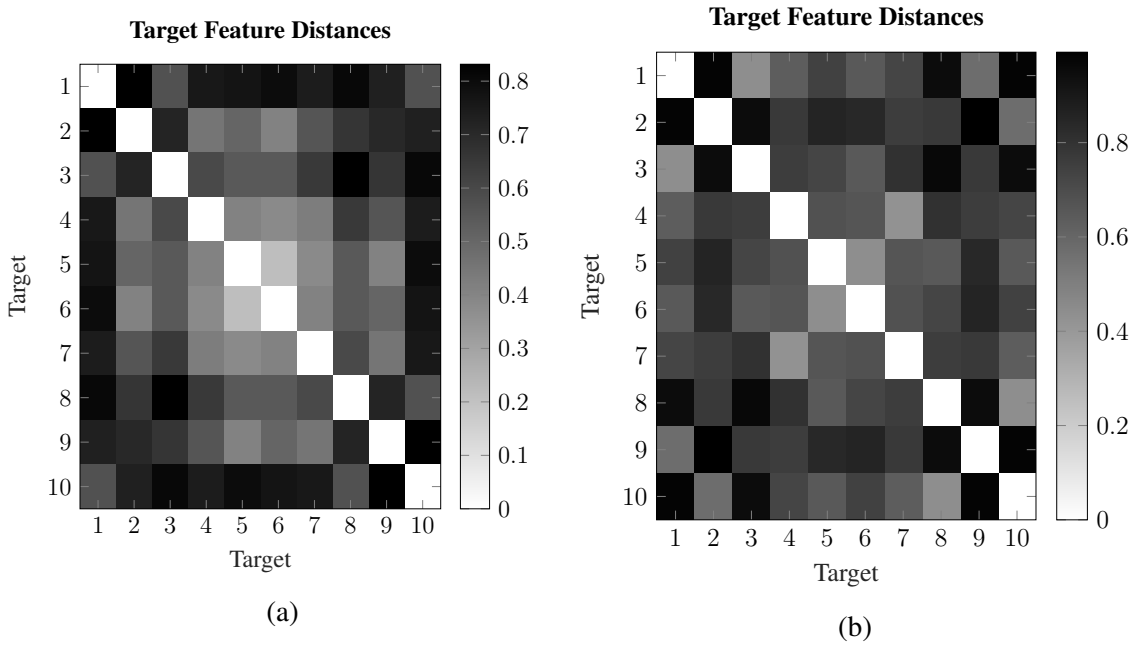

(a) (b)

Figure 10.5: Similarity matrix between simulated targets both before (a) and after (b) applying preprocessing.

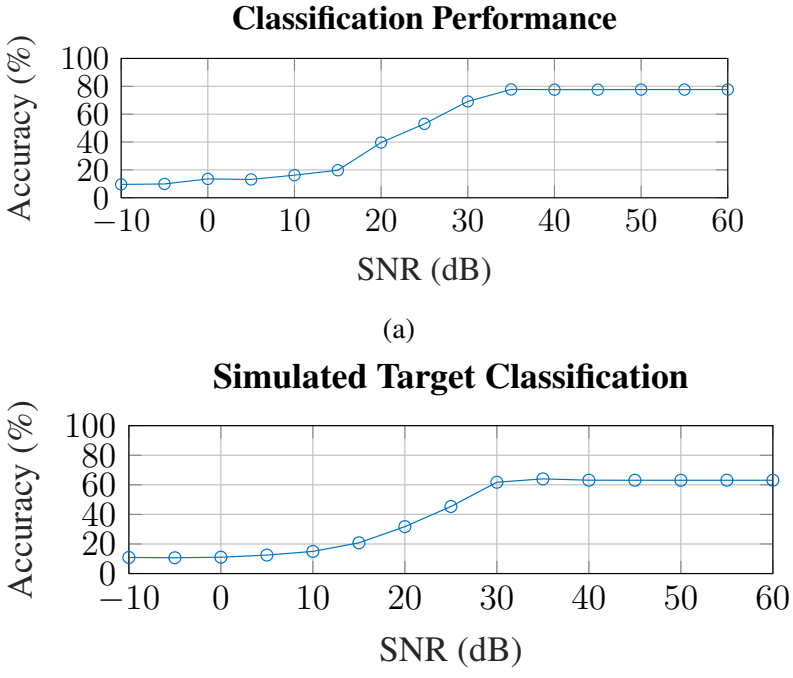

(a)

(b)

Figure 10.6: Classification performance versus SNR for the reference targets (a) and simulated targets (b) over multiple target orientations.

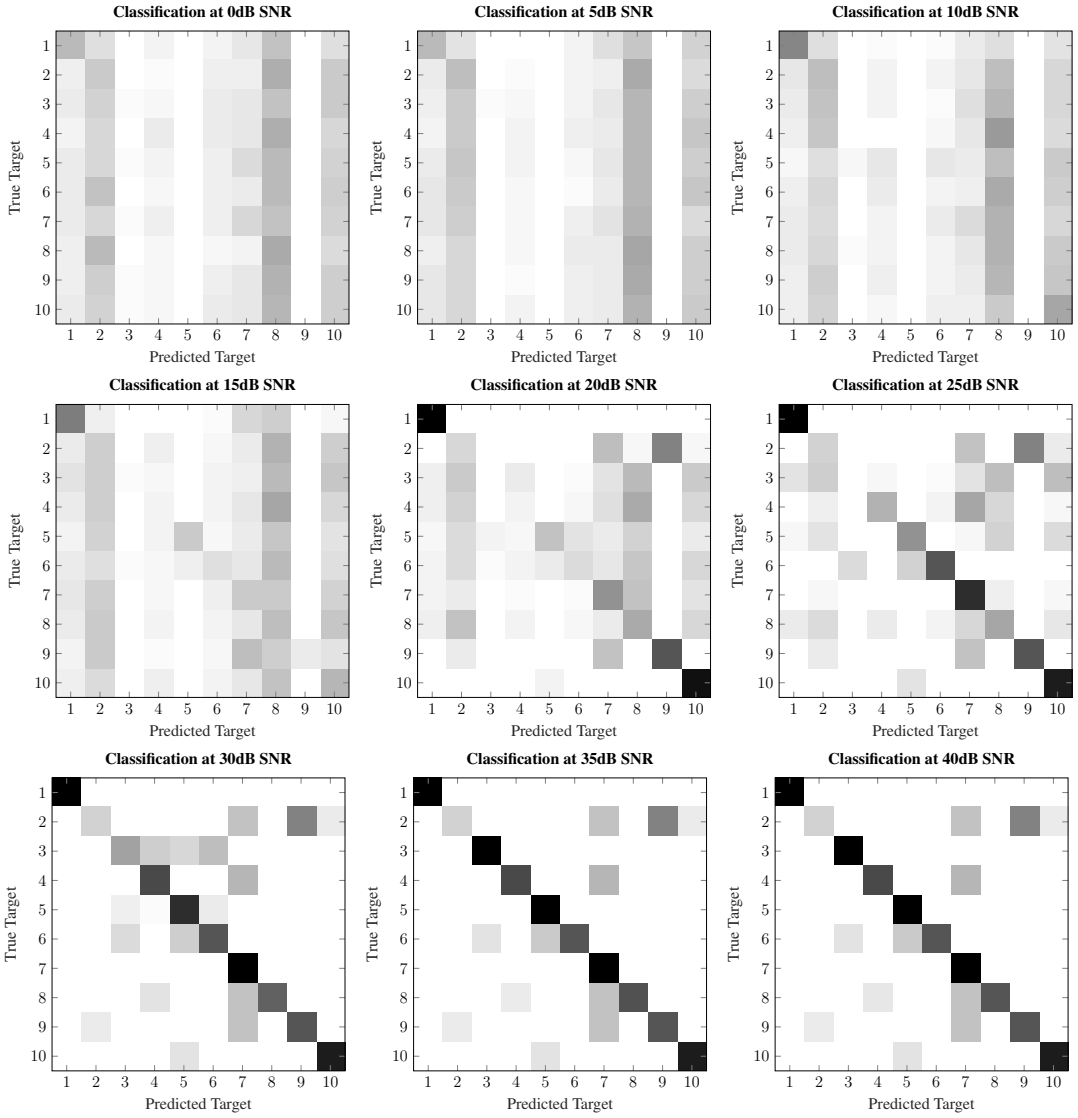

Figure 10.7: Target classification confusion matrices at different SNRs for the reference targets.

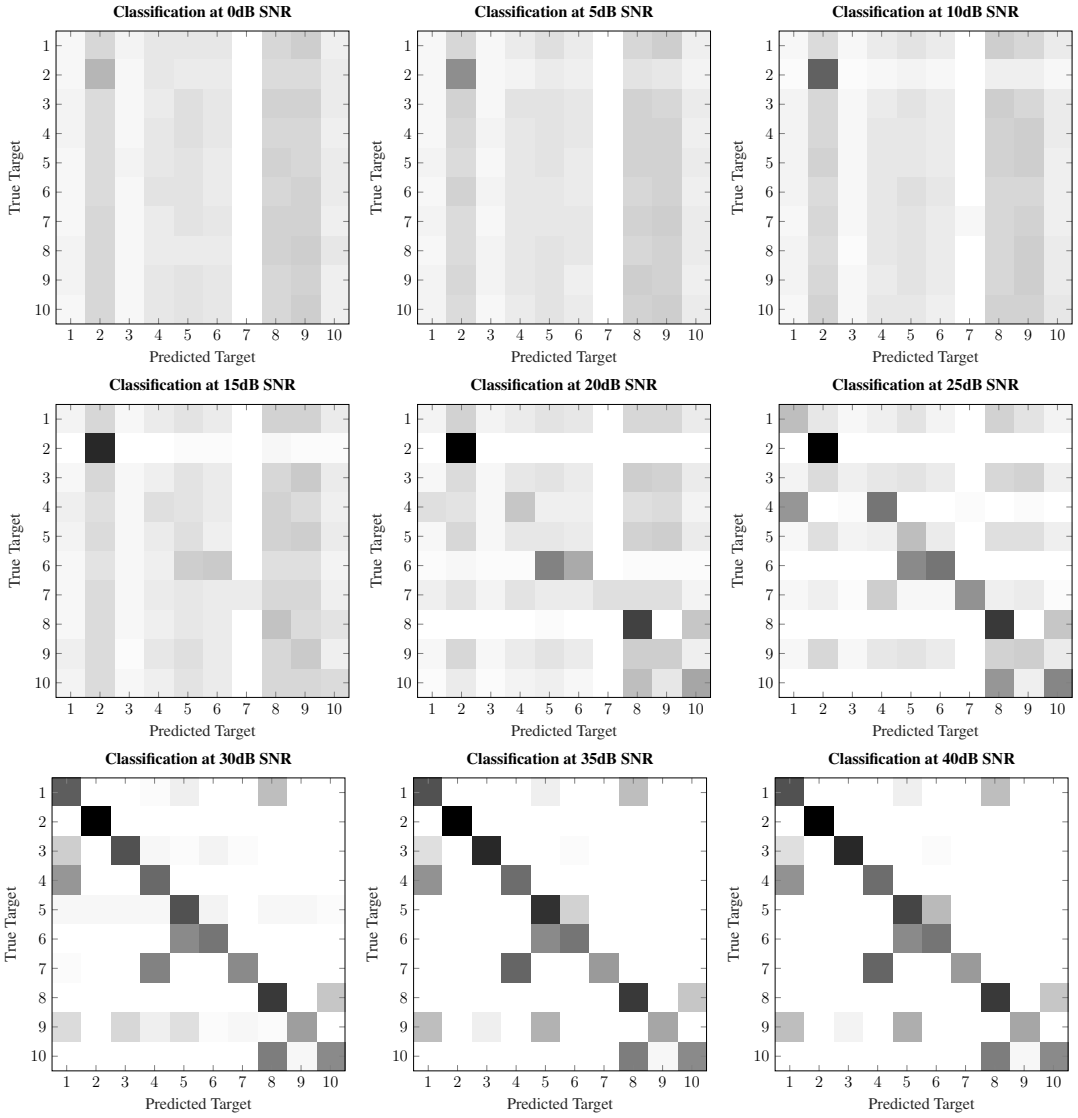

Figure 10.8: Target classification confusion matrices at different SNRs for the simulated targets.

10.3.2 Classification Investigation

The problem of reaching perfect classification is not achieved above, even for the simulated targets that are not similar. In order to better understand this problem, it is worth investigating the assumptions made for classification. The primary assumption was that an ideal EMI sensor was used. In order to test this assumption, the eigenvalues of Eig$\{\mathbf{H}\mathbf{H}^T\}$ are shown in Fig. 10.9. As can be seen, the eigenvalues of the scan pattern used are far from ideal even with the over-sampling applied. There is over a 20dB drop in one direction of the measurement. This is a recognized problem with EMI sensors where they can have a 'blind spot' in one or more directions. This impacts the ability of the target classification because it violates the assumptions made in the distance matrix constraints.

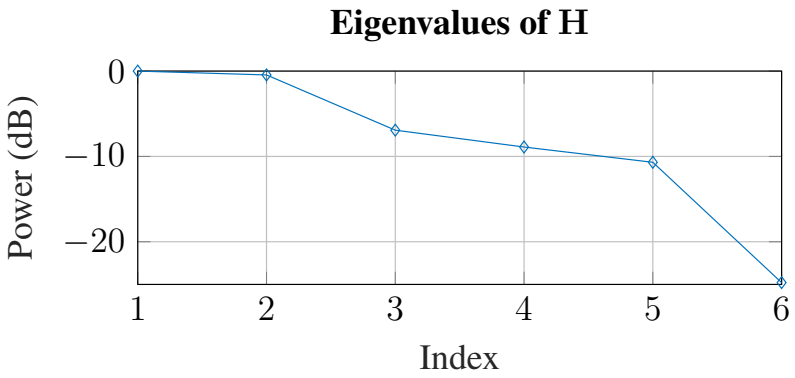

Figure 10.9: Eigenvalues of $\mathbf{H}\mathbf{H}^T$ to determine the validity of the ideal sensor assumption.

In order to test the impacts of the non-ideal sensor, the target classification was performed on the same reference and simulated targets except these simulations use the same target orientation of 0° throughout. Without the need for all of the orientation angles, the simulations were limited to 100 Monte Carlo runs per target per SNR. The resulting performance curves are shown in Fig. 10.10.

As can be seen, removing the orientation changes has caused the simulated targets to reach 100% classification at 30dB SNR. The classifier still fails at 0dB SNR. The reference targets reach 100% classification at 35dB SNR. The confusion matrices for the classification results are shown in Figures 10.11 and 10.12 respectively. The modified RT-03 is the

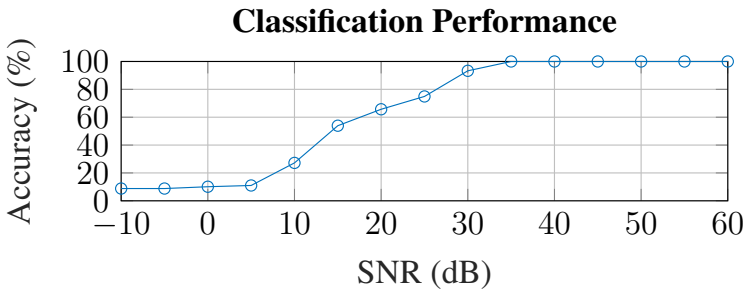

(a)

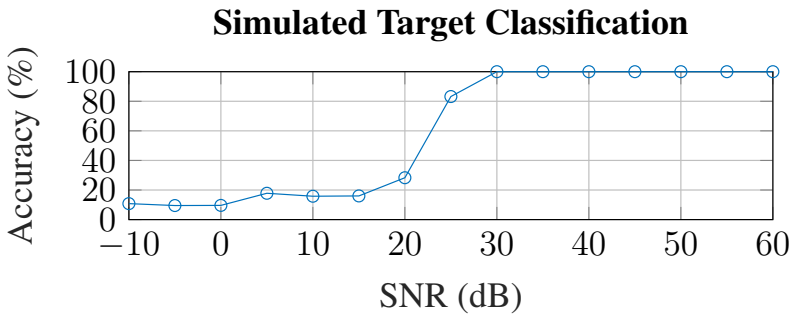

(b)

Figure 10.10: Classification performance versus SNR for the reference targets (a) and simulated targets (b) using the same orientation.

last to be completely classified, which shows that it is more difficult to distinguish slight relaxation frequency changes than the amplitude changes of RT-09 and RT-10.

Based on these results, it clearly indicates that the main limitation of the current classification method is due to the rotation of targets. Fortunately for targets of interest such as landmines, the orientation of the target will be fairly consistent. It is feasible that further classification constraints could be incorporated so the eigenvalues of $\mathbf{\Lambda}_{\boldsymbol{QU}}$ are all estimated in future research.

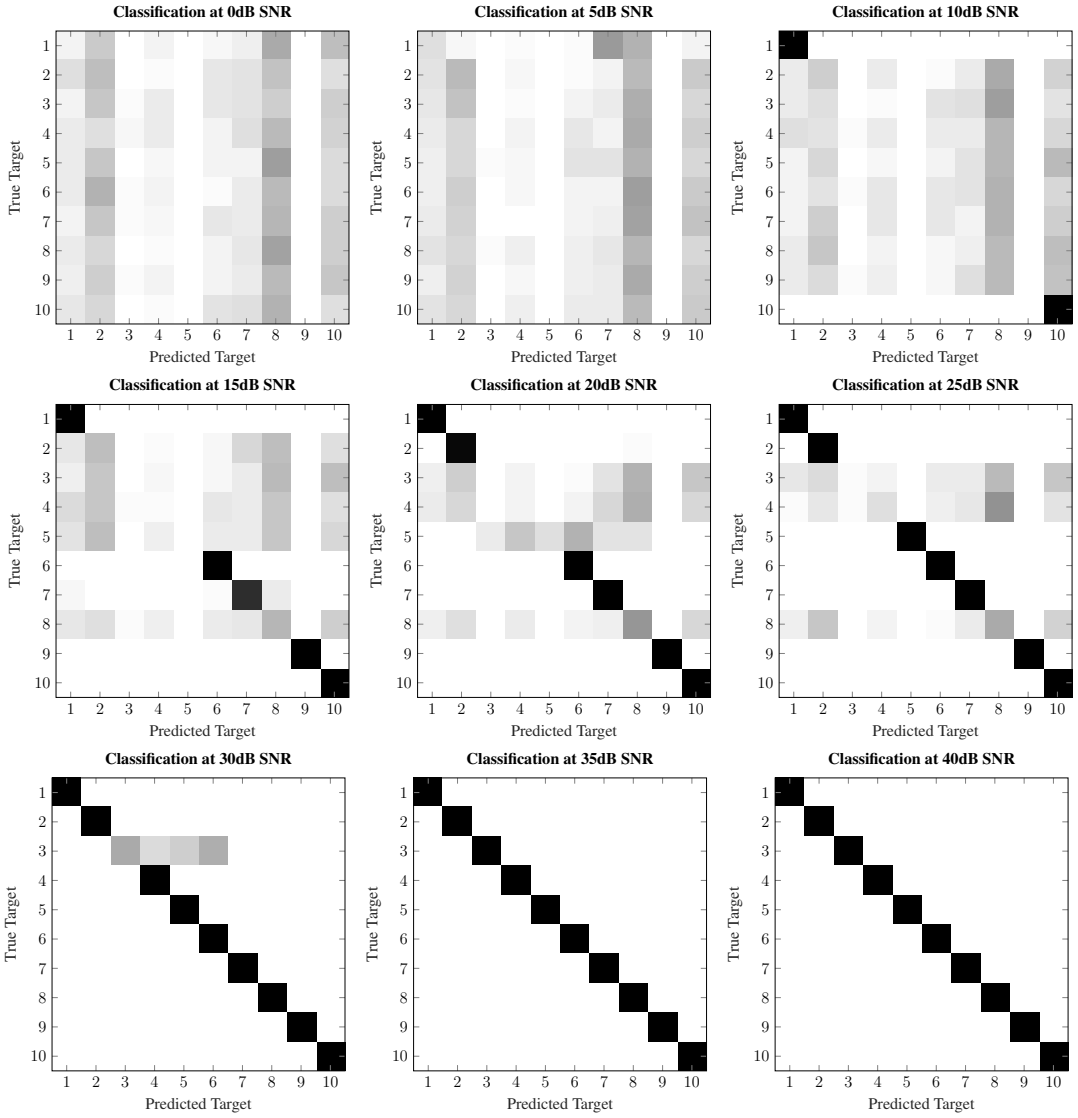

Figure 10.11: Target classification confusion matrices at different SNRs for the reference targets.

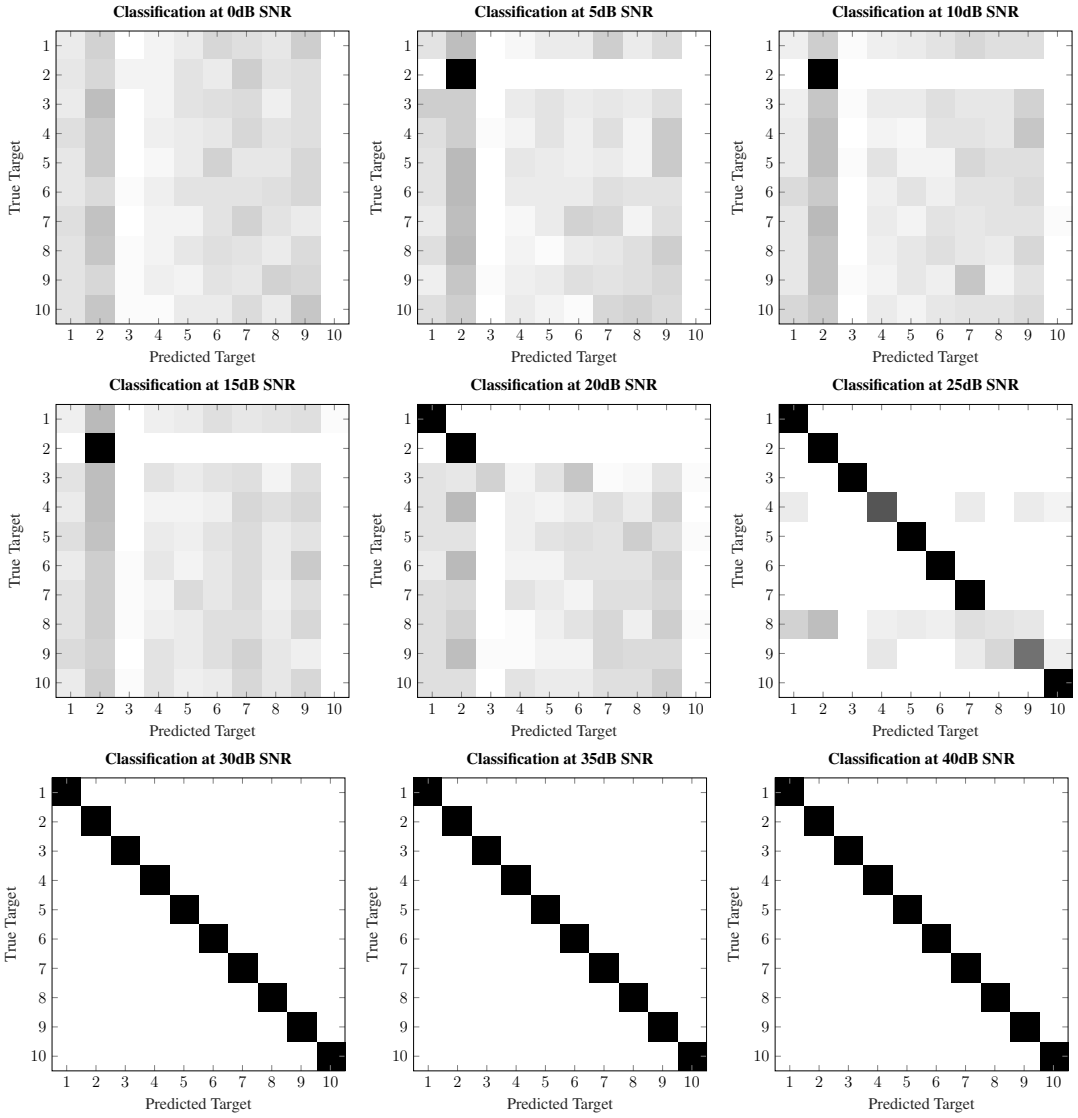

Figure 10.12: Target classification confusion matrices at different SNRs for the simulated targets.

CHAPTER 11

LOCATING TARGETS AND RECOVERING TENSORS

11.1 Locating Targets with EMI Data

Target localization can be applied to EMI data to estimate where the target is buried underground before digging it up. Based on the relative measurements from the EMI sensor near the target, the location can be estimated relative to the sensor. It was shown previously in (5.22) that

$$\min_{\boldsymbol{\mathcal{H}}} \min_{\mathbf{Q_V}} \|\mathbf{V_M}\boldsymbol{\Sigma}_\mathbf{M} - \mathbf{H}_i\mathbf{C}^i_\mathbf{V}\|_F \tag{11.1}$$

can be used as an optimization problem to find the target location. This corresponds to using the known sensor location and employing the Biot-Savart Law to create the $\mathbf{H}_i$ terms for different possible relative target locations. As shown in App. B, the maximum likelihood estimate can be found for each location. Then (11.1) becomes a maximum likelihood search over the selected grid points. This is analogous to the back projection method for radar [43] and direct position determination for radio frequency geolocation [44].

11.1.1 Convexity of the Localization Problem

One of the primary questions for localizing the target is determining the convexity of the search space over $\boldsymbol{\mathcal{H}}$. If the space has multiple minima, then the optimization problem becomes much more computationally demanding. Worst case scenario, a large grid must be created and every location in the grid must be computed or an intelligent grid search algorithm must be employed. If the space is convex, then a straight forward gradient descent approach can be used to find the optimal $\mathbf{H}$.

To explore the convexity of the search space, a search grid was created for the scan pattern used with the reference targets in Section 5.6. The search grid ranged from -10 to

10 cm in the X and Y direction in steps of 0.5 cm and 0 to 20 cm in steps of 0.5 cm in the Z direction relative to the sensor. The entire grid was compared to the $\mathbf{H}$ for $(0, 0, -10)$ cm relative to the sensor. The distance between these locations using the canonical subspace distance[1] and its negative gradient are shown in Fig. 11.1. Slices at the true X, Y, and Z locations are shown. As can be seen, the search space is convex in all X-Y-Z dimensions. Combining these results with the fact that EMI location measurements are shift-invariant [45] implies that the location inversion for EMI sensors can be assumed convex.

Another observation from Fig. 11.1 is the sensitivity of the EMI location depending on direction. The X direction provides the most sensitivity, followed by Z and then Y. This makes sense because there are many more measurements in the X direction and the Y direction is where the sensor tends to have a blind spot.

11.2 Tensor Recovery

Once the left and right subspaces are recovered, the remaining term is the tensor information in the middle. It was shown previously in (5.14) that the center tensor is recovered as

$$\mathbf{G}^T = \mathbf{C}_{\mathbf{U}} \mathbf{\Sigma}_{\mathbf{M}}^{-1} \mathbf{C}_{\mathbf{V}}^T. \tag{11.2}$$

The $\mathbf{G}$ contains the *tensor amplitudes* of the *magnetic polarizability* . This holds the target's orientation and the rank of the *magnetic polarizability* . This chapter focuses on the error incurred on $\mathbf{G}$ by using the subspace recovery techniques and also using the recovered tensor to learn more from the target.

11.2.1 Recovery Results

Monte Carlo simulations were run to study the impact of the subspace recovery methods on the tensor recovery. A three orthogonal loop target like RT-02 was used throughout the simulation. The target had random relaxation frequencies, target orientation, and location. For

[1] The canonical subspace distance is $\| \boldsymbol{P}_{\mathbf{H}_i} - \boldsymbol{P}_{\mathbf{H}_j} \|_F$.

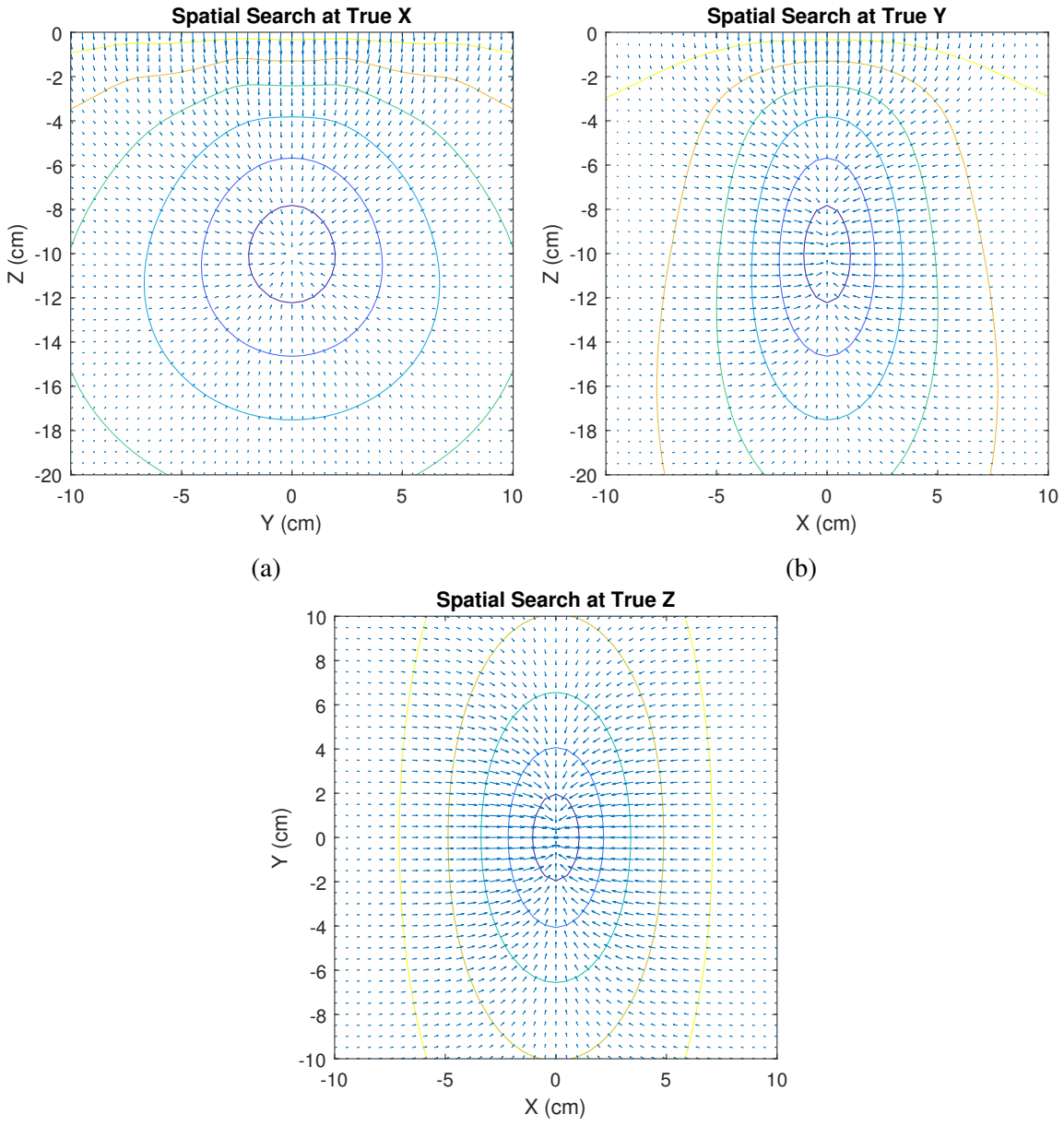

Figure 11.1: Slices of localization search space showing that the problem is convex as long as the target is not right next to the sensor. Slices of the (a) Y-Z axis, (b) X-Z axis, and (c) X-Y axis, are shown.

a baseline, a heavily constrained solution was used where the relaxation frequencies, target coordinate system, and target location were known. In this specialized case, the recovery of $\mathbf{G}$ is primarily inverting the rotation and scaling introduced from the SVD. This specialized recovery problem was minimally altered to study the impacts of the subspace selection (SS), sparse subspace creation (SSC), and subspace projection (SP) recovery techniques. For SSC, the DSRF inversion problem was used to recover the relaxation frequencies while everything else remained known. For SP, the correct location and relaxation frequencies were used but the target orientation was unknown and had to be recovered. For SS, the location was recovered by searching over a grid while the relaxation frequencies and orientation were known. The normalized average error of the estimated $\mathbf{G}$ versus SNR is shown in Fig. 11.2 for 100 random targets per SNR.

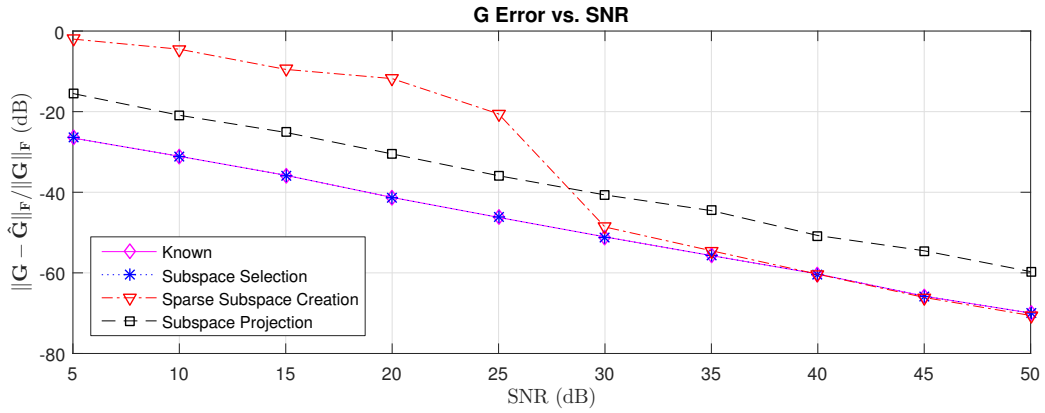

Figure 11.2: The error vs. SNR curve for recovering $\mathbf{G}$ from simulated EMI data.

The results in Fig. 11.2 are enlightening. The tensor recovery when everything is known provides a lower bound for optimal performance. The SS method was able to meet this bound exactly. This was expected because SS is an MLE recovery method that is identical to the known case when the SNR is high enough to pick the correct position. The SSC was able to reach the bound while the SNR is large enough for the sparse recovery method to accurately predict the relaxation frequencies. As the sparse solver fails, the wrong relaxation frequencies are chosen and the tensors become inaccurate due to the inaccuracies of the selected left basis. The SP method consistently performs multiple dB worse than the bound

because of the least-squares operation into the smaller subspace. An actual implementation of the recovery algorithm would use a combination of these algorithms to perform the full inversion. These results provide intuition into the errors occurred when combining these methods and the performance impact that can be expected.

11.2.2 Reference Targets

The rank of an ortho-point target is known to be $R \leq R_{\vec{\mathbf{\Lambda}}}$, where $R_{\vec{\mathbf{\Lambda}}} = \text{rank}\{\boldsymbol{\mathcal{M}}\}$ and the inequality is only needed for degenerate targets. This means that the rank of the *magnetic polarizability* can be used for classification between normal and degenerate targets when compared to R. For instance, RT-03 and RT-05 are identical targets except RT-03 is degenerate and RT-05 is not. It was discussed in previous chapters that the left singular vectors used for classification cannot distinguish these two targets; however, the rank of the recovered tensor should provide a difference between the targets for classification.

To demonstrate this, the tensor information $\mathbf{G}$ was recovered for all of the reference targets at 50dB SNR. Once $\mathbf{G}$ was recovered, each tensor was reshaped into a 3×3 real, symmetric matrix and combined into $\boldsymbol{\mathcal{M}}_K$. The $\boldsymbol{\mathcal{M}}_K$ tensor is mathematically described as

$$\boldsymbol{\mathcal{M}}_K = \sum_k \alpha_k \boldsymbol{\mathcal{M}}_k \tag{11.3}$$

where the tensor differs from the *magnetic polarizability* because it does not contain the relaxation terms f and is the sum of the *tensor amplitudes*. The rank of the recovered tensor is then computed using an eigenvalue decomposition[2] and the eigenvalues are shown in Fig. 11.3. The eigenvalues are normalized so that the largest value equals one, and any eigenvalue below -50dB is assumed noise.

Based on the results of the reference target inversion, all of the reference targets' *magnetic polarizability* rank $R_{\vec{\mathbf{\Lambda}}}$ were successfully recovered. Even the general targets of RT-07 and RT-08 have the correct rank. Most notably, RT-03 and RT-04 clearly have a rank

[2]For real-valued tensors, the eigenvalue decomposition is equivalent to the Autonne-Takagi factorization.

of three which means that $R_{\vec{\mathbf{\Lambda}}} > R$ where $R = 1$ and $R = 2$ respectively. This provides a clear and useful tool for distinguishing degenerate targets, and it also provides a method for distinguishing RT-03 and RT-05 because the $R_{\vec{\mathbf{\Lambda}}}$ is clearly different between the two targets.

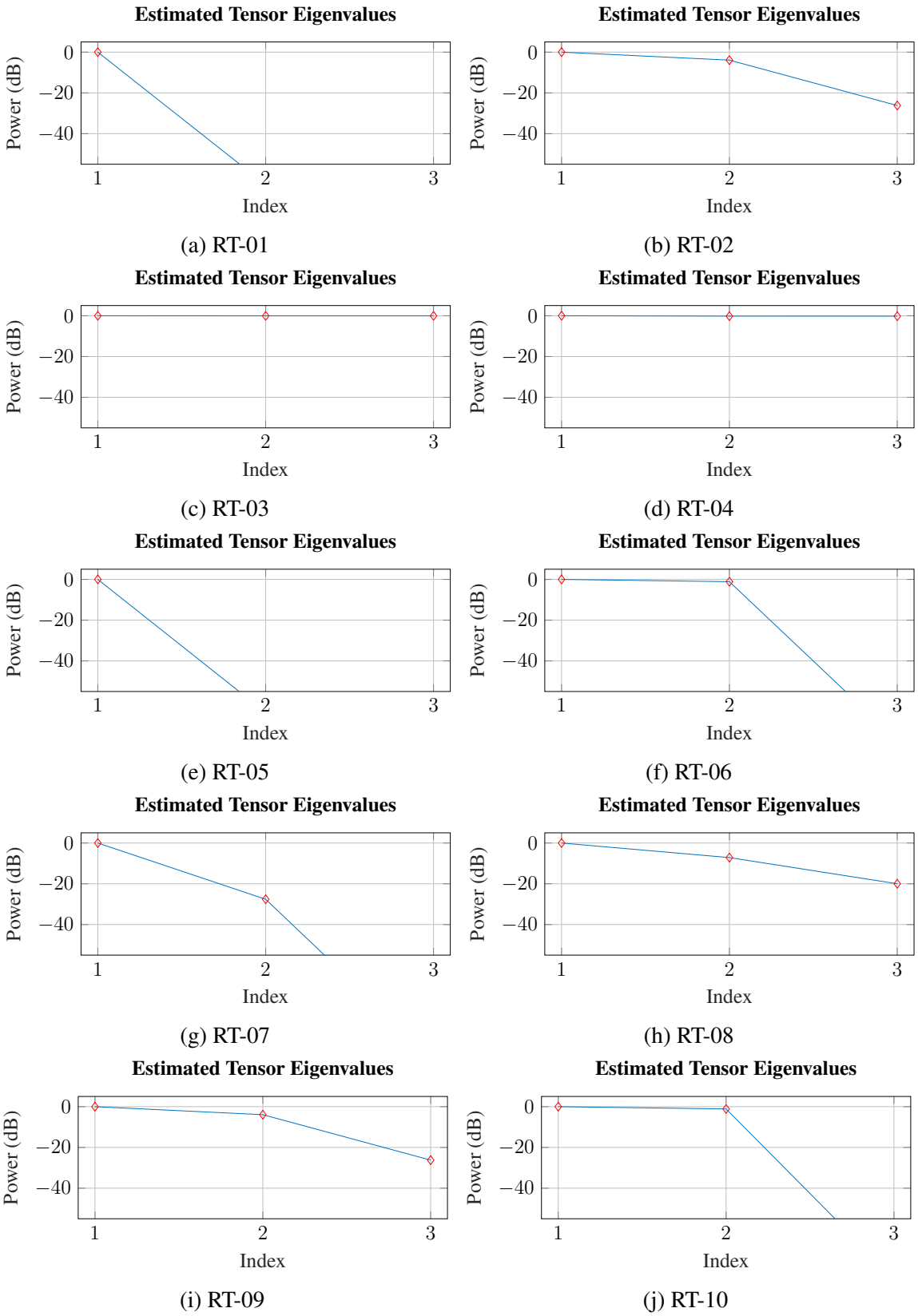

(a) RT-01 (b) RT-02

(c) RT-03 (d) RT-04

(e) RT-05 (f) RT-06

(g) RT-07 (h) RT-08

(i) RT-09 (j) RT-10

Figure 11.3: Eigenvalues for reference targets' 3×3 orientation tensor after recovering $\mathbf{G}$.

CHAPTER 12

CONCLUSION

This thesis developed a new low-rank model for multi-measurement EMI data. It was shown in (4.4) that for a general EMI point target, the model can be defined as

$$\mathbf{S} = \mathbf{F}(\boldsymbol{\omega})\mathbf{W}^T\boldsymbol{\Phi}^T\mathbf{H}(\boldsymbol{\Delta p}) \tag{12.1}$$

where $\mathbf{F}(\boldsymbol{\omega})\mathbf{W}^T$ captures frequency dependence, $\boldsymbol{\Phi}^T$ is the orientation tensor, and $\mathbf{H}(\boldsymbol{\Delta p})$ depends on target location. This model for the signal matrix $\mathbf{S}$ will have a maximum rank of six and the rank is equal to the number of linearly independent orientation tensors of the target. The special case for ortho-point targets which is often used for man-made targets was shown in (4.9) to have a further restricted low-rank model of

$$\mathbf{S}(\phi, \boldsymbol{\Delta p}) = \vec{\boldsymbol{X}}(\phi)\vec{\boldsymbol{D}}^T\vec{\boldsymbol{\Phi}}^T\mathbf{H}(\boldsymbol{\Delta p}) \tag{12.2}$$

where the maximum rank is limited to three, which is the rank of $\vec{\boldsymbol{D}}^T$. This derivation is a sum of tensors, and it can be expanded to the usual sum of dipoles low-rank model

$$\mathbf{S}(\phi, \boldsymbol{\Delta p}) = \mathbf{F}(\phi)\vec{\mathbf{W}}^T\vec{\boldsymbol{D}}^T\vec{\boldsymbol{\Phi}}^T\mathbf{H}(\boldsymbol{\Delta p}) \tag{12.3}$$

as was shown in (4.11). Ten reference targets are given as examples and described in terms of the new low-rank model in Sec. 4.4.

The new low-rank models were compared to previous EMI processing models in Sec. 4.5. The low-rank model is the only one that can elegantly model degenerate EMI targets that occur often due to physical symmetry. It is the only model that explicitly shows the correct rank of a matrix formed from EMI measurements for both general and ortho-point targets. The low-rank model can be used on a large variety of EMI sensors and also leads to a general processing framework that can be implemented using well-established linear algebra approaches.

The new low-rank processing framework is shown in Fig. 5.1. The first step of the new framework is a preprocessing stage. A newly designed EMI preprocessing strategy, described in Ch. 6, moves away from classical filter based approaches [17] and relies on projection matrices created from knowledge of the EMI sensor, target, and interference. The new preprocessing mitigates the impact of both the sensor's self response and the soil response, whereas previous filters only removed the self response. This enables the creation of a smaller matrix that concentrates the target's signal, isolates it from the known interference, and provides an accurate noise floor estimation from the remaining measurements. It is also shown in Ch. 9 that the new preprocessing improves the ability of recovering the target's features.

After preprocessing, the new framework exploits the low-rank model by using a singular value decomposition (SVD) on the measured data. The three fundamental relationships

$$\mathbf{U_M \Sigma_M} = \mathbf{F C_U} \tag{12.4a}$$

$$\mathbf{\Sigma_M V_M^T} = \mathbf{C_V^T H} \tag{12.4b}$$

$$\mathbf{C_U \Sigma_M^{-1} C_V^T} = \mathbf{G}^T \tag{12.4c}$$

were formulated in Sec. 5.1 to create mechanisms for recovering the low-rank model from the SVD measurements where $\mathbf{G}$ is the center matrix for the various models containing the orientation tensor information. The limitation of an SVD in noise and the choice of how to use the singular values was also discussed in Ch. 5.

Multiple applications within the EMI framework were investigated and implemented in this thesis. The new preprocessing was applied to EMI data from a field collection with the GT EMI sensor [28]. The average sample power of the different measured components were estimated and are summarized in Table 12.1[1]. Previous filter-based pre-

Self response	-50dB
Soil response	-95dB
Noise floor	-130dB or lower
Target Signal	most between -60 to -80dB

Table 12.1: Measured signal components' average sample power from field data.

processing is able to isolate the target from the self response. This created targets with a signal-to-interference-and-noise-ratio of $25-45$dB for most targets[2]. The new preprocessing removes both the self response and soil response. Combining the improved interference isolation with further processing on the same targets improves the signal-to-noise ratio to roughly $50-70$dB. The preprocessing is shown for the reference targets in Sec. 6.4.

Chapter 7 develops a matched subspace detector and the associated constant false alarm rate detector for EMI data based on the low-rank model. The results are applied to field data and receiver operating characteristic (ROC) curves are provided. A joint detection strategy is developed that can appropriately exploit the target signal that is orthogonal to the soil response and the target that remains mixed with the soil response. The ROC curves for the various detectors are provided in Figs. 7.6 and 7.7.

[1] Where the average sample power has been normalized to the size of $\mathbf{M_S}$

[2] Assuming the filter added an extra 10dB of processing gain over the soil response from the average sample power.

Chapter 8 demonstrates rank estimation on EMI data for simulated targets. The Akaike information criterion and Bayesian information criterion were both developed and applied to EMI data. Simulation results in Fig. 8.1 show that the rank can be detected in Gaussian noise down to almost 20dB SNR reliably.

Chapter 9 focuses on recovering a target's discrete spectrum of relaxations from the subspace spanned by the left singular vectors. Previously, a sparse recovery problem was used for target classification with EMI data. This chapter develops (9.4), which is the following sparse recovery problem defined within the low-rank framework,

$$\min_{\mathbf{C}_{\vec{\mathbf{W}}}} \|\mathbf{U}_{\mathbf{M}}\mathbf{\Sigma}_{\mathbf{M}} - \mathbf{A}_{\boldsymbol{P}}\mathbf{C}_{\vec{\mathbf{W}}}\|_F^2 + \lambda\|\mathbf{C}_{\vec{\mathbf{W}}}^{\ell_2}\|_1 \tag{12.5}$$

A comparison to the well-known angle-of-arrival problem for array processing illustrates the difficulties of sparse recovery for EMI data and shows that classical algorithms such as MUSIC and greedy sparse inversion algorithms fail when used on EMI data. A novel nonnegative rotational least-squares solver is developed for EMI data which removes the ℓ_1 constraint and replaces it with a nonnegative constraint based on the low-rank model's connection with the SVD. Results of the inversion process on simulated targets are shown in Figs. 9.8 and 9.9. In addition, the nonnegative rotational least-squares solver is compared to LARS (least angle regression), IAA (iterative adaptive approach), and FOCUSS, which are competing multi-measurement sparse recovery algorithms. The inversion methods are accurate down to 10dB SNR when the rank is known, and the new nonnegative rotational least squares algorithm consistently outperforms the standard sparse solvers.

Chapter 10 uses the left singular vectors that contain the sum of tensors as a new method for target classification. A maximum likelihood classifier is designed in (10.7) as

$$\min_{\boldsymbol{\mathcal{X}}} \min_{\mathbf{R},\lambda_{\boldsymbol{QU}}} \|\mathbf{U}_{\mathbf{M}}\mathbf{\Sigma}_{\mathbf{M}} - \lambda_{\boldsymbol{QU}}\vec{\boldsymbol{X}}\mathbf{R}\|_F^2 \tag{12.6}$$

under an ideal EMI sensor assumption. Classification results on the reference targets and

ten simulated targets are shown for fixed target rotation and various target rotations in Figs. 10.10 and 10.6, respectively. The simulated separable targets are classified reliably down to 30dB SNR when the target orientation is fixed. The impact of a non-ideal EMI sensor is also discussed.

Finally, Ch. 11 discusses the ability of the low-rank framework to recover the target's location and orientation tensors. Figure 11.1 shows that the location search space in the low-rank framework is a convex problem which can lend it self to computationally efficient search algorithms. Figure 11.2 shows the performance of the tensor recovery relative to the method that was used for recovering the row and column subspaces. Section 11.2.2 shows that the orientation tensor can be converted back to the original EMI model and the rank can be accurately estimated. The variation between this rank and the rank of the low-rank model provides a clear indication for degenerate EMI targets. These results are shown for the reference targets.

This thesis developed a new low-rank model for EMI data and compared it to previous EMI multi-measurement models. The low-rank model has shown promise for creating new signal processing applications that can isolate targets from strong interference, detect targets, estimate the rank, recover EMI target features, classify targets, localize targets, and determine the target's orientation. Results have been demonstrated for all of the different framework applications and multiple pre-existing signal processing algorithms have been integrated into the EMI processing framework. The results presented in this thesis indicate that the new low-rank framework can increase the processing gain by tens of dBs compared to previous processing techniques, provides a natural separation of information extraction for targets, and leads to straightforward processing techniques that require minimal computations to obtain similar or superior performance. Many of these findings and results have been published [29, 27, 26, 46, 20, 47, 28, 48, 49].

Appendices

APPENDIX A

DETAILS OF EMI MODEL

A.1 EMI Response of a Single Eddy Current

The SoD model for EMI targets was provided in (2.2). This equation is based on a superposition of unique relaxation frequencies in the target; however, this is still a simplification of the sum of dipole model. To arrive at the complete SoD model, it is useful to derive the single dipole model. This discussion will focus on a dipole formed by induced eddy currents. This means that it covers all relaxations from (2.2) except the special case of $\mathcal{m}_0$ which is due to the magnetic permeability of the target.

A single eddy current dipole can be thought of as a loop of electrical current induced by a magnetic field. To conceptualize an eddy current, it is possible to use a single wire loop as shown in Fig. A.1. The loop represents the path that an induced electrical current will take when a time-varying magnetic field is present. The electrical path can be described by a unit vector, $\mathbf{u}_d$, in a direction normal to the electrical path[1].

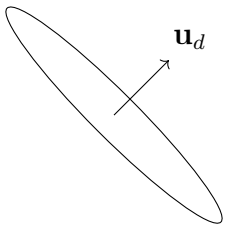

Figure A.1: Single wire loop to visualize an eddy current dipole

The unit vector $\mathbf{u}_d$ has a very specific structure. For a single dipole, it is useful to select a coordinate system where $\mathbf{u}_d$ aligns with the x-axis in an x-y-z coordinate system. This creates a unit vector in the "target's coordinate system" such that $\vec{\mathbf{u}}_d = [1, 0, 0]^T$. From $\vec{\mathbf{u}}_d$,

[1]Note that the sign of $\mathbf{u}_d$ is arbitrary because there is no right-hand rule until the the magnetic field is present. Also, it will be shown that this sign has no impact on the model once developed.

an arbitrary coordinate system can be obtained by applying an Euler angles rotation (e.g., roll-pitch-yaw). This is defined with three rotation angles, φ-θ-ψ, that create three rotation matrices

$$\mathbf{R}_{\varphi} = \begin{bmatrix} 1 & 0 & 0 \\ 0 & \cos(\varphi) & -\sin(\varphi) \\ 0 & \sin(\varphi) & \cos(\varphi) \end{bmatrix} \tag{A.1a}$$

$$\mathbf{R}_{\theta} = \begin{bmatrix} \cos(\theta) & 0 & \sin(\theta) \\ 0 & 1 & 0 \\ -\sin(\theta) & 0 & \cos(\theta) \end{bmatrix} \tag{A.1b}$$

$$\mathbf{R}_{\psi} = \begin{bmatrix} \cos(\psi) & -\sin(\psi) & 0 \\ \sin(\psi) & \cos(\psi) & 0 \\ 0 & 0 & 1 \end{bmatrix}. \tag{A.1c}$$

These rotations can be applied to the target coordinate system to create an arbitrary coordinate system using

$$\mathbf{u}_d = \mathbf{R}\vec{\mathbf{u}_d} = \mathbf{R}_{\psi}\mathbf{R}_{\theta}\mathbf{R}_{\varphi}\vec{\mathbf{u}_d} \tag{A.2}$$

where the rotation matrix $\mathbf{R}$ is equivalent to the product of Euler rotation matrices $\mathbf{R}_{\psi}\mathbf{R}_{\theta}\mathbf{R}_{\varphi}$.

When a time-varying magnetic field is present, it will induce an electrical current (the eddy current). Faraday's law states that the electromotive force (voltage) will be

$$\mathcal{V}(\omega) = j\omega \int_A \mathcal{B} dA = -j\omega\mu_0 A(\mathbf{u}_d{}^T \mathbf{h}_T) \tag{A.3}$$

where A is the area surrounded by the loop and μ_0 is the magnetic permeability of the space. This generates a current in the loop equal to

$$\mathcal{I}(\omega) = \frac{\mathcal{V}(\omega)}{R + j\omega L} = \frac{\mu_0 A}{L}\left(\frac{j\omega/\zeta}{1 + j\omega/\zeta}\right)(\mathbf{u}_d{}^T \mathbf{h}_T) \tag{A.4}$$

where R is the resistance of the loop, L is the self inductance of the loop, and the relaxation frequency is $\zeta = {}^{R}/_{L}$. This clearly shows how the $f(\omega)$ term connects to the physics of a single eddy current. The induced current creates the magnetic dipole moment

$$\boldsymbol{m}(\omega) = -A\mathcal{I}(\omega)\mathbf{u}_d = -\frac{\mu_0 A^2}{L} f(\omega)\mathbf{u}_d(\mathbf{u}_d{}^T\mathbf{h}_T) \tag{A.5}$$

where the direction of the field must repel the source field according to Lenz's Law.

The *magnetic polarizability* can be described from (A.5) as

$$\boldsymbol{\mathcal{M}}_{dipole} = -\alpha f(\omega)\mathbf{u}_d\mathbf{u}_d{}^T \tag{A.6}$$

where $\alpha = {}^{\mu_0 A^2}/_{L} \in \Re_+$. The directional tensor of a single dipole is defined as[2]

$$\boldsymbol{\mathcal{M}}_k = \mathbf{u}_d\mathbf{u}_d{}^T. \tag{A.7}$$

This illustrates why a single dipole's $\boldsymbol{\mathcal{M}}_k$ must be real, symmetric, and PSD.

The full SoD model is obtained by recognizing that each k$^{\text{th}}$ term in (2.2) is a summation of dipoles. This means that

$$\alpha_k f_k \boldsymbol{\mathcal{M}}_k = f_k \sum_i \alpha_i \mathbf{u}_{di}\mathbf{u}_{di}^T \tag{A.8}$$

where all of the dipoles with the same f_k characteristics are combined into a single term. The f_k terms remain unchanged in (A.8) and thus can be pulled out of the summation. This means that $\alpha_k\boldsymbol{\mathcal{M}}_k$ is PSD and symmetric because it is a summation of PSD, symmetric matrices $\sum_i \alpha_i \mathbf{u}_{di}\mathbf{u}_{di}^T$. A normalization strategy must be chosen to define the values α_k

[2]This also shows why the sign of $\mathbf{u}_d$ is arbitrary. It is only used in the context of $\mathbf{u}_d\mathbf{u}_d{}^T$ which cancels out the sign.

and $\mathcal{M}_k$. This thesis uses the normalization strategy

$$\|\mathcal{M}_k\|_2 = 1 \tag{A.9}$$

which forces the largest eigenvalue to be set to 1. This is consistent with (A.7), where a rank-one matrix is formed as the outer product of a unit vector with itself. For $\mathcal{M}_k$ matrices with a rank larger than one, the strongest direction will be an outer product of unit vectors. This normalization scheme implies that

$$\alpha_k = \|\sum_i \alpha_i \mathbf{u}_{di}\mathbf{u}_{di}^T\|_2. \tag{A.10}$$

A.2 Degenerate Target

Degenerate targets can be a common occurrence for man-made metallic targets. Mathematically, a degenerate target can be defined as a target with a *magnetic polarizability* that is invariant to a non-trivial rotation matrix[3]. This property can be written as

$$\mathcal{M} = \mathbf{R}\mathcal{M}\mathbf{R}^T \tag{A.11}$$

where $\mathbf{R} \in \Re^{3\times3}$ is a non-trivial rotation matrix. An alternative method for testing target degeneracy of ortho-point targets is to determine if $\mathcal{M}$ contains any repeating eigenvalues.

Degenerate targets are caused by a special form of symmetry. A simple example can best illustrate how a degenerate target is formed. Figure A.2 represents a target that is composed of three magnetic dipoles. The dipoles have the same strength, the same relaxation frequencies, and the three unit vectors lie in the same plane at equally spaced angles. Without loss of generality, the dipole unit vectors can be described as

[3]Non-trivial implying that the rotation matrix is not an identity matrix

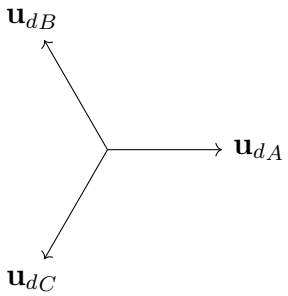

Figure A.2: Unit vectors of three dipoles that create a simple degenerate target.

$$\begin{aligned}
\mathbf{u}_{dA} &= \begin{bmatrix} \cos(0) & \sin(0) & 0 \end{bmatrix}^T \\
\mathbf{u}_{dB} &= \begin{bmatrix} \cos(2\pi/3) & \sin(2\pi/3) & 0 \end{bmatrix}^T \\
\mathbf{u}_{dC} &= \begin{bmatrix} \cos(4\pi/3) & \sin(4\pi/3) & 0 \end{bmatrix}^T
\end{aligned} \tag{A.12}$$

and all of the α_i terms in (A.8) can be set to 1. Because all of the relaxation frequencies are the same, the $\mathcal{M}_k$ component is the only one of interest, so (A.8) evaluates to

$$\begin{aligned}
\mathcal{M}_k = &\begin{bmatrix} \cos^2(0) & \cos(0)\sin(0) & 0 \\ \cos(0)\sin(0) & \sin^2(0) & 0 \\ 0 & 0 & 0 \end{bmatrix} \\
+ &\begin{bmatrix} \cos^2(2\pi/3) & \cos(2\pi/3)\sin(2\pi/3) & 0 \\ \cos(2\pi/3)\sin(2\pi/3) & \sin^2(2\pi/3) & 0 \\ 0 & 0 & 0 \end{bmatrix} \\
+ &\begin{bmatrix} \cos^2(4\pi/3) & \cos(4\pi/3)\sin(4\pi/3) & 0 \\ \cos(4\pi/3)\sin(4\pi/3) & \sin^2(4\pi/3) & 0 \\ 0 & 0 & 0 \end{bmatrix}.
\end{aligned} \tag{A.13}$$

Using the identity $\cos(a)\sin(a) = 1/2\sin(2a)$, the off-diagonal terms become $1/2\sum_k \sin(2ak)$. This summation around the unit circle is equal to 0, which causes the off-diagonal term to be 0. The diagonal terms each consist of a summation of $\sum_k \cos^2(ak)$ or $\sum_k \sin^2(ak)$,

respectively, and these two sums are equal[4] when $a = 2\pi/3$. This means that once normalized,

$$\mathcal{M}_k = \begin{bmatrix} 1 & 0 & 0 \\ 0 & 1 & 0 \\ 0 & 0 & 0 \end{bmatrix} \tag{A.14}$$

which satisfies the degenerate conditions of (A.11) for any rotation matrix that operates on the first two dimensions.

Notice that (A.14) meets the qualifications for a degenerate target. The matrix $\mathcal{M}_k$ remains unchanged for any non-trivial rotation matrix that corresponds to the model

$$\begin{bmatrix} \mathbf{R}_2 & \begin{matrix} 0 \\ 0 \end{matrix} \\ \begin{matrix} 0 & 0 \end{matrix} & 1 \end{bmatrix} \begin{bmatrix} 1 & 0 & 0 \\ 0 & 1 & 0 \\ 0 & 0 & 0 \end{bmatrix} \begin{bmatrix} \mathbf{R}_2^T & \begin{matrix} 0 \\ 0 \end{matrix} \\ \begin{matrix} 0 & 0 \end{matrix} & 1 \end{bmatrix} \tag{A.15}$$

where $\mathbf{R}_2 \in \Re^{2\times 2}$ is a non-trivial rotation matrix. Alternatively, $\mathcal{M}_k$ has two identical eigenvalues.

This example demonstrates how a symmetric target's *magnetic polarizability* can be greatly simplified. More complicated symmetric targets are also affected in the same manner. For instance, a cylinder will have the same degenerate nature as the above target, but it can have an infinite number of dipoles. The main condition for degenerate targets is that the dipoles are spread in a uniform manner around the unit circle. This causes the off-diagonal terms to cancel when the coordinate system is aligned with the axis of symmetry. This symmetry can also be trivially extended to multiple relaxation frequencies.

[4]For $a = 2\pi/3$, $\sum_k \cos^2(ak) = 1 + 0.5^2 + 0.5^2 = 1.5$, and $\sum_k \sin^2(ak) = 0 + 0.866^2 + 0.866^2 = 1.5$. Aside: same is true for $a = \pi/3$.

A.3 Specialized Autonne-Takagi Factorization

This derivation shows that it is possible to recover the diagonal model of the *magnetic polarizability* that is present under the ortho-point target assumption. For time domain sensors, $\mathcal{M}$ is a real-valued matrix which means that $\vec{\mathbf{\Lambda}}$ will also be real-valued. For frequency domain sensors, $\mathcal{M}$ becomes a complex matrix where the complex terms come from the complex-valued $\vec{\mathbf{\Lambda}}$. In both cases, $\mathcal{M}$ is symmetric (but not Hermitian symmetric in the complex case). This derivation will focus on the complex-valued $\mathcal{M}$ and the real-valued $\mathcal{M}$ can be considered a special case where all of the imaginary components are set to 0.

Theorem 1 *A complex-valued, symmetric matrix $\mathcal{M}$ can be factorized into $\mathcal{M} = \mathbf{U}\mathbf{D}\mathbf{U}^T$ where $\mathbf{U} \in \mathfrak{C}^{3\times 3}$ is a unitary matrix and $\mathbf{D} \in \Re^{3\times 3}$ is a nonnegative, diagonal matrix.*

This Theorem is known as Autonne-Takagi factorization and exists for any symmetric, complex-valued matrix. Note that $\mathbf{U}$ is complex, but its transpose (not Hermitian) appears in the factorization; in other words, the factorization is not an eigenvalue decomposition.

Lemma 1 *The **magnetic polarizability** of an EMI target can be modeled by a sum of magnetic dipoles (SOD) and is written as $\mathcal{M} = \sum_{k=0}^{K} c_k \mathcal{M}_k$ where $c_k \in \mathfrak{C}$ and $\mathcal{M}_k \in \Re^{3\times 3}$ is a symmetric matrix.*

This is the sum of dipoles model shown in (2.4) where $c_k = -\alpha_k f_k$. Note that the c_k term is heavily constrained based on the electromagnetic properties, and this model assumes a point source for the EMI target. [2]

Lemma 2 *Under the ortho-point assumption, there exists a SOD for each* magnetic polarizability *where all of the dipoles can be jointly diagonalized by the same unitary matrix.*

Lemma 1 states that

$$\mathcal{M} = \sum_{k=0}^{K} c_k \mathcal{M}_k, \tag{A.16}$$

where $\boldsymbol{\mathcal{m}}$ and c_k are the only complex terms. Due to $\boldsymbol{\mathcal{m}}_k$ being real-valued, symmetric, and positive semidefinite, it is possible to represent each one as

$$\boldsymbol{\mathcal{m}}_k = \vec{\mathbf{E}}_k \vec{\boldsymbol{\Lambda}}_k \vec{\mathbf{E}}_k^T, \tag{A.17}$$

where $\vec{\mathbf{E}}_k \in \Re^{3\times 3}$ is unitary matrix and $\vec{\boldsymbol{\Lambda}}_k \in \Re^{3\times 3}$ is diagonal and nonnegative. On the other hand, Lemma 2 states that all the $\boldsymbol{\mathcal{m}}_k$ matrices are diagonalizable by the same real unitary matrix $\vec{\mathbf{E}}$, i.e.,

$$\boldsymbol{\mathcal{m}}_k = \vec{\mathbf{E}} \vec{\boldsymbol{\Lambda}}_k \vec{\mathbf{E}}^T. \tag{A.18}$$

After substituting (A.18) in (A.16), we get a summation expression for $\boldsymbol{\mathcal{m}}$

$$\boldsymbol{\mathcal{m}} = \sum_{k=0}^{K} c_k \vec{\mathbf{E}} \vec{\boldsymbol{\Lambda}}_k \vec{\mathbf{E}}^T \tag{A.19}$$

According to the Autonne-Takagi Theorem, the PSD symmetric matrix $\boldsymbol{\mathcal{m}}$ can be expressed as $\boldsymbol{\mathcal{m}} = \mathbf{U}\mathbf{D}\mathbf{U}^T$, so

$$\mathbf{U}\mathbf{D}\mathbf{U}^T = \vec{\mathbf{E}} \underbrace{\left(\sum_{k=0}^{K} c_k \vec{\boldsymbol{\Lambda}}_k \right)}_{\text{diagonal, but complex}} \vec{\mathbf{E}}^T = \vec{\mathbf{E}} \vec{\boldsymbol{\Lambda}} \vec{\mathbf{E}}^T \tag{A.20}$$

where $\mathbf{D}$ is diagonal with nonnegative real entries and $\mathbf{U}$ is complex. One important fact embedded in (A.20) is the following theorem:

Theorem 2 *There exists a decomposition of every* magnetic polarizability *under the ortho-point assumption that can be written as* $\boldsymbol{\mathcal{m}} = \vec{\mathbf{E}} \vec{\boldsymbol{\Lambda}} \vec{\mathbf{E}}^T$ *where* $\vec{\mathbf{E}} \in \Re^{3\times 3}$ *is unitary and* $\vec{\boldsymbol{\Lambda}}_k \in \mathfrak{C}^{3\times 3}$ *is diagonal.*

The diagonal of $\vec{\boldsymbol{\Lambda}}$ can have a large variety of complex values based on the physical target. To match the two sides of (A.20), we need the following property

Lemma 3 *The* magnetic polarizability *of any ortho-point EMI target has an Autonne-*

Takagi factorization where the unitary matrix is $\mathbf{U} = \vec{\mathbf{E}}\mathbf{B}$ *where* $\vec{\mathbf{E}} \in \Re^{3\times 3}$ *is unitary and* $\mathbf{B} \in \mathfrak{C}^{3\times 3}$ *is diagonal with each diagonal entry having a magnitude of one.*[5]

Based on Lemma 3, the matrices $\mathbf{B}$ and $\mathbf{D}$ can be obtained from $\vec{\mathbf{\Lambda}}$ as follows

$$\mathcal{m} = \mathbf{U}\mathbf{D}\mathbf{U}^T = \vec{\mathbf{E}}\mathbf{B}\mathbf{D}\mathbf{B}\vec{\mathbf{E}}^T = \vec{\mathbf{E}}\vec{\mathbf{\Lambda}}\vec{\mathbf{E}}^T \tag{A.21a}$$

$$\Rightarrow \quad \mathbf{B}\mathbf{D}\mathbf{B} = \vec{\mathbf{\Lambda}} \tag{A.21b}$$

Since $\mathbf{B}$ and $\mathbf{D}$ are diagonal, they commute and $\mathbf{B}\mathbf{D}\mathbf{B} = \mathbf{D}\mathbf{B}^2$. If the entries of $\vec{\mathbf{\Lambda}}$ are expressed in polar form with magnitude and phase, then the entries of $\mathbf{D}$ are the magnitude, which is real and nonnegative, and the entries of $\mathbf{B}$ are $\exp\{j\frac{1}{2}\text{Phase}\{\vec{\mathbf{\Lambda}}\}\}$ which is complex with unit magnitude.

A.4 Autonne-Takagi Algorithm

```
function [U,D] = autonneTakagi(M)
[V1,lam] = eig(M'*M);
C = V1.'*M*V1;   % C is guaranteed to be diagonal
Us = diag(exp(-0.5j*angle(diag(C))));
U = (Us*V1.')';
D = real(U'*M*conj(U));
end
```

The matrix $\boldsymbol{C}$ is guaranteed to be diagonal because $\mathcal{m}^H = \bar{\mathcal{m}}$, the conjugate of $\mathcal{m}$. Introducing the identity matrix $\bar{\boldsymbol{V}}_1\bar{\boldsymbol{V}}_1^H$ in the following equation, we obtain

$$\mathbf{\Lambda} = \boldsymbol{V}_1^H\mathcal{m}^H\mathcal{m}\boldsymbol{V}_1 = \boldsymbol{V}_1^H\bar{\mathcal{m}}\mathcal{m}\boldsymbol{V}_1 = \boldsymbol{V}_1^H\bar{\mathcal{m}}\bar{\boldsymbol{V}}_1\bar{\boldsymbol{V}}_1^H\mathcal{m}\boldsymbol{V}_1 \tag{A.22}$$

The terms $\boldsymbol{V}_1^H\bar{\mathcal{m}}\bar{\boldsymbol{V}}_1$ and $\boldsymbol{C} = \bar{\boldsymbol{V}}_1^H\mathcal{m}\boldsymbol{V}_1$ are complex conjugates. In addition, they must

[5]Matrix $\vec{\mathbf{E}}\mathbf{B}$ is unitary, since $(\vec{\mathbf{E}}\mathbf{B})^H(\vec{\mathbf{E}}\mathbf{B}) = \bar{\mathbf{B}}(\vec{\mathbf{E}}^T\vec{\mathbf{E}})\mathbf{B} = \bar{\mathbf{B}}\mathbf{B} = \mathbf{I}$. Bar denotes complex conjugate.

both be diagonal, because their product is a diagonal matrix $\mathbf{\Lambda}$ with nonnegative entries.

For ortho-point targets, we would like to be able to test the output of the Autonne-Takagi factorization and determine whether the following is true

$$\mathbf{U}\mathbf{D}\mathbf{U}^T = \mathcal{M} = \vec{\mathbf{E}}\vec{\mathbf{\Lambda}}\vec{\mathbf{E}}^T \tag{A.23}$$

where $\mathbf{D}$ is diagonal and real, $\vec{\mathbf{E}}$ is real, and $\vec{\mathbf{\Lambda}}$ is diagonal and complex. One approach is to use $\mathbf{U} = \vec{\mathbf{E}}\mathbf{B}$ from Lemma 3, where the entries of the diagonal matrix $\mathbf{B}$ are complex exponentials, $\exp\{j\frac{1}{2}\text{Phase}\{\vec{\mathbf{\Lambda}}\}\}$. Since $\mathbf{B}$ is a phase-only diagonal matrix, it can be constructed from the diagonal of $\mathbf{U}$ by extracting the phase of $\text{diag}\{\mathbf{U}\}$. It turns out that it could also be constructed from the phase of any row of the $\mathbf{U}$ matrix as long as nonzero terms are used to estimate the phase. The ortho-point test requires that $\vec{\mathbf{E}} = \mathbf{U}\bar{\mathbf{B}}$ be a purely real matrix, as in the MATLAB code below:

```
% Test for ortho-point: E real and E*Lam*E.' = M = U*D*U.'
[U,D] = autonneTakagi(M)
B = diag(exp(j*diag(angle(U)))); %
Lam = B*D*B;  % NOT needed for test, (complex) eigenvalues of M
E = U*conj(B);
% E has to be real for ortho-point
if (norm(imag(E),'fro')>1e-10), error('E is not REAL'), end
```

A.4.1 Applying the Ortho-Point Target Test

The Autonne-Takagi factorization can be used for practical applications as a test for ortho-point targets. To demonstrate this, the Autonne-Takagi factorization was applied to the ortho-point target RT-02 and the general target RT-07. The *magnetic polarizability* was measured at 9kHz. Both targets were rotated 45° in the roll direction so they are no longer aligned with the measured coordinate system. The Autonne-Takagi factorization is similar

to an eigenvalue decomposition where repeated eigenvalues give rise to subspaces spanned by two or more eigenvectors, so the orthonormal eigenvector basis is not unique. The result is a non-unique unitary matrix. To make the unitary matrix unique, the amplitudes of the dipoles in the reference targets were altered to create unique diagonal components.

Ortho-Point Target

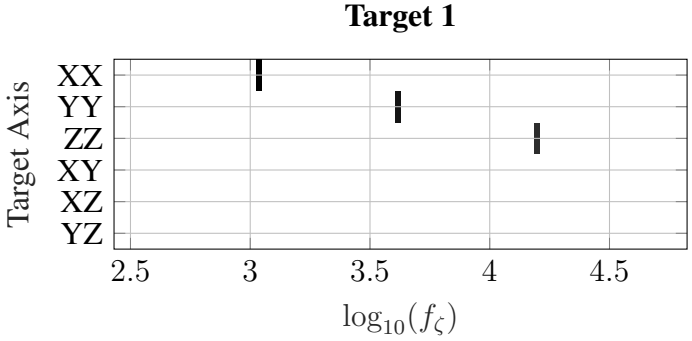

Figure A.3: Example ortho-point target for Autonne-Takagi factorization.

RT-02 was used as an example ortho-point target. The target is shown in Fig. A.3. Each dipole was weighted ($[1.1, 1, 0.9]$ respectively) to force a unique factorization. The *magnetic polarizability* is

$$\mathcal{M} = \begin{bmatrix} 0.62e^{i1.33\pi} & 0 & 0.80e^{i1.90\pi} \\ 0 & 1.00e^{i1.27\pi} & 0 \\ 0.80e^{i1.90\pi} & 0 & 0.62e^{i1.33\pi} \end{bmatrix}. \tag{A.24}$$

The Autonne-Takagi factorization is applied to the *magnetic polarizability* to obtain

$$\mathbf{U} = \begin{bmatrix} 0.71e^{i1.83\pi} & 0.71e^{i1.54\pi} & 0 \\ 0 & 0 & 1.00e^{i0.64\pi} \\ 0.71e^{i1.83\pi} & 0.71e^{i0.54\pi} & 0 \end{bmatrix} \tag{A.25a}$$

$$\mathbf{D} = \begin{bmatrix} 0.90 & 0 & 0 \\ 0 & 1.10 & 0 \\ 0 & 0 & 1.00 \end{bmatrix} \tag{A.25b}$$

where $\mathcal{M} = \mathbf{U}\mathbf{D}\mathbf{U}^T$. By extracting the common phase from each column of $\mathbf{U}$, the matrices

$$\vec{\mathbf{E}} = \begin{bmatrix} -0.71 & -0.71 & 0 \\ 0 & 0 & 1.00 \\ -0.71 & 0.71 & 0 \end{bmatrix} \tag{A.26a}$$

$$\mathbf{B} = \begin{bmatrix} e^{i0.83\pi} & 0 & 0 \\ 0 & e^{i0.54\pi} & 0 \\ 0 & 0 & e^{i0.64\pi} \end{bmatrix} \tag{A.26b}$$

can be formed where $\mathbf{U} = \vec{\mathbf{E}}\mathbf{B}$, $\vec{\mathbf{E}} \in \Re^{3\times 3}$, and $\mathbf{B}$ is a diagonal matrix containing the extracted phases. The fact that $\mathbf{U}$ can be separated in this manner is possible because it is ortho-point [6]. Now $\vec{\mathbf{\Lambda}} = \mathbf{B}\mathbf{D}\mathbf{B}$ is a complex diagonal matrix with the amplitude of $\mathbf{D}$ and twice the phase of $\mathbf{B}$

$$\vec{\mathbf{\Lambda}} = \begin{bmatrix} 0.90e^{i1.66\pi} & 0 & 0 \\ 0 & 1.10e^{i1.08\pi} & 0 \\ 0 & 0 & 1.00e^{i1.28\pi} \end{bmatrix}. \tag{A.27}$$

General Target

RT-07 was used as an example general target that is not ortho-point. The target is shown in Fig. A.4. Each dipole was weighted ($[1, 1.1]$ respectively) to force a unique factorization.

[6] This is not proof, as a general target can be formulated like this for special measurement frequencies when only a few dipoles dominate the *magnetic polarizability* . However, only ortho-point targets can be separated like this for all frequencies.

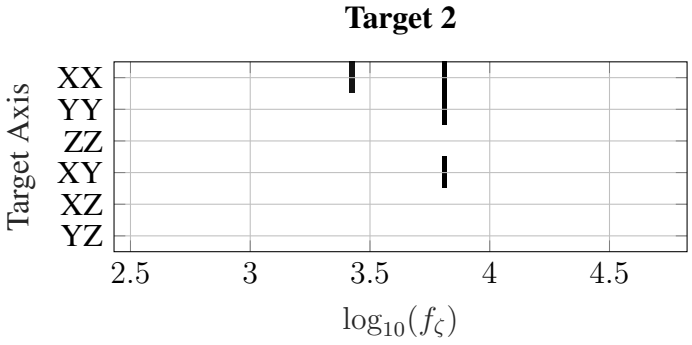

Figure A.4: Example general target for Autonne-Takagi factorization.

The *magnetic polarizability* is

$$\mathcal{M} = \begin{bmatrix} 0.99e^{i1.29\pi} & 0.78e^{i1.40\pi} & 0.99e^{i0.29\pi} \\ 0.78e^{i1.40\pi} & 1.10e^{i1.40\pi} & 0.78e^{i0.40\pi} \\ 0.99e^{i0.29\pi} & 0.78e^{i0.40\pi} & 0.99e^{i1.29\pi} \end{bmatrix}. \tag{A.28}$$

The Autonne-Takagi factorization is applied to the *magnetic polarizability* to obtain

$$\mathbf{U} = \begin{bmatrix} 0.71e^{i0.63\pi} & 0.39e^{i0.57\pi} & 0.59e^{i0.65\pi} \\ 0 & 0.83e^{i1.64\pi} & 0.56e^{i0.72\pi} \\ 0.71e^{i0.63\pi} & 0.39e^{i1.57\pi} & 0.59e^{i1.65\pi} \end{bmatrix} \tag{A.29a}$$

$$\mathbf{D} = \begin{bmatrix} 0 & 0 & 0 \\ 0 & 0.40 & 0 \\ 0 & 0 & 2.70 \end{bmatrix} \tag{A.29b}$$

where $\mathcal{M} = \mathbf{U}\mathbf{D}\mathbf{U}^T$. Attempting to extract the phase of the columns of $\mathbf{U}$ as before creates

$$\vec{\mathbf{E}} = \begin{bmatrix} 0.71e^{i0.00\pi} & 0.39e^{i1.97\pi} & 0.59e^{i1.98\pi} \\ 0 & 0.83e^{i1.03\pi} & 0.56e^{i0.04\pi} \\ 0.71e^{i0.00\pi} & 0.39e^{i0.97\pi} & 0.59e^{i0.98\pi} \end{bmatrix} \tag{A.30a}$$

$$\mathbf{B} = \begin{bmatrix} e^{i0.63\pi} & 0 & 0 \\ 0 & e^{i0.60\pi} & 0 \\ 0 & 0 & e^{i0.67\pi} \end{bmatrix} \tag{A.30b}$$

where $\mathbf{U} = \vec{\mathbf{E}}\mathbf{B}$. Note that a common phase does not exist for each column, so $\vec{\mathbf{E}}$ remains a complex-valued matrix. This is proof that RT-07 is not an ortho-point target. This can be used as a test to verify if the ortho-point assumption is valid for a point target.

APPENDIX B

MAXIMUM LIKELIHOOD ESTIMATION OF MATRIX PARAMETERS

Maximum likelihood (ML) estimation is a powerful tool for estimating parameters. If the ML estimate can be found, then it is known to be consistent and efficient. The ML estimate is consistent, which means that given enough samples (or as the sample size approaches infinity) the estimated value corresponds to the true value being estimated. The ML estimate is also efficient which means that given enough samples its performance attains the Cramer-Rao lower bound (CRB) which is the minimum mean-squared error of all consistent estimators.

The EMI signal processing arrives at a common parameter estimation problem when exploiting the low-rank physical model. The recurring problem is

$$\mathbf{D} = \mathbf{B}\mathbf{C} + \mathbf{E} \tag{B.1}$$

where $\mathbf{D}$ is a matrix of measured data that can be modeled by $\mathbf{B}$ with an unknown linear scaling and rotation function $\mathbf{C}$ applied to it plus random Gaussian noise $\mathbf{E}$. The elements of the matrix $\mathbf{E}$ are assumed to be independent and identically distributed (i.i.d.) as $\mathcal{N}(0, \sigma^2)$. The following sections will derive several ML parameter estimates based on different assumptions on $\mathbf{C}$.

B.1 General Transformation

The ML estimate is found by defining the measured data distribution, identifying the parameters in the model, and then maximizing over the desired parameters. Based on the

model in (B.1), the measured data distribution can be written as

$$p(\mathbf{D} \mid \mathbf{B}, \mathbf{C}, \sigma^2) = \frac{1}{\sqrt{(2\pi\sigma^2)^N}} e^{-\frac{1}{2\sigma^2}\|\mathbf{D}-\mathbf{BC}\|_F^2} \tag{B.2}$$

which is a multivariate Gaussian distribution based on $\mathbf{E}$, with a mean of $\mathbf{BC}$. The fact that the noise is i.i.d. allows the variance to be pulled out and the error to be described with a Frobenius norm instead of reshaping the data into a vector. To arrive at the expression in (B.2), a deterministic model has been used where $\mathbf{B}$ and $\mathbf{C}$ are assumed to be unknown, fixed parameters. For measured data, this same function is used as the likelihood function of the model parameters given the data and it will be written as $\ell(\mathbf{B} \mid \mathbf{D})$.

The ML estimate is found by maximizing the loglikelihood function

$$\max_{\mathbf{B}} \mathcal{L}\{\mathbf{B}\} = \max_{\mathbf{B}} \ln \ell(\mathbf{B} \mid \mathbf{D}) = \max_{\mathbf{B}} \frac{N}{2}\ln(2\pi) + \frac{N}{2}\ln(\sigma^2) - \frac{1}{2\sigma^2}\|\mathbf{D}-\mathbf{BC}\|_F^2. \tag{B.3}$$

It is necessary to point out that when only the measurement $\mathbf{D}$ is available, then the extra parameters $\mathbf{C}$ and σ^2 are also unknown. These are known as nuisance parameters. During this work, it will be assumed that the noise power (σ^2) can be obtained through external information.[1] This still leaves the nuisance parameter $\mathbf{C}$ in the equation. A common technique to deal with nuisance parameters that will be used in this work is to maximize over them along with the desired parameter. This essentially becomes a joint estimation problem, where the nuisance parameter solution can be ignored in the end result. This means the optimization problem of interest becomes

$$\min_{\mathbf{B},\mathbf{C}} \{-\mathcal{L}\{\mathbf{B}\}\} = \min_{\mathbf{B},\mathbf{C}} \|\mathbf{D}-\mathbf{BC}\|_F^2 \tag{B.4}$$

where the constant values have been ignored because they do not impact the optimization problem and the maximization has been switched to a minimization of $-\mathcal{L}\{\mathbf{B}\}$. Some-

[1] This is possible for the EMI data because of the noise subblocks created during the preprocessing stages.

times it is useful to further simplify (B.4) by expanding the norm into

$$\|\mathbf{D}-\mathbf{BC}\|_F^2 = \text{tr}\big((\mathbf{D}-\mathbf{BC})^T(\mathbf{D}-\mathbf{BC})\big) \tag{B.5a}$$

$$= \text{tr}\big(\mathbf{D}^T\mathbf{D}+\mathbf{C}^T\mathbf{B}^T\mathbf{BC}-\mathbf{D}^T\mathbf{BC}-\mathbf{C}^T\mathbf{B}^T\mathbf{D}\big) \tag{B.5b}$$

$$\propto \text{tr}\big(\mathbf{C}^T\mathbf{B}^T\mathbf{BC}\big)-2\text{tr}\big(\mathbf{D}^T\mathbf{BC}\big) \tag{B.5c}$$

where the constant terms of the norm have been dropped.

The first step in finding the optimal solution is to solve for the nuisance parameter $\mathbf{C}$ in terms of $\mathbf{B}$. This is done by setting $\frac{d}{d\mathbf{C}}\mathcal{L}\{\mathbf{B}\}=0$ and then solving for $\mathbf{C}_{opt}$. The derivative becomes

$$\frac{d}{d\mathbf{C}}\mathcal{L}\{\mathbf{B}\} = \frac{d}{d\mathbf{C}}\text{tr}\big(\mathbf{C}^T\mathbf{B}^T\mathbf{BC}\big)-2\text{tr}\big(\mathbf{D}^T\mathbf{BC}\big) \tag{B.6a}$$

$$= 2\mathbf{B}^T\mathbf{BC}-2\mathbf{B}^T\mathbf{D} \tag{B.6b}$$

which, when set equal to zero, yields the least-squares solution $\mathbf{C}_{opt}=(\mathbf{B}^T\mathbf{B})^{-1}\mathbf{B}^T\mathbf{D}$.

Now that $\mathbf{C}_{opt}$ is defined in terms of $\mathbf{B}$, it is possible to define $\mathcal{L}\{\mathbf{B}\}$ in terms of a single operator. This becomes

$$\min_{\mathbf{B}}\{-\mathcal{L}\{\mathbf{B}\}\} = \|\mathbf{D}-\mathbf{B}(\mathbf{B}^T\mathbf{B})^{-1}\mathbf{B}^T\mathbf{D}\|_F^2 \tag{B.7a}$$

$$= \|\boldsymbol{P}_{\mathbf{B}}^{\perp}\mathbf{D}\|_F \tag{B.7b}$$

where it is observed that the ML estimate is the one that leaves the least amount of energy when projected away from the subspace of $\mathbf{B}$. It can also be pointed out that (B.7) has multiple trivial solutions.[2] The only thing that prevents these trivial solutions is the fact that the model $\mathbf{B}$ is actually a physical model based on the parameter set $\boldsymbol{\Phi}$. In other

[2] Any matrix that spans the same subspace as the data will arrive at a global minimum solution of 0.

words, the ML estimation problem is actually

$$\min_{\mathbf{\Phi}} \|\boldsymbol{P}_{\mathbf{B}}^{\perp}(\mathbf{\Phi})\mathbf{D}\|_F \tag{B.8}$$

where the physical constraints of the model $\mathbf{B}(\mathbf{\Phi})$ can significantly restrict the solution space. However, the model parameter specifics vary based on the problem, so for all of the following derivations the intermediary step of forming the matrix $\mathbf{B}(\mathbf{\Phi})$ will be used and further model constraints will be combined during application.

Unfortunately, minimizing (B.7) is a nonlinear function with no guarantees of being convex and can have multiple local minima. It can however be easily solved by any unconstrained function minimization algorithm such as a gradient descent or downhill simplex approach.[3] An alternative approach to solving (B.4) discussed here is Alternating Least Squares (ALS). ALS has been successfully used in similar matrix completion problems such as Nonnegative Matrix Factorization (NMF) and has strong convergence properties for finding a local solution. ALS is related to Expectation-Maximization (EM) and Coordinate Descent methods. In these methods, one unknown parameter is assumed known while the other is optimized. The recently optimized variable is then fixed while the first parameter is optimized. These iterations continue until a convergence metric is achieved.

B.2 Invertible $\mathbf{C}$ Approximation

It was shown above that the optimal $\mathbf{B}$ could be found by using the projection matrix $\boldsymbol{P}_{\mathbf{B}}^{\perp}$. However, this requires creating a new projection matrix for multiple $\mathbf{B}$ during the search process. If $\mathbf{C}$ is invertible, or if an approximation of the inverse of $\mathbf{C}$ is allowed, then (B.7) can be simplified. Returning to the original model, it is possible to isolate the model mean $\mathbf{B}$ such that

$$\mathbf{B} = \mathbf{D}\mathbf{C}^{\dagger} + \mathbf{E}\mathbf{C}^{\dagger} \tag{B.9}$$

[3] This can be directly implemented with tools such as Matlab's fminunc or fminsearch functions.

where $\mathbf{C}^{\dagger} = \mathbf{C}^{-1}$ when possible, or is the pseudo inverse when necessary. It is also worth noting that a sign change is possible because $\mathbf{E}$ is a zero-mean random variable, and a sign change does not affect the model. This model leads to the minimization problem of

$$\min_{\mathbf{B},\mathbf{C}} \|\mathbf{B} - \mathbf{D}\mathbf{C}^{\dagger}\|_F^2 \tag{B.10}$$

as was shown above. This is only an approximate solution though because it is dependent on $\mathbf{E}\mathbf{C}^{\dagger}$ being i.i.d. noise. Unless $\mathbf{C}$ is a pure rotation matrix, this assumption is only an approximation.

Based on this approximation, the optimal nuisance parameter is $\mathbf{C}^{\dagger}_{opt} = (\mathbf{D}^T\mathbf{D})^{-1}\mathbf{D}^T\mathbf{B}$. Plugging this result back into (B.10) becomes

$$\min_{\mathbf{B}} \|\boldsymbol{P}^{\perp}_{\mathbf{D}}\mathbf{B}\|_F^2 \tag{B.11}$$

which has clear similarities to (B.7); however, now the projection matrix is unchanged while searching for the model parameter. This can potentially be used to reduce the computation cost of estimating the model parameters.

B.3 Rotation and Scale Transformation

In some applications, it is useful to restrict the nuisance parameters of the model when obtaining the ML solution. One such model of interest is when the data has only been altered by a rotation matrix and a scaling factor. This problem can be written mathematically as

$$\mathbf{D} = \mathbf{B}\mathbf{R}\boldsymbol{I}a + \mathbf{E} \tag{B.12}$$

where $\mathbf{R}$ is a square, orthonormal rotation matrix and $a \in \Re$ is a scaling factor. This creates the Gaussian distribution of

$$p(\mathbf{D} \mid \mathbf{B}, \mathbf{R}, a, \sigma^2) = \frac{1}{\sqrt{(2\pi\sigma^2)^N}} e^{-\frac{1}{2\sigma^2}\|\mathbf{D}-\mathbf{B}\mathbf{R}\boldsymbol{I}a\|_F^2} \tag{B.13}$$

that must be maximized. Using the same simplifications as before arrives at the minimization problem

$$\min_{\mathbf{B},\mathbf{R},a} \{-\mathcal{L}\{\mathbf{B}\}\} = \min_{\mathbf{B},\mathbf{R},a} \|\mathbf{D} - \mathbf{B}\mathbf{R}\boldsymbol{I}a\|_F^2 \tag{B.14}$$

where the first step is to optimize out the nuisance parameters of $\mathbf{R}$ and a.

In order to estimate $\mathbf{R}$, it is useful to point out that the scaling factor a can be moved in the equation to create

$$\min_{\mathbf{R}} \|\mathbf{D} - a\mathbf{B}\mathbf{R}\|_F^2 \tag{B.15}$$

where $a\mathbf{B}$ can be treated as a single known matrix. This becomes a classic problem of finding the optimal rotation matrix to align two matrices known as the Procrustes problem that has a known solution [50]. This rotation matrix can be found by taking the SVD of the matrix $a\mathbf{B}^T\mathbf{D}$ such that

$$\mathbf{U}\mathbf{\Sigma}\mathbf{V}^T = a\mathbf{B}^T\mathbf{D}. \tag{B.16}$$

Using this SVD, the optimal rotation matrix, $\mathbf{R}$, is given by computing

$$\mathbf{R} = \mathbf{V}\mathbf{U}^T. \tag{B.17}$$

It is also trivial to show that a in (B.16) will only effect the singular values $\mathbf{\Sigma}$. This means that the estimation of $\mathbf{R}$ is only dependent on the matrices $\mathbf{D}$ and $\mathbf{B}$.

An analytical expression for a can also be derived. Starting from the expression in (B.5), the $\mathbf{C}$ term can be replaced with $\mathbf{R}\boldsymbol{I}a$ and the scalar terms can be pulled out of the

trace operator to arrive at

$$\|\mathbf{D} - \mathbf{BR}\boldsymbol{I}a\|_F^2 \propto \text{tr}\big(\mathbf{R}^T\mathbf{B}^T\mathbf{BR}\big)a^2 - 2\text{tr}\big(\mathbf{D}^T\mathbf{BR}\big)a. \tag{B.18}$$

Taking the derivative of this loglikelihood function with respect to a becomes

$$\frac{d}{da}\{-\mathcal{L}\{\mathbf{B}\}\} = 2\text{tr}\big(\mathbf{R}^T\mathbf{B}^T\mathbf{BR}\big)a - 2\text{tr}\big(\mathbf{D}^T\mathbf{BR}\big) \tag{B.19}$$

which can be set to zero to arrive at the analytical solution for a of

$$a = \frac{\text{tr}\big(\mathbf{D}^T\mathbf{BR}\big)}{\text{tr}(\mathbf{R}^T\mathbf{B}^T\mathbf{BR})}. \tag{B.20}$$

These results show that given measurements of interest $\mathbf{D}$ and a candidate model $\mathbf{B}$, the nuisance parameters can be found with a few simple calculations by first determining $\mathbf{R}$ using (B.17) and then using the solution for $\mathbf{R}$ to calculate a using (B.20).

APPENDIX C

IMPORTANT DEFINITIONS

C.1 Important Equations

(2.1)	Traditional bilinear matrix-vector model of a single EMI measurement
(2.4)	Target's *magnetic polarizability* sum of dipole expansion
(2.5)	Dipole response for a frequency-domain sensor
(2.6)	Dipole response for a time-domain sensor
(2.7)	All-pass dipole response for a frequency-domain sensor
(2.9)	Sum of Dipole expansion for ortho-point targets
(2.13)	Diagonal representation of ortho-point target's *magnetic polarizability*
(3.5)	Joint diagonalization model for exploiting multiple measurements
(3.7)	DSRF matrix model for exploiting multiple measurements
(3.8)	Reshaping the bilinear measurement model to a linear product
(4.3)	Low-rank model
(4.4)	Low-rank model highlighting minimum rank
(4.6)	Vectorization of symmetric matrix
(4.9)	Low-rank model of ortho-point targets
(4.11)	Low-rank model of ortho-point targets with relaxation frequencies
(5.1)	General signal plus noise model for measurements.
(5.3)	Connection between the signal model and SVD
(5.8)	Signal plus noise model for the column subspace connection
(5.10)	Optimal column subspace solution when unconstrained
(5.11)	Signal plus noise model for the row subspace connection
(5.12)	Optimal row subspace solution when unconstrained
(5.14)	Solution for recovering the center terms from the SVD
(5.21)	Noise weightings depending on weightings chosen for subspace recovery
(5.22)	Subspace selection optimization problem
(5.25)	Sparse subspace creation optimization problem
(6.4)	Measurement model of an EMI system containing interference components

Continued on next page

Table C.1 – continued from previous page

(6.5)	Model of the EMI system's sensor self response
(6.7)	Model of the EMI system's soil response
(6.11)	Creation of measurement subblocks using projection matrices
(6.15)	Partitioning the DSRF matrix based on the soil response model
(6.16)	Definition of the proposed measurement dimension projection matrix
(6.17)	Definition of the proposed spatial dimension projection matrix
(6.20)	Improved SNR calculation for $\mathbf{M_S}$
(6.22)	Separating the $\mathbf{M}_{\bar{\mathbf{G}}\mathbf{S}}^{\bar{\mathbf{R}}\mathbf{S}}$ subblock into a signal and noise portion
(6.24)	Increased SNR calculation for the low-rank exploited model of $\mathbf{M_S}$
(6.31)	Separating the $\mathbf{M}_{\mathbf{GG}}^{\bar{\mathbf{R}}\mathbf{S}}$ subblock into a signal and noise portion
(7.4)	Matched Subspace Detection metrics for EMI data
(7.5)	Constant False Alarm Rate detection metric for EMI data using $\mathbf{M}_{\mathbf{GG}}^{\bar{\mathbf{R}}\mathbf{S}}$
(7.6)	Constant False Alarm Rate detection metrics for EMI data using $\mathbf{M}_{\mathbf{GG}}^{\bar{\mathbf{R}}\mathbf{S}}\mathbf{P}_{\mathbf{S}}^{T}$
(7.7)	Constant False Alarm Rate detection metrics for EMI data using $\mathbf{M}_{\bar{\mathbf{G}}\mathbf{S}}^{\bar{\mathbf{R}}\mathbf{S}}$
(7.8)	Constant False Alarm Rate detection metrics for EMI data using $\mathbf{\Sigma}_{\mathbf{S}}^{\mathbf{M_S}}$
(7.13)	Joint Detection metrics for EMI data
(8.3)	Model order estimation equations
(9.11)	NRLS optimization problem
(10.7)	Target subspace optimization problem used for classification

Table C.1: List of the some of the primary equations developed in this thesis.

C.2 Mathematical Variables

Dimensions	
K	Number of unique relaxation frequencies
N_T	Number of transmitter locations
N_R	Number of receiver locations
N	Number of total relative measurement positions
M	Number of measurements
R	Rank of a target (Number of linearly independent tensors)
$R_{\vec{\mathbf{\Lambda}}}$	Rank of a targets *magnetic polarizability*
O	Number of measurement dimensions kept in the projection to $\mathbf{M_S}$
P	Number of spatial dimensions kept in the projection to $\mathbf{M_S}$
Z	Number of DSRF terms sampled in $\mathbf{A}$
Single Measurement Model for EMI Target	
$\boldsymbol{m}$	*magnetic polarizability* matrix
$\mathbf{h}_T$	Transmitter magnetic scene
$\mathbf{h}_R$	Receiver magnetic scene
ℓ_{TX}	Location of the transmitter
ℓ_{RX}	Location of the receiver
ℓ_M	Location of the target
Δp	Location short-hand denoting $(\ell_{TX} - \ell_M)$ and $(\ell_{RX} - \ell_M)$
S	Single measurement of an EMI system
EMI Sensor Measurement Type	
t	Denotes time measurement from the sensor
ω	Denotes frequency measurement from the sensor
ϕ	Denotes general measurement from the sensor (either t or ω)
Sum of Dipole Model	
$\boldsymbol{m}_k$	Target's directional tensor for the k$^{\text{th}}$ dipole
f_k	Modeled interaction between the k$^{\text{th}}$ dipole and the primary electromagnetic field of the sensor
α_k	Positive magnitude for the strength of the k$^{\text{th}}$ dipole
$\mathbf{u}_d$	Unit vector of a magnetic dipole's normal vector
ζ	Relaxation frequency of a dipole
τ	Relaxation decay rate of a dipole

Continued on next page

Table C.2 – continued from previous page

$g(t)$	Transfer function for a dipole
$\mathcal{G}(s)$	Laplace transform of the transfer function for a dipole
Ortho-Point Target Model	
$\vec{\mathbf{E}}$	Rotation matrix to convert arbitrary x-y-z coordinates to target's coordinate system
$\vec{\mathbf{\Lambda}}_k$	Diagonal directional tensor for the k$^{\text{th}}$ dipole in the target's coordinate system
$\vec{\mathbf{\Lambda}}$	Diagonal *magnetic polarizability* of a ortho-point target in the target's coordinate system
$\vec{\mathbf{h}}_T$	Transmitter magnetic scene defined in the target's coordinate system
$\vec{\mathbf{h}}_R$	Receiver magnetic scene defined in the target's coordinate system
Reference Targets	
$\mathcal{A}$	Set of relaxation frequencies (and amplitudes) defined for reference targets
Measurement Model for EMI Targets	
$\mathbf{S}$	Multiple measurements combined into a large matrix or tensor
Joint Diagonalization	
$\boldsymbol{\ell}_{\boldsymbol{TX}}$	Vector of all transmitter locations
$\boldsymbol{\ell}_{\boldsymbol{RX}}$	Vector of all receiver locations
$\mathbf{H}_T$	Expansion of transmitter magnetic scene to multiple locations
$\mathbf{H}_R$	Expansion of receiver magnetic scene to multiple locations
$\vec{\mathbf{H}}_T$	Expansion of transmitter magnetic scene to multiple locations in target's coordinate system
$\vec{\mathbf{H}}_R$	Expansion of receiver magnetic scene to multiple locations in target's coordinate system
$\mathbf{\Delta p}$	Vector of all relative measurement locations
Discrete Spectrum of Relaxation Frequencies	
g_k	Short hand for the target's position and orientation information
Least Squares	
$\mathbf{m}$	Linearized form of $\mathcal{M}$
$\mathbf{h}$	Linearized form for the bilinear product of $\mathbf{h}_R$ and $\mathbf{h}_T$
$\mathbf{H}$	Expansion of linearized magnetic scenes to multiple locations
Low-rank Model	
$\mathbf{F}$	Matrix of active relaxation frequencies in a target
$\mathbf{G}$	Matrix of *tensor amplitudes* for a target

Continued on next page

Table C.2 – continued from previous page

$\mathbf{\Phi}$	Matrix of linearly independent tensor basis for a target
$\mathbf{W}$	Matrix of weights mapping tensor basis to relaxation frequencies for a target
$\vec{\lambda}^{\vec{\mathbf{\Lambda}}}$	Diagonal value of $\vec{\mathbf{\Lambda}}$ for ortho-point targets
$\vec{\mathbf{e}}$	Rotation vector of $\vec{\mathbf{E}}$ for ortho-point targets
$\mathfrak{e}^5$	Vectorized rotation tensor of $\vec{\mathbf{e}}$ for ortho-point targets
$\vec{\mathbf{\Phi}}$	Matrix of linearly independent tensor basis aligned with a ortho-point target's coordinate system
$\vec{\boldsymbol{x}}_{\vec{\mathbf{\Lambda}}}$	Vector of the diagonal values of $\vec{\mathbf{\Lambda}}$ for ortho-point targets
$\vec{\boldsymbol{D}}$	Matrix combining degenerate tensor basis for ortho-point targets
$\vec{\boldsymbol{x}}$	Vector of the unique diagonal values of $\vec{\mathbf{\Lambda}}$ for ortho-point targets
$\vec{\mathbf{W}}$	Matrix of weights mapping tensor basis to relaxation frequencies for ortho-point targets
Low-rank Framework	
$\mathbf{M}$	Measurement matrix obtained by an EMI sensor
$\mathcal{E}$	Gaussian noise matrix that is added to $\mathbf{M}$
σ_ϵ^2	Noise variance of each noise sample
$\mathbf{U_M}$	Left singular vectors of the measured data
$\mathbf{\Sigma_M}$	Singular values of the measured data
$\mathbf{V_M}$	Right singular vectors of the measured data
$\mathcal{E}_\mathbf{U}$	Gaussian noise matrix for the left singular vector model
$\mathcal{E}_\mathbf{V}$	Gaussian noise matrix for the right singular vector model
$\mathbf{B_U}$	Symmetric, PSD matrix in the middle of the low-rank model of $\mathbf{M}\mathbf{M}^T$
$\mathbf{B_V}$	Symmetric, PSD matrix in the middle of the low-rank model of $\mathbf{M}^T\mathbf{M}$
$\mathbf{Q_U}$	Symmetric, PSD matrix equal to $\mathbf{B}_\mathbf{U}^{1/2}$ for the left singular vectors
$\mathbf{Q_V}$	Symmetric, PSD matrix equal to $\mathbf{B}_\mathbf{V}^{1/2}$ for the right singular vectors
$\mathbf{R}$	Generic orthonormal unitary matrix
$\mathbf{C_U}$	Rectangular matrix combining $\mathbf{Q_U}$ with the relevant internal matrices of the low-rank model
$\mathbf{C_V}$	Rectangular matrix combining $\mathbf{Q_V}$ with the relevant internal matrices of the low-rank model
$\mathbf{U_S}$	Left singular vectors of the target response
$\mathbf{\Sigma_S}$	Singular values of the target response
$\mathbf{V_S}$	Right singular vectors of the target response

Continued on next page

Table C.2 – continued from previous page

Subspace Recovery	
$\boldsymbol{\mathcal{H}}$	Set of all possible $\mathbf{H}$
$\mathbf{A}$	Over-complete dictionary of DSRF terms
$\vec{\mathbf{W}}_{\mathbf{A}}$	Sparse matrix of weights mapping tensor basis to DSRF dictionary
$\mathbf{C}_{\vec{\mathbf{W}}}$	Rectangular matrix combining $\mathbf{Q}_{\mathbf{U}}$ with the sparse $\vec{\mathbf{W}}_{\mathbf{A}}$ weightings
$\mathbf{T}$	Constrained subspace matrix for the model that has dimension equal to the rank
SVD Perturbation	
$\sigma_{\mathbf{M}}$	Single singular value from $\mathbf{\Sigma}_{\mathbf{M}}$
$\sigma_{\mathbf{S}}$	Single singular value from $\mathbf{\Sigma}_{\mathbf{S}}$
$\overline{\sigma_{\mathbf{M}} - \sigma_{\mathbf{S}}}$	The average error between the signal and measured singular values
$\mathbf{\Sigma}_{\mathcal{E}}$	Singular values that makeup the noise dimensions of $\mathbf{\Sigma}_{\mathbf{M}}$
δ_{σ}	The difference between the weakest target singular value and the strongest noise singular value
$\boldsymbol{P}_{\mathbf{V}_{\mathbf{M}}}$	Projection matrix into the $\mathbf{V}_{\mathbf{M}}$ subspace
$\boldsymbol{P}_{\mathbf{V}_{\mathbf{S}}}$	Projection matrix into the $\mathbf{V}_{\mathbf{S}}$ subspace
δ_{σ}	The difference between the weakest target singular value and the strongest noise singular value
Interference Model	
$\tilde{m}$	Complex-valued frequency-domain EMI system measurement
$\tilde{s}$	Complex-valued single value EMI target response
$\tilde{g}$	Complex-valued single value EMI soil response
$\tilde{r}$	Complex-valued single value EMI sensor self response
$\tilde{\epsilon}$	Complex-valued single value random noise measured by EMI system
σ_{ϵ}^2	Noise variance of an EMI sensor measurement
$\tilde{\mathbf{M}}$	Complex-valued measurement matrix obtained by a frequency-domain EMI system
$\tilde{\mathbf{S}}$	Complex-valued measurement matrix for EMI target response
$\tilde{\mathbf{G}}$	Complex-valued measurement matrix for EMI soil response
$\tilde{\mathbf{R}}$	Complex-valued measurement matrix for EMI sensor self response
$\tilde{\mathcal{E}}$	Complex-valued random noise matrix measured by EMI system
$\mathbf{S}$	Measurement matrix for EMI target response
$\mathbf{G}$	Measurement matrix for EMI soil response
$\mathbf{R}$	Measurement matrix for EMI sensor self response

Continued on next page

Table C.2 – continued from previous page

$\mathcal{E}$	Real-valued random noise matrix measured by EMI system
$\mathbf{1}$	Vector of all ones
$\boldsymbol{r}$	Vector representing the unknown sensor coupling response across the measurement dimension
ξ	Random variable describing the spatial dependence of an EMI system's soil response
g	Mean of the soil response's spatial distribution
σ_g^2	Variance of the soil response's spatial distribution
$\boldsymbol{\Psi}$	Model of the EMI system's known soil response model across measurements
$\boldsymbol{\Xi}$	Random variables representing the EMI system's soil response model across positions
Preprocessing	
$\mathbf{P_R}$	Projection matrix for the spatial dimension that isolates the self response into a low-dimensional subspace
$\mathbf{P_G}$	Projection matrix for the measurement dimension that isolates the soil response into a low-dimensional subspace
$\mathbf{P_{GG}}$	Projection into the soil subspace
$\mathbf{P_{GG}^{\perp}}$	Projection away from the soil subspace
$\mathbf{U_G^A}$	Left singular vectors of the DSRF matrix that has been projected into the soil subspace
$\mathbf{\Sigma_G^A}$	Singular values of the DSRF matrix that has been projected into the soil subspace
$\mathbf{V_G^A}$	Right singular vectors of the DSRF matrix that has been projected into the soil subspace
$\mathbf{U_{\bar{G}}^A}$	Left singular vectors of the DSRF matrix that has been projected away from the soil subspace
$\mathbf{\Sigma_{\bar{G}}^A}$	Singular values of the DSRF matrix that has been projected away from the soil subspace
$\mathbf{V_{\bar{G}}^A}$	Right singular vectors of the DSRF matrix that has been projected away from the soil subspace
$\mathbf{U_{\bar{G}S}^A}$	Left singular vectors of the DSRF matrix that has been projected away from the soil subspace and is above the noise cutoff
$\mathbf{\Sigma_{\bar{G}S}^A}$	Singular values of the DSRF matrix that has been projected away from the soil subspace and is above the noise cutoff

Continued on next page

Table C.2 – continued from previous page

$\mathbf{V}^{\mathbf{A}}_{\bar{\mathbf{G}}\mathbf{S}}$	Right singular vectors of the DSRF matrix that has been projected away from the soil subspace and is above the noise cutoff
$\mathbf{U}^{\mathbf{A}}_{\bar{\mathbf{G}}\mathcal{E}}$	Left singular vectors of the DSRF matrix that has been projected away from the soil subspace and is below the noise cutoff
$\mathbf{\Sigma}^{\mathbf{A}}_{\bar{\mathbf{G}}\mathcal{E}}$	Singular values of the DSRF matrix that has been projected away from the soil subspace and is below the noise cutoff
$\mathbf{V}^{\mathbf{A}}_{\bar{\mathbf{G}}\mathcal{E}}$	Right singular vectors of the DSRF matrix that has been projected away from the soil subspace and is below the noise cutoff
$\lambda_{\mathbf{G}\mathcal{E}}$	Desired SNR cutoff for measurement dimension preprocessing stage
$\mathbf{P}_{\bar{\mathbf{G}}\mathbf{S}}$	Projection away from the soil subspace that contains signal
$\mathbf{P}_{\bar{\mathbf{G}}\mathcal{E}}$	Projection away from the soil subspace that does not contain a significant amount of signal
δ_g	Ratio of the remaining signal power in the DSRF matrix after projected away from the soil to the original matrix power
$\boldsymbol{\mathcal{D}}$	The Discrete Cosine Transform matrix
$\boldsymbol{\mathcal{D}}_L$	The low frequency/ long spatial wavelength DCT components
$\boldsymbol{\mathcal{D}}_M$	The target frequency/ target spatial wavelength DCT components
$\boldsymbol{\mathcal{D}}_S$	The high frequency/ short spatial wavelength DCT components
$\mathbf{P}_{\mathbf{RR}}$	Projection into the sensor's self response subspace
$\mathbf{P}_{\bar{\mathbf{R}}\mathbf{S}}$	Projection away from the sensor's self response subspace that contains the signal
$\mathbf{P}_{\bar{\mathbf{R}}\mathcal{E}}$	Projection away from the sensor's self response subspace that does not contain a significant amount of signal
Measurement Subblocks	
$\mathbf{M}^{\mathbf{RR}}_{\bar{\mathbf{G}}\mathbf{S}}$	Measurement subblock containing the self response in the spatial dimension and the target response in the measurement dimension
$\mathbf{M}^{\bar{\mathbf{R}}\mathbf{S}}_{\bar{\mathbf{G}}\mathbf{S}}$	Measurement subblock containing the target response in the spatial dimension and the target response in the measurement dimension
$\mathbf{M}^{\bar{\mathbf{R}}\mathcal{E}}_{\bar{\mathbf{G}}\mathbf{S}}$	Measurement subblock containing noise in the spatial dimension and the target response in the measurement dimension
$\mathbf{M}^{\mathbf{RR}}_{\bar{\mathbf{G}}\mathcal{E}}$	Measurement subblock containing the self response in the spatial dimension and noise in the measurement dimension
$\mathbf{M}^{\bar{\mathbf{R}}\mathbf{S}}_{\bar{\mathbf{G}}\mathcal{E}}$	Measurement subblock containing the target response in the spatial dimension and noise in the measurement dimension

Continued on next page

Table C.2 – continued from previous page

$\mathbf{M}_{\bar{\mathbf{G}}\mathcal{E}}^{\bar{\mathbf{R}}\mathcal{E}}$	Measurement subblock containing noise in the spatial dimension and noise in the measurement dimension
$\mathbf{M}_{\mathbf{GG}}^{\mathbf{RR}}$	Measurement subblock containing the self response in the spatial dimension and the soil response in the measurement dimension
$\mathbf{M}_{\mathbf{GG}}^{\bar{\mathbf{R}}\mathbf{S}}$	Measurement subblock containing the target response in the spatial dimension and the soil response in the measurement dimension
$\mathbf{M}_{\mathbf{GG}}^{\bar{\mathbf{R}}\mathcal{E}}$	Measurement subblock containing noise in the spatial dimension and the soil response in the measurement dimension
$\mathbf{M_S}$	Desirable measurement subblock that contains high SNR signal and no interferers
$\mathbf{S_S}$	The modeled target response in the $\mathbf{M_S}$ subblock
$\mathcal{E}_\mathbf{S}$	The noise matrix in the $\mathbf{M_S}$ subblock
Low-Rank Preprocessing	
$\mathbf{U}_{\mathbf{M_S}}$	Left singular vectors of the $\mathbf{M_S}$ subblock
$\mathbf{\Sigma}_{\mathbf{M_S}}$	Singular values of the $\mathbf{M_S}$ subblock
$\mathbf{V}_{\mathbf{M_S}}$	Right singular vectors of the $\mathbf{M_S}$ subblock
$\mathbf{U}_\mathbf{S}^{\mathbf{M_S}}$	Strongest left singular vectors of $\mathbf{U}_{\mathbf{M_S}}$ that contain the target information
$\mathbf{\Sigma}_\mathbf{S}^{\mathbf{M_S}}$	Strongest singular values of $\mathbf{\Sigma}_{\mathbf{M_S}}$ that contain the target information
$\mathbf{V}_\mathbf{S}^{\mathbf{M_S}}$	Strongest right singular vectors of $\mathbf{V}_{\mathbf{M_S}}$ that contain the target information
$\mathbf{U}_\mathcal{E}^{\mathbf{M_S}}$	Weaker left singular vectors of $\mathbf{U}_{\mathbf{M_S}}$ that contain noise measurements
$\mathbf{\Sigma}_\mathcal{E}^{\mathbf{M_S}}$	Weaker singular values of $\mathbf{\Sigma}_{\mathbf{M_S}}$ that contain noise measurements
$\mathbf{V}_\mathcal{E}^{\mathbf{M_S}}$	Weaker right singular vectors of $\mathbf{V}_{\mathbf{M_S}}$ that contain noise measurements
$\lambda_\mathcal{E}^{\mathbf{M_S}}$	The common singular value of $\mathcal{E}_\mathbf{S}$
$\mathbf{P_S}$	Adaptive spatial projection matrix to consolidate target response based on the measured target's $\mathbf{V}_\mathbf{S}^{\mathbf{M_S}}$
$\mathbf{P}_\mathbf{S}^\perp$	Adaptive spatial projection matrix away from the target response based on the measured target's $\mathbf{V}_\mathbf{S}^{\mathbf{M_S}}$
Detection Theory	
$\boldsymbol{K}_\epsilon$	The known covariance structure of the measurement noise
$\mathbf{z}$	Projected version of the measurements that isolates the signal
$\mathbf{z}_1$	The portion of $\mathbf{z}$ that contains signal and noise
$\mathbf{z}_2$	The portion of $\mathbf{z}$ that contains only noise
γ	Detection value that is compared to a threshold
$\boldsymbol{P}_d$	Projection matrix that isolates the signal from the noise

Continued on next page

Table C.2 – continued from previous page

$\mathbf{Z}_1$	A matrix containing signal and noise
$\mathbf{Z}_2$	A matrix containing only noise
MSD Detection	
$\gamma_{\mathbf{S}}$	Detection metric based on $\mathbf{M_S}$
$\gamma_{\mathbf{G}}$	Detection metric based on $\mathbf{M}_{\mathbf{GG}}^{\bar{\mathbf{R}}\mathbf{S}}$
$\gamma_{\mathbf{\Sigma S}}$	Detection metric based on $\mathbf{\Sigma}_{\mathbf{S}}^{\mathbf{M_S}}$
$\gamma_{\mathbf{\Sigma G}}$	Detection metric based on $\mathbf{M}_{\mathbf{GG}}^{\bar{\mathbf{R}}\mathbf{S}}\mathbf{P}_{\mathbf{S}}^{T}$
CFAR Detection	
$\gamma_{\mathcal{E}}^{\mathbf{G}}$	Detection metric converting $\gamma_{\mathbf{G}}$ to CFAR by using $\mathbf{M}_{\mathbf{GG}}^{\bar{\mathbf{R}}\mathcal{E}}$ as a noise matrix
$\gamma_{\mathcal{E}}^{\mathbf{\Sigma G}}$	Detection metric converting $\gamma_{\mathbf{\Sigma G}}$ to CFAR by using $\mathbf{M}_{\mathbf{GG}}^{\bar{\mathbf{R}}\mathcal{E}}$ as a noise matrix
$\gamma_{\mathbf{\Sigma}\mathcal{E}}^{\mathbf{\Sigma G}}$	Detection metric converting $\gamma_{\mathbf{\Sigma G}}$ to CFAR by using $\mathbf{M}_{\mathbf{GG}}^{\bar{\mathbf{R}}\mathbf{S}}\mathbf{P}_{\mathbf{S}}^{\perp T}$ as a noise matrix
$\gamma_{\mathbf{\Pi}}^{\mathbf{\Sigma G}}$	Detection metric converting $\gamma_{\mathbf{\Sigma G}}$ to CFAR by using all available noise matrices
$\gamma_{\mathcal{E}}^{\mathbf{S}}$	Detection metric converting $\gamma_{\mathbf{S}}$ to CFAR by using $\mathbf{M}_{\bar{\mathbf{G}}\mathcal{E}}^{\bar{\mathbf{R}}\mathcal{E}}$ as a noise matrix
$\gamma_{\mathbf{G}\mathcal{E}}^{\mathbf{S}}$	Detection metric converting $\gamma_{\mathbf{S}}$ to CFAR by using $\mathbf{M}_{\bar{\mathbf{G}}\mathcal{E}}^{\bar{\mathbf{R}}\mathbf{S}}$ as a noise matrix
$\gamma_{\mathbf{R}\mathcal{E}}^{\mathbf{S}}$	Detection metric converting $\gamma_{\mathbf{S}}$ to CFAR by using $\mathbf{M}_{\bar{\mathbf{G}}\mathbf{S}}^{\bar{\mathbf{R}}\mathcal{E}}$ as a noise matrix
$\gamma_{\mathbf{\Pi}}^{\mathbf{S}}$	Detection metric converting $\gamma_{\mathbf{S}}$ to CFAR by using all available noise matrices
$\gamma_{\mathcal{E}}^{\mathbf{\Sigma S}}$	Detection metric converting $\gamma_{\mathbf{\Sigma S}}$ to CFAR by using $\mathbf{M}_{\bar{\mathbf{G}}\mathcal{E}}^{\bar{\mathbf{R}}\mathcal{E}}$ as a noise matrix
$\gamma_{\mathbf{G}\mathcal{E}}^{\mathbf{\Sigma S}}$	Detection metric converting $\gamma_{\mathbf{\Sigma S}}$ to CFAR by using $\mathbf{M}_{\bar{\mathbf{G}}\mathcal{E}}^{\bar{\mathbf{R}}\mathbf{S}}$ as a noise matrix
$\gamma_{\mathbf{R}\mathcal{E}}^{\mathbf{\Sigma S}}$	Detection metric converting $\gamma_{\mathbf{\Sigma S}}$ to CFAR by using $\mathbf{M}_{\bar{\mathbf{G}}\mathbf{S}}^{\bar{\mathbf{R}}\mathcal{E}}$ as a noise matrix
$\gamma_{\mathbf{\Sigma}\mathcal{E}}^{\mathbf{\Sigma S}}$	Detection metric converting $\gamma_{\mathbf{\Sigma S}}$ to CFAR by using $\mathbf{\Sigma}_{\mathcal{E}}^{\mathbf{M_S}}$ as a noise matrix
$\gamma_{\mathbf{\Pi}}^{\mathbf{\Sigma S}}$	Detection metric converting $\gamma_{\mathbf{\Sigma S}}$ to CFAR by using all available noise matrices
Joint Detection Theory	
$\mu_{\mathbf{S}}$	Scalar multiplier for the signal strength in the $\mathbf{M}_{\bar{\mathbf{G}}\mathbf{S}}^{\bar{\mathbf{R}}\mathbf{S}}$ subblock
$\mu_{\mathbf{G}}$	Scalar multiplier for the signal strength in the $\mathbf{M}_{\mathbf{GG}}^{\bar{\mathbf{R}}\mathbf{S}}$ subblock
$\mathbf{z_{JS}}$	The signal and noise vector for joint detection using subblocks
$\mathbf{z_{J\Sigma}}$	The signal and noise vector for joint detection using consolidated subblocks
$\boldsymbol{R}_{\mathbf{G}\mathcal{E}}$	The known covariance structure of the joint detection vector
$\sigma_{g\epsilon}^2$	Variance of the noise and soil terms combined
Rank Estimation	
$\mathbf{\Lambda_M}$	Eigenvalues of the full-rank covariance matrix associated with $\mathbf{M}$
$\mathbf{U_\Lambda}$	All of the left singular vectors of $\mathbf{M}$
$\mathbf{\Sigma_\Lambda}$	All of the singular values of $\mathbf{M}$
$\mathbf{V_\Lambda}$	All of the right singular vectors of $\mathbf{M}$

Continued on next page

Table C.2 – continued from previous page

DSRF Inversion	
$\mathbf{A}_{\boldsymbol{P}}$	Projected version of the DSRF Dictionary
λ	Tuning parameter of the sparse recovery optimization problem
$\mathbf{\Lambda}_{\boldsymbol{QU}}$	Eigenvalues of the matrix $\mathbf{Q}_{\mathbf{U}}$
$\mathbf{R}_{\boldsymbol{QU}}$	Eigenvectors of the matrix $\mathbf{Q}_{\mathbf{U}}$
$\lambda_{\boldsymbol{QU}}$	Common eigenvalue of the matrix $\mathbf{Q}_{\mathbf{U}}$ for an ideal EMI sensor
$\vec{\boldsymbol{W}}_{\boldsymbol{Q}\mathbf{A}}$	Sparse nonnegative matrix of weights mapping tensor basis to DSRF dictionary and also containing $\lambda_{\boldsymbol{QU}}$
Target Classification	
$\mathbf{B}_{\mathbf{U}}$	Arbitrary square matrix mapping the model subspace to the left singular vectors
$\boldsymbol{\mathcal{X}}$	Set of all targets' subspace models

Table C.2: List of all variables used in this thesis.

C.3 Mathematical Operations

$\in$	Value is part of a set
$\mathfrak{R}$	Set of real numbers
$\mathfrak{R}_+$	Set of nonnegative real numbers
$\mathfrak{R}_-$	Set of non-positive real numbers
$\mathfrak{C}$	Set of complex numbers
$*$	Convolution operator
$\square^T$	Transpose operator
$\square^H$	Hermitian operator
$\mathfrak{F}\{\square\}$	Fourier transform
$\vec{\square}$	Indicates a variable is in an ortho-point target coordinate system
Eig$\{\square\}$	Eigenvalue decomposition
s-vec$\{\square\}$	Convert a symmetric matrix into a vector and ignore repeated terms
$\mathcal{N}(\mu, \sigma^2)$	Normally distributed random variable with mean (μ) and variance (σ^2)
$\mathcal{CN}(\mu, \sigma^2)$	Complex normally distributed random variable with mean (μ) and variance (σ^2)
$\tilde{\square}$	Indicates a variable is a complex value
$\Re\{\square\}$	Take the real part of a complex value
$\Im\{\square\}$	Take the imaginary part of a complex value
$\|\square\|_2$	The ℓ_2 norm of a vector
$\|\square\|_1$	The ℓ_1 norm of a vector
$\|\square\|_F$	The Frobenius norm of a matrix
vec $\{\square\}$	Convert a matrix into a vector
$\square^\dagger$	The Psuedo-inverse of a matrix defined as $(\square^T\square)^{-1}\square^T$
$\mathcal{L}\{\square\}$	Loglikelihood function
$\ln(\square)$	Natural log function

Table C.3: List of mathematical operations used in this thesis.

C.4 Acronyms

SVD	Singular Value Decomposition
EMI	Electromagnetic Induction
SoD	Sum of Dipoles
PSD	Positive Semi-Definite
RT-01	Reference target 1: single coil
RT-02	Reference target 2: three orthogonal coils
RT-03	Reference target 3: a rotationally symmetric target in three dimensions
RT-04	Reference target 4: a rotationally symmetric target in the y-z dimensions
RT-05	Reference target 5: a target with the same relaxations as RT-03 all in the x dimension
RT-06	Reference target 6: a target with the same relaxations as RT-04 split between the x and y dimensions
RT-07	Reference target 7: two coils that violate the ortho-point assumption
RT-08	Reference target 8: size coils that violate the ortho-point assumption
RT-09	Reference target 9: the same as RT-02 but with varying magnitudes
RT-10	Reference target 10: the same as RT-06 but with varying magnitudes
DSRF	Discrete Spectrum of Relaxation Frequencies
SNR	Signal to Noise Ratio
SINR	Signal to Interference and Noise Ratio
DFT	Discrete Fourier Transform
DCT	Discrete Cosine Transform
i.i.d.	Independent Identically Distributed
ROC	Receiver Operating Characteristic
ROC	Receiver Operating Characteristic
SS	Subspace Selection
SSC	Sparse Subspace Creation
SP	Subspace Projection
GT	Georgia Tech
AIC	Akaike Information Criterion
BIC	Bayesian Information Criterion
DOA	Direction of Arrival
DS	Delay-and-Sum

Continued on next page

Table C.4 – continued from previous page

MP	Matching Pursuit
NNLSQ	Nonnegative Least Squares
LARS	Least Angle Regression
IAA	Iterative Adaptive Approach
FOCUSS	FOCal Underdetermined System Solver
NRLS	Nonnegative Rotational Least Squares
NMF	Nonnegative Matrix Factorization
EMD	Earth Mover's Distance
MLE	Maximum Likelihood Estimation

Table C.4: List of acronyms used in this thesis.

REFERENCES

[1] L. Robledo, M. Carrasco, and D. Mery, "A survey of land mine detection technology," *International Journal of Remote Sensing*, vol. 30, no. 9, pp. 2399–2410, 2009. eprint: http://dx.doi.org/10.1080/01431160802549435.

[2] C. E. Baum, "Low-frequency near-field magnetic scattering from highly, but not perfectly, conducting bodies," in *Detection and identification of visually obscured targets*, CRC Press, 1998, ch. 6, pp. 163–218.

[3] W. R. Scott Jr. and G. D. Larson, "Modeling the measured EM induction response of targets as a sum of dipole terms each with a discrete relaxation frequency," in *Geoscience and Remote Sensing Symposium (IGARSS), 2010 IEEE International*, 2010, pp. 4188–4191.

[4] T. H. Bell, B. J. Barrow, and J. T. Miller, "Subsurface discrimination using electromagnetic induction sensors," *IEEE Transactions on Geoscience and Remote Sensing*, vol. 39, no. 6, pp. 1286–1293, 2001.

[5] M.-H. Wei, "Electromagnetic induction spectroscopy for the detection of subsurface targets," PhD thesis, Georgia Institute of Technology, 2012.

[6] F. Shubitidze, J. P. Fernandez, I. Shamatava, B. E. Barrowes, and K. O'Neill, "Joint diagonalization applied to the detection and discrimination of unexploded ordnance," *Geophysics*, vol. 77, no. 4, WB149–WB160, 2012.

[7] L.-P. Song, D. W. Oldenburg, and L. R. Pasion, "Estimating source locations of unexploded ordnance using the multiple signal classification algorithm," *Geophysics*, vol. 77, no. 4, WB127–WB135, 2012.

[8] L.-P. Song, L. R. Pasion, and D. W. Oldenburg, "Space-time music imaging of emi sensing data and a subspace partition study," *Journal of Electromagnetic Waves and Applications*, vol. 31, no. 15, pp. 1520–1540, 2017.

[9] D. A. Steinhurst, G. R. Harbaugh, J. B. Kingdon, T Furuya, D. A. Keiswetter, and D. C. George, *Emi array for cued uxo discrimination. estcp project mm-0601 final report*, 2010.

[10] M.-H. Wei, W. R. Scott, and J. H. McClellan, "Robust estimation of the discrete spectrum of relaxations for electromagnetic induction responses," *IEEE Transactions on Geoscience and Remote Sensing*, vol. 48, no. 3, pp. 1169–1179, 2010.

[11] K. R. Krueger, W. R. Scott Jr., and J. H. McClellan, "Extracting target orientation for different electromagnetic induction sensing geometries," in *2014 IEEE Geoscience and Remote Sensing Symposium*, 2014, pp. 3156–3159.

[12] K. R. Krueger, W. R. Scott Jr., and J. H. McClellan, "Location and orientation estimation of buried targets using electromagnetic induction sensors," *Proc. SPIE*, vol. 8357, pp. 83570D–83570D–12, 2012.

[13] M.-H. Wei, W. R. Scott, and J. H. McClellan, "Landmine detection using the discrete spectrum of relaxation frequencies," in *Geoscience and Remote Sensing Symposium (IGARSS), 2011 IEEE International*, IEEE, 2011, pp. 834–837.

[14] M.-H. Wei, W. R. Scott Jr., and J. H. McClellan, "Adaptive prefiltering for non-negative discrete spectrum of relaxations," *Geoscience and Remote Sensing Letters, IEEE*, vol. 12, no. 5, pp. 1018–1022, 2015.

[15] S. L. Tantum and L. M. Collins, "A comparison of algorithms for subsurface target detection and identification using time-domain electromagnetic induction data," *IEEE Trans. Geoscience and Remote Sensing*, vol. 39, no. 6, pp. 1299–1306, 2001.

[16] L. S. Riggs, J. E. Mooney, and D. E. Lawrence, "Identification of metallic mine-like objects using low frequency magnetic fields," *IEEE Trans. Geoscience and Remote Sensing*, vol. 39, no. 1, pp. 56–66, 2001.

[17] C. Bruschini, "A multidisciplinary analysis of frequency domain metal detectors for humanitarian demining," PhD thesis, Vrije Universiteit Brussel, 2002.

[18] J. T. Smith and H. F. Morrison, "Estimating equivalent dipole polarizabilities for the inductive response of isolated conductive bodies," *IEEE Transactions on Geoscience and Remote Sensing*, vol. 42, no. 6, pp. 1208–1214, 2004.

[19] K. R. Krueger, J. H. McClellan, and W. R. Scott Jr., "Tensor amplitude extraction in sensor array processing," in *2013 IEEE International Conf. Acoustics, Speech and Signal Processing*, 2013, pp. 3895–3899.

[20] C. E. Hayes, W. R. Scott, and J. H. McClellan, "Low-rank model for wideband electromagnetic induction sensors," *IEEE Geoscience and Remote Sensing Letters*, vol. 14, no. 12, pp. 2413–2417, 2017.

[21] C. Eckart and G. Young, "The approximation of one matrix by another of lower rank," *Psychometrika*, vol. 1, no. 3, pp. 211–218, 1936.

[22] D. Malioutov, M. Cetin, and A. S. Willsky, "A sparse signal reconstruction perspective for source localization with sensor arrays," *IEEE Trans. Signal Processing*, vol. 53, no. 8, pp. 3010–3022, 2005.

[23] T. Yardibi, J. Li, P. Stoica, M. Xue, and A. Baggeroer, "Source localization and sensing: A nonparametric iterative adaptive approach based on weighted least squares," *IEEE Trans. Aerospace and Electronic Systems*, vol. 46, no. 1, pp. 425–443, 2010.

[24] S. Cotter, B. Rao, K. Engan, and K. Kreutz-Delgado, "Sparse solutions to linear inverse problems with multiple measurement vectors," *IEEE Trans. Signal Processing*, vol. 53, no. 7, pp. 2477–2488, 2005.

[25] G. W. Stewart, *Perturbation theory for the singular value decomposition*, 1998.

[26] C. E. Hayes, J. H. McClellan, and W. R. Scott Jr., "Novel model based EMI processing framework," *Proc. SPIE*, vol. 10182, pp. 1 018 218–1018218–17, 2017.

[27] C. E. Hayes, J. H. McClellan, W. R. Scott, and A. J. Kerr, "Improved electromagnetic induction processing with novel adaptive matched filter and matched subspace detection," in *Detection and Sensing of Mines, Explosive Objects, and Obscured Targets XXI*, International Society for Optics and Photonics, vol. 9823, 2016, 98230E.

[28] W. R. Scott Jr., G. D. Larson, C. E. Hayes, and J. H. McClellan, "Experimental detection and discrimination of buried targets using an improved broadband CW electromagnetic induction sensor," *Proc. SPIE*, vol. 9072, pp. 90720C–90720C–15, 2014.

[29] C. E. Hayes, J. H. McClellan, and W. R. Scott Jr., "Sparse recovery using an SVD approach to interference removal and parameter estimation," in *2015 IEEE Signal Processing & SP Education Workshop*, 2015.

[30] M. H. Wei, W. R. Scott Jr., and J. H. McClellan, "Robust estimation of the discrete spectrum of relaxations for electromagnetic induction responses," *IEEE Trans. Geoscience and Remote Sensing*, vol. 48, no. 3, pp. 1169–1179, 2010.

[31] L. L. Scharf and B. Friedlander, "Matched subspace detectors," *IEEE Trans. Signal Processing*, vol. 42, no. 8, pp. 2146–2157, 1994.

[32] S. Kraut, L. Scharf, and R. Butler, "The adaptive coherence estimator: A uniformly most-powerful-invariant adaptive detection statistic," *IEEE Trans. Signal Processing*, vol. 53, no. 2, pp. 427–438, 2005.

[33] P. Stoica and Y. Selen, "Model-order selection: A review of information criterion rules," *IEEE Signal Processing Magazine*, vol. 21, no. 4, pp. 36–47, 2004.

[34] D. H. Johnson and D. E. Dudgeon, *Array signal processing: concepts and techniques*. PTR Prentice Hall Englewood Cliffs, 1993, pp. 390–393.

[35] C. E. Hayes, J. H. McClellan, and W. R. Scott, "Sparse recovery using an svd approach to interference removal and parameter estimation," in *Signal Processing and Signal Processing Education Workshop (SP/SPE), 2015 IEEE*, IEEE, 2015, pp. 202–207.

[36] H. L. Van Trees, *Optimum array processing: Part IV of detection, estimation, and modulation theory*. John Wiley & Sons, 2004.

[37] R. Schmidt, "Multiple emitter location and signal parameter estimation," *IEEE Transactions on Antennas and Propagation*, vol. 34, no. 3, pp. 276–280, 1986.

[38] S. F. Cotter, "Multiple snapshot matching pursuit for direction of arrival (doa) estimation," in *2007 15th European Signal Processing Conference*, IEEE, 2007, pp. 247–251.

[39] E. Al-Ardi, R. Shubair, and M. Al-Mualla, "Computationally efficient high-resolution doa estimation in multipath environment," *Electronics Letters*, vol. 40, no. 14, pp. 908–910, 2004.

[40] B. Efron, T. Hastie, I. Johnstone, R. Tibshirani, *et al.*, "Least angle regression," *The Annals of statistics*, vol. 32, no. 2, pp. 407–499, 2004.

[41] D. D. Lee and H. S. Seung, "Algorithms for non-negative matrix factorization," in *Advances in neural information processing systems*, 2001, pp. 556–562.

[42] J. Kim and H. Park, "Toward faster nonnegative matrix factorization: A new algorithm and comparisons," in *2008 Eighth IEEE International Conference on Data Mining*, IEEE, 2008, pp. 353–362.

[43] M. Richards, *Fundamentals of Radar Signal Processing, Second Edition*. McGraw-Hill Education, 2014.

[44] A. J. Weiss, "Direct position determination of narrowband radio frequency transmitters," *IEEE signal processing letters*, vol. 11, no. 5, pp. 513–516, 2004.

[45] K. R. Krueger, "Model design for algorithmic efficiency in electromagnetic sensing," PhD thesis, Georgia Institute of Technology, 2013.

[46] C. E. Hayes, J. H. McClellan, and W. R. Scott, "Low-rank physical model recovery from low-rank signal approximation," in *Acoustics, Speech and Signal Processing (ICASSP), 2017 IEEE International Conference on*, IEEE, 2017, pp. 3131–3135.

[47] C. E. Hayes, W. R. Scott, and J. H. McClellan, "Exploiting measurement subspaces for wideband electromagnetic induction processing," in *Detection and Sensing of*

Mines, Explosive Objects, and Obscured Targets XXIII, International Society for Optics and Photonics, vol. 10628, 2018, p. 106280M.

[48] A. J. Kerr, W. R. Scott, C. E. Hayes, and J. H. McClellan, "Target location estimation for single channel electromagnetic induction data," in *Detection and Sensing of Mines, Explosive Objects, and Obscured Targets XXII*, International Society for Optics and Photonics, vol. 10182, 2017, p. 1 018 212.

[49] W. R. Scott Jr, C. E. Hayes, and J. H. McClellan, "Classification using low-rank features from an electromagnetic induction sensor," in *Detection and Sensing of Mines, Explosive Objects, and Obscured Targets XXIV*, International Society for Optics and Photonics, vol. 11012, 2019, 110120R.

[50] P. H. Schönemann, "A generalized solution of the orthogonal procrustes problem," *Psychometrika*, vol. 31, no. 1, pp. 1–10, 1966.

VITA

Charles Ethan Hayes was born and raised in North Carolina, U.S.A. He received a Bachelor of Science (2013), Master of Science (2015), and Doctor of Philosophy (2020) in Electrical and Computer Engineering from the Georgia Institute of Technology. His area of studies was digital signal processing. His doctoral research under Prof. James H. McClellan and Waymond R. Scott, Jr. focused on improving the signal processing of electromagnetic induction sensors for detecting, classifying, and localizing buried landmines. Dr. Hayes has been employed as a controls engineer for General Mills, algorithm engineer for LED lighting at Cirrus Logic, radar algorithm engineer for Raytheon, and an RF algorithm and machine learning engineer at Northrop Grumman. Dr. Hayes' research interests primarily concern integrating and applying physical and mathematical models into signal processing, machine learning, and convex optimization applications.